Université de Lille

Sciences et Technologies

Ecole Doctorale Sciences Pour l'Ingénieur

Thèse de doctorat

Électronique, Microélectronique, Nanoélectronique et Micro-ondes

Ultrasensitive detection of ricin-like proteins by innovative graphene-based sensors, using mass spectrometry

Détection ultrasensible de la toxine de ricine par des capteurs innovant à base de graphène, utilisant la spectrométrie de masse

Ioana Silvia Hosu

Soutenue le 11/02/2020

Membres du jury:

Président	Tuami Lasri	Professeur Université de Lille, IEMN
Rapporteur	Celine Elie-Caille	Maître de conférences, Université de Franche-Comté, FEMTO-ST
Rapporteur	Yann Chevolot	Directeur de recherche CNRS, Ecole centrale de Lyon, INL
Examinateur	Rabah Boukherroub	Directeur de recherche CNRS, Université de Lille, IEMN
Examinateur	Claudia Muracciole Bich	Maître de conférences, Université de Montpellier, IBMM
Directeur de thèse	Yannick Coffinier	Charge de recherche CNRS, Université de Lille, IEMN
Invité	Didier Hilaire	DGA, Paris

© 2020 Tous droits réservés.

lilliad.univ-lille.fr

Thèse de Ioana Silvia Hosu, Université de Lille, 2020

Abstract

Bio-terroristic attacks have become more frequent in the past years and the wide range of bio-terroristic agents makes this an important issue to overcome. Ricin is part of the ribosome-inactivating proteins (RIP). RIPs are vegetable toxins, water soluble, which can be easily extracted from plants (ricin from castor beams, abrin from rosary pea) or from bacteria (Shiga toxin). These proteins are composed of two chains: ricin A chain, a glycosidase that insures the toxicity by removal of adenine (depurination) from the RNAr 28S from the 60S ribosomal subunits, followed by the inhibition of protein synthesis, and ricin B chain, a lectin that binds to specific sugar moieties on the surface of the cells, assuring transportation the cell uptake. As they inhibit protein synthesis, depending of the administration take-up (oral, inhalation, intravenously) and the dose received, cell death also occurs. In the absence of efficient counter measurements, detection methods of these toxins have to be fast, reliable, selective and suitable, especially pre-assimilation analysis. The current used methods do not overcome all these requirements.

Even though mass spectrometry was used for ricin detection, it cannot be performed without long and tedious sample preparation, meaning through enzymatic digestion, extraction/purification and identification of the proteins based on the peptide analysis, followed by comparison with an existent database (mass fingerprint). In this work, we describe how carbon-based materials (carbon nanowalls and others) can be used as nanostructured materials for specific ricin-like proteins sensors, using surface assisted laser/desorption ionization mass spectrometry (SALDI-MS) and other techniques. The suitability of the carbon nanowalls (CNWS) was proven initially for other smaller bio-molecules (saccharides, peptides up to 5800 m/z, carbohydrates, lipids and glucose, which was also quantified using SALDI-MS).

When it comes to proteins, literature describes they are hard to ionize and to detect using SALD-MS, due, in part, to their big molecular weight. The ability of CNWs to desorb and ionize proteins required a lot of experimental optimization steps of the SALDI-MS method (salt nature, concentration, and pH, incubation time, physicochemical characteristics of the nanowalls, such as height, boron doping and morphology).

A systematic optimization was done using a model protein, the cytochrome C (Mw= 12,384 Da). From this, we were able, for the first time, to detect Ricin B chain (Mw= 32kDa) without the use of organic matrix. To go further in improving Ricin detection performances, carbon nanowalls were then covalently modified using specific lectin sugars (galactosamine)

© 2020 Tous droits réservés.

lilliad.univ-lille.fr

Thèse de Ioana Silvia Hosu, Université de Lille, 2020

and the ability to detect Ricin B chain in real samples such as soft drinks and blood serum was demonstrated within10 minutes. We obtained a limit of detection (80 ng/0.5 μL) that is 3 times lower than the lowest median lethal dose (LD_{50} = 10 μg/kg).

Multifunctional surfaces are described as perspectives for more powerful bimodal analytical tools, by combining two techniques, such as: SPR(Surface Plasmon Resonance)/SALDI-MS, SERS(Surface Enhanced Raman Spectroscopy)/SALDI-MS and EC(Electrochemistry)/SALDI-MS. Special attention was focused on SPR/SALDI-MS as it can achieve both quantitative and molecular interactions in real-time (SPR) and precise identification of the analytes (MS).

In order to obtain a surface that is compatible with two complementary techniques, we had to determine which is the best material, taking in consideration the thickness of the material layer, the physical chemistry and the morphological structure of the material, as well as the substrate on which is deposited. To obtain this compatibility and ensure the optimal surface coverages, we studied different depositions methods of graphene-like materials: 1) bubble surfactant method of graphene oxide, 2) wet transfer of CVD pristine graphene, 3) electrophoretic deposition of graphene, 4) layer by layer using a polycation and graphene oxide, 5) drop casting of both graphene and reduced graphene oxide. Cytochrome C (as model protein) was detected using the first three methods and only peptides were detected for the last two methods. The order in which these deposition methods are mentioned is in correlation with decreasing SALDI-MS efficiency towards proteins.

In this thesis, we described the first world wide ricin-like proteins SALDI-MS sensor, which is able to detect below the lethal dose in humans and bring an important contribution to the fight against eventual terroristic attacks. The systematic study of different parameters that influence this LDI-MS process is also presented. The dual surfaces studied, in particular the SPR/MS bimodal techniques, presented reliable consistency for further approaches in creating more powerful analytical tools.

Keywords: MALDI-MS, carbon nanowalls, SALDI-MS, graphene, ricin, laser desorption ionization mass spectrometry

© 2020 Tous droits réservés.

lilliad.univ-lille.fr

Thèse de Ioana Silvia Hosu, Université de Lille, 2020

Résume

Les attaques bioterroristes sont devenues plus fréquentes ces dernières années et le large éventail d'agents bioterroristes en fait un problème important à résoudre. La ricine appartient à la famille des protéines inactivant les ribosomes (RIP). Les RIP sont des toxines biologiques, solubles dans l'eau, qui peuvent être facilement extraites de plantes (ricine de graines de *Ricinus communis* et abrine de graines d'*Abrus precatorius*) ou de bactéries (toxine de Shiga). La ricine est composée de deux chaînes: la chaîne A de la ricine, une N-glycosidase induisant la toxicité par élimination de l'adénine (action de dépurination) de l'ARNr 28S des sous-unités ribosomales 60S, inhibant la synthèse protéique, et la chaîne B, une lectine qui se lie aux fragments de sucre spécifiques sur la membrane extracellulaire, assurant l'absorption de la toxine. Comme ils inhibent la synthèse des protéines, en fonction de la voie d'absorption (orale, par inhalation, par voie intraveineuse) et de la dose reçue, la mort peut survenir. En l'absence de contre-mesures efficaces, les méthodes de détection de ces toxines doivent être rapides, fiables, sélectives et sans aucune ambiguïté. Les méthodes actuelles ne répondent pas à toutes ces exigences.

Même si la spectrométrie de masse a été utilisée pour la détection de la ricine, elle ne peut pas être réalisée sans une longue et fastidieuse préparation d'échantillon, c'est-à-dire une digestion enzymatique, une extraction /purification et une identification de protéines sur la base d'une analyse peptidique suivie d'une comparaison avec des bases de données existantes. Dans ce travail, nous avons montré comment les matériaux à base de carbone (nanomurs de carbone) pourraient être appliqués comme matériaux nanostructurés pour la détection de la ricine par désorption/ionisation laser de surface pour la détection par spectrométrie de masse (SALDI-MS). Tout d'abord, l'adéquation des nanomurs de carbone (CNWs) en tant que bonne surface SALDI a été initialement étudiée pour des biomolécules plus petites (saccharides, peptides jusqu'à 5800 m/z, glucides, lipides et glucose, qui a également été quantifié à l'aide de SALDI-MS).

En ce qui concerne les protéines, la littérature a montré qu'elles sont difficiles à ioniser et à détecter avec la méthode SALDI-MS, en raison de leur grand poids moléculaire. La capacité des CNWs à désorber et à ioniser les protéines a nécessité de nombreuses étapes expérimentales d'optimisation (réalisée pour la détection de protéines en jouant avec la nature et la concentration de sels, le temps d'incubation, les caractéristiques physico-chimiques des nanomurs (comme la hauteur, le dopage au bore ou la morphologie).

© 2020 Tous droits réservés.

lilliad.univ-lille.fr

Résume

Pour ce faire, le cytochrome C (Mw= 12,384 Da) a été utilisé comme protéine modèle. Enfin, des nanomurs de carbone alignés verticalement ont ensuite été modifiés à l'aide de sucres à lectine spécifiques (galactosamine), pour la détection spécifique de la chaîne B de la ricine (Mw= 32kDa) dans des échantillons réels, tels que des boissons sans alcool et du sérum sanguin. Nous avons obtenu une limite de détection (80 ng/0.5 µL) soit trois fois inférieure à la dose létale médiane la plus faible (DL_{50} = 10 µg/kg). Cette détection peut être réalisée dans les 10 min.

Dans la dernière partie, des résultats préliminaires concernant la mise au point d'outils analytiques bimodaux seront présentés. Il s'agit de combinaisons telles que: SPR (résonance plasmonique de surface)/SALDI-MS, SERS (Spectroscopie Raman Exaltée de Surface)/SALDI-MS et EC(Électrochimie)/SALDI-MS. Une attention particulière a été portée sur la SPR / SALDI-MS car elle permet d'obtenir des interactions quantitatives et moléculaires en temps réel (SPR) et une identification structurelle des analytes (MS).

Afin d'obtenir une surface compatible avec deux techniques complémentaires, nous avons dû déterminer quel est le meilleur matériau, en tenant compte de l'épaisseur de la couche de matériau, de la chimie physique et de la structure morphologique du matériau, ainsi que du substrat sur lequel est déposé. Pour obtenir cette compatibilité et assurer les couvertures de surface optimales, nous avons étudié différentes méthodes de dépôt de matériaux de type graphène: 1) méthode de surfactant à bulle d'oxyde de graphène, 2) transfert par voie humide de graphène CVD, 3) dépôt électrophorétique de graphène, 4) couche par couche en utilisant un polycation et un oxyde de graphène, 5) coulée en goutte à goutte de graphène et d'oxyde de graphène réduit. Le cytochrome C (en tant que protéine modèle) a été détecté en utilisant les trois premières méthodes et seuls les peptides ont été détectés pour les deux dernières méthodes. L'ordre dans lequel ces méthodes de dépôt sont mentionnées est en corrélation avec la diminution de l'efficacité de SALDI-MS vis-à-vis les protéines.

Cette thèse décrit pour la première fois le dévelopement d'un capteur de type SALDI-MS, capable de détecter la ricine à une dose inférieure à la dose mortelle chez l'homme et d'apporter ainsi une contribution importante à la lutte contre d'éventuelles attaques terroristes. L'étude systématique de différents paramètres qui influencent ce processus LDI-MS est également présentée. Les techniques bimodales comme la SPR-MS, présentent des alternatives intéressantes permettant de créer des outils analytiques plus puissants.

Mots-clés: MALDI-MS, nanomurs de carbone, SALDI-MS, graphène, ricine, spectrométrie de masse à désorption- ionisation par laser.

© 2020 Tous droits réservés.

lilliad.univ-lille.fr

Thèse de Ioana Silvia Hosu, Université de Lille, 2020

Table of content

Abstract……I
Résumé……III
Table of content……1
Acknowledgements……5
Acronyms……7
General Introduction……11
Chapter I. Bibliography: State of the art……15
I.1. Introduction……17
I.2. Background of the subject: Facts about ricin-like toxins……18
I.2.1. Mechanism of toxicity of ricin-like toxins……20
I.3. Methods for ricin-like toxins detection……23
I.3.1. Methods that cannot identify biologically active ricin……23
I.3.1.1 Mass spectrometry……26
I.3.1.2 Ricin-like toxins and Surface Plasmon Resonance (SPR)/ Localized Surface Plasmon Resonance (LSPR)……28
I.3.2. Methods that can identify biologically active ricin……29
I.4. Matrix-free LDI (laser desorption ionization)-Mass Spectrometry……33
I.4.1. Drawbacks of matrix-assisted desorption/ionization……34
I.4.2. Surface-assisted desorption/ionization mass spectrometry (SALDI-MS)……37
I.4.2.1 SALDI-MS mechanism……40
I.4.2.2 Variety of materials used in SALDI-MS and their properties……41
I.4.2.2.a. Semiconductors……42
I.4.2.2.b. Metal/metal oxide nanoparticles/nanostructures……42
I.4.2.2.c. Carbon based materials for SALDI-MS……43
I.4.2.3 Chemical functionalization……43
I.5. Conclusions……45
I.6. References……48
Chapter II. Carbon nanowalls for matrix-free laser desorption/ionization mass spectrometry detection of small compounds in real samples……55
II.1. Introduction ……57
II.2. Optimization of CNWS for SALDI-MS detection of small compounds …… 54
II.2.1. Surface characterization of boron doped CNWs surface …… 61
II.2.1.1 Morphological characterization of CNWs ……61
II.2.1.2 Optical characterization of CNWs ……61
II.2.1.3 Other physical characteristics of CNWs important in SALDI-MS ……64
II.2.1.4 Determination of internal energy for the CNWs …… 65
II.2.2. Detection of small biomolecules diluted in buffers …… 68
II.2.2.1 Detection of peptides …… 68
II.2.2.2 Optimization of important detection parameters using saccharides …… 69
II.2.2.2.a. Influence of the laser power on the SALDI-MS background …… 69
II.2.2.2.b. Influence of alkaline metals on MS performances …… 71
II.2.2.2.c. Influence of the surface chemistry ……72
II.2.2.2.d. Detection of disaccharides ……76
II.2.2.2.e. Studying the homogeneity of drop casted sugars ……77
II.3. Quantitative measurements of glucose in blood serum and soft drinks …… 80
II.4. Detection of melamine, creatinine and paracetamol in urine samples …… 87
II.5. Detection of phosphatidylcholine in lecithin food supplements …… 89
II.6. Conclusions …… 91
II.7. References……93
Chapter III. Carbon nanowalls for matrix-free laser desorption/ionization mass spectrometry detection of ricin B chain from complex media……99
III.1 Introduction ……101
III.1.1. Detecting proteins with SALDI-MS …… 104

© 2020 Tous droits réservés.
lilliad.univ-lille.fr

Table of content

III.2 Optimization of CNWS for SALDI-MS. Detection of cyt C and ricin B chain …….....106
III.2.1 Surface characterization of boron doped CNWs 106
III.2.1.1 Morphological characterization of CNWs 107
III.2.1.2 Optical properties of carbon nanowalls 112
III.2.1.3 Other physical characteristics of CNWS important in SALDI-MS.....114
III.2.1.4 Comparison of physical characteristics of CNWs with literature.....117
III.2.1.5 Surface characterization of ex-situ boron doped CNWs.....119
III.2.2 Optimization of SALDI-MS parameters using cyt C on B-CNWs…….…122
III.2.2.1 Sample deposition methods for SALDI-MS 122
III.2.2.1.a. Incubation of the analyte with CNWS SALDI-MS platform. 122
III.2.2.1.b. Buffer in CNWS SALDI-MS procedure..... 124
III.2.2.2 Boron doping levels and heights of CNWs in SALDI-MS 125
III.2.2.3 Correlation between SALDI-MS signals of cyt C and internal energies 128
III.2.2.4 Sensibility of the CNWs method towards Cytochrome C..... 129
III.2.3 Optimization of parameters using ricin B chain on in-situ doped CNWs..... 134
III.2.3.1 Sample deposition methods for SALDI-MS 134
III.2.3.1.a. Incubation of the analyte with CNWS SALDI-MS platform. 134
III.2.3.1.b. Buffer in CNWS SALDI-MS procedure 135
III.2.3.2 Boron doping levels and nanowalls heights of CNWs in SALDI-MS …….. 136
III.2.3.3 Sensitivity of the CNWs method towards ricin B chain 138
III.3 Affinity strategies for detection of ricin B chain on in-situ boron doped CNWs …….…139
III.3.1 Optimization of SALDI-MS, using non-covalent galactosamine moieties ……..... 140
III.3.2 Optimization of SALDI-MS, using covalent binding of galactosamine..... 141
III.3.3 Surface characterization of NH_2GAL in-situ boron doped CNWs surfaces …….... 145
III.4 Detection of ricin B chain in real samples, using NH_2GAL-CNWS 147
III.4.1 Detection of ricin B chain in Coca-Cola® samples..... 147
III.4.2 Detection of ricin B chain in blood serum samples 148
III.6 Conclusions 150
III.7 References..... 153
Chapter IV. Dual surfaces: Preliminary results and perspectives……157
IV.1 Introduction..... 160
IV.2 SPR-MS using gold/graphene-based interfaces 162
IV.2.1 Important parameters when we combine SPR with MS……..162
IV.2.2 LSPR-MS……..166
IV.2.2.1 Different methods for gold particles' network fabrication 168
IV.2.2.1.a. Deposition of citrated gold nanoparticles (suspension, 20 nm) 168
IV.2.2.1.b. Creating AuNPs through metallization and annealing (dewetting) 170
IV.2.2.1.c. Dots on the Fly..... 171
IV.2.2.2 LSPR-MS conclusions 172
IV.2.3 Graphene-SPR-MS……...174
IV.2.3.1 Graphene and graphene-like (graphene oxid/reduced graphene oxide) methods of deposition on glass/gold surfaces 176
IV.2.3.1.a. Drop-casting 176
IV.2.3.1.a.1. Drop casting conclusions 178
IV.2.3.1.b. Electrophoretic deposition (EPD) 179
IV.2.3.1.b.1. Sample deposition method..... 183
IV.2.3.1.b.2 Electropheoretic deposition conclusions..... 183
IV.2.3.1.c. The transfer of CVD graphene through wet-transfer method …..... 184
IV.2.3.1.c.1. Insulating layer between gold and graphene..... 188
IV.2.3.1.c.2 Use of pyrene-COOH 192
IV.2.3.1.c.3 CVD graphene wet transfer – conclusions..... 193
IV.2.3.1.d. Layer by layer (LBL) 195
IV.2.3.1.d.1. Layer by layer conclusions 199
IV.2.3.1.e. Bubble method..... 200
IV.2.3.1.e.1. Bubble method conclusions 201

© 2020 Tous droits réservés.

lilliad.univ-lille.fr

Table of content

IV.3 SERS-MS using CNWs 202
IV.3.1 Carbon nanowalls - Plasmon-free for SERS/MS for ricin B chain ……..206
IV.4 EC-MS using CNWs 209
IV.4.1 EC and detection of ricin……..……..217
IV.5 Conclusions and perspectives 218
IV.5.1 LSPR-MS graphene based dual surfaces……..218
IV.5.2 SPR-MS graphene based dual surfaces……218
IV.5.3 SERS-MS graphene based dual surfaces…….....…..220
IV.5.4 EC-MS dual surfaces……220
IV.5.5 Dual surfaces conclusion and perspectives……..220
IV.6 References 224
General Conclusions and Perspectives……..……..233
General conclusions and perspectives 235
Publications and scientific presentation of the results 240
References 242
Appendix-Experimental part-Procedures.……..……..…….243
V.1. Materials 246
V.2. Synthesis of organic compounds 247
V.3. Preparation of surface based materials. 247
V.3.1 Synthesis and modification of carbon boron doped nanowalls 247
V.3.2 Growth of carbon boron-doped nanowalls (CNWs) 247
V.3.3 Ionic implantation of boron atoms on undoped CNWs 248
V.3.4 Functionalization of CNWs with OTS and surface patterning 248
V.3.5 Modification of the carbon nanowalls with 1-Pyrenecarboxylic acid (pyrene-COOH CNWs) 249
V.3.6 Functionalization of the carbon nanowalls with D-(+)-Galactosamine hydrochloride (NH2GAL CNWs) 249
V.3.7 Functionalization of the carbon nanowalls with ovalbumin (OVA CNWs) ……..….. 249
V.3.8 Ligand exchange (AuNPs with citrate ligand into thiol ligand) 250
V.4. Graphene and graphene-like deposition methods. 250
V.4.9 Electrophoretic deposition 250
V.4.10 Preparation of drop casted graphene based sensors 250
V.4.11 Prepartion of layer by layer graphene based sensors 250
V.4.12 Modification with CVD graphene through a wet-transfer procedure …..... 251
V.4.13 Preparation of thin bubble graphene sensors..... 252
V.5. Deposition of SiOx films by Plasma-enhanced chemical vapor deposition (PECVD)……..….252
V.6. Glucose determination in serum 252
V.7. Preparing the solutions of analyte 253
V.7.14 Preparing the stock solution of ricin B chain 253
V.7.15 Preparing the blood serum samples 253
V.7.16 Preparation of peptides mixture from calibration kit for analysis of peptides…… 253
V.8. Preparing real samples for SALDI-MS analysis 254
V.9. How to calculate/approximate the thickness of the film of glucose on the surface carbon nanowalls: 255
V.10. UV-VIS parameters for LSPR measurements 255
V.11. Sample deposition and mass spectrometry measurements 255
V.12. Instrumentation 256
V.13. References..... 259
Annexe1-4 ……..……..……260

© 2020 Tous droits réservés.

lilliad.univ-lille.fr

Acknowledgments

Acknowledgments

First of all, I would like to acknowledge my family for all the love and the support that they offered me. Special acknowledgment goes to my mother, as she is my strength and my weakness, all together.

My professional appreciation and gratitude goes to my supervisor, Yannick Coffinier, and to the other members of the NBI team: Rabah Boukherroub, Sabine Szunerits and Alexandre Barras. I've learned a lot from them and it will help me a lot in my scientific carrier. I would also like to acknowledge the funding institutions: University of Lille and DGA. I would like to say thanks to Soukaina Bensalk, for the company, laughs and help and to all the scientists and the members of technical team that did offer me advices in the IEMN's clean room facility, especially to David Guérin, for the productive and nice discussions in the organic chemistry room. Hervé Drobecq is acknowledged for the training with the MALDIMS. Robert Bogdanowicz and his team in Poland are acknowledged, for providing us the carbon nanowalls.

My sincere thanks go to my magnificent friends in Lille: Aleksandra Loczechin and Milica Budimir. They are the closest thing to family I had in Lille. For the good and the bad days, it was all worth it due to you. Vedi also joined our small foreign family, later on. I would also like to say thanks to Andrei Vladut for being there for me and to the other friends and colleagues from Lille (Anna Voronova, Vlad Mishyn, Mathias Dolci, Giulio Calimici, Giuliana Pellegrino).

Special acknowledgments are given to each and every Cartoline member. Special appreciation (wink wink) goes to my beloved friends (Teleșpan, Mogoș, Codruț and Nenciu) for reading my long nocturnal expressed thoughts. I appreciate that they answered to me, as well :D I couldn't have done it without you guys! I am also grateful for the laughs born from Ema's random word arrangements, for the daily reminders of Drăghiciu that I should start working, for Cristina's promises related to the sweets I will get after finishing this manuscript. And for the great summer with Plăieșii din Vamă. I cannot mention each and one of you guys, because you know how my comments look like: endless and boring. And I only have one page. This paragraph will eventually become a meme and I am proud of it.

Last but not least, I would like to tell Febo that he will be forever in my soul. He will not be forgotten. This work is dedicated to him, the kindest soul that touched Earth, and to the other family members that I lost.

© 2020 Tous droits réservés.

lilliad.univ-lille.fr

Acknowledgments

Blank page

© 2020 Tous droits réservés.

lilliad.univ-lille.fr

Acronyms

AA - ascorbic acid

ACN - acetonitrile

APTMS - 4-aminopropyltrimethoxysilane

Au NPs - gold nanoparticles

BDD-NWs - boron doped diamond based nanowires

BSA - bovine serum albumin

C60 - fullerene

$CDCl_3$ – deuterated chloroform

CNFs - carbon nanofibers

CNWs - carbon nanowalls

CNT - carbon nanotubes

EtOH – ethanol

Cu (I) - copper iodide

CuI(PPh3) - Copper iodide triphenylphospine

Cu NPs - Copper nanoparticles

CV - Cyclic Voltammetry

CVD - Chemical vapor deposition

DA - dopamine

DCC - N,N'-dicyclohexylcarbodiimide

DCM - dichloromethane

DHC - diammonium hydrogen citrate (ammonium citrate dibasic)

DMAP - 4-Dimethylaminopyridine

DMF - dimethylformamide

DMSO - dimethyl sulfoxide

DPV - Differential Pulse Voltammetry

DRS - Diffuse reflectance spectroscopy

EDC - N-(3-Dimethylaminopropyl)-N'-ethylcarbodiimide hydrochloride

EDTA - Ethylenediaminetetraacetic acid

EDX - Energy dispersive X-ray spectroscopy

ELISA - Enzyme-Linked Immunosorbent Assays

© 2020 Tous droits réservés.
lilliad.univ-lille.fr

Acronyms

EPD - Electrophoretic Deposition

ESI - Electrospray ionization

EtOH – ethanol

FDA - Food and Drug Administration

FTIR – Fourier-transform infrared spectroscopy

G - graphite particles

GC - glassy carbon

GFP - green fluorescence protein

GO - graphene oxide

GOx - glucose oxidase

GRM - graphene related materials

HOPG - highly oriented pyrolytic graphite

HNO_3 - nitric acid

H_2SO_4 - sulfuric acid

HRTEM - High-resolution transmission electron microscopy

IPA - isopropyl alcohol

IBD - Inflammatory bowel disease

KBr - potassium bromide

LDI – Laser Desorption Ionization

LOD - Limit Of Detection

MALDI-MS – Matrix Assisted Laser Desorption/Ionization Mass Spectrometry

MRI - Magnetic Resonance Imaging

MSI - Mass spectrometry imaging

NaCl - sodium chloride

NaOH - sodium hydroxide

NCNT - nitrogen-doped carbon nanotubes

ND - nanodiamond

NHS - N-Hydroxysuccinimide

NIH - National Institute of Health

NMR - Nuclear Magnetic Resonance

NPs - nanoparticles

OTS - Octadecyltrichlorosilane

PBS - phosphate buffered saline

PGC - nanoporous graphitic carbon

© 2020 Tous droits réservés.

lilliad.univ-lille.fr

Acronyms

PL - photoluminescence

PEG - polyethylene glycol

pKa - Ionization constant

rGO - reduced graphene oxide

RSD - Relative Standard Deviation

RNA - ribonucleic acid

ROS - reactive oxygen species

SDS - sodium dodecyl sulfate

SALDI-MS – Surface Assisted Laser Desorption/Ionization Mass Spectrometry

SEM - Scanning Electron Microscopy

SERS - Surface Enhanced Raman Spectroscopy

$NaHCO_3$ - sodium bicarbonate

Na_2CO_3 - sodium carbonate

TEM - Transmission Electron Microscopy

TEOS - tetraethyl orthosilicate

THF - tetrahydrofuran

Tyr - tyrosine

TRIS - trisaminomethane

UA - Uric acid

UV-Vis - Ultraviolet-visible spectrophotometry

VA-CNT - vertically aligned carbon nanotubes

VA-NCNT - vertically aligned nitrogen-doped carbon nanotubes

XPS - X-ray photoelectron spectroscopy

XRD - X-ray diffraction

© 2020 Tous droits réservés.

lilliad.univ-lille.fr

Acronyms

Blank page

© 2020 Tous droits réservés.

lilliad.univ-lille.fr

Thèse de Ioana Silvia Hosu, Université de Lille, 2020

General Introduction

© 2020 Tous droits réservés.
lilliad.univ-lille.fr

Thèse de Ioana Silvia Hosu, Université de Lille, 2020

General Introduction

This thesis presents the experimental and literature study of an ultrasensitive detection of ricin toxin by innovative graphene-based sensors, using mass spectrometry, namely surface assisted laser desorption/ionization mass spectrometry (SALDI-MS).

Initially, the main goal was to combine SPR (surface plasmon resonance) with SALDI-MS for dual detection of ricin. SPR is well known and used for the detection of proteins, while this is not the case for SALDI-MS, as big molecules are hard to desorb/ionize with LDI-MS as intact proteins. So, my biggest challenge was to demonstrate that a nanostructured surface could be able to detect a protein of this molecular weight (64 kDa). Extensive amount of studies were performed in order to optimize this kind of surface, as in literature there are only few examples of SALDI-MS used for bigger proteins.

In **Chapter I**, I will present the bibliographic study related to all aspects of my thesis. I'll describ ricin as ribosome-inactivating protein (composed of two chains: ricin B chain, a lectin that bind to cell membrane, through galactosamine moieties and ricin A chain, a glycosidase that depurinates ribosomal RNA involved in protein synthesis) and its potential to be used as biological warfare agent, by terrorist organization. Background facts and studies showed that this toxin was used several times in the recent history for criminal purposes. I will also enumerate the classical methods used for its detection. Matrix assisted laser desorption/ionization mass spectrometry (MALDI-MS) was the most used method to determine if ricin is biologically active (promoting cell death), but the time required to perform the measurements is long, notably because protein digestion needs to be performed to cut the protein in smaller fragments (peptides). But this requires a specific database containing the cleaved peptides and reconstruction of the protein sequence.

SALDI-MS is an improvement of MALDI-MS, by replacing the organic matrix, with an inorganic material/surface. Even though this was developed initially because MS signals were contaminated by huge background in the low molecular mass range coming from organic matrix fragmentation thus hindering the detection of small analytes, it has been proven to be more effective from different points of view: much more easy preparation, thus decreasing the time of measurements, high specific area (as usual materials have nanostructuration), salt tolerance (more suitable for complex media), lower background and no "sweet points". Nevertheless SALDI-MS is adaptable for any MALDI-MS instrument. So, SALDI-MS presented potential for ricin detection, but no literature references are describing related to this subject. This chapter also described the variety of SALDI-MS materials while the LDI-

© 2020 Tous droits réservés.

lilliad.univ-lille.fr

General Introduction 7 MS mechanism is not well understood yet. From all these materials, carbon based ones seem to be the less expensive and many parameters can be tuned to enhance LDI-MS process. There are also some references that described SALDI-MS detection of small proteins. So, from that, boron doped carbon nanowalls (CNWs) will be investigated as potential SALDIMS platforms. All the carbon nanowalls used in this thesis are provided by Prof. Robert Bogdanowicz and his team from Gdansk University of Technology.

In **Chapter II**, we'll propose to assess these CNWs as being platforms for SALDI-MS detection of small molecules. It is known that the bigger the molecule, the more difficult is to be detected by LDI-MS processes. Therefore, going step by step: we'll first test small molecules and then bigger molecules, as it could be easier to study the influence of different parameters and having a starting point for bigger molecules. In this chapter, we'll focus on playing with parameters such as proton donors, influence of power of the laser on LDI-MS and salt concentration. As glucose (Mw=180 Da)is an important biological molecule, present in blood serum, related to diabetes or other diseases and it may act as an inhibitor for lectin (ricin B chain, Mw= 32 kDa) binding to specific carbohydrates (galactosamine moieties), we want to study these parameters for its quantification and detection with SALDI-MS. This will help us assess the suitability of CNWs for SALDI-MS, by comparing our results for glucose detection with the ones described in literature. Only after we have done that, we can go further to detect proteins (model proteins, as cytochrome C and/or lectins, as ricin B chain).

This brought us to important questions in our work:

- How could we compare different types of materials, as they exhibit different morphological, physico-chemical characteristics, different chemistry and different functional groups? The method that we proposed was using "thermometer molecules" that could show us how much energy is deposited on the SALDI-MS material and transferred to the analyte.

- How could we optimize a SALDI-MS method for the detection of ricin? It has to be noticed that special laboratory conditions are required for the use of ricin itself and ordering and manipulation are subjected to special authorization. As ricin B chain is a lectin and known to be harmless when separated from the ricin A chain, we decided to only use this B chain.

Chapter III concerns our approach for the detection of proteins using CNWs. For this purpose, we decided to pay more attention for the tuning of the substrate itself. We will characterize CNWs with different boron doping levels leading to morphology changes together with electrical conductivity and their heights. To do so, SEM, EDX, FTIR, Raman

© 2020 Tous droits réservés.
lilliad.univ-lille.fr

Thèse de Ioana Silvia Hosu, Université de Lille, 2020

and XPS will help us to correlate the physico-chemical properties with SALDI-MS efficiencies. For the optimization step, cytochrome C (Mw= 12 kDa) will be used as model protein. Analytes deposition methods will be also assessed. This could allow us, in correlation with the "thermometer molecules", to optimize the method.

Thanks to the optimized protocol obtained from Cytochrome C, ricin B chain detection will be attempted from pure solution and more complex media as blood serum and soft drinks. We'll try to answer the following question: Could we calibrate the SALDI-MS method so that we can quantify ricin B chain in real samples?

Finally, in **Chapter IV** we'll present some perspectives for the development of ricin detection means based on dual surfaces. For this purpose, different methods will be investigated such as SALDI-MS with SPR (surface plasmon resonance), SERS (surface enhanced Raman Spectroscopy) and EC (electrochemistry).

© 2020 Tous droits réservés.

lilliad.univ-lille.fr

Chapter I
Bibliography
State of the art

© 2020 Tous droits réservés.
lilliad.univ-lille.fr

Thèse de Ioana Silvia Hosu, Université de Lille, 2020

Chapter I. Bibliography: State of the art

I.1. Introduction....17
I.2. Background of the subject: Facts about ricin-like toxins....18
I.2.1. Mechanism of toxicity of ricin-like toxins....20
I.3. Methods for ricin-like toxins detection....23
I.3.1. Methods that cannot identify biologically active ricin....23
I.3.1.1 Mass spectrometry....26
I.3.1.2 Ricin-like toxins and Surface Plasmon Resonance (SPR)/ Localized Surface Plasmon Resonance (LSPR)....28
I.3.2. Methods that can identify biologically active ricin....29
I.4. Matrix-free LDI (laser desorption ionization)-Mass Spectrometry....33
I.4.1. Drawbacks of matrix-assisted desorption/ionization....34
I.4.2. Surface-assisted desorption/ionization mass spectrometry (SALDI-MS)....37
I.4.2.1 SALDI-MS mechanism....40
I.4.2.2 Variety of materials used in SALDI-MS and their properties....41
I.4.2.2.a. Semiconductors....42
I.4.2.2.b. Metal/metal oxide nanoparticles/nanostructures....42
I.4.2.2.c. Carbon based materials for SALDI-MS....43
I.4.2.3 Chemical functionalization....43
I.5. Conclusions....45
I.6. References....48

© 2020 Tous droits réservés.
lilliad.univ-lille.fr

I.1. Introduction

This first chapter will cover the bibliographic study concerning the theme of this thesis: detection of ricin using graphene-based surface-assisted laser desorption/ionization mass spectrometry.

In the first part we will talk about the background of the subject, historical facts of ricin-like proteins, together with describing the use of ricin for several terroristic attacks, which were important red-flags for national and international safety. We will describe ricin as a protein (part of ribosome-inactivating proteins family) and its biological influence in nature, especially in cell death, followed by the mechanism of toxicity.

Methods of ricin detection will be also described and categorized into being able or not to distinguish between biologically active ricin from inactive one. As these methods lack rapidity, sensitivity or/and selectivity, we do describe matrix-assisted laser desorption/ionization mass spectrometry (MALDI-MS) as an alternative to the classical methods. Presenting the working principles, the advantages and the disadvantages of MALDI-MS towards detection of ricin (and proteins in general) is also achieved in this chapter. Several MALDI-MS ricin detection literature studies are also described.

Surfaces-assisted laser desorption/ionization mass spectrometry (SALDI-MS) is also described as a technique, as it is the improved version of MALDI-MS, whereas the organic matrix in MALDI-MS is replaced with inorganic compounds, to enhance LDI-MS processes.

This bibliographic chapter represents the state-of-the art for detection of ricin, using MALDI-MS, as there are no SALDI-MS methods described for this purpose. We will mention the difficulties to overcome for the use SALDI-MS methods for ricin detection (and proteins in general).

© 2020 Tous droits réservés.
lilliad.univ-lille.fr

I.2. Background of the subject: Facts about ricin-like toxins

Nowadays, the world is confronting with different threats and one of the most dangerous one is the desire of certain organizations to harm a large mass of people, with the purpose of obtaining different advantages. The Center for Disease Control and Prevention (CDC, Atlanta USA) categorizes ricin and abrin as B category bio-terrorism agents, because they are relatively moderate to spread, they cause moderate illness rates and low death rates and not least, they require specific enhancements of CDC's laboratory capacity and enhanced disease monitoring.[1] Being two of the most toxic glycoproteins in the vegetable world, they are water soluble and can be easily used to contaminate water sources that are provided for large populations. The effects caused are not contagious, but different objects that were in contact and have traces of these toxins should be discarded. Other different ways of spreading these natural occurring toxins, such as food poisoning or air/aerosol contamination, can be used for malicious purposes. The extraction of these toxins from jequirity seeds (abrin) and castor seeds (ricin) is a simple procedure,[2] making these toxins a prefered tool for bioterrorism, and in general criminal purposes. Moreover, a quite good thermal and a wide pH range stability increases the potential use of this toxins for the same purposes. Thus, sensitive and rapid analytical techniques are required for the analysis of serum, food and clinical samples.[3]

Ricin became a more real concern since the first edition of The Anarchist CookBook appeared, in 1971. This book describes procedures for manufacturing several weapons including ricin. In 1978, a bulgarin dissident named Georgi Markov was killed using ricin, in London. Being one of the first documented attacks, it separated the facts from fiction.[4,5] During history this toxin has been used in several incidents and the most recent ones include Cologne terrorist plot, where police have found large amount of Castor Beans and ricin powder and paste and instructions with explosive devices. It was the first time a jihadi terrorist in the West has successfully produced the toxic biological agent. Earlier that year, two men were charged after French police foil Paris ricin terror plot, only 6 days after the latter knife attack in Paris. They were communicating, using Telegram, how to prepare/build ricin-based poisons.[6] In both cases the prevention measures caused no victims, but the danger was there. On-scene pictures from these cases are presented in **Figure I.2-1**.

© 2020 Tous droits réservés.
lilliad.univ-lille.fr

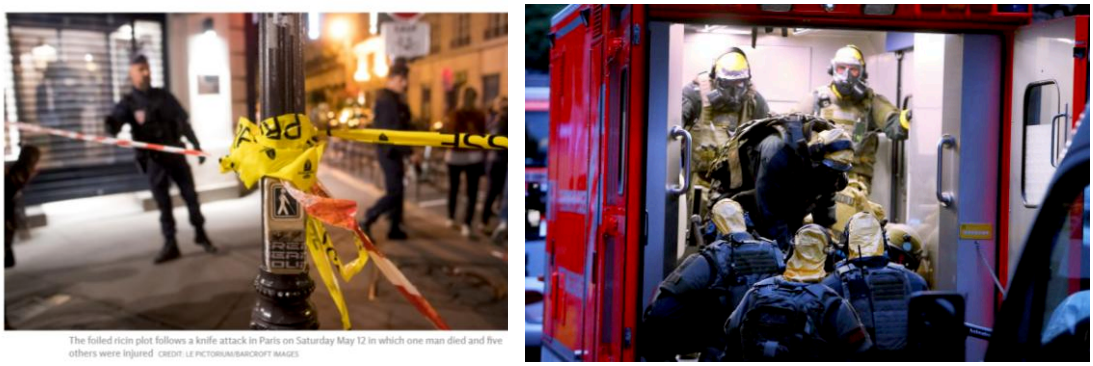

(A) **(B)**

Figure I.2-1 (A) News presented in The Telegraph, about the ricin foil attack, in Paris, 2018. **(B)** Police officers of a special unit wear protective clothes and respiratory masks during an operation on June 12, 2018, in Cologne's Chorweiler district, western Germany, where police found toxic substances after storming an apartment.[6]

The toxicity depends of the means of exposure. Skin and eye exposure makes the toxicity more unlikely, because normal skin do not absorb ricin. Ingestion of entire castor bean seeds (the plant from which ricin can be extracted) is the least toxic, due the hard shell of the seeds and the partial incapacity of the stomach to digest it. Oral uptake or intra-gastric delivery is considered to be 1000 less toxic than injection or inhalation.[7] In the intended cases of intoxication, almost 50% of the cases are fatal. These remarks are summarized and represented in **Figure I.2-2.**

Humans	Accidental Cases (Total/Fatal)	Intended Cases (Total/Fatal)
oral	875/13	5/0
injection	1/0	6/5
total	876/13 (1.5%)	11/5 (45.5%)

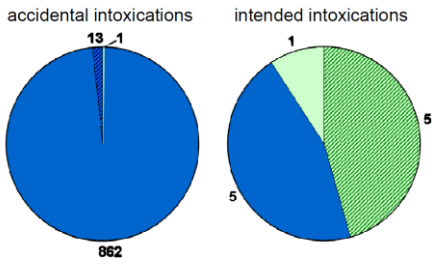

(A) **(B)**

Figure I.2-2 The number of human intoxication cases reported in ref.[7] with the number of oral cases (blue), number of injection cases (green) and the number of fatal cases (hatched).

Injection of ricin has the highest lethal statistical percentage even if the LD_{50} = 10 µg/kg[8] is comparable to LD_{50} = 5-10 µg/kg for inhalation and the less dangerous is the oral ingestion, with LD_{50} = 1-20 mg/kg.[9] There is not current approved counter-measure against ricin intoxication, but different measures are taken when such intoxication is suspected: intravenous fluids administration (IV fluids, usually hypertonic, or slightly hypertonic fluids to induce hipovolemia, with different electrolytes), activated carbo – charcoal ingestion for gastric absorption of the toxin, gastric lavage, emetics administration to cause vomiting,[7] suppression of hypertension by administration of dopamine or atropine.[10] Antibodies show

© 2020 Tous droits réservés.
lilliad.univ-lille.fr

the best promise for therapeutics and this was proved by Paul Ehrlich who explained how blood from immunized animals against ricin can transfer protection to other animals, in the 1890's.[11] Neutralizing monoclonal or polyclonal antibodies are described in literature, as prophylactic and therapeutic measures.[12] There are also two cases of vaccines that are in the phase 1 clinical trials (first-in-man-studies), involving mutant ricin A chain (RiVax®) and truncated ricin A chain (RVEc). A recent drug delivery system is presented by Respaud et al.[13] A nebulizer was used to deliver the anti-ricin neutralizing monoclonal antibody (IgG 43RCA-G1), to treat intoxication by inhalation, as intravenous route does not deliver enough mAbs for respiratory tract.

Beside ricin, there are components in castor beans that can be extracted and some of them are described in literature.[14] Regarding the interest of this thesis, one of the most relevant is tetrameric agglutinin (RCA120, commonly named RCA, *R. communis* agglutinin), that is far less toxic than the dimeric form, ricin. The sequence similarity of A and B chains is 93% and 84%, respectively, and mass spectrometry is one of the techniques that can differentiate between them, despite the structural similarities, because of the tetrameric form.[15]

Ricin can be inactivated through heating at a temperature higher than 80°C, during 10 min.[16] Ricinine, an alkaloid present in the seeds in a percentage of 0.2%, is considered to be a biomarker for ricin and is very stable to thermal treatment. When ricin is used in a laboratory, in literature there are some suggestions of cleaning the labware and disposable containers: soaking in 3% hypochlorite solution for at least 24 h.[17] The need of the biosafety 2nd class laboratory is also required. This laboratory has high energy particulate air (HEPA) filters[3] and special glove boxes and specific protocol for manipulating samples containing ricin and all solution/vessel in contact with it.

I.2.1. Mechanism of toxicity of ricin-like toxins

Both toxins (ricin and abrin) are belonging to type II ribosome inactivating proteins (RIP II) and are composed of two units RTA and RTB (that are linked through a disulfide bond). A comprehensive and detailed mechanism of toxicity of ricin is presented by Audi et al.[10] as shown in **Figure I.2-3**. Briefly, in 1972, Olsens and Pihl observed the RIP II toxins preserve the polyribosome structures, but inhibit the component that helps in the elongation of the formed polypeptide chains. Furthermore, it was discovered that the A chain is a *rRNA N*-glycosidase (EC 3.2.2.22) that removes one adenine (depurination reaction) from GAGA sequence of the 28 S ribosomal RNA loop. This loop is involved in binding elongation

© 2020 Tous droits réservés.
lilliad.univ-lille.fr

factors and the modified ribosome cannot support anymore protein synthesis, leading to (animal) cell death. One A chain is able to inactivate from 1500[10] to 2000 ribosomes/min.[16]

The **B chain** is a lectin and is responsible for binding cell surfaces through galactosyl residues (B-D-galactopyranoside moieties) and enables the entire protein to enter the cell. Also, the agglutinating activity is attributed to this B chain. Many plants have related ribosome inactivating proteins, but they are not toxic due to the lack of B chain, important in binding to the target cells.

This understanding of the mechanism of toxicity can help us to develop specific, selective and sensitive sensors, using as toxin ligands (bio-recognition element) moieties containing galactose, which will bind selectively the B chain of the toxins (analyte).

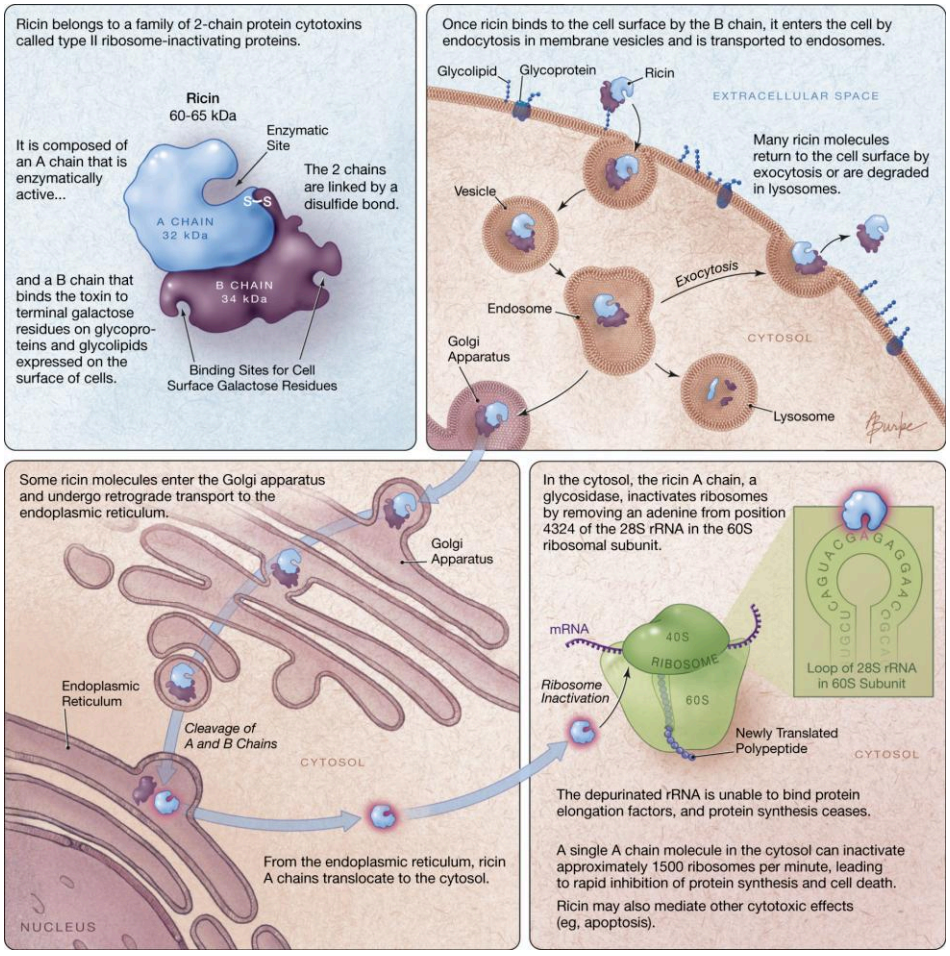

Figure I.2-3 Mechanism of toxicity for ricin-like toxins, presented in ref.[10]

Ricin is highly toxic only if: (1) both A and B chains are present, (2) the B chain retains its glycan-binding ability, and (3) the A chain is catalytically active. First of all, this can help us to use only one chain of the toxin in our experiments, as the toxicity lacks in this case. The ones that favor our experiments is the B chain, being the one that can bind to sugar moieties. If the B chain retains its ability to bind the glycans from the surface of the sensors, it also

© 2020 Tous droits réservés.
lilliad.univ-lille.fr

Thèse de Ioana Silvia Hosu, Université de Lille, 2020

means that the entire ricin molecule keeps its potential activity. It is also due to drastic manipulation safety rules and the need of specific authorization to manipulate the whole molecule of ricin.

The catalytical activity of A chain is translated in the removal of adenine (depurination reaction) from ribosomal RNA. Thus, monitoring the release of free adenine provides a convenient means for assessing the catalytic activity of ricin. In the detection of ricin, there are methods that can identify biologically active ricin or not. The methods that can do so are of more practical value. The next sub-headlines will describe the classical methods of detection, with the mentioning of their ability to distinguish between active or inactive ricin (due the depurination activity in the A chain).

Therefore, when detecting ricin, the following indicators are to be followed:

- The presence of other chemicals (biomolecules) found in castor beans (like ricinine) for indirect detection, after poisoning and in presumed contaminated samples.
- The presence of ricin itself in food samples, water or on solid surfaces.
- To assess if ricin is active, because this is the only important fact in using it like a bioterrorist agent, inactive ricin render this toxin harmless.

© 2020 Tous droits réservés.
lilliad.univ-lille.fr

I.3. Methods for ricin-like toxins detection

I.3.1. Methods that cannot identify biologically active ricin

The classical direct methods for the detection of ricin is based on ELISA[18] (Enzyme-Linked Immunosorbent Assay) and other immune assay methods (radioimmunasssay,[19] aptamer or glycosphinogolipids based chips[20,21]), SPR (surface plasmon resonance). A long variety of methods used for ricin is presented in **Table I.3-1**. These are the classical methods, but that cannot distinguish between active or inactive ricin. We have separated these methods on different fields: Immunoassay, FTIR (unusual method), capillary electrophoresis, mass spectrometry and optical (surface plasmon resonance and colorimetric).

ELISA is sensitive and quite used method, but it is time consuming, because of several washing steps involved and also limited throughput. For an inexpensive and rapid detection of biological warfare agents, both colorimetric and chemiluminescence ELISA would not have met these requirements.[22] Indirect methods (such as ELISA, colorimetric and SPR) can also present the disadvantage of false-positives, due to the binding of antibodies from the samples to the antibodies from the interfaces.

Antibody has been the crucial element for immunoassay technology. However, due to its sensitivity to high temperature that could cause denaturation, its storage life is short and the price is high. This issue could be resolved by a change of the receptor to either aptamer chips or glycosphingolipids (GSLs). Antibodies were replaced by microspheres[23] or gold-coated magnetoelastic sensor.[24]

Most detection techniques for ricin had been focused on bioassay principle. From replacement of various formats, labels, detection modules and receptors, the ultimate aims are to increase the sensitivity and speed of analysis, which also allows multiple samples detection. But for typical bioassays techniques, the well known problems are that they may cause cell death and cross-react.[22]

Table I.3-1 Ricin direct methodologies along history adapted from reference [22] and reference**.** [25]

Year and reference	Technique	Ricin methodologies	Identification of biologically active ricin	Lowest level of detection (LOD)	Matrix involved	Detection time	Drawbacks
1982 [19]	**Immunoassay**	**Radioimmunoassay (RIA)** - rabbit antiserum	**NO**	100 pg	0.1% sodium azide and 0.1% bovine serum albumin in 0.05M sodium phosphate buffer	-	lengthy incubation time and difficulties in handling and disposing of radioisotopes, radioactive
1980 [18]		Enzyme-linked **immunosorbent** assay (**ELISA**)	**NO**	(a) 5–40 ng/ml (Colorimetric)	Rabbit body fluid	-	Expensive, lengthy assay time due to several washing steps involved and also
1994 [26]			**NO**	(b) 100 pg/ml	Human serum,	-	

© 2020 Tous droits réservés.
lilliad.univ-lille.fr

				(Enhanced colorimetric)	human urine and normal goat serum in phosphate-buffered saline (PBS)		limited throughput
1994 [26]			NO	(c) 0.1–1 ng/ml (Chemiluminescence)	Human serum, human urine and normal goat serum in PBS	-	
2002 [27]			NO	(d) 50 ng/ml (Colloidal gold particles)	PBS	10 minutes	
				(e) 100 pg/ml (Gold particles with silver enhancement)	PBS		
2004 [28]		Fluorescence-based fiber optic immunoassay	NO	(a) 100 pg/ml	Buffer solution	20 minutes	organic fluorophores are still subjected to complication such as occurrence of multiple spectral characteristics that made data analysis more challenging, irreproducible
				(b) 1 ng/ml	River water		
2004 [29]		Fluorescence-based immunoassay using quantum dots	NO	30 ng/ml	buffer	-	
1998 [30]		Planar array immunosensor with charge-coupled device (CCD)	NO	25 ng/ml	PBS containing 0.05% (v/v) Tween −20	15 minutes	
2003 [31]				10 ng/ml (Flow-based platform)	PBSTB		
2004 [20]		Aptamer microarray	NO	320 ng/ml	PBS containing 5mM MgCl2	-	
2005 [21]		GSLs with QCM	NO	5 ug/ml	PBS	-	
2005 [32]		Protein gel-based microchip immunoassay	NO	0.7 ng/ml	PBS containing 0.15% polyvinyl alcohol (PVA) and 0.15% polyvinyl pyrrolidone (PVP)	Several hours of analysis	lengthy assay time due to several washing steps involved
2000 [23]		immunoassay Magnetic microsphere (a) ECL or (b) FCL	NO	0.5 pg/ml	SuperBlockTM blocking buffer in PBS	-	
				1000 pg/ml		-	
2004 [24]		immunoassay Gold-coated magnetoelastic sensor	NO	5 ng/ml	Aqueous media such as water, blood or serum	-	
2000 [33]	FTIR	Fourier transform near-infrared reflectance spectrometry	NO	1.5 mg/500 mg	Wheat flour	-	Very low sensitivity
1994 [34]	Capillary electrophoresis	Capillary electrophoresis with (a) UV or (b) MS	NO	(a) 10 mg/ml (b) Characterization done but no limit of detection reported	buffer	-	The method is only presented as a perspective, not a tool of detection, using MS. High LOD using UV.
2003 [35]		Capillary electrophoresis CZE, CGE	NO	25 nM, 5 nM	buffer		
2012 [36]		Inca bioanalytical microarray platform Antibody conjugated to	NO	0.5–1 ng/ml	Buffer and milk	90 min	lengthy assay time

© 2020 Tous droits réservés.
lilliad.univ-lille.fr

		IncaSlide					
2008 [37]	MS	**Immunocapture** and **MALDI-TOF/MS** Antibody conjugated to magnetic particles	**NO**	50 ng/ml	Buffer and milk	6 hours	lengthy assay time
2011 [38]		Nano LC–**MS** Lactose-immobilized monolithic spin column	**NO**	8 ng/ml	Buffer	5 hours	lengthy assay time
2008 [39]	**Optical: SPR**	**SPR** Glycans conjugated to SPR chip	**NO**	10 pg/ml	Buffer	**5 min**	
2008 [40]		**SPR** Antibody conjugated to SPR chip Buffer and environmental samples	**NO**	0.1 ng/ml	Buffer and environmental samples	**15 min**	
2013 [41]		Localized **SPR** β-lactoside-coated Au nanoparticle SPR chip Buffer 30 ng/ml	**NO**	30 ng/ml	Buffer	**7.5 min**	
2013 [42]		**SPR** sdAb conjugated to SPR chip	**NO**	0.7 ng/ml	Buffer	**2–6 min**	
2001 [43]	**Optical: Colorimetric**	Lectin pull-down **colorimetric** Galactose-magnetic iron-oxide nanoparticles	**NO**	2–4 ng/ml	Buffer and serum	3 h	lengthy assay time

Even though the immunoassay techniques are quite sensitive and, during time, the length of the assay time was diminished, they still lack the ability to underline if the ricin is active or not.

Other methods, except the direct methods, are the indirect detection methods. Usually in this case, small molecules specific to crude ricin extract from plants can be present. An example of this kind of method is using liquid chromatography-MS identification of small molecules that are co-extracted from plants containing the toxic protein and therefore can be considered as bio-markers for the toxins.[44] The easiest way to determine exposure to ricin is the detection of ricinine, in urine or biological fluids, with the help of LC-MS/MS.[7] (**Figure I.3-1A**)

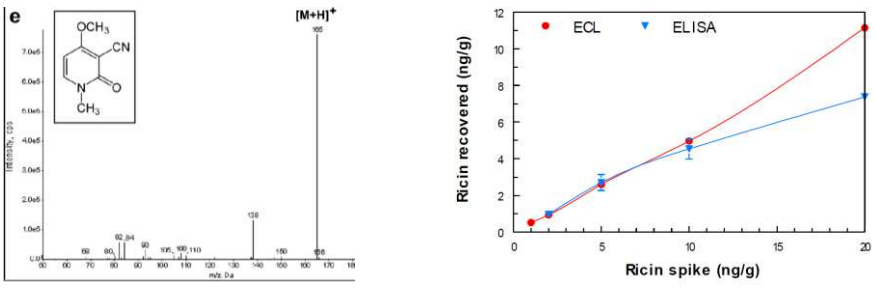

(A) **(B)**

Figure I.3-1. (A) LC-MS/MS of ricinine in dog's urine, the 165 m/z represents the protonated adduct of ricinine, M_W=164.2; **(B)** Ricin recovery from the ELISA and electrochemiluminescence measurements (ECL).[7]

© 2020 Tous droits réservés.
lilliad.univ-lille.fr

Thèse de Ioana Silvia Hosu, Université de Lille, 2020

More cost effective indirect detection of abrin was developed using L-abrine (*N*-methyl-L-tryptophan), which is a part of *Abrus precatorius* in a percentage of 0.5-1.0%. [44] The colorimetric detection is based on the use of two enzymes, that will catalyze the degradation of L-abrine in indole or ammonia, that were further reacted with specific reagents to obtain a colored reaction. Indirect detection of these can also be performed by PCR (polymerase chain reaction). In that case, a simultaneous detection of abrin and ricin was done using the DNA clones of both natural occurring seeds and used this DNA to get positive or negative answers from the negative and positive DNA controls and from bread containing crude or grounded seeds.[17] Immunoassays-based indirect detection is also described in the literature. ELISA and electrochemiluminescence (**Figure I.3-1**B) methods were compared as ricin recoveries.[45]

I.3.1.1. Mass spectrometry

Being a glycoprotein with a molecular weight of 64 kDa, the entire molecule is difficult to be ionized and to be detected by mass spectrometry with high sensitivity and specificity. To overcome this difficulty, enzymatic digestion of the protein of interest is thus performed before detection.[37]

There are direct methods of detecting ricin and some of the ones that cannot detect its biological activity are presented in **Table I.3-1**. Hines et al. present in 1994[34] a capillary electrophoretic method using different buffers for the elution of ricin at a specific time and a UV detector at 200 nm. Nevertheless, they described the possibility of using an ESI-MS ion source and detector for further studies.

The usage of direct detection of ricin using a tryptic digested sample is presented by Duriez et al. in 2008, using immunocapturated B chain antibody attached to magnetic beads and MALDI-ToF-MS. For the confirmation of peptide sequences the samples were also analyzed with LC-ESI MS. The authors also compared the MS spectra of RCA (*R. communis* agglutinin) with pure ricin product. The ion at *m*/*z* 1013.6 (although not providing the lower limit of detection) was used for accurate detection purposes, but also 1310.6 *m*/*z* was used for higher levels of ricin. Both ions correspond to A-chain fragments. No ion corresponding to B-chain was used for detection, due to the influence that the immunocapture step may have over the peaks. An ion at *m*/*z* 1728.9, which accounts for a peptide sequence occurring in both ricin and RCA, was also used to estimate RCA contamination.[37] It is to be noticed that the whole procedure takes 6 hours, which is too long when the necessity of detecting this kind of toxins and dispel doubt are mandatory.

Kataoka et al.[38] described nanoLC-MS method using lactose-immobilized monolithic silica spin column as ricin extraction method from sample solutions. Tryptic digestion of the

© 2020 Tous droits réservés.
lilliad.univ-lille.fr

eluate from lactose-immobilized monolithic silica extraction was analyzed by LC-MS. Even though the recovery of ricin was more than 40% and the LOD 8 ng/ml, the whole procedure takes 5 hours. Again, this method is time and reagent consuming. Other MS reports of detection are described in the literature, having the same drawbacks: lengthly time of analysis, reagent consuming, no possibility to determine if ricin is active or not, mass fingerprinting (PMF) after protein digestion.[3,46]

© 2020 Tous droits réservés.
lilliad.univ-lille.fr

I.3.1.2. Ricin-like toxins and Surface Plasmon Resonance (SPR)/ Localized Surface Plasmon Resonance (LSPR)

SPR (Surface Plasmon resonance or propagating Surface Plasmon Resonance) and LSPR (Localized Surface Plasmon Resonance) are both techniques that use the same principle: the resonant oscillation of conductive electrons at an interface with opposite electric properties (metal-dielectric interface), stimulated by incident light (photons). This phenomenon is sensitive to any changes in refractive indexes (at or near the surface, for a maximum distance of 100 nm) when, for example, lectin will bind to a sugar residue (or when any another type of molecule will bind/adsorb). The SPR uses the propagating surface resonant plasmons on a planar thin gold surface, which will create a resonance angle shift whereas LSPR uses the quantum confinement of nanoparticles to localize the surface plasmons, which will create a shift in the extinction (absorption) band.[47] A schematic representation of both principles is presented in **Figure I.3-2**.

Nanoparticles exhibit intense absorption at a specific wavelength (depending on size, shape and arrangement). The advantages of LSPR compared to SPR are: low cost and simplicity of the equipment, easier measuring conditions, tunable sensitivity for a specific target (by tuning size, shape etc), no bulk effect, temperature independence of the signal, creating array-based sensors with parallel screening of multiple interactions.

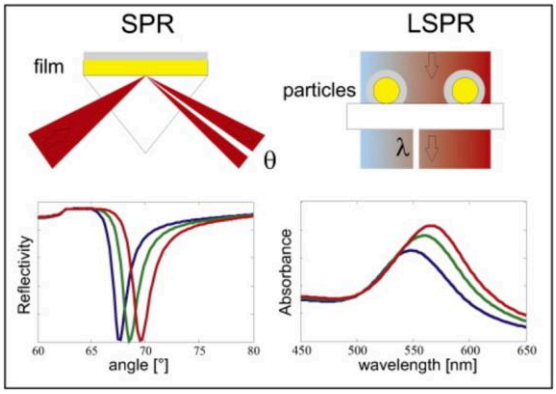

Figure I.3-2 Schematics of the sensing principle for the studied pSPR (left) and lSPR (right) systems. The graphs below show the calculated shift of dip/peak upon adsorption of 10 nm (green line) and 20 nm (red line) thick molecular film with an refractive index of 1.48 in water (n = 1.33), which mimics the properties of biomolecules.[48]

A recent SPR study detailed the development of antibody-sandwich like method to distinguish between RCA and ricin.[49] They also present a different method of assessing the enzymatic biological activity of ricin's depurination ability. Monoclonal antibodies targeting A chain (mAb R18) or B chain (mAb R109) were used. They used a CM5 chip sensors (that has carboxylic functions on the interface) and a standard amine coupling technique

© 2020 Tous droits réservés.
lilliad.univ-lille.fr

(NHS/EDC strategy) to immobilize effectively the mAb R109. Both ricin and RCA are then injected and captured on the modified CM5 chip. Then, in a second step, an injection of mAb R18 is performed binding only the captured ricin. A normalized method of quantification and the schematic principle is presented in **Figure I.3-3**.

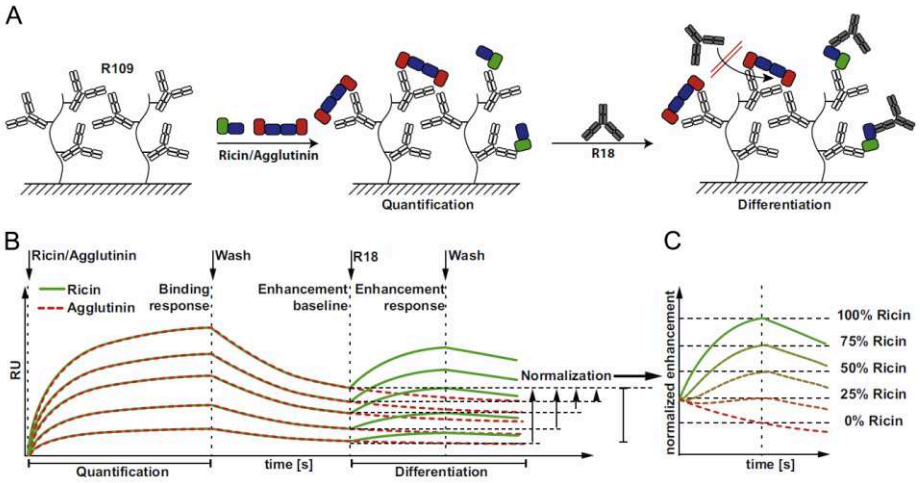

Figure I.3-3. Schematic principle of the sandwich bio-sensor **(A)** Schematic binding curve and normalized response for the differentiation of ricin and RCA **(B)**.[49]

I.3.2. Methods that can identify biologically active ricin

Mass spectrometry is the most important method that can identify the removal of free adenines because of the difference in mass due to the loss of adenine (Mw=135 kDa). Even so, when different methods that require digestion of ricin protein, this becomes unrealistic, because one main condition of catalytical biological activity and toxicity of ricin is that A and B chains are not separated and both are present. As in digestion, the ricin if fragmented in different peptide sequences, simultaneous detection and identification of enzymatic activity of biological activity of ricin, is not possible. **Table I.3-2** presents some literature examples or methodologies able to assess if ricin is biologically active or not.

Becker et al.[50] used monoclonal antibodies directed against the B chain immobilized on magnetic beads. The beads were incubated 2 hours, at 37°C, in HEPES solution containing 1 mg/ml BSA and ricin. After rinsing, RNA was incubated to the ricin modified beads, during 4 or 24 hours. Free adenine molecules, released from RNA digestion by ricin modified beads, were analyzed by LC-ESI-MS/MS. Even though the CV values were 10%, with a limit of detection of 0.1–0.3 ng/ml in real samples, the method takes even 24 hours to be completed. The ESI-MS spectra is presented in **Figure I.3-4**, where the 136 m/z peak is observed and it corresponds to $[adenine+H]^{+1}$.

© 2020 Tous droits réservés.
lilliad.univ-lille.fr

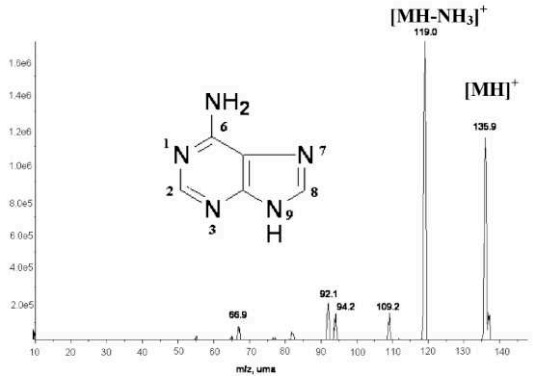

Figure I.3-4 ESI-MS/MS spectra of (A) m/z 136 of unlabeled adenine added to a mixture of mobile phase A and B (50/50). [50]

Similar method is described by Schieltz et al.[9] MALDI-ToF MS indirect detection of ricin, describes a method proving the ricin activity by depurination of a DNA mimicking the natural substrate of 28 S loop ribosomal RNA, containing (GCGCGAGAGCGC) sequence, with a M_w= 3696.[9] By doing so, it can be assessed if the protein is active or inactive. Indeed, after depurination, another MS peak was observed at 3579 m/z, corresponding to the loss of [adenine-NH_3]$^+$ (-118 m/z, as in **Figure I.3-4**). **Figure I.3-5** presents the MALDI-MS spectra of the DNA mimic incubated with ricin 4 h and the DNA mimic incubated with ricin 20 h. In addition to Becker et al. work, they also perform a mass spectrometric protein identification analysis by nLC/MS/MS and database searching, using tryptic digestion of proteins. Even more important is the fact that they used real samples recovered from a crime scene and compared to other techniques (Dissociation- Enhanced Lanthanide Fluorescence Immuno Assay Time-Resolved Fluorometry and PCR) and their method had similar and satisfactory results.

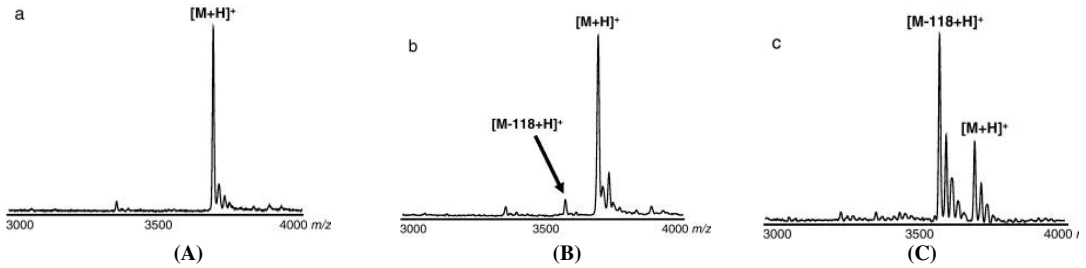

Figure I.3-5. MALDI-TOF spectra showing the ricin activity after incubation with the DNA mimic sample. The negative control presents a m/z peak at 3697, corresponding to the protonated form (a). After the incubation of the sample with ricin for 4h (b) and for 20 h (c), the removal of adenine residue can be observed at 3579 m/z (-118 kDa), along with the 3697 m/z.[9]

There are few methods described in literature that are able to detect the protein and also to identify the biologically active ricin. McGrath et al.[51] described in 2011 one of these methods. They used two MS methods: one for quantification of ricin (LC/product ion

© 2020 Tous droits réservés.
lilliad.univ-lille.fr

monitoring (PIM) MS) and one for enzymatic assay of the toxin (MALDI-MS). Antibody conjugated beads were used to capture ricin from a ricin-agglutinin mixture. After the extraction of ricin, trypsin was used for the digestion of the protein, and the same peptides were used for identification of both A and B chains and also to distinguish from agglutinin (RCA120). The calibration and quantification were done using heavy isotope internal standard peptides. Liquid chromatography was used for separating peptides, which were introduced in the orbital ion trap, using ESI-MS, for quantification with internal standards. Ricin and ricin magnetic beads conjugates are incubated separately with a synthetic DNA mimic of the toxin's natural rRNA target, and the product of the reaction is detected by MALDI-ToF-MS, using 3-hydroxypicolinic acid as organic matrix. All these complex and lengthy assay time steps, as well as usage of several expensive equipments and reagents, are the main drawbacks of this method.

In 2012, Zhao et al.[52] performed MALDI-MS experiments on different serum peptides from intoxicated mice subjects. They also used magnetic beads with different functionalities to select between peptides that can be used as biomarkers for ricin intoxication in comparison with serum controls. They did use 1 µg/ml solution of ricin in PBS (0.02 M, pH 7.4) to inject the mice and studied the serum after 1 hour prior to the injection. The weak ion exchange magnetic beads (MB-WCX) seem to give the less overlapping of controls vs infected samples.

Table I.3-2 Ricin methodologies of detection and assays of biological enzymatic activities.

Year and reference	Ricin methodologies	Lowest level of detection (LOD)	Matrix involved	Detection time	Drawbacks
2007 [50]	Immunoaffinity and **LC–MS** adenine release assay, antibody conjugated to magnetic beads	0.1–0.3 ng/ml	Water milk	4–24 h	lengthy assay time, detection of ricin is only assessed through the possibility of having free adenine
2011 [9]	Immunoaffinity and **MALDI-TOF** adenine release assay, from antibody conjugated to magnetic beads + **LC-MS** protein identification of digested ricin	10 µg/mL	Buffer + 6 samples acquired from a crime scene	20 hours	lengthy assay time, multiple complex and reagent consuming steps, using several expensive equipments
2011 [51]	Isotope dilution **MS** and deadenylase activity assay Antibody conjugated to magnetic beads	0.6 ng/ml	Water, milk, and juice	4-6 hours	lengthy assay time, multiple complex and reagent consuming steps, using several expensive equipments.
2012 [52]	Serum peptide profiling by **MALDI-TOF/MS**, magnetic beads	1 µg/ml	Serum	Not reported	Usage of animal subjects that were infected with ricin.

© 2020 Tous droits réservés.
lilliad.univ-lille.fr

2015 [53]	Magnetic beads used in isotope dilution mass spectrometry (**IDMS**)	1.0 ng/mL	Crude seed extracts	-	Crude seed extracts, with lower toxicity.
2016 [49]	Simultaneous differentiation and quantification of ricin and agglutinin by an antibody-sandwich **surface plasmon resonance (SPR)** sensor	3 ng/mL	Buffer and liquid food matrices	25 min	Costly SPR equipment
2019 [54]	antifouling polymer brush modified magnetic beads modified with ricin monoclonal antibody (for **immunomagnetic**) and AuNP/QDs (**fluorescence**)	7.46 ng/mL	juice, ham, sandwich, milk, coffee, and human plasma serum	> 1.5 hours	lengthy assay time

© 2020 Tous droits réservés.
lilliad.univ-lille.fr

I.4. Matrix-free LDI (laser desorption ionization)-Mass Spectrometry

Mass spectrometry is considered to be the gold standard in analytical chemistry due to high sensitivity, limits of detections, speed and diversity of its applications. Most applications in analytical chemistry are correlated to bio-problems related to proteome, metabolome, metabolism, drug consumption, food control, forensic science, pollution control, process monitoring and others. Mass spectrometry ionizes the analytes and sorts the ions according to mass to charge ratio.

Mass spectrometry is based on the analysis of the ratio between the molecular weight "m" and their charge "z", denoated as "m/z". The m/z ratio allows retrieving information about the composition and the real molecular weight of the analytes.

Each mass spectrometer is composed of three elements (**Figure I.4-1**): ionization source (which allows the production of positive or negative ions), mass analyzer (which allows the separation of ions based on their m/z) and detector: which accounts for the ions and their m/z.

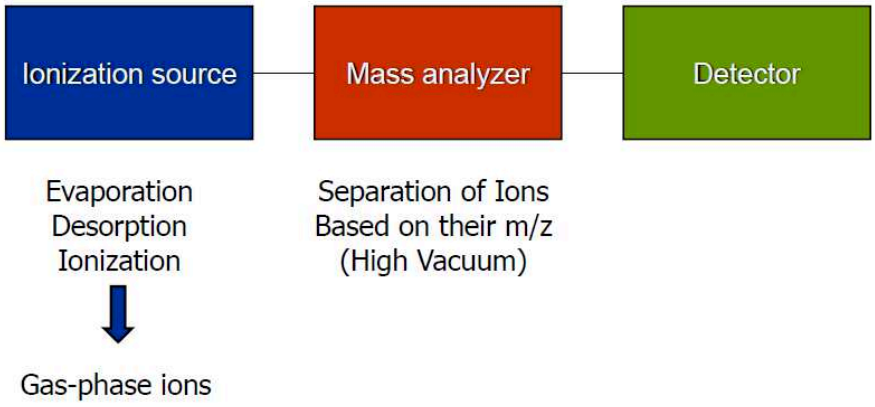

Figure I.4-1 The main components of a mass spectrometer.

Depending on the ionization source, the mass spectrometry techniques can be separated in two classes: soft and hard ionization techniques, depending on the energy imparted to the analyzed molecules, thus the degree of fragmentation. Also, different ion sources are linked to the properties of the molecules to ionize (the atoms present, the polarizability, electrophility, basicity etc) and their environment. The choice of ion sources is made in function of the nature of the sample (gas, liquid, solide, volatile or thermolability) or the required analyse type (fundamental, structural etc). The main ion sources are briefly described in **Table I.4-1**.

© 2020 Tous droits réservés.
lilliad.univ-lille.fr

Thèse de Ioana Silvia Hosu, Université de Lille, 2020

Table I.4-1 The main ion sources used in mass spectrometry.

Ionization method	Abbreviation	Description	Method type	Analytes
Electron Impact	EI	A beam of electrons passes through a gas-phase sample and collides with analyte to produce a positively charged ion or a fragment ion	Hard	Small volatiles chemicals
Chemical Ionization	CI	A reagent gas is ionized by electron impact and then subsequently reacts with analyte to produce analyte ions.	Soft	Small volatiles
Electrospray Ionization	ESI	A solution is nebulized under atmospheric pressure and exposed to a high electrical field which creates a charge on the surface of the droplet. Droplets rapidly become much smaller through vaporization of solvent and into an analyzer.	Soft	Peptides, proteins non-volatile chemicals
Fast Atom bombardment	FAB	A beam of high energy atoms strikes a surface to create ions.	Soft	Carbohydrates, organometallics, peptides, nonvolatile
Matrix Assisted Laser Desorption Ionization	MALDI	The sample in a matrix material is irradiated with a pulsed laser which triggers ablation and desorption of sample and matrix.	Soft	Peptides, proteins nucleotides

In this work, we are interested in the laser desorption/ionization techniques (LDI) because it is a soft ionization technique that can be used to detect peptides and proteins, that are big, unstable polar molecules and macromolecules and require soft ionization, to avoid fragmentation. The most representative method of the LDI process is matrix-assisted mass spectrometry (MALDI-MS) that was introduced in the 80' by Karas et Hillenkamp.[55] In comparison with electron-spray ionization mass spectrometry (ESI-MS), that is another soft ionization technique, the MALDI-MS presents the advantage of high throughput, by analyzing a high number of samples, which is essential in the health applications.

A variety of analyzers were also developed during history (time-of-flight, ion trap, orbitrap, quadrupole, quadrupole-ion trap etc), but we will focus on ToF (time-of-flight) for this thesis, due to increased mass accuracy and mass resolution, greater sensitivity, rapid acquisition, and increased dynamic range when profiling over a broad molecular weight range.

I.4.1. Drawbacks of matrix-assisted desorption/ionization

In MALDI-MS (matrix-assisted desorption/ionization mass spectrometry) the production of ions is achieved by desorption/ionization after laser irradiation with ns UV-laser (or IR) impulsions of an analyte co-crystallized with a matrix. Dissolving the analyte together with a specific light-absorbing organic compound (matrices) and co-crystallize, enhances the MS signal and influences the fragmentation pattern. The matrix also protects the direct exposure

© 2020 Tous droits réservés.

lilliad.univ-lille.fr

Thèse de Ioana Silvia Hosu, Université de Lille, 2020

of the analyte to the UV laser, limiting aggregation and facilitating the evaporation/sublimation of molecules to be detected, together with proton transfer, in function of the acido-basic character.

The mechanism of LDI is still unknown, but three of the most used matrixes are: 2, 5-dihydroxybenzoic acid (DHB), sinapinic acid (SA) or Alpha-cyano 4hydroxycinnamic acid (CHCA). Very different spectral characteristics are obtained according to the matrix i.e. charge states, peak width, background, signal intensity, number of matrix peaks, presence of adducts (salts, matrix). Nevertheless, a great variety of matrixes are described in literature and the fact that a large number of macromolecules that couldn't be analyzed before, can be analyzed now using with the discovery of MALDI-MS,[55] was a very important moment in analytical chemistry and all sorts of practical domains (presented in **Table I.4-2**).

Table I.4-2 Main applications for MALDI-MS.

Fields of study	Applications
Proteomics	• Determine protein structure, function, folding and interactions • Identify a protein from the mass of its peptide fragments • Detect specific post-translationnal modifications throughout complex biological mixtures • Quantitate (relative or absolute) proteins in a given sample • Monitor enzyme reactions, chemical modifications and protein digestion
Drug discovery	• Determine structures of drugs and metabolites • Screen for metabolites in biological systems
Clinical testing	• Detect disease biomarkers (ex. metabolic diseases, Ab-peptides detection from Cerebrospinal fluid (CSF)...)
Genomics	• Sequence oligonucleotides
Environment	• Test water quality, soil and food contamination
Forensics	• Illicit drug abuse detection from saliva or fingerprint • Explosive detection

The common characteristics of the organic compounds used as matrix are: presence of carboxylic and other acidic groups (H^+ donors), UV absorbing organic molecules with conjugated π systems and assuring the energy transfer from laser to analyte.

The MALDI process is summarized in **Figure I.4-2.** After the pulsed UV irradiation, the LDI process takes place in three important steps: the absorption of the energy of the light beam, ablation/desorption generates a plume, ionization of analytes during desorption and during the plum formation.

© 2020 Tous droits réservés.

lilliad.univ-lille.fr

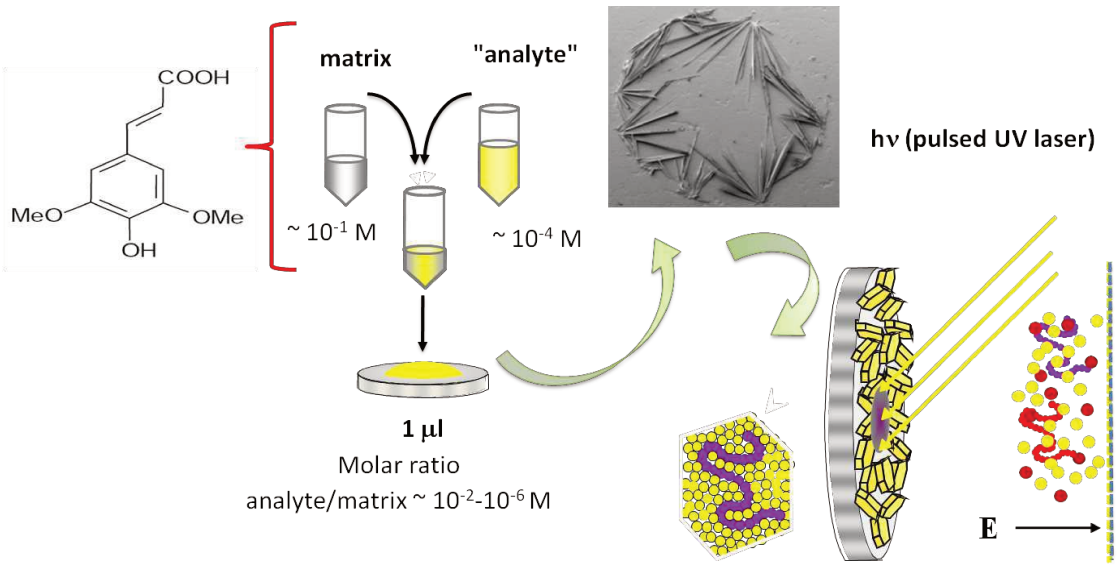

Figure I.4-2 Schematic representation of the MALDI-MS flow.

The formed ions are accelerated using a voltage and they arrive in the analyzer. The acceleration of the ions will take place differently, according to their molecular weight. The smaller ions will be accelerated quicker and they arrive faster to the detector. Correlating and calibrating the time of flight of each molecule until it reaches the detector, with the mass, allows having a very good precision of the molecular weight detected.

Due to all the vast domains of application (**Table I.4-2)** and all the parameters that can be tuned during MALDI-MS analysis (delayed extraction time, high mass detectors, reflecton of linear mode, applied voltages, power of the laser etc) the technique has become a very powerful tool. The choice of matrix as well as the deposition method has become essential.

As it can be observed **Figure I.4-2**, the co-crystallization can be sometimes heterogenic, and this will lead to a creation of "sweet spots", that will decrease in sensitivity and reproducibility, during MALDI-TOF analytical processes. The use of matrix also has another important drawback: the noise background makes difficult the detection of molecules with m/z smaller than 700 m/z. Using UV matrix in excess favors desorption, but has an important impact on the quality of the MS spectrum. Moreover, the pollution from the matrix (adducts, fragments, aggregates) will hinder the detection of analytes in the same mass range. IR-MALDI-MS provides lower yield of metastable fragmentation in comparison with UV-MALDI-MS, which can in particular be of advantage for the analysis of very labile biomolecules like large nucleic acids. It is a softer ionization technique than UV-MALDI-MS, but requires higher pulsed energy.[56]

The variety of the matrix to be used can become a problem itself, as there is no universal matrix, which implies a preliminary knowledge of the investigated compounds. Another

© 2020 Tous droits réservés.
lilliad.univ-lille.fr

drawback is that quantitative analysis are not quite possible, due to inhomogeneous matrix-analyte co-crystallization.[57]

I.4.2. Surface-assisted desorption/ionization mass spectrometry (SALDI-MS)

Matrix-free laser desorption/ionization (LDI) process has been developed to overcome the presence of huge background in the low molecular mass region of the MS spectrum. This background is essentially coming from adducts and fragments of organic matrices when matrix assisted laser desorption ionization mass spectrometry (MALDI-MS) is used thus making difficult the detection of small compounds below 700 Da. Alternative solution appeared in 1988, when Tanaka replaced the organic matrix by ultra-fine particles mixed to glycerol, allowing the detection of proteins up to 100 kDa,[63] giving rise to surface-assisted laser desorption/ionization mass spectrometry (SALDI–MS). Chronological development of SALDI-MS methods are presented in **Figure I.4-3**. In blue, there are the methods that were developed world wide and in purple the methods that were developed in our research group.

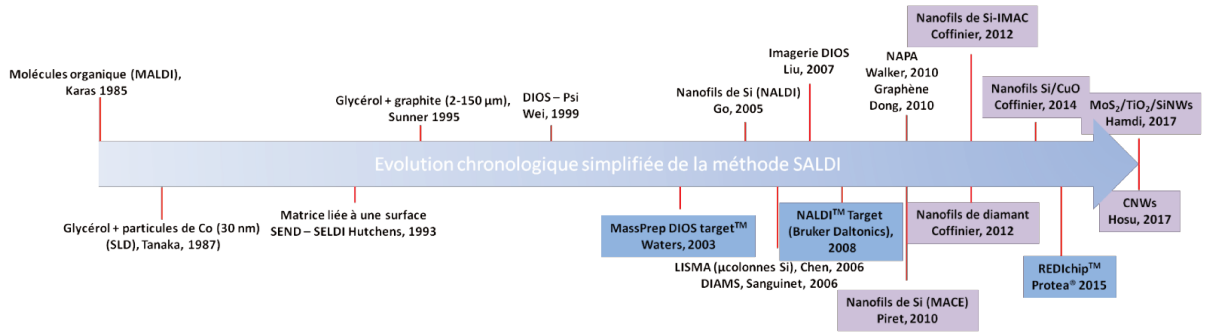

Figure I.4-3 Chronological evolution of SALDI-MS.

Matrix-free LDI process using nanomaterials, provides several advantages concerning the analysis of small compounds.[64] Indeed, the co-crystallization of the sample with an appropriate organic matrix is not anymore required, and subsequently, intense matrix peaks responsible for strong background in the low-mass range of the spectra hampering sensitive detection of small molecules are suppressed[65-67] (see **Figure I.4-4**). In addition, sample deposition becomes very straightforward and reproducible, both mandatory for rapid data acquisition (high throughput analyses) and integration within lab-on-chip devices.[68,69]

© 2020 Tous droits réservés.
lilliad.univ-lille.fr

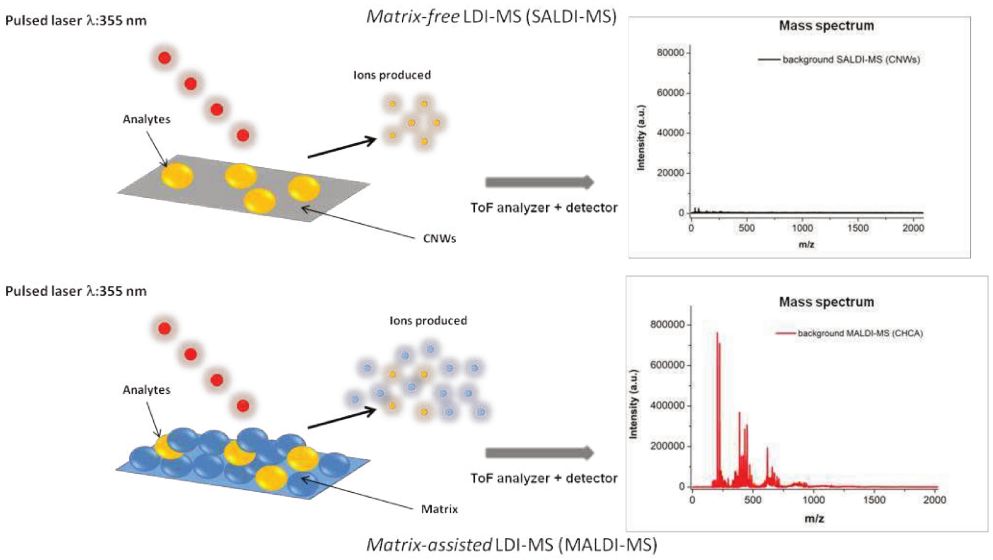

Figure I.4-4 Mass spectra showing the difference of background in the low mass range obtained either by SALDI (CNWs) (top) or by MALDI-MS (bottom).

Moreover, recent advances in material sciences led to prepare various materials presenting the required/desired optical, electrical and thermal properties with well controlled morphologies for SALDI-MS applications.[64-70] For decades, semi-conductors (Si, Ge, GaN), metals (Ag, Au, Pt), metal oxides (Fe_2O_3, TiO_2, ZnO) and carbon based structures (graphite, fullerene, diamond, carbon nanotubes) presenting different shape and dimensions such as nanowires/nanotubes and film/sheet have been tested as LDI materials.[71-73] The main interest of SALDI surfaces is mainly due to their interesting anti-reflective optical and thermal properties (high thermal capacity and low thermal conductivity) thus leading to confined heat and high transfer of internal energy) (see **Table I.4-3**).[74]

Table I.4-3 SALDI interfaces properties and their advantages *vs* MALDI

Surface properties	**Advantages/MALDI**
Optical properties: UV absorbent, Anti-reflectives, low photoluminescence	No organic matrices Simple deposition method, uniform distribution of analytes - No "hot spots"
Thermal properties: Low thermal conductivity, heat confinement, low melting point	Low laser fluence- Limitation of fragmentation Low background Higher deposited internal energy
Chemical modifications : Reproducibility, Affinity capture, Activation energy, wettability	High specific surface area Great adsorption capacity of analytes
Other parameters influencing LDI performances : Porosity, nanostructure's dimensions, doping, high electrical conductivity	Sensitive towards small compounds <10000 Da Salt tolerant, adaptable to any MALDI-ToF instrument

© 2020 Tous droits réservés.
lilliad.univ-lille.fr

Analyzing biological sample is usually time and reagent consuming. For a better understanding of the complexity, **Figure I.4-5** presents all the possible steps in sample preparation and analysis procedures of ricin. A very important drawback is that most of the big molecules (as ricin) require the fragmentation into smaller parts for a sensitive MALDI-TOF detection. The protein digestion can be done enzymatically (bottom-up method) or nonenzymatically (top-down method) or using an acidic baser digestion. All types of digestion require protein sequence reconstruction and comparison with a pre-acquired data base of composing peptides and their position.

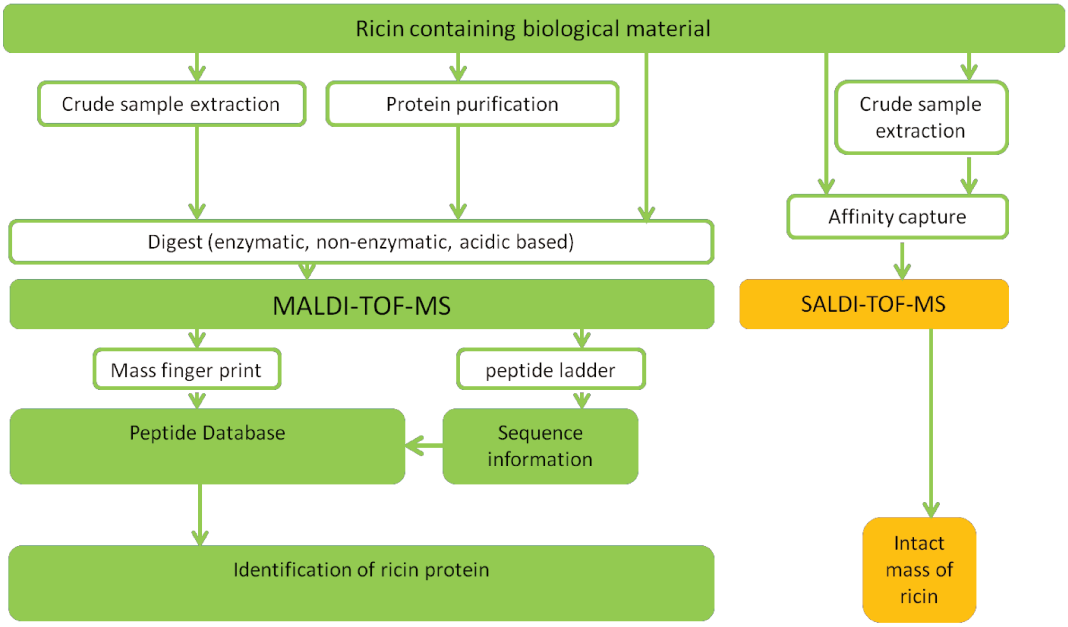

Figure I.4-5 MALDI-MS vs SALDI-MS analysis of ricin: schematic overview of possible analysis procedures.[58]

Special attention is accorded to MALDI-MS methods used to detect ricin, as SALDI-MS is a method derived from MALDI, which uses surfaces instead of organic matrix. Some MALDI-MS methods of detection are presented in **Table I.4-3**. It is important to mention that there is no SALDI-MS method ever described for detection of ricin. Even though the limits of detection are quite low, all the methods suffer from the complexity of sample preparation we describe above. Nevertheless, these kinds of methods are a source of inspiration for further development of SALDI-MS substrates (especially in selecting buffers, interfering species and other measurements conditions).

© 2020 Tous droits réservés.
lilliad.univ-lille.fr

Thèse de Ioana Silvia Hosu, Université de Lille, 2020

Table I.4-4 Literature study for the detection ricin using MALDI/MS techniques detection using matrix.

MS technique	Year and reference	Details about the measurements [a)]	Real samples [b)]	Analyte	m/z	Interfering species studied	Other conditions (buffer/pH)	LOD (pmol/0.5 µL)[c)]
MALDI MS (tryptic digest or ricin)	2009 [59]	Antiricinus agglutinin modified Dynabeads Protein G immunoprecipitation system	milk, apple juice, serum and saliva	Ricin (RCA_{60})	≈64 kDa	RCA_{120}	10 mM ammonium citrate + 1 mM EDTA + TFA (pH 4)	5 pmol
ESI MS of intact ricin	2000 [60]	50 µl injection loop (measuring multi charged ions)	-	Ricinus communis extracted from castor beans	≈63 kDa	-	0.5 mM NaCl + acetic acid + ACN/H_2O+ formic acid pH 4	50 pmol
MALDI TOF MS	2008 [37]	Magnetic beads with Protein G modification with ricin B chain antibody for ricin extraction	milk, bean pulp slurry	Ricinus communis extracted from castor beans	1013.6 1310.6 1728.9	-	50 mM HEPES + 1mg/ml BSA/ CHCA as matrix (pH 7.3)	4 fmol (32 fmol in milk)
MALDI TOF MS	2009 [61]	Combined mixture of ricin samples + CHCA matrix	endogenous seed proteins	ricin from Ricinus communis (castor bean)	≈64 kDa	-	aqueous buffer 0.01% Tween 80/ CHCA as matrix (pH ≈ 7)	16 fmol
MALDI MS	2017 [62]	Ovalbumin encapsulated gold nanoclusters (AuNCs@ew)	white chalk powder spiked with ricin B	Ricin B chain	≈32 kDa	*Mb, Cyt C, Lys, RNAase, BSA, Try, PA, cel lysate	HEPES buffer (pH 7.5)/CHCA as matrix	3,9 fmol (10pmol in white chalk sample)

* myoglobin, cytochrome C, lysozyme, ribonuclease A, ubiquitin, BSA, trypsin, peanut agglutinin, cell lysate

I.4.2.1. SALDI-MS mechanism

The matrix-free LDI process is believed to be mainly based on thermal driven mechanism divided into several steps i.e. photon energy absorption, energy pooling, radiation coupling and transfer, desorption, and ionization steps.[75] Thus, to perform SALDI-MS analyses, the interfaces should primarily be able to absorb photons from the pulsed laser (λ=337-355 nm) corresponding to photon energy (3.68-3.49eV).[75] Then, thanks to a thermal mechanism relaxation via non-radiative recombination (phonons' scattering) of electrons and holes, the desorption/ionization of analytes can occur. From this, it's clear that SALDI surfaces morphology, dimension, aspect ratio, porosity, density and periodicity are strongly related to their physical properties. Indeed, it's well known that when critical dimensions of the nanostructures are below characteristic lengths i. e. phonon mean free path, thermal

© 2020 Tous droits réservés.

lilliad.univ-lille.fr

dissipation length, optical absorption length..., modes of transport of the corresponding materials e. g., ballistic vs diffusive, energy confinement (phonon scattering), plasmon resonances, and local field are enhanced.[76] Thus, by controlling the nanostructures' dimension/physical properties, we can expect to better control the LDI performances.

I.4.2.2. Variety of materials used in SALDI-MS and their properties

Figure I.4-6 shows a summary of nanoparticle screening for small molecule metabolite analysis.[77] Ion signals are normalized to the highest ion signal for each analyte and shown as a heat map. In red are represented the peaks that have 100% normalized intensity and in green the ones with less than 5%. This scheme presents in clear way the LDI enhancement of some substrates for different chemical functionalized small analytes.

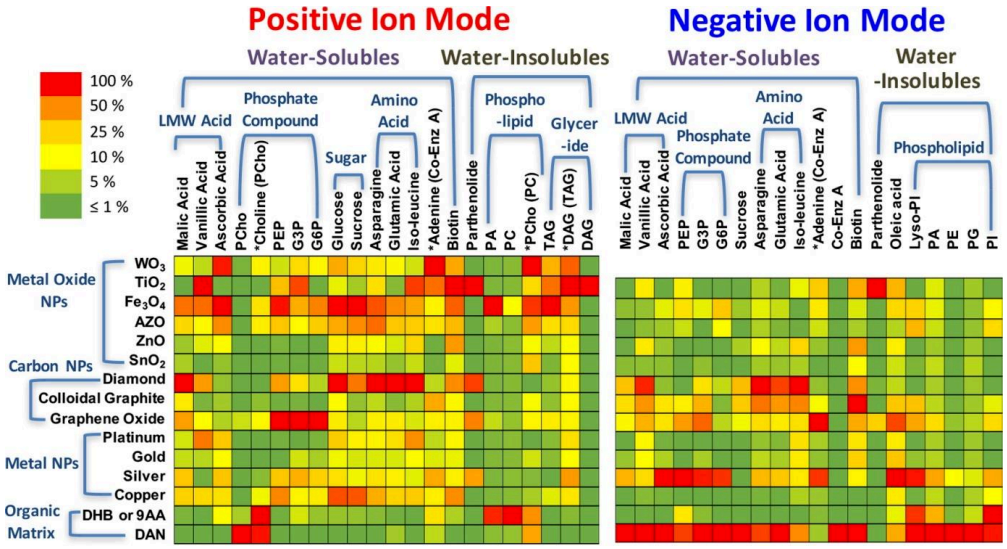

Figure I.4-6 LDI-MS performances of different types of particles for the detection of small molecules, with different physic-chemical characteristics.[77]

In our group there were also described during time different nanomaterial based SALDI-MS platforms. **Figure I.4-7** shows SEM monographs of the developed surfaces and their references of the works already published. In this subsection we will try to categorize and describe the most important parameters that should be considered for the development of such SALDI-MS surfaces.

© 2020 Tous droits réservés.
lilliad.univ-lille.fr

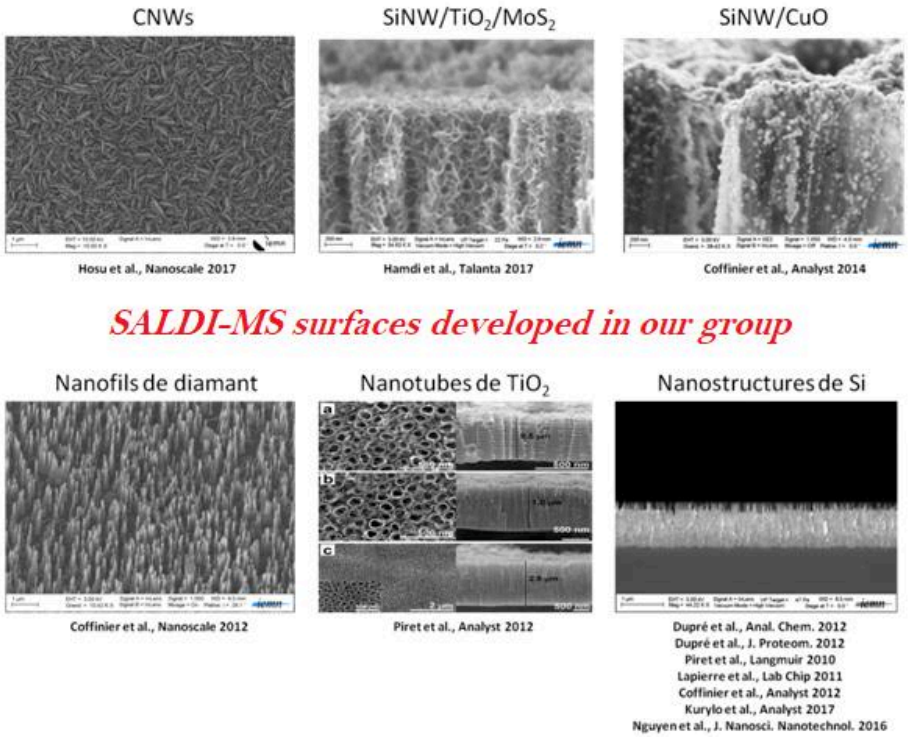

Figure I.4-7 SALDI-MS surfaces developed in our group during time as stated in the described references.

I.4.2.2.a. Semiconductors

In the 90's, desorption ionization on silicon (DIOS) was first used for detection of small molecules.[78] The upper mass limit of such SALDI-MS platform are usually limited to 2500 Da, using UV lasers and upper limits were achieved using IR lasers.[79] The upper mass limit is the drawback that exclude this materials for the goals of this thesis. Silicon nanoparticles have shown lower LOD than DIOS and up to 8 times less energy required for LDI process.[80] Our group used different silicon based materials and the work is described in detail in a book chapter.[81]

A special part of the semiconductors are quantum dots with size < 10 nm. Presenting different advantages over classical organic matrix: improved the signal-to-noise ratio, spectrum quality, increase the number of detected peptides and the overall sequence coverage. The most important drawback is that, being composed of heavy metals (CdSe, CdTe, HgTe, ZnS), nanoparticles are toxic.

I.4.2.2.b. Metal/metal oxide nanoparticles/nanostructures

Metallic nanoparticles are usually used for bigger molecular weight compounds, such as proteins, because of their good surface to volume ratios (higher direct contact with the analyte, thus better analyte loading), optical tunable UV band gaps etc. One of the key factors of using metal nanoparticles for LDI-MS, seems to be the aggregation (density) on the MS

© 2020 Tous droits réservés.
lilliad.univ-lille.fr

Thèse de Ioana Silvia Hosu, Université de Lille, 2020

plate.[82] Metallic nanoparticles are expensive. They tend to aggregate in the absence of stabilizing agents that sometime cause interference in the mass range < 500 Da. Nobel metals Ag, Au, and Pt, showed higher LDI efficiency compared to transition metals and organic matrices. Nevertheless, they represent a good way to go in combining different techniques to create dual methods. [80]

I.4.2.2.c. Carbon based materials for SALDI-MS

Carbon based materials in SALDI-MS are usually used for low molecular weight compounds MS detection.[83] Similar morphological features are important for carbon nanostructured surfaces, which started to compete with the use of metal nanoparticles and semiconductors in SALDI-MS.

The use of carbon materials as interfaces for SALDI MS is an encountered practice in MS and the efficiency of different interfaces is compared using "thermometer molecules", Unsubstituted or para substituted benzylpyrridinium compounds, are used to determine the desorption efficiency and internal energy transfer of the carbon materials used in SALDI, and it was established that both parameters are related to the surface area of the material. Thus the large surface area of carbon nanotubes (CNTs) enhances better ion desorption efficiency.[84] Since then, other SALDI surfaces, such as the ones based on metal nanoparticles, used this method.[85]

Nanostructured materials, due to several potential benefits, including: an extended dynamic range (due to an increased surface area and analyte loading capacity); improved reproducibility (due to intimate analyte incorporation and deposition homogeneity); superior sensitivity and energy-transfer efficiency (due to the unique optical and thermal properties of nanomaterials).[57]

I.4.2.3. Chemical functionalization

Chemical composition and functionalization can affect several parameters: stability of MS signal (as, for examples oxidized carbon species can create more background signals, and the reproducibility of the analyte signal is lower), groups for protonation process (as, for example, carboxylic groups on the surface of materials can also act as proton donors and enhance LDI), wettability, thus analyte confinement and interactions with the material (as, for example, fluorinated materials can create hydrophobic surfaces, that will confine the analyte on a smaller surface) and activation energy (as, for example you can control the efficiency of the ionization and the deposited internal energies on the surface, by playing with different carbon-based materials or different nanoparticles).[84]

© 2020 Tous droits réservés.
lilliad.univ-lille.fr

Another important parameter described in the literature, regarding the use of carbon materials as SALDI substrate, is the oxidation of the surface. Oxidation of CNTs improved the efficiency of DI processes compared with non-oxidized CNTs for the detection of amino acids.[86] In fact, by increasing the solubility in water (that increases the proximity of the amino acids to the SALDI substrate), the energy transfer efficiency is also increased.[87] Also oxidized graphitized carbon black nanoparticles (oxGCB NPs) enhanced the desorption/ionization of propranolol, and the authors observed that carboxylic groups improve the sensitivity towards more hydrophobic compounds.[88] On the other hand, Lim et al. proved that APTES, (3-Aminopropyl)triethoxysilane, modified carbon black particles can enhance the sensitivity towards polar molecules (e.g. amino acids) and PTEOS (Phenyltriethoxysilane) magnetic modified carbon back particles enhances the sensitivity for the nonpolar molecules (e.g. fatty acids). This behavior is explained by electrostatic interaction (for polar groups) and hydrophobic interactions (for non-polar groups).[89]

The specificity of any SALDI-MS method can be achieved by conjugation of the material with a recognition element [83] or introducing affinity functional groups at the surface of the material. One of the characteristic to be avoided is that the interaction between the recognition element and the analyte not be too strong, because desorption from the SALDI-MS substrate can be impossible in this case. Nevertheless, a too weak interaction could not offer enough specificity.

© 2020 Tous droits réservés.
lilliad.univ-lille.fr

I.5. Conclusions

Ricin is one of the most toxic vegetable proteins world-wide. As it is easy to extract and water soluble, it is used for terroristic acts. The mechanism of toxicity of this protein consists in inhibition of proteins synthesis, by depurination of rom the RNAr 28S from the 60S ribosomal subunits (by the A chain), but the B chain helps in the transportation phase of the toxin through membranes. As the B chain is a lectin, it binda specifically to galactosamine moieties. The toxicity mechanism can be used as an affinity recognition element in developing ricin sensors.

When it comes to detection of ricin, many classical methods as ELISA and other immunoassay methods, SPR, colorimetric and MS, are used. As these methods are quite sensitive, the most important disadvantages are the lack of rapidity, distinguishing if ricin is active or not, distinguishing between ricin and other RIP proteins. Determining the biological activity of ricin is usually assessed by determining the depurination enzymatic ability of ricin.

The most important efficient method that can both assess enzymatic activity of ricin and detect/quantify ricin, is mass spectrometry, especially matrix assisted mass spectrometry (MALDI-MS). This method is a soft ionization technique and is a subclass of the LDI (laser desorption ionization) ionization sources. The use of laser to assure desorption and ionization is based mainly of the ability of organic matrixes to absorb light and transfer it to the analyte, without further fragmentation. The main disadvantages when organic matrix is used (mainly aromatic conjugated systems, that have acidic groups on them, that acts as proton donors), is that the matrix itself can give rise to MS peaks, that will interfere with the analyte peaks (usually bellow <500 kDa). Also this method is not suitable usually for quantification, as the MS signal stability fluctuates with the inhomogeneity of sweet spots, due to co-crystallization of organic matrix. The main drawback of MALDI-MS, when it comes to protein, is that usually it cannot detect intact big molecules, as the necessary energies required for desorbing and ionizing this kind of big molecules, are not efficiently transferred to the analyte. Because of this reason, digestion of proteins is usually employed, and the detected obtained peptides are to be compared with an already prepared database, for the identification of the protein itself. The supplementary steps, are time and reagent consuming. The ideal case it to be able to detect the intact protein mass.

To overcome these drawbacks, replacement of organic matrix was done with inorganic materials, creating a new LDI method, called surface assisted matrix laser desorption ionization. The advantages of SALDI-MS over MALDI-MS are the following: simple

© 2020 Tous droits réservés.
lilliad.univ-lille.fr

deposition methods, not “sweet spots”, limitation of fragmentation, higher deposited energy, low background peaks, high specific surface area, great adsorption capacity, salt tolerance, adaptable to any MALDI-TOF instrument, sensitive towards small compounds.

The variety of nanoparticles used for SALDI-MS is vast, but three main categories can be identified: semiconductors, carbon based materials and metal nanoparticles. Scheme presented in **Figure I.5-1** shows the summary of most important nanoparticles/nanostructures ever developed for SALDI-MS.

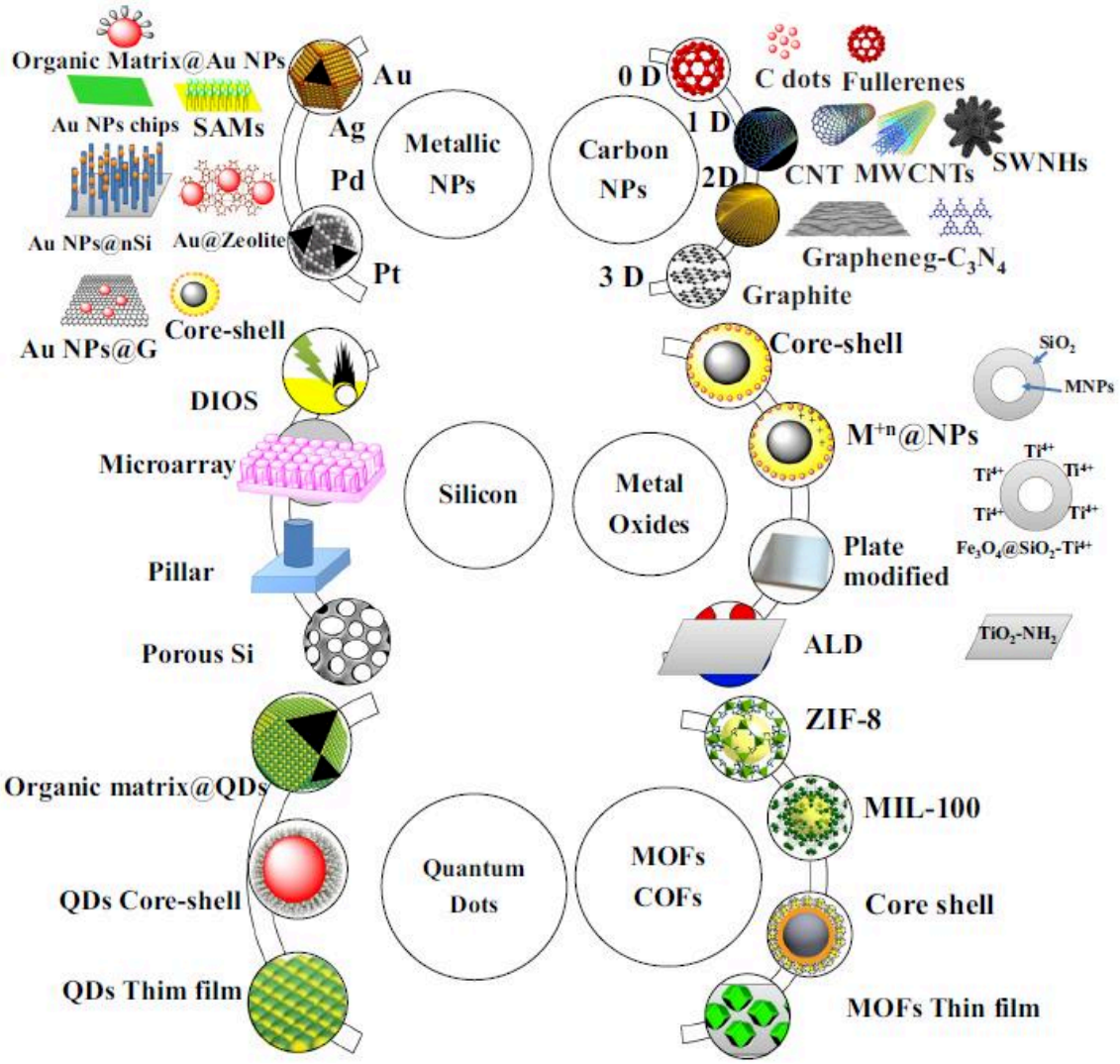

Figure I.5-1 Variety of materials used in SALDI-MS.[80]

All these parameters discussed with the variety of materials influence the MALDI-MS process and they should be taken into account when a SALDI-MS surface/material is to be developed. An extensive review of different parameters influencing SALDI-MS was written by Abdelhamid in 2019.[80] **Figure I.5-1** presents the connection of these parameters and their magnitude in influence.

© 2020 Tous droits réservés.
lilliad.univ-lille.fr

Figure I.5-2 Analysis of key parameters affecting nanoparticles performance including composition, surface, concentration, thickness, additives, surface area, pore size, and MALDI-MS instrument parameters**.** [80]

Imaging is also possible in MALDI-MS: multiplex analysis of thousands of analytes across a samples surface yielding 2-dimensional molecular maps that elucidate both the localization and relative abundance of endogenous species.[90] This can be fully extended to SALDI-MS, with the appropriate effort, as there as several SALDI-MS platforms used for imaging.[91]

As we conclude, carbon based materials are already used for detection of some molecules in SALDI-MS. That is why, in this thesis we do use graphene-based materials for detection of small molecules first (Chapter II) and further optimize the SALDI-MS method for detection of proteins (especially ricin, Chapter III). In all cases we will characterize and describe the materials and the parameters that will influence the SALDI-MS process. As SALDI-MS is also suitable for combination with other techniques, we will also describe in Chapter IV how these dual surfaces could be used for detection of ricin.

© 2020 Tous droits réservés.
lilliad.univ-lille.fr

I.6. References

1 Rotz, L. D., Khan, A. S., Lillibridge, S. R., Ostroff, S. M. & Hughes, J. M. Public health assessment of potential biological terrorism agents. *Emerging Infectious Diseases* **8**, 225-230 (2002).

2 Kumar, O., Nashikkar, A., Jayaraj, R., Vijayaraghavan, R. & Prakash, A. Purification and Biochemical Characterisation of Ricin from Castor Seeds. *Defence Science Journal* **54**, 345 (2004).

3 Zhao, Y.-Q. *et al.* Rapid Detection of Ricin in Serum Based on Cu-Chelated Magnetic Beads Using Mass Spectrometry. *Journal of The American Society for Mass Spectrometry* **27**, 748-751, doi:10.1007/s13361-016-1340-1 (2016).

4 Crompton, R. & Gall, D. Georgi Markov — Death in a Pellet. *Medico-Legal Journal* **48**, 51-62, doi:10.1177/002581728004800203 (1980).

5 Schep, L. J., Temple, W. A., Butt, G. A. & Beasley, M. D. Ricin as a weapon of mass terror — Separating fact from fiction. *Environment International* **35**, 1267-1271, doi:https://doi.org/10.1016/j.envint.2009.08.004 (2009).

6 Fade, F. The June 2018 Cologne Ricin Plot: A New Threshold in Jihadi Bio Terror. *CTC Sentinel* **11**, 1-4 (2018).

7 Worbs, S. *et al.* Ricinus communis Intoxications in Human and Veterinary Medicine-A Summary of Real Cases. *Toxins (Basel)* **3**, 1332-1372, doi:10.3390/toxins3101332 (2011).

8 Fetter, L. *et al.* Electrochemical aptamer scaffold biosensors for detection of botulism and ricin toxins. *Chemical Communications* **51**, 15137-15140 (2015).

9 Schieltz, D. M. *et al.* Analysis of active ricin and castor bean proteins in a ricin preparation, castor bean extract, and surface swabs from a public health investigation. *Forensic Science International* **209**, 70-79 (2011).

10 Audi, J., Belson, M., Patel, M., Schier, J. & Osterloh, J. Ricin poisoning: A comprehensive review. *JAMA* **294**, 2342-2351, doi:10.1001/jama.294.18.2342 (2005).

11 Ehrlich, P. Experimentelle untersuchungen über immunität. I. Ueber Ricin. *DMW-Deutsche Medizinische Wochenschrift* **17**, 976-979 (1891).

12 Chen, H. Y., Foo, L. Y. & Loke, W. K. in *Toxinology: Biological Toxins and Bioterrorism* (ed P. Gopalakrishnakone) 1-20 (Springer Netherlands, 2013).

13 Respaud, R. *et al.* Development of a drug delivery system for efficient alveolar delivery of a neutralizing monoclonal antibody to treat pulmonary intoxication to ricin. *Journal of Controlled Release* **234**, 21-32, doi:https://doi.org/10.1016/j.jconrel.2016.05.018 (2016).

14 Final report on the safety assessment of Ricinus Communis (Castor) Seed Oil, Hydrogenated Castor Oil, Glyceryl Ricinoleate, Glyceryl Ricinoleate SE, Ricinoleic Acid, Potassium Ricinoleate, Sodium Ricinoleate, Zinc Ricinoleate, Cetyl Ricinoleate, Ethyl Ricinoleate, Glycol Ricinoleate, Isopropyl Ricinoleate, Methyl Ricinoleate, and Octyldodecyl Ricinoleate. *International Journal of Toxicology* **3**, 31-77 (2007).

15 Worbs, S. *et al.* Characterization of Ricin and R. communis Agglutinin Reference Materials. *Toxins (Basel)* **7**, 4856 (2015).

16 Bradberry, S. Ricin and abrin. *Medicine* **40**, 80-81 (2012).

17 Felder, E., Mossbrugger, I., Lange, M. & Wölfel, R. Simultaneous detection of ricin and abrin DNA by real-time PCR (qPCR). *Toxins (Basel)* **4**, 633-642 (2012).

18 Koja, N., Shibata, T. & Mochida, K. Enzyme-linked immunoassay of ricin. *Toxicon* **18**, 611-618, doi:https://doi.org/10.1016/0041-0101(80)90088-4 (1980).

© 2020 Tous droits réservés.
lilliad.univ-lille.fr

Thèse de Ioana Silvia Hosu, Université de Lille, 2020

19 Ramakrishnan, S., Eagle, M. R. & Houston, L. L. Radioimmunoassay of ricin A- and B-chains applied to samples of ricin A-chain prepared by chromatofocusing and by DEAE Bio-Gel A. *Biochimica et Biophysica Acta (BBA) - General Subjects* **719**, 341-348, doi:https://doi.org/10.1016/0304-4165(82)90108-8 (1982).

20 Kirby, R. *et al.* Aptamer-Based Sensor Arrays for the Detection and Quantitation of Proteins. *Analytical Chemistry* **76**, 4066-4075, doi:10.1021/ac049858n (2004).

21 Stine, R., Pishko, M. V. & Schengrund, C.-L. Comparison of Glycosphingolipids and Antibodies as Receptor Molecules for Ricin Detection. *Analytical Chemistry* **77**, 2882-2888, doi:10.1021/ac048126s (2005).

22 Ler, S. G., Lee, F. K. & Gopalakrishnakone, P. Trends in detection of warfare agents: Detection methods for ricin, staphylococcal enterotoxin B and T-2 toxin. *Journal of Chromatography A* **1133**, 1-12, doi:https://doi.org/10.1016/j.chroma.2006.08.078 (2006).

23 Yu, H., Raymonda, J. W., McMahon, T. M. & Campagnari, A. A. Detection of biological threat agents by immunomagnetic microsphere-based solid phase fluorogenic- and electro-chemiluminescence. *Biosensors and Bioelectronics* **14**, 829-840, doi:https://doi.org/10.1016/S0956-5663(99)00068-8 (2000).

24 Ruan, C. *et al.* A Magnetoelastic Ricin Immunosensor. *Sensor Letters* **2**, 138-144 (2004).

25 Bozza, W. P., Tolleson, W. H., Rivera Rosado, L. A. & Zhang, B. Ricin detection: Tracking active toxin. *Biotechnology Advances* **33**, 117-123 (2015).

26 Poli, M. A., Rivera, V. R., Hewetson, J. F. & Merrill, G. A. Detection of ricin by colorimetric and chemiluminescence ELISA. *Toxicon* **32**, 1371-1377, doi:https://doi.org/10.1016/0041-0101(94)90409-X (1994).

27 Shyu, R. H., Shyu, H. F., Liu, H. W. & Tang, S. S. Colloidal gold-based immunochromatographic assay for detection of ricin. *Toxicon* **40**, 255-258 (2002).

28 Narang, U., Anderson, G. P., Ligler, F. S. & Burans, J. Fiber optic-based biosensor for ricin. *Biosensors and Bioelectronics* **12**, 937-945, doi:https://doi.org/10.1016/S0956-5663(97)00027-4 (1997).

29 Goldman, E. R. *et al.* Multiplexed Toxin Analysis Using Four Colors of Quantum Dot Fluororeagents. *Analytical Chemistry* **76**, 684-688, doi:10.1021/ac035083r (2004).

30 Wadkins, R. M., Golden, J. P., Pritsiolas, L. M. & Ligler, F. S. Detection of multiple toxic agents using a planar array immunosensor. *Biosensors and Bioelectronics* **13**, 407-415, doi:https://doi.org/10.1016/S0956-5663(97)00113-9 (1998).

31 Delehanty, J. B. & Ligler, F. S. A Microarray Immunoassay for Simultaneous Detection of Proteins and Bacteria. *Analytical Chemistry* **74**, 5681-5687, doi:10.1021/ac0256311 (2002).

32 Rubina, A. Y. *et al.* Quantitative immunoassay of biotoxins on hydrogel-based protein microchips. *Analytical Biochemistry* **340**, 317-329, doi:https://doi.org/10.1016/j.ab.2005.01.042 (2005).

33 Rodriguez-Saona, L. E., Fry, F. S. & Calvey, E. M. Use of Fourier Transform Near-Infrared Reflectance Spectroscopy for Rapid Quantification of Castor Bean Meal in a Selection of Flour-Based Products. *Journal of Agricultural and Food Chemistry* **48**, 5169-5177, doi:10.1021/jf000604m (2000).

34 Hines, H. B. & Brueggemann, E. E. Factors affecting the capillary electrophoresis of ricin, a toxic glycoprotein. *Journal of Chromatography A* **670**, 199-208, doi:https://doi.org/10.1016/0021-9673(94)80295-5 (1994).

35 Yeung, W. S. B., Luo, G. A., Wang, Q. G. & Ou, J. P. Capillary electrophoresis-based immunoassay. *Journal of Chromatography B* **797**, 217-228, doi:https://doi.org/10.1016/S1570-0232(03)00489-6 (2003).

© 2020 Tous droits réservés.

lilliad.univ-lille.fr

Thèse de Ioana Silvia Hosu, Université de Lille, 2020

36 Weingart, O. G. *et al.* A bioanalytical platform for simultaneous detection and quantification of biological toxins. *Sensors* **12**, 2324-2339 (2012).

37 Duriez, E. *et al.* Detection of ricin in complex samples by immunocapture and matrix-assisted laser desorption/ionization time-of-flight mass spectrometry. *Journal of Proteome Research* **7**, 4154-4163 (2008).

38 Kanamori-Kataoka, M. *et al.* Determination of ricin by nano liquid chromatography/mass spectrometry after extraction using lactose-immobilized monolithic silica spin column. *Journal of Mass Spectrometry* **46**, 821-829, doi:doi:10.1002/jms.1953 (2011).

39 Uzawa, H. *et al.* A novel sugar-probe biosensor for the deadly plant proteinous toxin, ricin. *Biosensors and Bioelectronics* **24**, 923-927, doi:https://doi.org/10.1016/j.bios.2008.07.049 (2008).

40 Tran, H., Leong, C., Loke, W. K., Dogovski, C. & Liu, C.-Q. Surface plasmon resonance detection of ricin and horticultural ricin variants in environmental samples. *Toxicon* **52**, 582-588, doi:https://doi.org/10.1016/j.toxicon.2008.07.008 (2008).

41 Nagatsuka, T. *et al.* Localized Surface Plasmon Resonance Detection of Biological Toxins Using Cell Surface Oligosaccharides on Glyco Chips. *ACS Applied Materials & Interfaces* **5**, 4173-4180, doi:10.1021/am4002937 (2013).

42 Anderson, G. P. *et al.* Single domain antibody–quantum dot conjugates for ricin detection by both fluoroimmunoassay and surface plasmon resonance. *Analytica Chimica Acta* **786**, 132-138, doi:https://doi.org/10.1016/j.aca.2013.05.010 (2013).

43 Liu, H.-Z. *et al.* Galactose-functionalized Magnetic Iron-oxide Nanoparticles for Enrichment and Detection of Ricin Toxin. *Analytical Sciences* **27**, 19-24, doi:10.2116/analsci.27.19 (2011).

44 Dodge, A. G. *et al.* Rapid Method Using Two Microbial Enzymes for Detection of l-Abrine in Food as a Marker for the Toxic Protein Abrin. *Applied and Environmental Microbiology* **81**, 1610-1615, doi:10.1128/aem.03492-14 (2015).

45 Brandon, D. L. Detection of ricin contamination in ground beef by electrochemiluminescence immunosorbent assay. *Toxins (Basel)* **3**, 398-408 (2011).

46 Fredriksson, S.-Å. *et al.* Forensic Identification of Neat Ricin and of Ricin from Crude Castor Bean Extracts by Mass Spectrometry. *Analytical Chemistry* **77**, 1545-1555, doi:10.1021/ac048756u (2005).

47 Yonzon, C. R. *et al.* A Comparative Analysis of Localized and Propagating Surface Plasmon Resonance Sensors: The Binding of Concanavalin A to a Monosaccharide Functionalized Self-Assembled Monolayer. *Journal of the American Chemical Society* **126**, 12669-12676, doi:10.1021/ja047118q (2004).

48 Jatschka, J., Dathe, A., Csáki, A., Fritzsche, W. & Stranik, O. Propagating and localized surface plasmon resonance sensing — A critical comparison based on measurements and theory. *Sensing and Bio-Sensing Research* **7**, 62-70, doi:https://doi.org/10.1016/j.sbsr.2016.01.003 (2016).

49 Stern, D. *et al.* Simultaneous differentiation and quantification of ricin and agglutinin by an antibody-sandwich surface plasmon resonance sensor. *Biosensors and bioelectronics* **78**, 111-117 (2016).

50 Becher, F., Duriez, E., Volland, H., Tabet, J. C. & Ezan, E. Detection of Functional Ricin by Immunoaffinity and Liquid Chromatography−Tandem Mass Spectrometry. *Analytical Chemistry* **79**, 659-665, doi:10.1021/ac061498b (2007).

51 McGrath, S. C., Schieltz, D. M., McWilliams, L. G., Pirkle, J. L. & Barr, J. R. Detection and Quantification of Ricin in Beverages Using Isotope Dilution Tandem Mass Spectrometry. *Analytical Chemistry* **83**, 2897-2905, doi:10.1021/ac102571f (2011).

© 2020 Tous droits réservés.

lilliad.univ-lille.fr

Thèse de Ioana Silvia Hosu, Université de Lille, 2020

52 Zhao, S. *et al.* Detection of ricin intoxication in mice using serum peptide profiling by MALDI-TOF/MS. *Int J Mol Sci* **13**, 13704-13712 (2012).

53 Schieltz, D. M. *et al.* Quantification of ricin, RCA and comparison of enzymatic activity in 18 Ricinus communis cultivars by isotope dilution mass spectrometry. *Toxicon : official journal of the International Society on Toxinology* **95**, 72-83, doi:10.1016/j.toxicon.2015.01.003 (2015).

54 Sun, J. *et al.* Ultrasensitive On-Site Detection of Biological Active Ricin in Complex Food Matrices Based on Immunomagnetic Enrichment and Fluorescence Switch-On Nanoprobe. *Analytical Chemistry* **91**, 6454-6461, doi:10.1021/acs.analchem.8b04458 (2019).

55 Karas, M. & Hillenkamp, F. Laser desorption ionization of proteins with molecular masses exceeding 10,000 daltons. *Analytical Chemistry* **60**, 2299-2301, doi:10.1021/ac00171a028 (1988).

56 Burlingame, A. L. *Mass Spectrometry: Modified Proteins and Glycoconjugates*. (Elsevier Science, 2005).

57 Picca, R. A., Calvano, C. D., Cioffi, N. & Palmisano, F. Mechanisms of Nanophase-Induced Desorption in LDI-MS. A Short Review. *Nanomaterials (Basel, Switzerland)* **7**, 75, doi:10.3390/nano7040075 (2017).

58 Bonk, T. & Humeny, A. MALDI-TOF-MS Analysis of Protein and DNA. *The Neuroscientist* **7**, 6-12, doi:10.1177/107385840100700104 (2001).

59 Kalb, S. R. & Barr, J. R. Mass Spectrometric Detection of Ricin and its Activity in Food and Clinical Samples. *Analytical Chemistry* **81**, 2037-2042, doi:10.1021/ac802769s (2009).

60 Despeyroux, D. *et al.* Characterization of Ricin Heterogeneity by Electrospray Mass Spectrometry, Capillary Electrophoresis, and Resonant Mirror. *Analytical Biochemistry* **279**, 23-36, doi:https://doi.org/10.1006/abio.1999.4423 (2000).

61 Brinkworth, C. S., Pigott, E. J. & Bourne, D. J. Detection of Intact Ricin in Crude and Purified Extracts from Castor Beans Using Matrix-Assisted Laser Desorption Ionization Mass Spectrometry. *Analytical Chemistry* **81**, 1529-1535, doi:10.1021/ac802240f (2009).

62 Selvaprakash, K. & Chen, Y.-C. Detection of ricin by using gold nanoclusters functionalized with chicken egg white proteins as sensing probes. *Biosensors and bioelectronics* **92**, 410-416, doi:https://doi.org/10.1016/j.bios.2016.10.086 (2017).

63 Tanaka, K. *et al.* Protein and polymer analyses up to m/z 100 000 by laser ionization time-of-flight mass spectrometry. *Rapid communications in mass spectrometry* **2**, 151-153 (1988).

64 Law, K. P. & Larkin, J. Recent advances in SALDI-MS techniques and their chemical and bioanalytical applications. *Analytical and Bioanalytical Chemistry* **399**, 2597-2622, doi:10.1007/s00216-010-4063-3 (2011).

65 Peterson, D. S. Matrix-free methods for laser desorption/ionization mass spectrometry. *Mass Spectrometry Reviews* **26**, 19-34, doi:10.1002/mas.20104 (2007).

66 Okuno, S. *et al.* Requirements for Laser-Induced Desorption/Ionization on Submicrometer Structures. *Analytical Chemistry* **77**, 5364-5369, doi:10.1021/ac050504l (2005).

67 Walker, B. N., Razunguzwa, T., Powell, M., Knochenmuss, R. & Vertes, A. Nanophotonic Ion Production from Silicon Microcolumn Arrays. *Angewandte Chemie International Edition* **48**, 1669-1672, doi:10.1002/anie.200805114 (2009).

68 Tsao, C.-W., Tao, S., Chen, C.-F., Liu, J. & DeVoe, D. L. Interfacing microfluidics to LDI-MS by automatic robotic spotting. *Microfluidics and Nanofluidics* **8**, 777-787, doi:10.1007/s10404-009-0510-x (2010).

© 2020 Tous droits réservés.

lilliad.univ-lille.fr

Thèse de Ioana Silvia Hosu, Université de Lille, 2020

69 Lapierre, F. *et al.* High sensitive matrix-free mass spectrometry analysis of peptides using silicon nanowires-based digital microfluidic device. *Lab on a Chip* **11**, 1620-1628, doi:10.1039/c0lc00716a (2011).

70 Silina, Y. E. & Volmer, D. A. Nanostructured solid substrates for efficient laser desorption/ionization mass spectrometry (LDI-MS) of low molecular weight compounds. *Analyst* **138**, 7053-7065, doi:10.1039/c3an01120h (2013).

71 Shi, C. Y. & Deng, C. H. Recent advances in inorganic materials for LDI-MS analysis of small molecules. *Analyst* **141**, 2816-2826, doi:10.1039/c6an00220j (2016).

72 Iakab, S. A., Rafols, P., García-Altares, M., Yanes, O. & Correig, X. Silicon-Based Laser Desorption Ionization Mass Spectrometry for the Analysis of Biomolecules: A Progress Report. *Advanced Functional Materials* **0**, 1903609, doi:10.1002/adfm.201903609 (2019).

73 Coffinier, Y., Szunerits, S., Drobecq, H., Melnyk, O. & Boukherroub, R. Diamond nanowires for highly sensitive matrix-free mass spectrometry analysis of small molecules. *Nanoscale* **4**, 231-238 (2012).

74 Go, E. P. *et al.* Desorption/Ionization on Silicon Nanowires. *Analytical Chemistry* **77**, 1641-1646, doi:10.1021/ac048460o (2005).

75 Zenobi, R. & Knochenmuss, R. Ion formation in MALDI mass spectrometry. *Mass Spectrometry Reviews* **17**, 337-366, doi:10.1002/(sici)1098-2787(1998)17:5<337::aid-mas2>3.0.co;2-s (1998).

76 Stolee, J. A., Walker, B. N., Zorba, V., Russo, R. E. & Vertes, A. Laser–nanostructure interactions for ion production. *Physical Chemistry Chemical Physics* **14**, 8453-8471, doi:10.1039/c2cp00038e (2012).

77 Yagnik, G. B. *et al.* Large Scale Nanoparticle Screening for Small Molecule Analysis in Laser Desorption Ionization Mass Spectrometry. *Analytical Chemistry* **88**, 8926-8930, doi:10.1021/acs.analchem.6b02732 (2016).

78 Wei, J., Buriak, J. M. & Siuzdak, G. Desorption-ionization mass spectrometry on porous silicon. *Nature* **399**, 243-246 (1999).

79 Rousell, D. J., Dutta, S. M., Little, M. W. & Murray, K. K. Matrix-free infrared soft laser desorption/ionization. *Journal of Mass Spectrometry* **39**, 1182-1189, doi:10.1002/jms.706 (2004).

80 Abdelhamid, H. N. Nanoparticle-based surface assisted laser desorption ionization mass spectrometry: a review. *Microchimica Acta* **186**, 682, doi:10.1007/s00604-019-3770-5 (2019).

81 Coffinier, Y. & Boukherroub, R. in *Handbook of Porous Silicon* (ed Leigh Canham) 869-885 (Springer International Publishing, 2014).

82 Kawasaki, H. *et al.* Layer-by-Layer Self-Assembled Mutilayer Films of Gold Nanoparticles for Surface-Assisted Laser Desorption/Ionization Mass Spectrometry. *Analytical Chemistry* **80**, 7524-7533, doi:10.1021/ac800789t (2008).

83 Chiang, C.-K., Chen, W.-T. & Chang, H.-T. Nanoparticle-based mass spectrometry for the analysis of biomolecules. *Chemical Society Reviews* **40**, 1269-1281, doi:10.1039/c0cs00050g (2011).

84 Tang, H.-W., Ng, K.-M., Lu, W. & Che, C.-M. Ion desorption efficiency and internal energy transfer in carbon-based surface-assisted laser desorption/ionization mass spectrometry: Desorption mechanism (s) and the design of SALDI substrates. *Analytical chemistry* **81**, 4720-4729 (2009).

85 Wu, L., Chu, H. S., Koh, W. S. & Li, E. P. Highly sensitive graphene biosensors based on surface plasmon resonance. *Optics Express* **18**, 14395-14400, doi:10.1364/oe.18.014395 (2010).

© 2020 Tous droits réservés.

lilliad.univ-lille.fr

Thèse de Ioana Silvia Hosu, Université de Lille, 2020

86 Pan, C. *et al.* Using Oxidized Carbon Nanotubes as Matrix for Analysis of Small Molecules by MALDI-TOF MS. *Journal of the American Society for Mass Spectrometry* **16**, 883-892 (2005).

87 Lim, A. Y., Ma, J. & Boey, Y. C. F. Development of Nanomaterials for SALDI-MS Analysis in Forensics. *Advanced Materials* **24**, 4211-4216 (2012).

88 Amini, N., Shariatgorji, M. & Thorsén, G. SALDI-MS Signal Enhancement Using Oxidized Graphitized Carbon Black Nanoparticles. *Journal of The American Society for Mass Spectrometry* **20**, 1207-1213 (2009).

89 Lim, A. Y., Gu, F., Ma, Z., Ma, J. & Rowell, F. Doped amorphous silica nanoparticles as enhancing agents for surface-assisted time-of-flight mass spectrometry. *Analyst* **136**, 2775-2785, doi:10.1039/c1an15172j (2011).

90 Daniel J Ryan, J. M. S., Richard M Caprioli. Protein identification strategies in MALDI imaging mass spectrometry: a brief review,. *Current Opinion in Chemical Biology* **48**, 64-72, doi:https://doi.org/10.1016/j.cbpa.2018.10.023. (2019).

91 Fais, M. *et al.* Surface plasmon resonance imaging of glycoarrays identifies novel and unnatural carbohydrate-based ligands for potential ricin sensor development. *Chemical Science* **2**, 1952-1959, doi:10.1039/c1sc00120e (2011).

© 2020 Tous droits réservés.

lilliad.univ-lille.fr

Blank page

© 2020 Tous droits réservés.

lilliad.univ-lille.fr

Thèse de Ioana Silvia Hosu, Université de Lille, 2020

Chapter II
Carbon nanowalls for matrix-free laser desorption/ionization mass spectrometry detection of small compounds in real samples

© 2020 Tous droits réservés.
lilliad.univ-lille.fr

Thèse de Ioana Silvia Hosu, Université de Lille, 2020

Chapter II. Carbon nanowalls for matrix-free laser desorption/ionization mass spectrometry detection of small compounds in real samples

II.1. Introduction 57
II.2. Optimization of CNWS for SALDI-MS detection of small compounds 61
II.2.1. Surface characterization of boron doped CNWs surface 61
II.2.1.1 Morphological characterization of CNWs 61
II.2.1.2 Optical characterization of CNWs 62
II.2.1.3 Other physical characteristics of CNWs important in SALDI-MS 64
II.2.1.4 Determination of internal energy for the CNWs 65
II.2.2. Detection of small biomolecules in buffers 68
II.2.2.1 Detection of peptides 68
II.2.2.2 Optimization of important detection parameters using saccharides 69
II.2.2.2.a Influence of the laser power on the SALDI-MS background 69
II.2.2.2.b Influence of alkaline metals on MS performances 71
II.2.2.2.c Influence of the surface chemistry 72
II.2.2.2.d Detection of disaccharides 76
II.2.2.2.e Studying the homogeneity of drop casted sugars 77
II.3. Quantitative measurements of glucose in blood serum and soft drinks 80
II.4. Detection of melamine, creatinine and paracetamol in urine samples 87
II.5. Detection of phosphatidylcholine in lecithin food supplements 89
II.6. Conclusions 91
II.7. References 93

© 2020 Tous droits réservés.

lilliad.univ-lille.fr

Chapter II. Carbon nanowalls for matrix-free laser desorption/ionization mass spectrometry detection of small compounds in real samples

II.1. Introduction

Carbon nanowalls (CNWs) consist in vertically aligned and packed nanosheets of graphene that can be grown by low temperature plasma based processes (DC, RF and microwave discharges). Whereas one of the most used technique is PECVD (plasma-enhanced chemical vapour deposition), its main advantage is the catalyst-free based process, making possible the growth of CNWs on different substrates, with no metallic contamination. Microwave plasma PECVD is known to create high quality and free-standing CNWs.[1]

Recently, many researchers showed a great interest to CNWs and many applications have already been described in the literature (**Figure II.1-1)** such as field electron emitters, catalyst support/template, and hydrophobic coating (due to the H or F terminations).[2] Thanks to the remarkable optical properties (very low reflectance, high specific absorbance in thin transparent films), there is the possibility to use CNWs as dark coating for a bolometer absorber.[3] The opportunity to tailor the band-gap of CNWs opens new gates in their usage in the modern nano-electronics, as they can have semiconducting features. After the modification of the CNWs with metal nanoparticles, the detection of Rhodamine 6G dye was performed using surface enhanced Raman spectrometry (SERS)[4] while the change in their resistivity was used to detect volatile organic compounds (VOCs).[5] Biocompatible scaffolds for osteoblast culture and tissue engineering were also created using CNWs.[6] Electrophoretic deposition can be used to fabricate composite CNWs/graphite electrode for electrochemical detection of DNA sequences with estimated zeptomolar LODs.[7]

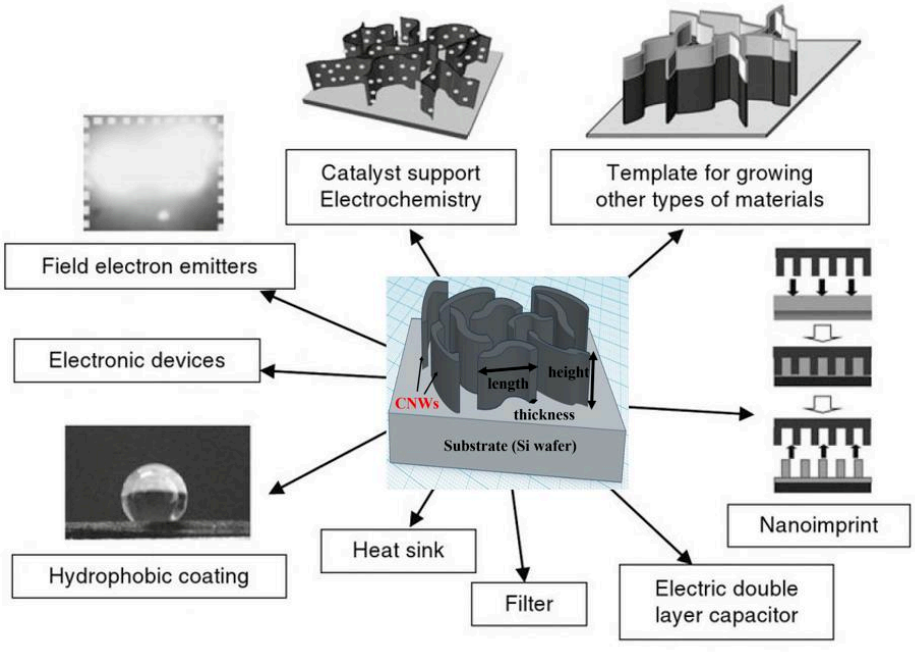

Figure II.1-1 Schematic representation of the CNWs potential applications. Adapted from ref.[2]

© 2020 Tous droits réservés.

lilliad.univ-lille.fr

Chapter II. Carbon nanowalls for matrix-free laser desorption/ionization mass spectrometry detection of small compounds in real samples

As described in bibliography chapter (Chapter I), MALDI-MS was discovered in the 80's[8] and concerns the mixing of analytes of interest together with specific light-absorbing organic compounds (organic matrix) thus allowing their co-crystallization, protonation and enhancing the MS signal while influencing the fragmentation patterns. The sample preparation method and the choice of the matrix greatly influence the quality of the MS spectra. However, the noise background generated by the presence of matrix makes difficult the detection of molecules with m/z smaller than 700 and co-crystallization of the organic matrix can create spots with different concentrations of the analyte ("sweet" or "hot" spots). These "sweet spots" usually diminishes the reproducibility and sensitivity. In **Figure II.1-2** we are presenting a comparison between a SALDI-MS and MALDI-MS spectra obtained from CNWS and CHCA (alpha-Cyano-4-hydroxycinnamic acid, an usual organic matrix) respectively. It can clearly be observed that below 1000 Da, there are a lot of interfering peaks from the matrix, by using the same laser relative power of 60%.

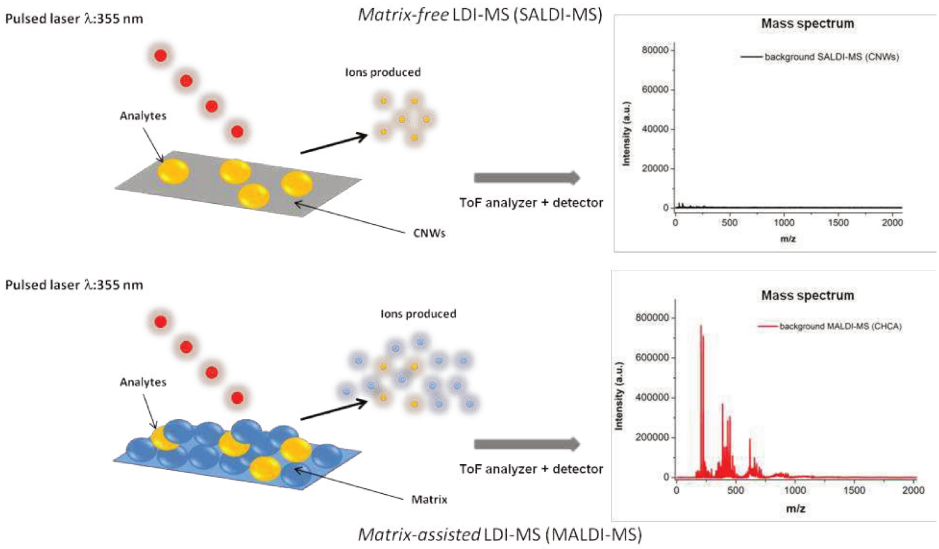

Figure II.1-2 Comparison of spectrum background between MALDI and SALDI method.

An alternative solution appeared in 1988, when Tanaka replaced the organic matrix by ultra-fine particles mixed to glycerol, allowing the detection of proteins up to 100 kDa[9], giving rise to surface-assisted laser desorption/ionization mass spectrometry (SALDI–MS). One of the first surfaces used in LDI-MS was described in 1999 and consisted of porous silicon, DIOS (Desorption/ionization on silicon).[10] The efficiency of DIOS in LDI was speculated to come from the nanosized pores that can effectively absorb UV light. Since then molecular weights <3000 Da were detected over time using DIOS or other silicon nanostructures.[11] SALDI offers many advantages over conventional matrix-based MS such as easy sample preparation and elimination of the "sweet spots", thus improving the

© 2020 Tous droits réservés.

lilliad.univ-lille.fr

Thèse de Ioana Silvia Hosu, Université de Lille, 2020

reproducibility of measurements.[12,13] Furthermore, the surfaces can be tuned/functionalized to perform *in situ* solid liquid extraction.[14] Other advantages to be underlined, compared to the usage of organic matrix, are high salt-tolerance, low cost, reproducibility and higher sensitivity, making probable the detection of small compounds in biological fluids.[15]

The substrates used in SALDI display strong absorption UV properties and are able to transfer the energy to the analyte, which will be desorbed and ionized. The inorganic substrates mainly used for SALDI usually are: metal-, metal-oxide-, carbon- or semiconductor-based.[16] Desorption efficiencies and internal energy transfer of materials used in SALDI are related to the surface area of the material, anti-reflectivity, porosity, length of nanostructures, thermal conductivity etc.[17,18] Calculating the deposited internal energy of the surfaces may help us in the screening of different surfaces for the selection on the appropriate ones to be used in SALDI-MS.

SALDI–MS is taking huge proportions due to high throughput and capability of creating a global profile of the biological matrices and tissue imaging.[18] Our group also brought a high contribution to the development of SALDI –MS reporting for the first time a diamond nanowire-based interface (BDD-NWs) for the detection of peptides and small molecules.[19] Also Ti and Si nanostructures were employed for LDI-MS detection of peptides, tryptic digest of proteins, while copper particles decorated silicon nanowires were used for peptide enrichment prior their LDI-MS detection.[20-24] The integration of SALDI-MS surfaces in digital microfluidic system, was proven to be useful for silicon nanowires. Indeed, electrowetting was achieved on superhydrophobic surfaces and made possible the peptides displacement and rinsing operation before MS analysis.[25]

Encouraged by high light absorption properties, high conductivity, high surface area, good mechanical resistance, hydrophobicity and other benefits, we propose herein and prove, for the first time, the ability of as-prepared boron-doped CNWs to act as SALDI substrate for the detection of various compounds such as sugars, catecholamine, melamine, paracetamol, creatinine, phospholipids and peptides. Also, the glucose levels were quantitatively detected in blood serum and soft drink samples whereas creatinine, melamine and paracetamol were detected in urine samples, and lecithin in food supplements.

So, in this chapter we study the efficiency of boron carbon nanowalls as SALDI-MS platforms, underlying and explaining why some of the characteristics on the materials are suitable for this. We will use these surfaces to detect small molecules and emphasize the advantages. We will also use them for detection in complex samples.

© 2020 Tous droits réservés.

lilliad.univ-lille.fr

Chapter II. Carbon nanowalls for matrix-free laser desorption/ionization mass spectrometry detection of small compounds in real samples

All the boron doped carbon nanowalls were synthesized by our collaborators from Poland, from Gdansk University of Technology. We did collaborate and discussed of possibility of tuning different parameters with them, for further studies, especially for the possibility of detection proteins, that is the main drawback of SALDI-MS in general. In this Chapter we will only describe the abilities of CNWS to be used as SALDI-MS platforms for small molecules.

© 2020 Tous droits réservés.

lilliad.univ-lille.fr

II.2. Optimization of CNWS for SALDI-MS detection of small compounds

II.2.1. Surface characterization of boron doped CNWs surface

Characterizations (morphological and optical properties) of the surface were performed in order to understand the LDI mechanism. Indeed, different parameters that can influence the MS response have been studied and discussed giving rise to several optimizations, allowing the detection of a wide range of small compounds. The most important characteristics of the surface, which will influence the LDI-MS process, are presented in **Table II.2-1**. We will approach some of them (the ones highlighted in red) in this chapter and a more complete and detailed analysis will be presented in Chapter III, where we will be approaching the detection of proteins. Herein, we will describe only one boron doping level (2.0 K), at only one period of growth (8 hours), as this was the available method of the synthesis, at that time.

Table II.2-1 Physical characteristics that influence LDI-MS process.

Nanostructuration	YES
Thermal conductivity	LOW
Specific heat capacity	LOW
Melting point	LOW
Mechanical Resistance	HIGH
Photoluminescence	LOW
Electrical resistivity	LOW
Deposited internal energy	HIGH
UV light Absorbant	HIGH
Hydrophobicity	HIGH
Specific surface area	HIGH

II.2.1.1 Morphological characterization of CNWs

Morphology plays an important role in the laser desorption/ionization processes[18,24] even though the mechanism is not yet well understood. The dimensions of walls may be important in different aspects: (a) if the dimensions are small enough (below 10 nm width), quantum confinement effect may occur, during UV irradiation, (b) if they are too high, the analyte can be trapped inside the porous structure[24] and the laser penetration depth (e. g. 100 nm in the case of silicon nanostructures) may be too superficial, (c) if they are high enough, they absorb better photons.[26] SEM images showed that the randomly vertically aligned nanowalls are formed on the silicon wafer, after the MW-PECVD growth (**Figure II.2-1**) and their height

© 2020 Tous droits réservés.

lilliad.univ-lille.fr

was about 3.95 µm. Also, the exposed nanowalls have a length in the 100 - 800 nm range and the thicknesses of the walls were in the range of 10-30 nm, thus quantum confinement is unlikely.

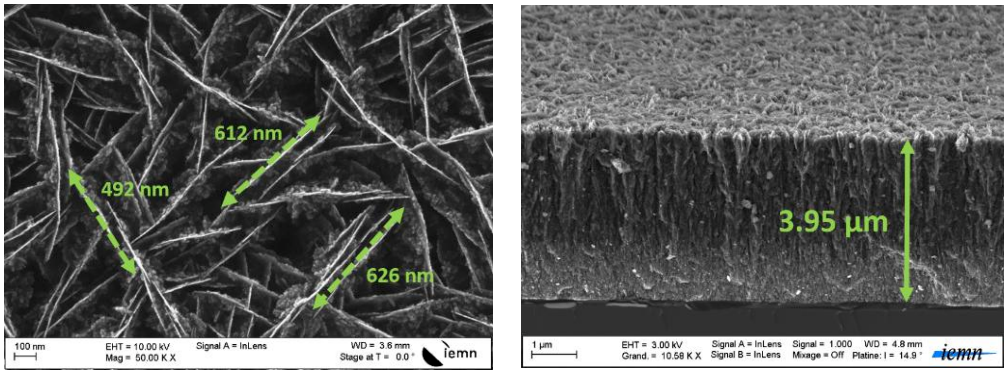

(A) **(B)**

Figure II.2-1 (A) Top-view and **(B)** cross-section SEM micrographs of CNWs.

II.2.1.2 Optical characterization of CNWs

The sub-bandgap absorption of photons and heat confinement was proposed by our group to explain the great desorption/ionization in SALDI-MS by using boron-doped diamond nanowires.[19] In that case, the large band-gap of diamond nanowire surface (5.5 eV) hinders the direct absorption of photons from the laser irradiation (3.64 eV). However, boron doping can tune the band gap, by the additional energy level above valence band (approximatively 0.38 V). The band-gap of the carbon nanowalls can be usually tuned in the meV range, in an approximate interval of 1.6-80 meV, depending on the doping agents, synthesis method and other parameters.[27,28] The above-bandgap absorption can be expected for CNWs, as the energy of the laser is ~3.49 eV.

The reflectivity measurements of the CNWs surface (1.39 %, at 355 nm) and the silicon <100> substrate (53.13%, at 355 nm), are displayed in **Figure II.2-2A**. By comparison with other CNWs reflectivity measurements presented in the literature, similar results were obtained.[3] Reflectance measurements are in accordance with the diffusion reflectance measurements of the CNWs surfaces (**Figure II.2-2B**). Due to the high absorption and large scattering of optical signal at CNWs, the Vis-NIR diffuse reflectance spectroscopy (DRS) has been studied. The Kubelka-Munk equation has been applied to estimate absorption of samples. The maximum of DRS graph has been registered at 1540 nm. It corresponds to the 0.81 eV of photon energy, which is attributed to the optical band gap. These low anti-reflective properties of CNWs make them good photon absorbers. A very high UV absorption (at 355 nm, mass spectrometer laser's wavelength) suggests that laser-induced energy transfer

© 2020 Tous droits réservés.
lilliad.univ-lille.fr

can take place, from the CNWs surface to the analyte, during MS analysis.[17,29] Also, the homogeneity of black nanowalls should contribute to the photon absorption.[19]

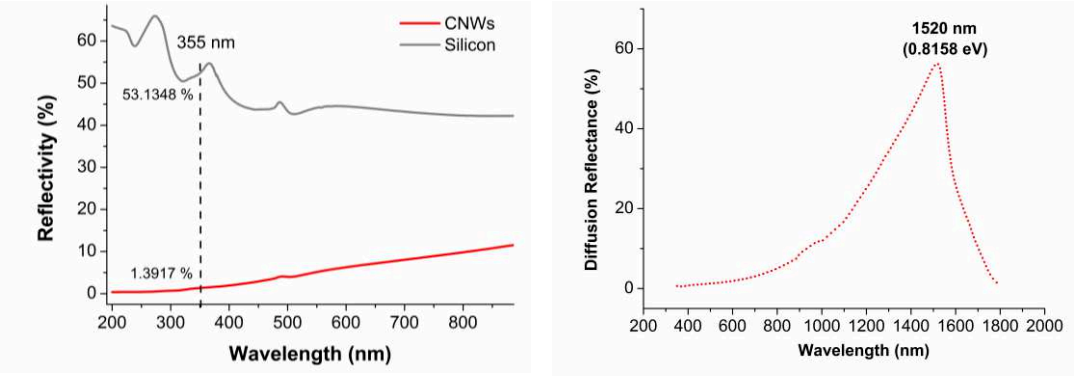

(A) **(B)**

Figure II.2-2 Reflectivity spectra **(A)** of CNW (red curve) and flat silicon (grey curve) surfaces, and diffusion reflectance **(B)** spectrum of CNWs.

Graphene has a broad emission spectrum at around 650 nm (depending on the dielectric medium). This emission originates from electron transitions among/between the non-oxidized carbon region and the boundary of oxidized carbon atom region. In the photoluminescence (PL) spectrum of CNWs (**Figure II.2-3**), it can be observed that, upon excitation at 351 nm, photons are emitted in the visible range, with the peaks centered at 440 nm (2.82 eV), 530 nm (2.33 eV) and 680 nm (1.82 eV), similar to the emission values reported by Wang et al.[30] The 680 nm peak (red band) can be attributed to defects band transition from oxygen atoms interfering with the electron transitions between π and π* bands,[22] whereas the blue and green photoluminescence peaks are related to the electron transitions between π and π* bands. Different thicknesses of the walls can exhibit different PL intensities, mainly due to low PL efficiency caused by defects and narrow band gap.[30] However, it is difficult to control the dimensions of the nanowalls, especially the thickness at dimensions lower than 10 nm. By comparison to literature, the doping level of boron did not shifted significantly the wavelengths of the emitted light.[30]

As the photoluminescence originates basically from the oxygen defects at the surface, it may suggest that the thermal conductivity has also to be discussed, as being the energy emitted as phonons, in non-radiative recombination process. CNWs with similar morphological characteristics as ours, are described in literature to have an intrinsic thermal conductivity of 300 $Wm^{-1}K^{-1}$, by comparison with CNTs (200 $Wm^{-1}K^{-1}$) and graphene (>3000 $Wm^{-1}K^{-1}$).[31] The decrease in thermal conductivity occurs due to the nano-structuration and the presence of voids. Nano-structuration lowers the heat dissipation and heat confinement occurs. Heat confinement may sustain the hypothesis of thermal

© 2020 Tous droits réservés.
lilliad.univ-lille.fr

Thèse de Ioana Silvia Hosu, Université de Lille, 2020

mechanism, as discussed in ref[19]. The uncertainty of the mechanism is still to be elucidated, as it seems that the combination of thermal and non-thermal processes contribute to SALDI-MS efficiencies, in carbon based materials.[17]

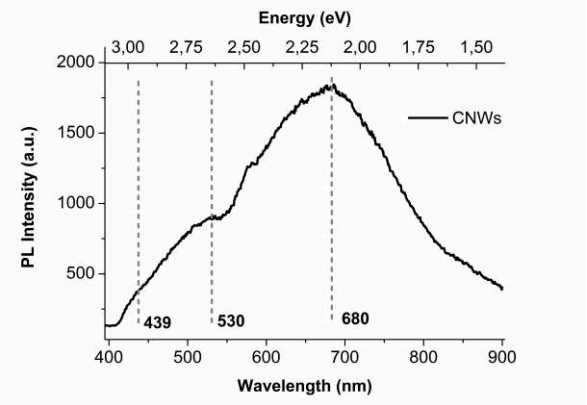

Figure II.2-3 Photoluminescence spectrum (λ_{ex}: 351 nm) of the CNWs.

The quantum yield was not studied here. However, the recent study of Wang *et al.* showed that elemental-doped graphene quantum dots (GQD) exhibit slightly higher quantum yield than undoped ones.[32] The PL quantum yield of GQDs was shown to be 0.8%, while that of B-GQDs was 1.68% and lead to a red-shifted emission. The CNW samples generate multi-PL peaks, which indicate that the PL mechanism is more complex than that of graphene. The weak intensity of PL of the CNWs is due to the low PL efficiency caused by the defects (e.g. vacancies, dangling bonds) and narrow band gap. The high optical absorption of the BCNWs impairs the depth of excitation suppressing the luminescence generation. For SALDI-MS substrate, poor PL materials are an important property and can be an advantage if we consider a thermal based mechanism. Indeed, the low PL tells us that the absorbed energy is mainly dissipated by heat *via* non-radiative recombination.

II.2.1.3 Other physical characteristics of CNWs important in SALDI-MS

In addition, Raman spectrum (**Figure II.2-4A**) showed the graphene like structure of the CNWs, as evidenced by the D-band at 1352 cm^{-1} (defects in the conjugated π system), the G-band at 1590 cm^{-1} (in plane vibrations of the sp^2 carbon atoms), the 2D band at 2727 cm^{-1} (two phonons double resonance processes, function of number of graphene layers) and the 2960 cm^{-1} band (sp^2 C-H stretching vibrations).[33] Actual reports of CNWs showed similar Raman peaks[7] and the I_D/I_G is still considered as the ratio describing the defects in a graphitized structure. In our case the I_D/I_G (1.2) and the I_{2D}/I_G (0.2) confirmed that several graphene layers are stacked to construct the carbon nanowalls. The presence of a broad peak at 480 cm^{-1} is related to boron modified carbon nanosheets[34] and after the deconvolution of the "first order" scattering peaks using Voight peaks (R^2=0.9986) other two peaks were

© 2020 Tous droits réservés.

lilliad.univ-lille.fr

clearly identified: 1220 cm^{-1} (monocrystalline diamond from seeding/grown during CVD)[35] and 1524 cm^{-1} (from C=C chains) (**Figure II.2-4B**).

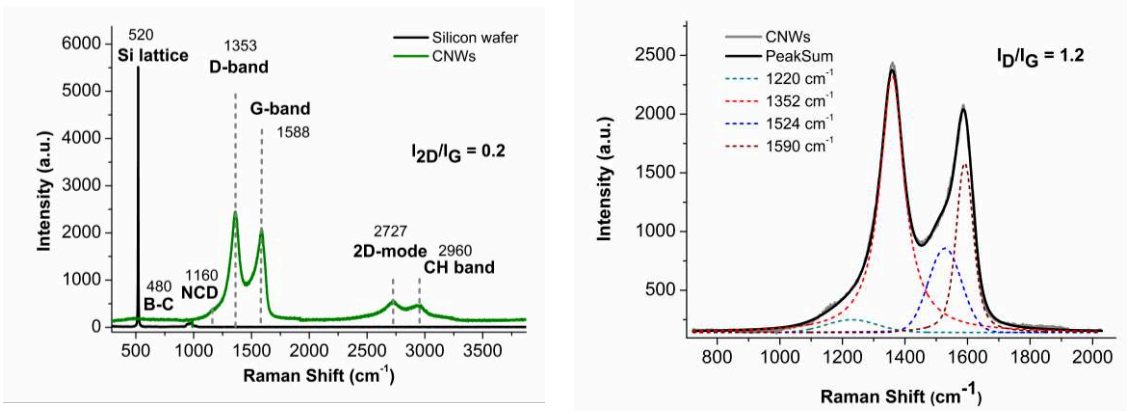

(A) **(B)**

Figure II.2-4 (A) Raman spectra of the silicon wafer (black) and CNWs (green) and **(B)** deconvoluted spectrum of CNWs, in the D and G-band regions, using a Voight model.

The wetting properties of the CNWs were examined by water contact angle measurements (**Figure II.2-5**). The as-deposited CNWs surface exhibits a WCA value of 127°, showing hydrophobic properties ascribed to H-termination of the surface. This level of hydrophobicity is suitable for the LDI-MS measurements, because it prevents the spreading of the drops placed on the surface and can confine the analyte inside a little spot presenting a surface area of approximatively 1.3 mm^2. The confinement greatly increases the sensitivity of detection.[24]

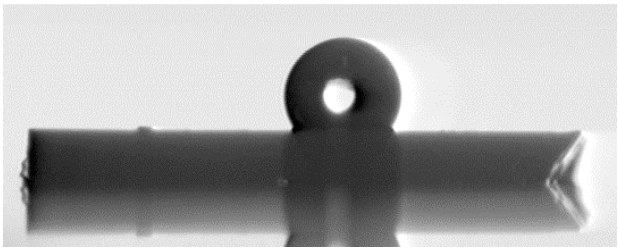

Figure II.2-5 Optical image of sessile water droplet on as-synthesized CNWs showing their hydrophobic behavior.

II.2.1.4 Determination of internal energy for the CNWs

To go further with the characterization of our interfaces and to provide useful information on parameters governing desorption/ionization process, we attempted to measure the internal energy transfer of CNWs.

In thermodynamics, the internal energy of a system is the total energy contained within the system. It is the energy necessary to create or prepare the system in any given state, but does not include the kinetic energy of motion of the system as a whole, nor the potential energy of the system as a whole due to external force fields which includes the energy of

© 2020 Tous droits réservés.

lilliad.univ-lille.fr

Thèse de Ioana Silvia Hosu, Université de Lille, 2020

displacement of the system's surroundings. It keeps account of the gains and losses of energy of the system that are due to changes in its internal state.[36]

Benzylpyridinium compounds are considered as "thermometer molecules" and can be used to determine the deposited internal energies. This survival yield method is used on the basis that all the ions having an internal energy over a certain critical energy (E_0 or E_{act}), undergoes dissociation. The dissociation pattern is simple (as depicted in **Scheme II.2-1)** making easy to calculate this survival yields (SY) (**Eq. 1**), whereas $I_{[M]}^+$ and $I_{[M-79]}^+$ represent the intensity of the molecular and the fragment ions in the mass spectra, respectively.[37] The internal energy distribution can be determined in two ways: (a) applying the derivative of the survival yield as a function of critical energies, using several ions having the same internal energies, but different critical energies,[37] or (b) comparing the experimental dissociation rate constant (k_{exp}) with the trend of the theoretical dissociation rate constants as a function of the internal energies, using the formula in **Eq. 2**, whereas k_{RRKM} represents the dissociation rate constant from the Rice - Ramsperger – Kassel – Marcus (RRKM) theory, $G^*(E\text{-}E_0)$ the total number of states between E_0 and E energy levels in the transitions state and ρ the density of states at the transition state and τ is the reaction time in the accelerating region.[38]

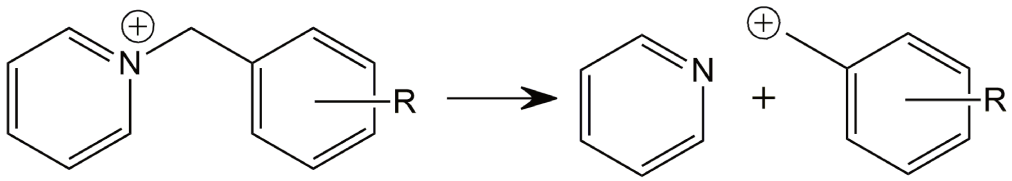

Scheme II.2-1 Dissociation pattern of benzylpyridinium compounds.

$$\eta = \frac{I_{[M]^+}}{I_{[M]^+} + I_{[M-79]^+}} = \int_0^{E_0} P(E)dE \qquad \textbf{Eq. 1}$$

$$k_{RRKM}(E) = \frac{G^*(E-E_0)}{h\rho(E)} = k_{exp} = -\left(1/\tau\right)\ln(SY) \qquad \textbf{Eq. 2}$$

As we are using a commercial instrument (Autoflex Speed, Brüker), it's difficult to know exactly the laser power that we are using, so we cannot compare the theoretical k_{RRKM} with the k_{exp}. Despite several attempts to ask Brüker about these values, they couldn't offer us this information. Without dosimeter we were not able to obtain laser power value. In addition, opening the instrument alone can lead to the loss of the warranty. Nevertheless, the typical values for common instruments, *i.e.* laser wavelength of 355 nm and laser spot diameter ~50-200 µm we can estimate the laser power to be between 0.003 and 0.06 J/cm^2 pe pulse.[39]

© 2020 Tous droits réservés.

lilliad.univ-lille.fr

For the above mentioned reason, for the calculation of the deposited internal energy, the approach that uses multiple benzylpyridinium's critical energies was used.[36] The SY values were plotted versus critical (**Figure II.2-6**), and the values at 62% were fitted with a Boltzman function (**Figure II.2-7A**, R^2= 0.9998). The second derivative was applied to determine the internal energy distribution ρ(E), of the deposited internal energies (**Figure II.2-7B**).

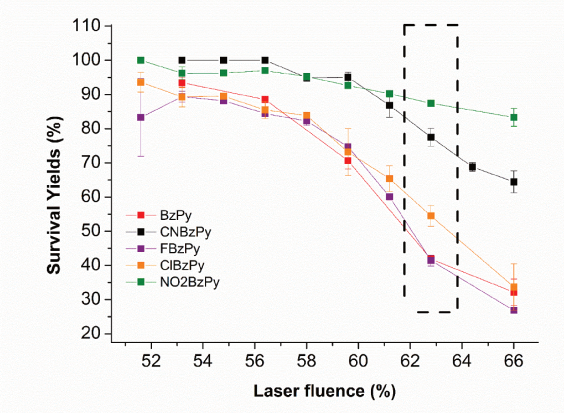

Figure II.2-6 Survival yields for 5 *p*-substituted benzylpyridinium ions (1 mM, water) as a function of laser fluence on CNWs.

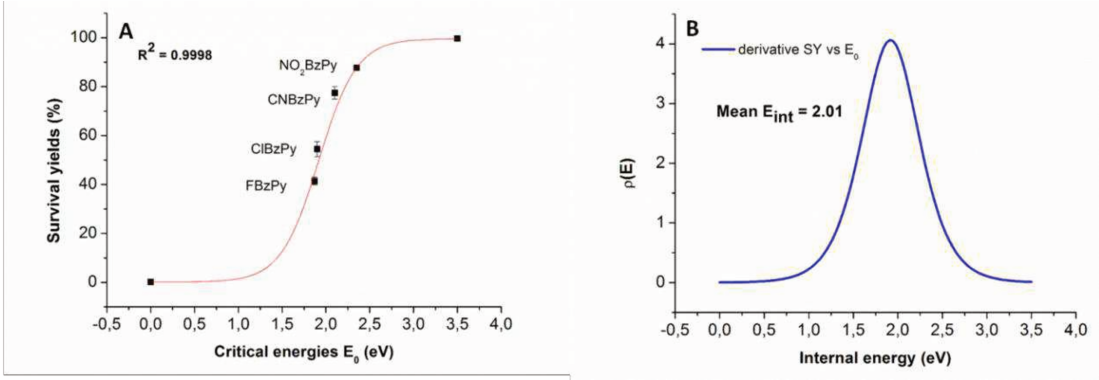

Figure II.2-7 Internal energy depositions for CNWs: **(A)** Survival yield values were plotted as a function of critical energy, E_o, at a laser fluence of 62% (3 measurements). **(B)** Derivatives of the sigmoidal curves produced the internal energy distributions *ρ*(E).

An internal energy transfer of 2.01 eV for CNWs was obtained, which corresponds to less than half of the values determined by Tang et al.[17] for different carbon based SALDI substrates such as nanodiamond (ND, 5.86 eV), graphite particles (G, 5.51 eV), highly oriented pyrolytic graphite (HOPG, 5.5 eV), fullerene (C60, 5.09 eV), nanoporous graphitic carbon (PGC, 4.96 eV) and carbon nanotubes (CNT, 4.71 eV). As the authors' conclusion, the ion desorption efficiency of thermometer compounds displayed a global opposite trend to the order of internal energy transfer to ion, with ND presenting the lowest desorption/ionization efficiency. Thus, it seems that CNWs may present better desorption/ionization efficiency than

© 2020 Tous droits réservés.

lilliad.univ-lille.fr

other carbon based materials, as described by Tang et al.[17] In addition, it was recently shown that boron doped diamond presented improved SALDI-MS performances.[19,40]

II.2.2. Detection of small biomolecules in buffers

II.2.2.1 Detection of peptides

SALDI-MS performances of CNWs were firstly assessed using commercially available calibration peptide mixtures, MIX 1 and MIX 2 solutions (for concentrations, see **Table V.7-1** in **Appendix**) in 1 mM ammonium citrate. Both reflectron and linear modes were used, for different concentrations of peptides. In **Figure II.2-8A**, we can see that all 4 peptides were detected, even Neurotensin ($[M+H]^+$ average at 1673.96 m/z) at a concentration of 12.5 fmol/0.5 µL with a signal to noise ratio (S/N) of 4 in linear mode and 10 in reflectron mode. The intra and inter spot RSDs were <30% in all cases, and <5% in the case of Des-Arg9-Bradykinin ($[M+H]^+$ monoisotopic at 904.5 m/z). In **Figure II.2-8B**, all the 5 calibrants ($[M+H]^+$ average ranging from 1296.7 to 5730.6 m/z), present in MIX 2 were also detected ($[M+H]^+$ with intra-spot RSDs below 15%. The highest molecular mass detected is insulin at 875 fmol/0.5µL (S/N of 5).

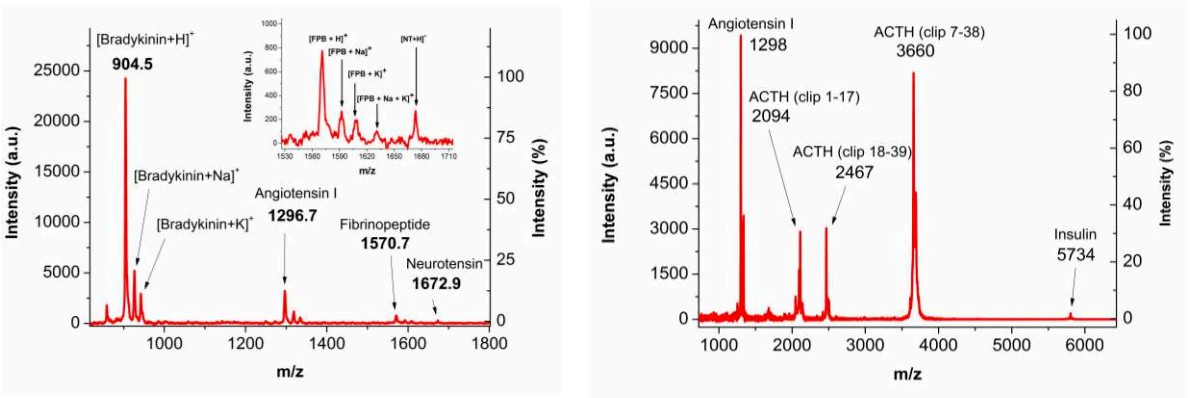

(A) **(B)**

Figure II.2-8 SALDI-MS spectra of **(A)** MIX 1 (250 fmol DAB, 325 fmol A1, 325 fmol FBP and 12.5 fmol NT) and **(B)** MIX 2 (500 fmol A1, 500 fmol ACTH1, 350 fmol ACTH18, 750 fmol ACTH7 and 875 fmol INS) obtained on CNWs. Peptides were diluted in ammonium citrate 1 mM and a laser power of 78% was used (linear mode). DAB=Des-Arg9-Bradykinin; A1=Angiotensin I; Fbp=Fibrinopeptide; NT=Neurotensin and Ins=Insulin.

Similar MS performances were obtained for peptides MIX 1 using the reflectron mode, when compared to boron-doped diamond nanowires, BDD-NWs[19] and silicon nanowires, SiNWs (**Table II.2-2**).[22] The S/Ns are in the same order of magnitude, with the exception of Angiotensin I, for which S/N of CNWs is an order of magnitude less than BDD-NWs and

© 2020 Tous droits réservés.
lilliad.univ-lille.fr

Thèse de Ioana Silvia Hosu, Université de Lille, 2020

SiNWs. By comparison, an advantage of the CNWs is that using linear mode, detection of peptides with a larger mass range (**Table V.7-1**), was namely found in MIX 2.

Table II.2-2 Performances of different SALDI-MS substrates, using MIX 1 peptides solution.

Signal/noise (S/N) for:			
Peptide	**CNWs (This work)**	**BDDNWs**[19a]	**SiNWs**[22b]
DAB	465	1078	641
A1	77	431	532
FBP	71	55	100
NT	10	59	40

[a] 25 fmol/0.5 µL of DAB, AI and FPB and 5 fmol/0.5 µL of NT, ref[19]

[b] 25 fmol/0.5 µL of DAB, AI and FPB and 5 fmol/0.5 µL of NT, ref[22]

II.2.2.2 Optimization of important detection parameters using saccharides

It is widely known that carbohydrates are detected by MALDI and SALDI-MS as sodium or potassium adducts. Mohr *et al.* studied the influence of the alkaline metals added to the carbohydrates and found that Cs^+ and K^+ ionize oligosaccharides about 3 times better than Na^+ ions, influencing also the quantum yield. As no small saccharides can be ionized by Cs^+, the expected glucose adducts in LDI-MS are the sodium and potassium ones.[41] Moreover, for some of the molecules, as in the case of saccharides, we can increase the sensitivity by optimizing the type and/or amount of alkaline metal ions added. To investigate the ability to our surfaces to detect various types of sugars, we studied the influence of several different parameters: the laser power, the salt type and its concentration, the confinement of analyte and the surface chemistry. Then, the results were compared in terms of signal to noise ratio and signal intensities to find the best experimental conditions to detect sugars by LDI-MS on CNWs.

II.2.2.2.a Influence of the laser power on the SALDI-MS background

Firstly, the influence of the substrate on the quality of the MS spectra of saccharides was taken into consideration. Indeed, carbon clusters or adducts may be desorbed and ionized from the surface itself under laser irradiation.[42] For this purpose, control sample (NaCl solution, 10 mM) and glucose sample (MW=180.16, 0.5 nmol in 10 mM NaCl solution) were both deposited on CNWs**. Figure II.2-9** shows the results from the substrate study that compares MS intensities obtained for the control and glucose samples, as a function of laser power. We can notice that the control and the glucose samples gave rise to similar MS profiles with three peaks at 138.8, 164.8 and 180.8 m/z for the control and an additional peak at 202.8 m/z, assigned to $[M(glucose)+Na]^+$ for the glucose sample. Thus, we can conclude that the three peaks (138.8, 164.8 and 180.8 m/z) are coming from the substrate. Indeed, even if the peak at 180.8 m/z could be confused with the $[M(glucose)+H]^+$, no reports of this ion

© 2020 Tous droits réservés.

lilliad.univ-lille.fr

have been reported in the literature, especially due to the high affinity of glucose for Na^+, and low proton affinity. In fact, this peak can be a cluster for C_{15}^+, from the carbon nanowalls substrate.

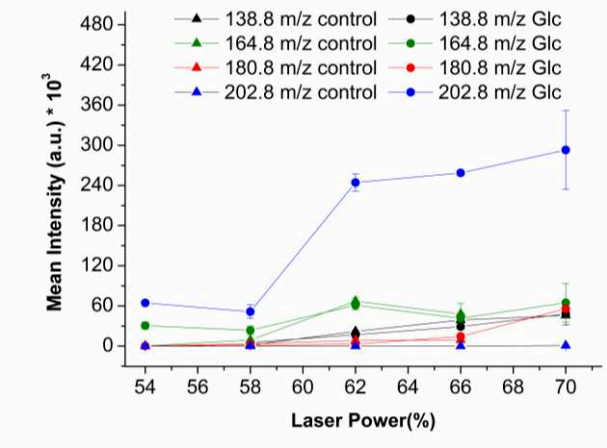

Figure II.2-9 Comparison of SALDI-MS spectra of the control (triangle) and 500 pmol Glc (circle) at different m/z: 138.8, 164.8, 180.8 and 202.8.

It has to be noticed that similar background fragments were obtained when galactose (MW=180.16, 0.5 nmol) was analysed in water (**Figure II.2-10**). As the laser increases, also the background peaks increase, and the best laser power to use, it is again 62%.

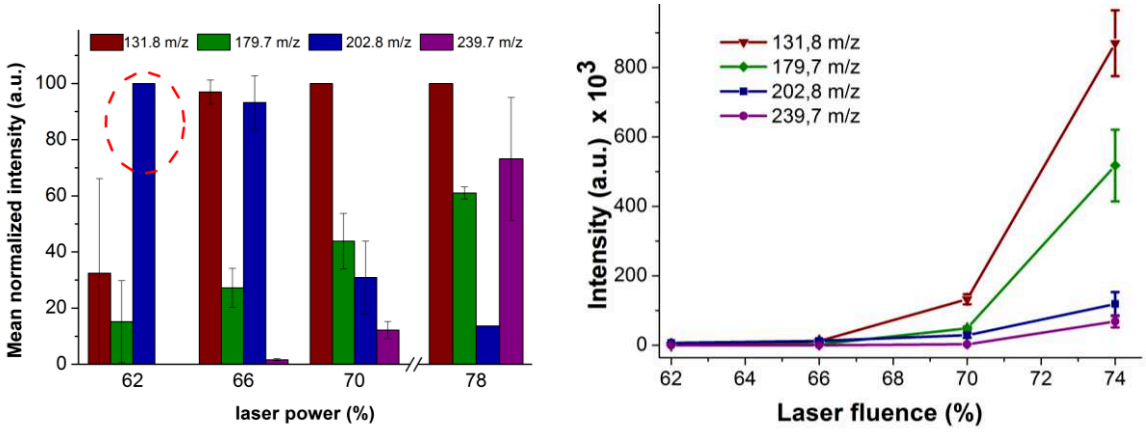

(A) **(B)**

Figure II.2-10 MS intensities of galactose in water as a function of laser powers for the most four intense peaks (138.8, 164.8, 180.8 and 202.8.m/z): **(A)** mean normalized intensities and **(B)** measured intensities**.**

Xylose (M_w=150.13), one of the smallest saccharides, was dissolved in water in absence and in presence of exogenous Na^+ and drop-casted on CNWs surface (5 nmol). MS spectra were recorded and the intensities were compared for different laser powers (**Figure II.2-11**). Even when Na^+ was not added, the intrinsically presence of Na^+ in the sugar's powder, determined that the main peak was 172.8 m/z corresponding to $([M_{xylose} + Na]^+$ adduct. The carbon isotopes can also be observed. The added sodium salt, besides increasing the sensitivity, also improved the reproducibility with better RSD values (*e.g.* RSD 16 % for

© 2020 Tous droits réservés.
lilliad.univ-lille.fr

added sodium compared with RSD 80% in absence of added sodium, at laser power of 66%). No response was obtained for smaller power than 62% in absence of added Na^+ sources.

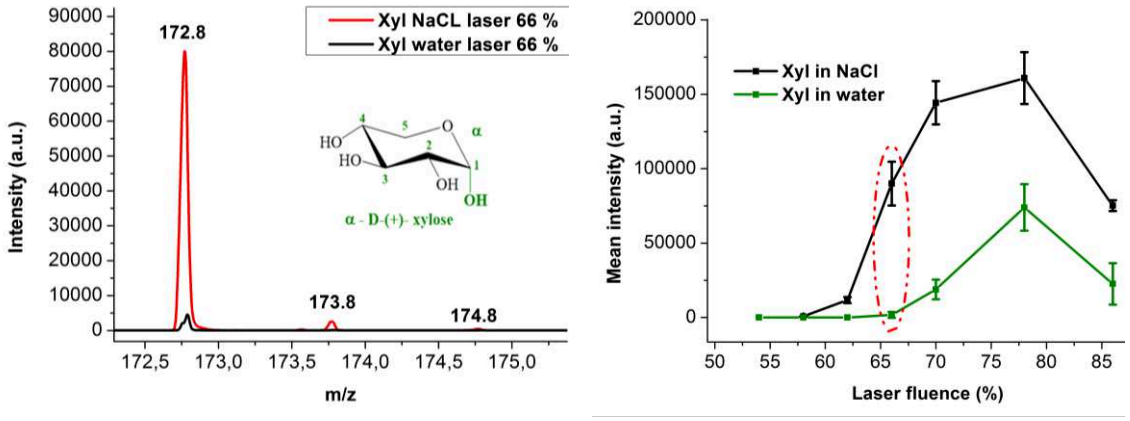

(A) **(B)**

Figure II.2-11 Mass spectra obtained for Xylose (500 pmol) in NaCl solution (10 mM) (red) and in water (black), at laser power 66 %. Main peak corresponds to [Xylose+Na]+ at 172.8 m/z. The presence of the two isotopes can be observed: ^{12}C(172.8 m/z) and ^{13}C(173.8) **(A).** The representation of MS signal intensities as a function of laser power for xylose in water (green) and xylose in NaCl (black) **(B).**

The laser power influence was also assessed in terms of signal intensity and the S/N ratio of $[M(glucose)+Na]^+$. In **Figure II.2-12A** the results for glucose sample (at 202.8 m/z) are presented as the signal to noise ratio as a function of laser power. It can be observed that even if the intensity of the peak at 202.8 m/z increases when increasing laser fluence (**Figure II.2-9**), the S/N ratios show a maximum at around 62%, for both glucose and galactose. Due to this observation, a laser power close to 62%, was used in further studies.

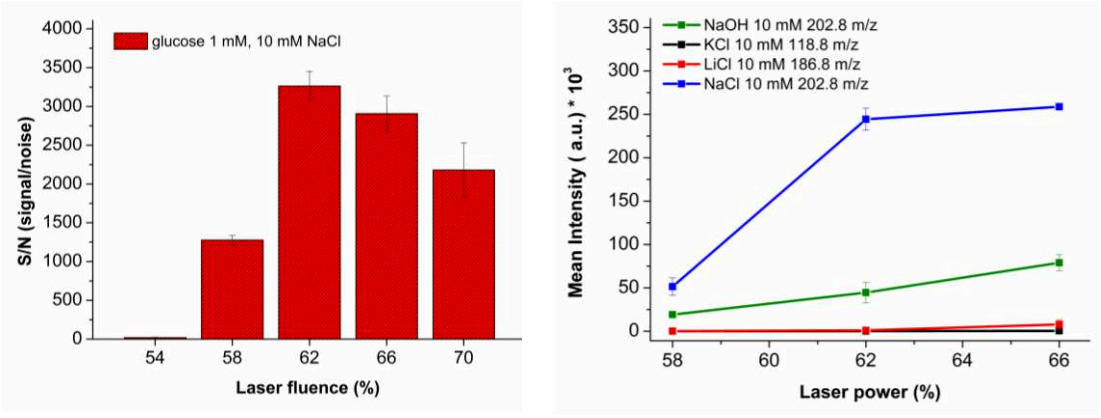

(A) **(B)**

Figure II.2-12 (A) Signal/noise ratios as a function of laser fluence for glucose (0.5 nmol in 10 mM NaCl); **(B)** Study of the influence of Na^+, K^+ and Li^+ added ions on the glucose (500 nmol) detection, performed on CNWs, using SALDI-MS.

II.2.2.2.b Influence of alkaline metals on MS performances

Another important parameter considered, was the influence of the alkaline metals on the MS spectra. Different sources of Na^+ were taken into consideration, and the comparison was

© 2020 Tous droits réservés.
lilliad.univ-lille.fr

done using 500 pmol of glucose at a fixed laser power @ 62%. As expected, NaCl ionizes better saccharides than NaOH, due to higher ionicity in the salt (**Figure II.2-12B**). Coordination of alkali metals to saccharides dictates the fragmentation pattern in MALDI-MS,[43] and usually the affinity order is the following Cs>K>Na>Li>H. However, due to the strong affinity of glucose towards Na^+ and the fact that Cs^+ is unable to ionize small molecules, the highest sensitivity was found when Na^+ was added to the glucose sample. To go further, the effect of NaCl concentration was also studied in order to fully optimize the process. In **Figure II.2-13**, it can be observed that the optimum NaCl concentration was 10 mM, similar to those used for the detection of glucose by wood charcoal matrix.[44]

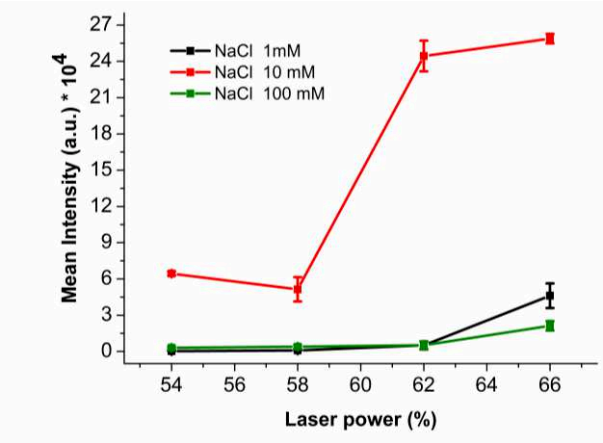

Figure II.2-13 Study of the NaCl concentration on the glucose (500 nmol) detection, performed on CNWs, using SALDI-MS.

II.2.2.2.c Influence of the surface chemistry

We also took into account the surface chemistry of the CNWs. So, we did prepare the following surfaces: as-synthesized with C-H terminations, octadecyltrichlorosilane (OTS) modified with $C\text{-}CH_3$ terminations and oxidized CNWs with C-OH/C-O-C/O-C=O terminations. For this purpose, we used piranha oxidation as cleaning and activating procedure prior to silanization by OTS (**Figure II.2-14**). It has to be noticed that piranha treatment didn't lead to morphological changes (see SEM images in **Figure II.2-15**) whereas a slight oxidation of CNWs occurred, as the C/O ratio decreased from 32.29 to 20.66, after piranha treatment, according to XPS (see **Table II.2-3**).

Table II.2-3 C/O ratios from XPS analyses from as-received CNWS and oxidized CNWs (Ox-CNWs) after piranha and oxygen plasma treatment.

XPS	Treatment	C/O
CNWs	As-synthesized	32.29
Ox-CNWs	Piranha (H_2SO_4/H_2O_2 3:1), 15 min	20.66
Ox-CNWs	oxygen plasma 30 sec, 200 W, 100 mTorr	9.69

© 2020 Tous droits réservés.
lilliad.univ-lille.fr

After OTS modification, the WCA value obtained was again 127°, thus the surface area of the drop casted was the same as for as-synthesized CNWs. To obtain apertures composed by oxCNWs surface, we performed optical lithography followed by oxygen plasma process on OTS modified "as-synthesized" CNWs as described in the literature.[25]

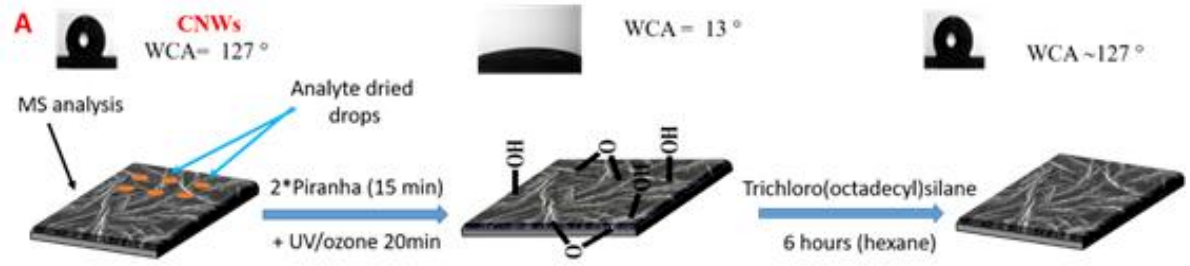

Figure II.2-14 Surface cleaning and oxidation with piranha and UV/ozone, followed by OTS-modification.

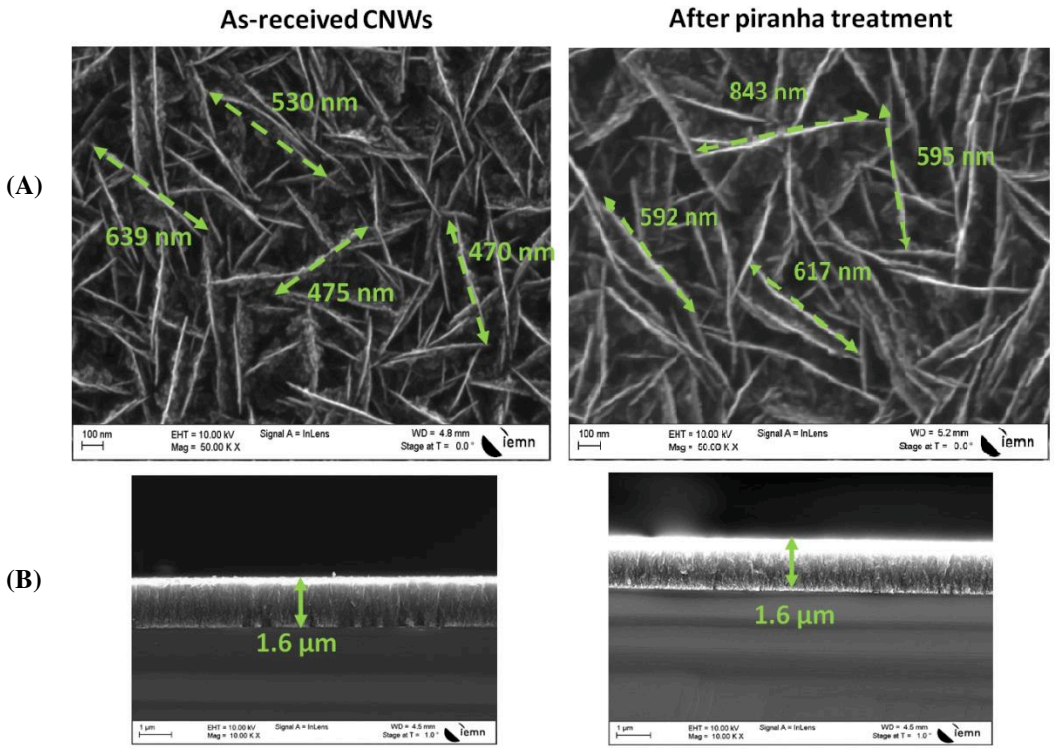

Figure II.2-15 SEM pictures of the **(A)** top view and **(B)** cross view of CNWs before (left) and after (right) piranha treatment.

Then, hydrophilic apertures of 800 µm in diameter were achieved (**Figure II.2-16**). The apertures formation was set to change the surface chemistry of CNWs and keep the deposited sample in confined area. Indeed, if all the entire CNWs surface are treated by oxygen plasma, the deposited sample will spread over the whole surface, thus diluting the sample, decreasing the sensitivity of detection.[20] Here, a stronger oxidation of CNWs was observed after oxygen plasma treatment without morphological changes (**Figure II.2-17**). Indeed, XPS analysis

© 2020 Tous droits réservés.

lilliad.univ-lille.fr

showed a strong decrease of C/O ratio with value of 9.69 (32.29 for as-received CNWs) (**Table II.2-3**).

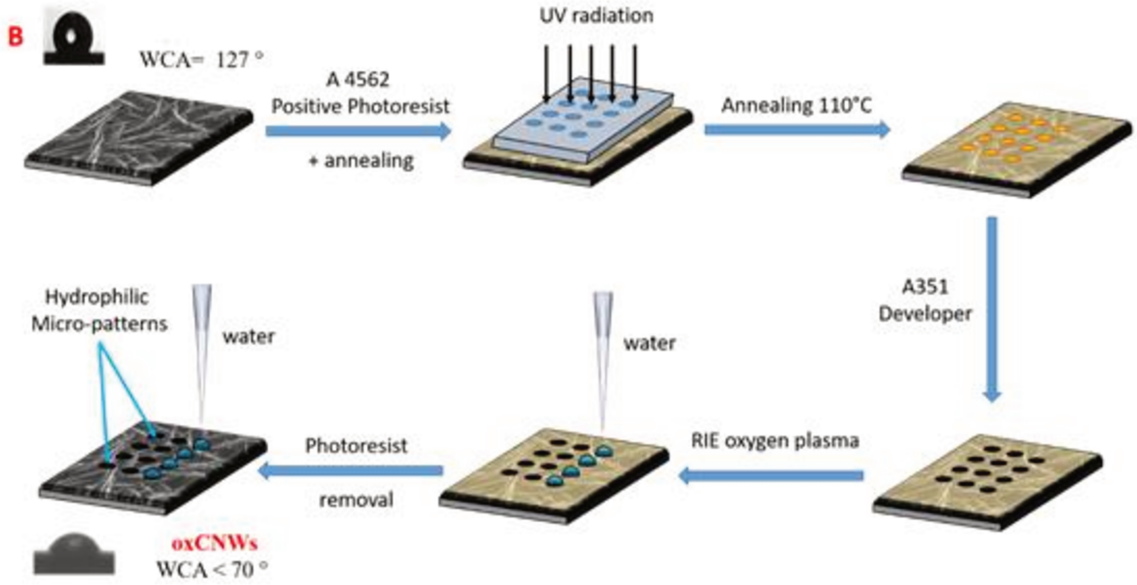

Figure II.2-16 Hydrophilic micro-patterns designing procedure.

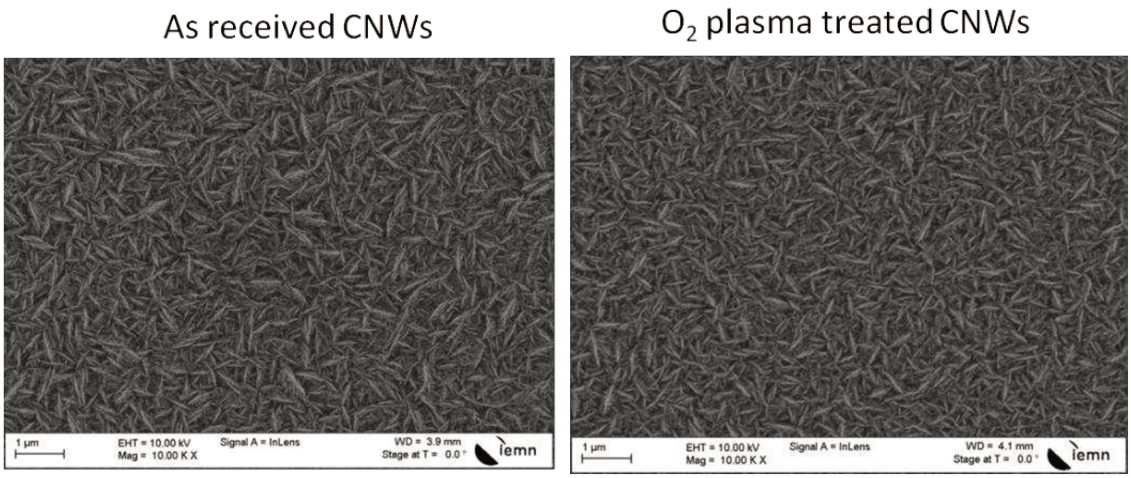

Figure II.2-17 SEM images of CNWs before and after oxygen plasma treatment.

Through high resolution XPS spectra we can also clearly see that oxygen plasma treatment introduced new chemical terminations such as C-OH/C-O-C/O-C=O. **Figure II.2-18** presents the XPS results of the C_{1s} and O_{1s} of the CNWS and the oxCNWs. For CNWs, the C_{1s} spectrum reveals that upon oxygen plasma during 30 s, the carbon atomic percentage decreases from 96.25 to 89.61 % (**Figure II.2-18A**), while the O_{1s} spectrum reveals that the atomic percentage of the oxygen increases from 2.98 to 9.25 % (**Figure II.2-18B**), meaning that oxidized carbon species are formed. The high resolution C_{1s} XPS spectrum of CNWs can be deconvoluted using CASA-XPS software into five peaks with binding energies at 281.9, 284.3, 285.8, 287.3 and 288.3 eV assigned to sp^2-hybridized

© 2020 Tous droits réservés.

lilliad.univ-lille.fr

carbon, C–H/C–C, C–O/O-C-O, C=O and O-C=O species, respectively (**Figure II.2-18C**). Similar deconvolution was performed for the oxCNWs (**Figure II.2-18D)**. Upon comparison, after oxygen plasma, the atomic percentage of the hydroxyl groups increased from 12.73 % to 26.23 % and carboxylic groups from 2.35% to 4.93%. As it can also be seen in the O_{1s} spectrum, the signal intensity decreases, in concordance with the above statement. As an overall argument, the C/O ratio decreases from 32.29 to 9.69, after the oxidation of CNWs by oxygen plasma. It has to be noticed that after piranha treatment, a C/O ratio value of 20.66 was obtained showing lower oxidation than after oxygen plasma treatment (see **Table II.2-3**).The presence of boron was also assessed and we can see that no significant changes were observed (data not shown). The presence of fluorine can be attributed to some contamination during the synthesis of CNWs, in the MW PECVD chamber and the presence of nitrogen was accounted for the use of N_2 during the synthesis of CNWs.[45]

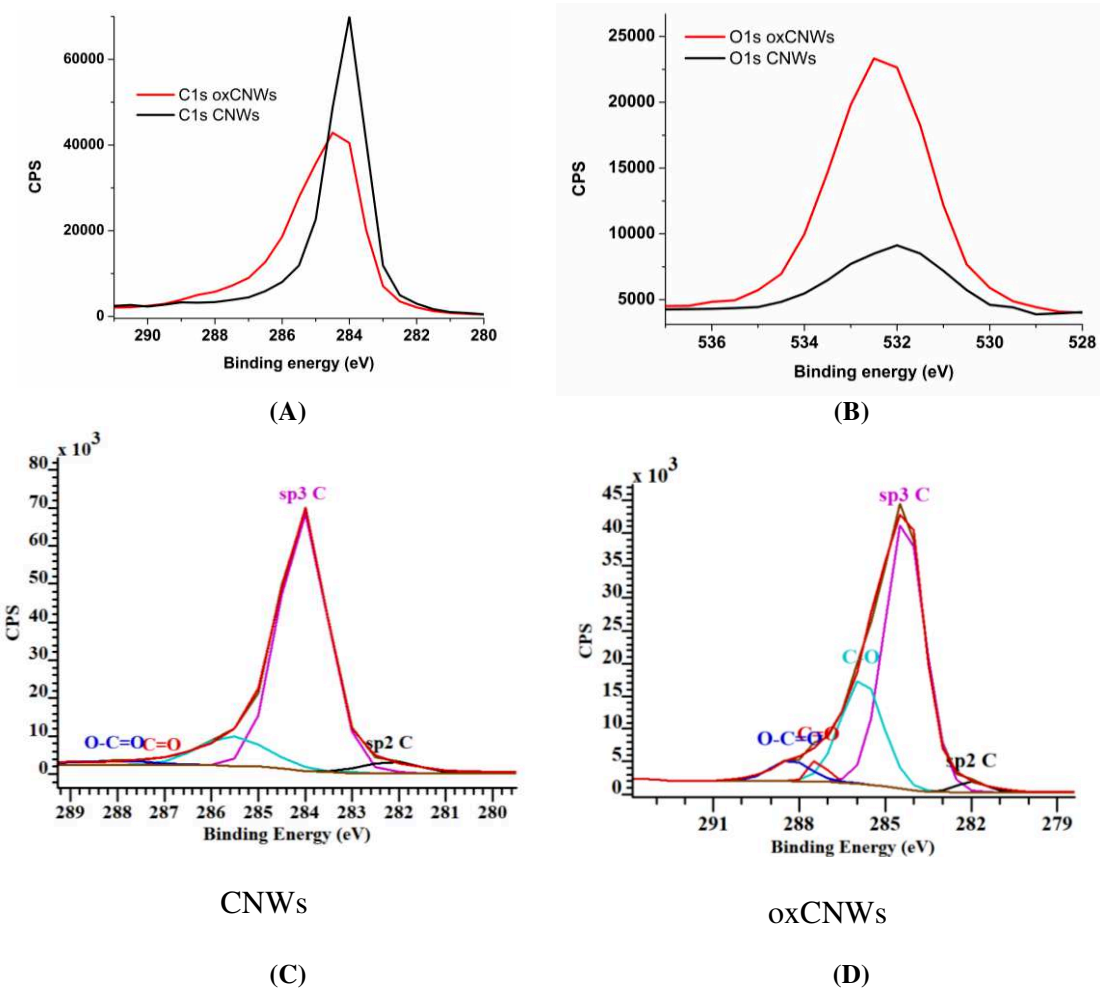

Figure II.2-18 High resolution of XPS spectra of **(A)** as-prepared CNWs (black) and after oxidation (plasma O_2) of CNWs (red) for C_{1s} region and **(B)** O_{1s} region. Deconvoluted XPS spectra of **(C)** C_{1s} for as-prepared CNWs and **(D)** after oxidation.

© 2020 Tous droits réservés.
lilliad.univ-lille.fr

Then, we compared the MS intensities of glucose (5 nmol/0.5 µL) obtained on the new synthesized CNWs and chemically modified CNWs: i) deposition of analytes on the OTS surface (CH_3-CNWs), or ii) inside the hydrophilic patterns (oxCNWs). It seems that the patterning improves the sensitivity for Glc (20 times), mainly due to the surface chemistry, as the surface area of the spots was ~ 1.3 ± 0.2 mm^2 in both cases. However, the MS peak intensity is still ~ 4 times lower (at laser power of 62%), compared with the MS intensity obtained on as-synthesized CNWs (**Figure II.2-19**).

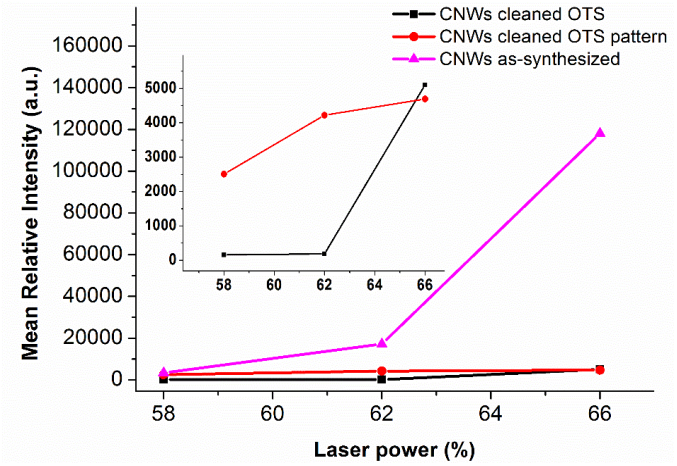

Figure II.2-19 Comparison of MS signal intensities of 5 nmol glucose at 10 mM in NaCl (10 mM), ($[Glc+Na]^+$ at 202.8 m/z). Glc was either drop casted on CNWs (pink), or on CNWs cleaned with piranha and modified with OTS (black) or on CNWs cleaned with piranha, modified with OTS and patterned via lithography and oxygen plasma (red). Inset: zoom for the cleaned oxCNWs surfaces.

II.2.2.2.d Detection of disaccharides

To go further, higher molecular weight saccharides were also studied. Sucrose (MW= 342.30), as expected was detected as $[M(sucrose)+Na]^+$ at 364.8 m/z and as $[M(sucrose)+K]^+$ adducts at 380.8 m/z. Also, the ion source fragmentation of the sucrose occurred, and glucose can be observed at 202.8 m/z $[M(glucose)+Na]^+$ (**Figure II.2-20**). The isotopic peaks can be also observed (**Figure II.2-21**).

© 2020 Tous droits réservés.

lilliad.univ-lille.fr

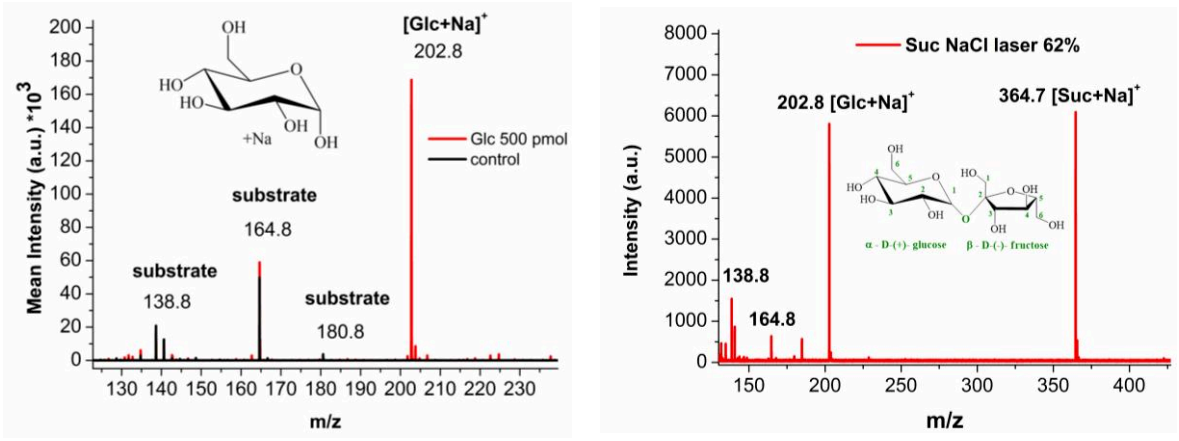

(A) **(B)**

Figure II.2-20 Glucose detection by LDI-MS spectra using CNWs. **(A)** control sample (NaCl 10 mM) and glucose sample at 500 pmol in 10 mM NaCl, both at laser power of 62%; **(B)** MS spectrum of 5 nmol sucrose: $[Suc+Na]^+$ and $[Glc+Na]^+$ adducts, in NaCl 10 mM.

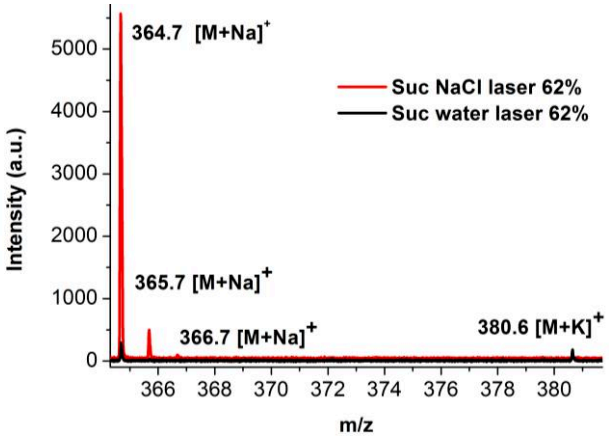

Figure II.2-21 MS spectra of sucrose (500 pmol in 10 mM NaCl) [Suc+Na]+ and [Suc+K]+ adducts. The presence of the two carbon isotopes can be observed in the presence of NaCl 10mM: ^{12}C(364.7 m/z) and ^{13}C(365.7 m/z). The peak at 366.7 m/z is the A+2 ion of the isotopic cluster showing the contribution of 180 and double incorporation of ^{13}C.

II.2.2.2.e Studying the homogeneity of drop-casted sugars

The deposition method is the following, unless otherwise stated: droplets of 0.5 µL were drop-casted on at least 3 different locations on 3 different as-received CNWs surfaces and were let to dry in air, during 1 h. Then, CNWs were fixed with a carbon conductive double-side adhesive tape on MTP TLC adapter (Bruker). The plate was then introduced into the mass spectrometer ion source. External calibration was performed with commercial peptide mixtures.

The presence of the "hot spot" formation was taken into account and it was noticed that this phenomenon does not occur. Indeed, as we can see in **Figure II.2-22**, MS imaging of glucose spot (m/z 202.8) showed that glucose was mainly located in the center of the spot

© 2020 Tous droits réservés.

lilliad.univ-lille.fr

(pink color representing the most abundant presence of 203 m/z and blue the least abundant). The control sample was also imaged (using NaCl) and we can clearly see that we do not have important interfering background intensities form the CNWS surface. That led to an inter-spot RSD value <17% (see **Table II.2-4**). In this table we took into account that calibration can be done with or without internal standards. Usually internal standards increase reproducibility because the ratio of the analyte signal to the internal standard signal (205/203 m/z ratio) is plotted as a function of the analyte known concentration of the standards. This way, the errors coming from background noise or the burial of the analyte inside the premixed sample hinders the LDI. We did use as internal standards (D-glucose-1,2-$^{13}C_2$), where the C-1 and C-2 were replaced with the isotope ^{13}C. The RSDs values decreased from 36% to 2.5% for inter-surface measurements and from 17% to 2.0 % for intra-sport measurements.

Taking in consideration the lack of "sweet spots" and good reproducibility of the results presented, we concluded that quantification could be done for glucose. And further detection of glucose in real samples could be performed.

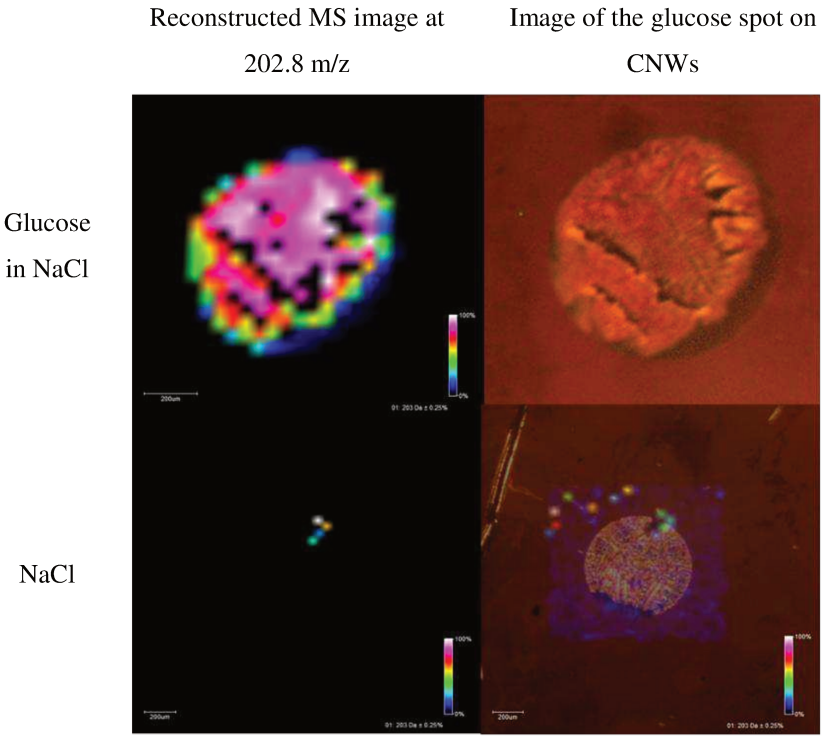

Figure II.2-22 Reconstructed MS Image 250 pmol glucose ($[M+Na]^+$ at 202.8 m/z) spot (in 10 mM NaCl) on CNWs. Visualized using Flex Imaging v3.0 software (Bruker Daltonics) Rough mean square (RMS) normalized.

© 2020 Tous droits réservés.

lilliad.univ-lille.fr

Table II.2-4 Comparison between SALDI-MS measurements (n=3 for surface-to-surface and intra-spot measurements and n=6 for inter-spot measurements) done without and with internal standard (250 pmol, D-glucose-2-^{13}C) for glucose (250 pmol, in 10 mM NaCl).

	Without internal standard (203 m/z)		With internal standard (205/203 m/z ratio)	
	Mean intensity (±SD)	RSDs (%)	Mean Intensity	RSDs (%)
Inter-spot	55122.67 ± 1468.71	< 9	0.936014 ± 0,018177	< 2
Intra-spot	71273.56 ±14785.08	< 17	0.959888 ± 0,021398	< 2
Inter-surface	56661.93 ± 20861.05	< 36	0.975792 ± 0,016804	< 2.5

© 2020 Tous droits réservés.

lilliad.univ-lille.fr

II.3. Quantitative measurements of glucose in blood serum and soft drinks

Diabetes is a chronic disease that has devastating human, social, and economic consequences. According to the World Health Organization (WHO) and the International Diabetes Federation, its worldwide prevalence is projected to double over the next couple of decades, from 347 million people in 2005 to 700 million people in 2030. Despite the lack of any known cure for diabetes, researchers managed to improve treatment efficiency to alleviate its symptoms and diminish its complications through appropriate medication and blood sugar monitoring, to improve treatment decisions and glucose control.[46] Thus, many efforts have been made to develop sensitive, reliable, and robust glucose sensors for glycemia monitoring. Among them, electrochemical sensors have been considered as excellent analytical tools for rapid and efficient glucose-determination. Most of them are based on the use of enzymes. But some drawbacks arised such as a lack of stability over time, difficulty to control the number of enzyme molecules (reliability) and poor reusability. As an alternative, the development of enzyme-free electrochemical glucose sensors, involving nanostructured electrodes to oxidize glucose directly on the surface, were developed and became of a great of interest.[47,48] Although good performances were obtained for the determination of glucose in samples, there is a lack of sensitivity, reliability and unambiguous detection of glucose in a straightforward way. SALDI-MS constitutes one of most promising method to measure glycemia in serum/blood. In this part we focused on glucose quantitation achieved in real sample both in blood serum and soft drinks.

Thus, to achieve quantitative measurements, a calibration curve was generated using the optimized quantity of extrinsically Na^+ source (NaCl 10 mM) and a laser power of 62% (y= 36.37*[glc/µM], where R^2= 0.9888, see **Figure II.3-1**). The linear range obtained is between 10 and 800 pmol. Above the upper value, a constant decrease of the signal intensity is observed (data not shown). The range is well suitable for glycemia measurements (normal glycemia value 3.5-6.1 nmol/µL) even if samples have to be slightly diluted prior measurements. The calibration curve and relative standard deviation calculations were obtained from inter-spot (I≥6), intra-spot (I≥3) and surface to surface (I≥3) mean values. Quantitative measurements of glucose in blood serum and soft drinks and detection of other compounds were also performed using 6 different drop-casted spots.

© 2020 Tous droits réservés.

lilliad.univ-lille.fr

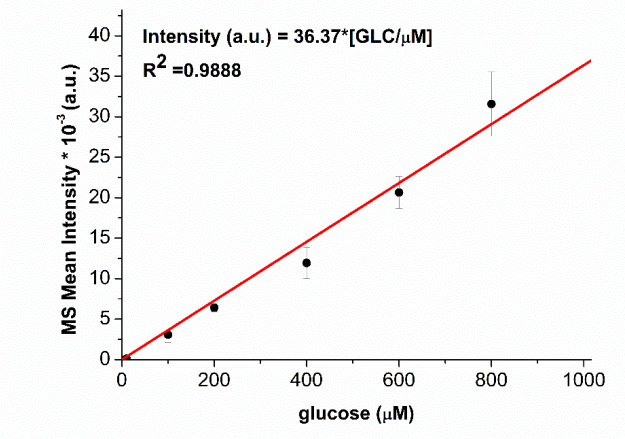

Figure II.3-1 Calibration curve of glucose, at 203 m/z, performed in 10 mM NaCl, using the proposed SALDI-MS method.

Table II.3-1 summarizes the state of the art of carbon-based materials used to detect glucose by LDI techniques. Comparing the results with the literature, CNWs exhibit much better inter-spot (<9%), intra-spot (<17%) and inter-surface (<36%) RSD values and the lowest concentration in the linear range (10 pmol) which is 4 times lower compared to wood charcoal.[44] By using as internal standard ^{13}C-glucose (**Figure II.3-2**), a strong improvement of the RSD values was observed with RSD values around 2-2.5% (see **Table II.2-4**). The calculated LOD was found to be 320 fmol, which is in the same order of magnitudes that those achieved using nano-porous suspension of carbon derived from metallic frameworks (NCMOFs), carbon nano-dots (CDs) or oxidized carbon nanotubes (oxCNTs), from pure glucose solutions.[49-51]

Table II.3-1 Literature study for the detection of glucose using carbon materials as SALDI interface or inorganic matrix.

SALDI interface or inorganic matrix	Details about the measurements [a]	Real samples [b]	Analyte	m/z	linear range (pmol) /0.5 µl	LOD (pmol/0.5 µL)[c]	RSD (%)	Ref.
Carbon nanotubes (CNTs)	Qualitative, Co-deposited	-	glucose	203	-	1.5 (aq.)	50.8	[52]
			sucrose	365	-	1.5 (aq.)	51.0	[52]
Wood Charcoal (Charcoal)	Qualitative, Co-deposited	-	glucose	203	-	50 (aq. NaCl)	-	[44]
			sucrose	365	-	500 (aq.NaCl)	-	[44]
Nanoporous carbons (NCMOFs)	Qualitative, Co-deposited	-	glucose	203	-	0.07 (aq.)	<12.0 %	[49]
Carbon nanodots (CDs)	Quantitative, Pre-mixed	blood samples	glucose (with D-glucose-1,2-^{13}C2 internal standard)	205/203 221/219	250 - 4500	0.01 (aq.)	<4.2 %	[50]
Graphene oxide (GO)	Qualitative, Pre-mixed	-	glucose	219	-	0.3 (aq.)	-	[50]
Oxidized carbon nanotubes (oxCNTs)	Qualitative, Co-deposited	urine	glucose (diabetic patient)	203 219	-	0.005 (aq)	-	[51]

© 2020 Tous droits réservés.
lilliad.univ-lille.fr

Carbon nanowalls (CNWs)	Quantitative, Surface Drop-casted	blood samples urine, soft drink, food supplement	glucose sucrose	202.8	5 - 400	0.32 (aq. NaCl)	<19%	this work
Carbon nanowalls (CNWs)	Qualitative, Surface Drop-casted	-	glucose (with D-glucose-1,2-^{13}C2 internal standard)	205/203	-	-	<2.5	this work

[a] refers to the type of analysis performed (qualitative or quantitative), if the carbon materials were pre-mixed with analyte (and deposited after on the MS target plate), co-deposited (matrix or analyte deposited first on the MS target plate, and the other on top) or as surface – assisted laser desorption/ionization
[b] it is specified if the measurements were also performed in real samples.
[c] it is specified if the LODs are achieved in aqueous solutions (aq), w/o adding NaCl.

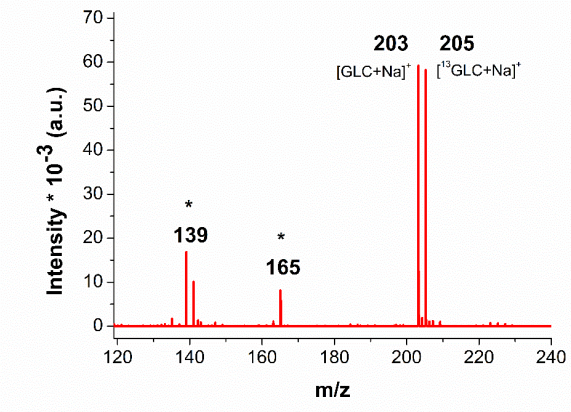

Figure II.3-2 MS spectrum of glucose (250 pmol) at 203 m/z and ^{13}C glucose (250 pmol) at 205 m/z. The peaks at 139 and 165 m/z correspond to background carbon adducts, as described in the main text.

Then, to go further, we attempted the detection of glucose in real samples such as serum and soft drinks. To do so, glucose was spiked in fetal bovine serum (FBS) diluted 10 times with NaCl (10 mM). FBS diluted 10 times was used as control experiment. As no peak was observed at 202.8 m/z, we took into consideration the possibility of high abundance proteins adsorbed on the surface of CNWs,[50] suppressing the MS signal for glucose.

In order to detect the glucose level in blood serum, freshly collected human samples were used. Prior to the MS analysis, the total carbohydrate detection was achieved using the phenol-sulfuric acid method proposed by DuBois.[53] Briefly, the freshly collected serum, was diluted 5 times and mixed to 5% phenol aqueous solution. Sulfuric acid was added rapidly to the mixture to obtain the furan derivative, a yellow-orange compound that absorbs at 490 nm. **Figure II.3-3A** depicts the UV-Vis spectra of the glucose standard solutions, other two samples (blood serum and Coca Cola) and the calibration curve. After determination of glucose level by DuBois UV method, the same stock serum sample was employed to perform MS analysis. In **Figure II.3-3B** the SALDI-MS spectra of controls (blood serum and pure glucose samples) and glucose spiked sample and their corresponding calibration curves are

© 2020 Tous droits réservés.
lilliad.univ-lille.fr

presented. The final concentrations determined were 4.52 mM with the colorimetric method and 5.61 mM using the SALDI-MS method. So, we can conclude that accurate and precise quantitative measurements can be done with RSDs <19% (intra-spot and inter-sp9ot measurements). In this work, the use of internal standards was not chosen, to reduce the cost of the measurements and to simplify the sample preparation and data processing. Nevertheless, experiments with ^{13}C glucose as internal standard were conducted and no strong improvement of RSD values was observed.

(A)

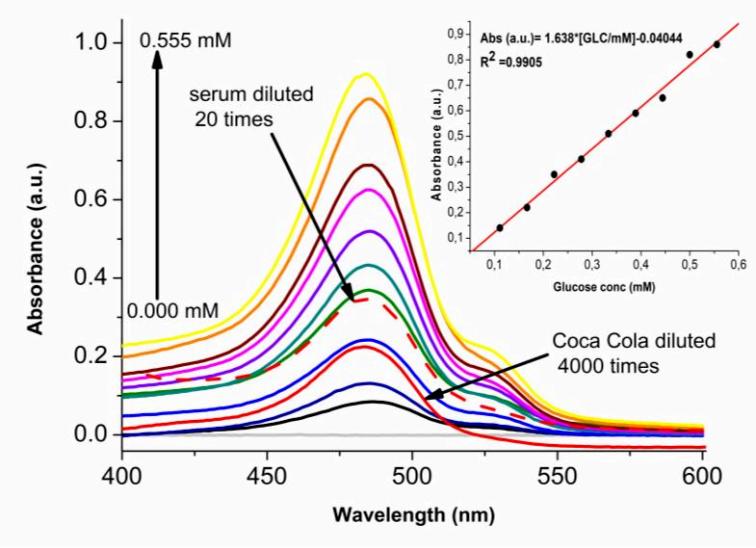

(B)

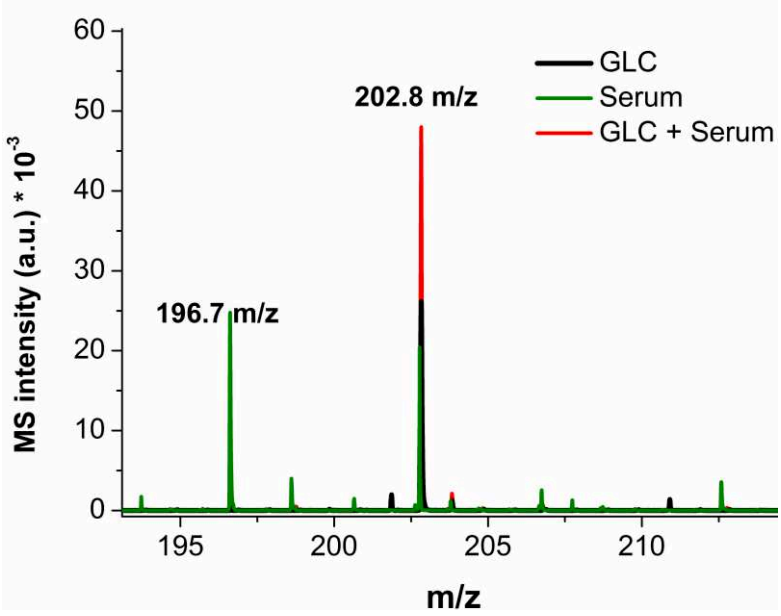

© 2020 Tous droits réservés.

lilliad.univ-lille.fr

(C)

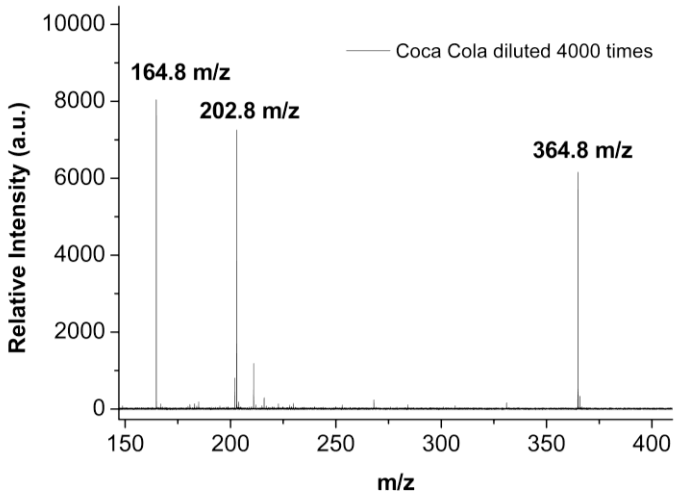

Figure II.3-3 (A) colorimetric method: UV-Vis spectra of different glucose concentrations, serum diluted 20 times (red dashed line) and Coca Cola diluted 4000 times (red solid line). Inset: calibration curve for glucose (0.1-0.55 mM); **(B)** CNW based SALDI-MS method: SALDI-MS spectra of serum (412 μM of glucose, green), glucose (500 μM black) and glucose spiked serum (red). The solutions were prepared in NaCl at 10 mM; **(C)** MS spectrum of Coca Cola diluted 800 times.

Furthermore, the detection of sugars in soft drinks (such as Coca Cola) was also investigated. The content of sugar stated by the Coca-Cola Company is stated to be 10.6 g/100 mL. However, no other specification is given concerning the sugar composition. Using cane sugar, sucrose would be the major sugar present, whereas using high fructose corn syrup, the major sugar would be fructose. Even though, the term "sugar" should refer exclusively to sucrose, many publications take in consideration the presence of fructose, glucose and sucrose in this beverage in different ratios, varying from 0-6.7 g/100 mL of fructose, 0-6.9 g/100 mL of glucose and 0-10.6 g/100 mL of sucrose.[54] For this purpose, Coca-Cola was diluted 500, 800, 1000, 2500 and 4000 times in water (for colorimetric detection) and in NaCl 10 mM (for MS detection). **Figure II.3-3C** depicts the SALDI-MS spectrum of Coca Cola diluted 4000 times. Both glucose/fructose (202.8 m/z) and sucrose (364.7 m/z) can be identified in the spectrum. With the colorimetric method we have obtained a final concentration of total carbohydrates of 10.9 g/100 mL (using the absorption at ~490 nm). Sucrose, being a disaccharide will be decomposed to glucose and fructose, due to the sulfuric acid hydrolysing action. Under these conditions, when all three saccharides are present, a concentration of 10.9 g of sugar/100 mL of Coca-Cola was determined, which is in good accordance with the producer's recipe.

The SALDI-MS analysis offered the possibility to complete the information of the colorimetric method, because an amount of 3.94 g glucose (or fructose)/100 mL was

© 2020 Tous droits réservés.

lilliad.univ-lille.fr

Thèse de Ioana Silvia Hosu, Université de Lille, 2020

obtained. As similar sucrose intensities were observed in MS (**Figure II.3-3**), we can assume that the total sugar content is in the range of 10 g/100 mL, as the producer sustains in the recipe. For a better comparison, sucrose can also be calibrated, using SALDI-MS proposed method in order to obtain the total amount of sugar, as in the colorimetric method.

Table II.3-2 summarizes the results obtained in comparison for both colorimetric and SALDI-MS methods. As the percentage errors between the conventional colorimetric method and our proposed method are lower than 20%, the detection of glucose from real biological fluids was achieved with good precision taking into consideration the complexity of the sample and the simplicity of the method. Thus, normal glucose ranges (approximatively 4-6 mM) can be detected by a 10-20 fold dilution in a 10 mM NaCl solution by simple drop-cast on the CNWs surface.

Using the conventional colorimetric method, a total sugar concentration of 605.5 mM (10.9 g/100mL) is recovered in Coca Cola, with only 2.83% error when compared to the total sugar content specified on the label, but the colorimetric method doesn't help us to distinguish between carbohydrates in general. The SALDI-MS method is able to differentiate between the disaccharides and monosaccharides giving a more precise concentration for glucose/fructose (286.9 mM).

Table II.3-2 Results of glucose detection in blood serum and soft drink samples: comparison between SALDI-MS and conventional colorimetric method.

Real samples	SALDI MS method $[M+Na]^+$		Colorimetric method		Comparison	
	RSD (%)	Concentration	RSD (%)	Concentration	RSD (%)	Percentage error (%)
serum	< 19	5.61 ± 0.21 mM	< 20	4.52 ± 0.160 mM	< 21	[c] 19.4
Coca Cola (label : sugar 10.6g/100ml)		[a] 219.38 ± 8.46 mM		[b] 605.55 ± 21.45 mM	-	[d] 2.83

a) equivalent of 3.94 g glucose (or fructose) /100 ml. b) equivalent of 10.9 g of total sugar/100 ml

c) $\frac{SALDI-colorimetric}{colorimetric} * 100$

d) total sugar content: $\frac{colorimetric-label}{label} * 100$

By comparison with other carbon based LDI-MS detection methods of glucose, the main disadvantage of the carbon materials in suspension (used as inorganic matrix for LDI-MS and described in **Table II.3-1**) is the contamination of the ion source, especially because the particles are not attached to the MS plate/substrate.[55,56] In the case of carbon nanotubes, another issue is the discharge behaviour in the ion source.[50] Even though the oxCNTs[51] were shorten and solubilized better in methanol (to decrease the ion source contamination), the MS samples were prepared by co-deposition with the analyte (using "matrix first method). Similar sample preparation was performed for the NCMOFs[49] and "pre-mixed method" for the CDs.[50] Burying the analyte inside the pre-mixed sample, hinders the LDI of the analyte

© 2020 Tous droits réservés.

lilliad.univ-lille.fr

Thèse de Ioana Silvia Hosu, Université de Lille, 2020

and decreases reproducibility. That is why, internal standard (D-Glucose-1,2-$^{13}C_2$) decreased the RSDs from > 30%. down to 4.2 %, in the case of glucose detection using CDs as matrix.[50]

In this section, we have shown that good RSD values for intra-spot, inter-surface and inter-spot for glucose detection can be obtained even without internal standard, meaning that accurate and precise quantitative measurements can be considered. The use of internal standard (^{13}C-Glucose) has strongly improved the RSD values (< 2%) for intra-spot, inter-spot and inter-surface quantitative measurements (see **Figure II.2-22** and **Table II.2-4**). It has to be noticed that when same experiments with internal standard were conducted in serum, no improvement of RSD values was observed. In addition, the choice of not using internal standard for quantitative measurement was motivated by the simplicity of the method and the cost of analysis.

To the best of our knowledge, there are no other reports of carbon based materials achieving such performances. The good reproducibility, LoD, simplicity, low-cost, time saving and the avoidance of ion source contamination and discharge effect of the proposed CNWs based SALDI-MS method, make this method as very powerful analytical tool for real samples. However, quantitative measurements by MS are still challenging, independently of the ionization method used. The variability of the background and peak intensities can have a strong impact on MS data quality. For that, crucial parameters have to take into account such as the surface homogeneity, the presence of proteins or other compounds contained in sample even after sample pre-treatment, the coffee ring effect, leading to heterogeneous distribution of sample inside the spot of analytes. Hydrophobic surface can reduce this effect, even if the quality of sample deposition is highly operator dependent. This is not the case here since we have shown, by MS imaging, that glucose was well located in the center of the spot and no "hot spots" were detected (see **Figure II.2-22**). One of the solutions would be to form hydrophilic patterns with size ranging from 100 µm to 800 µm to ensure homogeneous distribution of sample inside the apertures. In addition, the patterning with size related to the laser beam diameter will allow the complete coverage of the spot of analytes by the laser beam, thus improving confidence intervals of data. Previous results have already shown that analytes confinement in hydrophilic apertures led to their better detection.[25] In addition, we can also consider the use of non-contact printing to: 1) ensure homogeneity of spot deposition and 2) to perform high throughput deposition of hundreds of spots within a minute in a reproducible way. That will, for sure, improve the accuracy of quantitative measurements on your interface.

© 2020 Tous droits réservés.

lilliad.univ-lille.fr

Thèse de Ioana Silvia Hosu, Université de Lille, 2020

II.4. Detection of melamine, creatinine and paracetamol in urine samples

To underline the versatility of our CNWs interface we also chose to detect other important biological molecules (melamine, paracetamol and dopamine) in real sample fluids. Melamine is a toxic compound that was illegally used in the past to increase the apparent "protein content" in food samples, because of the high content of nitrogen. Animals that consumed a lot of melamine tainted products suffered, in consequence, of bladder stones, and when is bonded to cyanuric acid (through hydrogen bonds), kidney stones.[57] The detection of melamine in milk, urine or kidney stones was performed for humans using different MS techniques and procedures, but due to the high concentration of salts, the MALDI-MS is not suitable for the detection in urine.[58] Dopamine and creatinine can be used as biomarkers for drug consumption, especially when it comes to urine illegal drug tests. Creatinine levels are also important for both establishing if the kidney is working properly. Dopamine works in brain as a neurotransmitter and oscillating levels can be a sign of illegal drug consumption or nervous system diseases.[59] Paracetamol and its metabolites in urine can be considered as oxidative stress biomarkers and is highly toxic for the liver in case of overdosage.[60]

Figure II.4-1 presents spectra of melamine (MEL), dopamine (DA) and paracetamol (acetaminophen, APAP) in pure water solution or mixed together either in water (**Figure II.4-1A**) or in urine (**Figure II.4-1B**). The three possible protonation sites (the amino groups) of melamine, increase the ionization efficiency, and thus the MS signals. The protonated form $[M+H]^+$ and sodium adducts $[M+Na]^+$ were observed for melamine (MW=126.12), at 127 and 149 m/z, with intra-spot RSDs of less than 15% (**Figure II.4-1A**). Dopamine (MW=153.19) is described in the literature to be detected as the protonated form at 154 m/z or as fragmented form at 137 m/z, due to the loss of one NH_3. Other two peaks can be identified for the sodium and the potassium adducts (at 176 and 192 m/z, respectively).[59] Paracetamol (MW=151.16) was detected at 152 m/z, as the protonated adduct. The concentration for each compound was 250 pmol/0.5 µL. Simultaneous detection of 250 pmol of dopamine, melamine and paracetamol was also performed in water. The intra-spot RSDs values were < 40%. All the peaks were observed as described for individual detection.

We also used the CNWs surface for the melamine spiked urine samples. The urine was diluted 10 times (in water) and spiked with 250 pmol melamine. Even though the complexity

© 2020 Tous droits réservés.

lilliad.univ-lille.fr

of the urine sample the peak at 127 m/z was still detected, and the intra-spot and inter-spot RSDs were improved to a value of <15% (**Figure II.4-1B**).

As mentioned above for glucose, the native high concentration of NaCl (approximatively 130 mM) present in urine can stabilize and/or improve the sensitivity. Other main peaks were observed from the melamine un-spiked urine (114, 136, 152 and 197 m/z). Creatinine (MW=113.12) levels in urine are in the range of 4.4-26.5 mM[60] and a 10 times dilution of urine can provide enough concentration for the detection of the 114 and 136 m/z, corresponding respectively to the protonated and the Na^+ adduct of creatinine. The 152 m/z peak can be assigned to the previously administrated paracetamol, for the protonated adduct. The 197 m/z is attributed and discussed in literature to the potential biomarker, 3 nitro-paracetamol, synthesized upon metabolic oxidative stress (one of the paracetamol metabolites).[60]

The urine samples used as collected, with no further treatment, decreased 3 times the MS signal for melamine, compared with the centrifuged and filtered urine samples (data not shown).

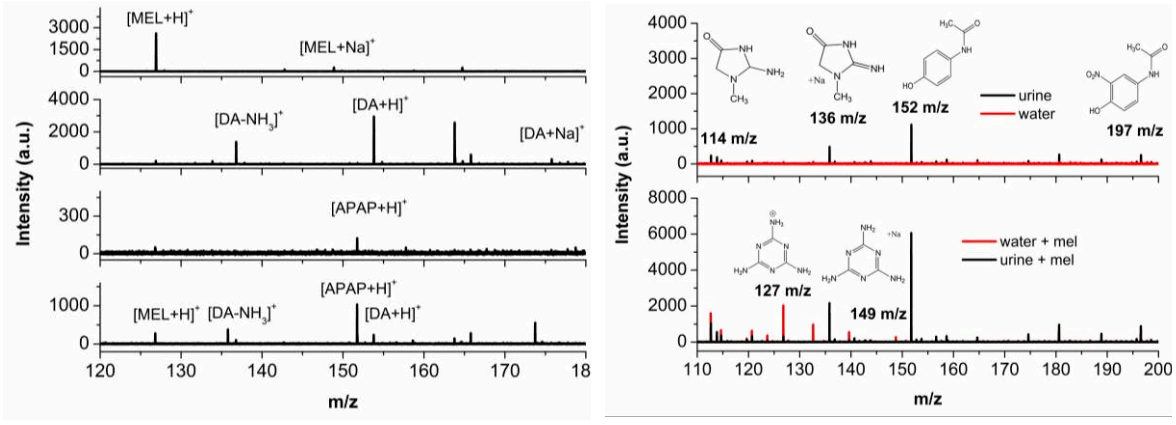

(A) **(B)**

Figure II.4-1 (A) MS spectra of separate and simultaneous detection of melamine (MEL, 250 pmol, at 127 and 149 m/z), dopamine (DA, 250 pmol, at 137 and 154 m/z) and acetaminophen (APAP, 250 pmol at 152 m/z) (in water, laser power 58%); **(B)** MS spectra of water (red) and urine diluted 10 times (black), in the absence (top) and in the presence (bottom) of 250 pmol MEL: 127 m/z $[M + H]^+$, 149 m/z $[M + Na]^+$. Other, naturally occurring, biomolecules: 114 m/z [creatinine + $H]^+$, 136 m/z [creatinine + $Na]^+$, 152 m/z [paracetamol + $H]^+$, 197 m/z [3-nitro-paracetamol$^+$ $H]^+$.

© 2020 Tous droits réservés.

lilliad.univ-lille.fr

II.5. Detection of phosphatidylcholine in lecithin food supplements

Fatty acids MS detections were also considered in our study. Classical MALDI-MS matrices seem to be inefficient for their ionization and subsequent detection. However, carbon materials such as graphene and/or graphene oxide have been successfully used to detect fatty acids.[61]

As fatty acids' source, we choose to study Soya Lecithin (a phosphatidylcholine, PC represented in **Figure II.5-1A**) which is used as pharmaceutical excipient or as food supplement. Palmitic (33%), oleic (31%), linoleic (15%) and stearic acids (13%) are the main fatty acids present in the PC's structure and they determine the complexity of the MS spectra. SALDI-MS experiments were conducted in positive reflectron mode (Fig. 8B). The average molecular weight of the PC is M=768 m/z. The $[M+Na]^+$ adduct was identified at 791.5 m/z and the 813.5 m/z corresponds to $[M-H+2Na]^+$.[62] Even if the MALDI-TOF method is usually a soft ionization technique, in the case of the SALDI- TOF proposed method, it is probable that ion source fragmentation occurs and different fragments can be identified.

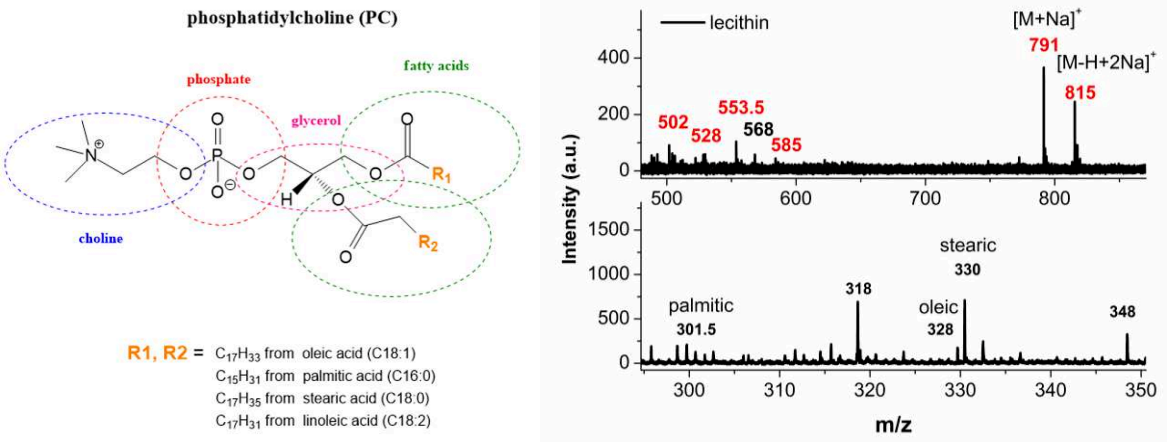

(A) **(B)**

Figure II.5-1 (A) Chemical structure of the phosphatidylcholine (PC) molecule and the different functional groups incorporated in its structure. **(B)** SALDI MS spectra of the food supplement containing lecithin (250 pmol): (up) Tryacylgliceride's mass range and (down) the fatty acid's mass range.

These fragments were attributed (according to Murphy et al.[63] and Calvano et al.[64]) to the neutral loss of different chemical groups that compose the tail, body and head of the PC molecule (**Table II.5-1**). The loss of other fragments gives rise also to the 568 m/z, but no specific interpretation was found. Other adducts (illustrated in **Scheme II.5-1**), attributed to neutral loss of RCOONa and RCOOH were also detected, <500 m/z (data not shown). The fatty acids from the soya lecithin were also identified, in the 300-350 m/z range, as $2Na^+$ adducts after the loss of a proton, $[M-H+2Na]^+$.[65] Palmitic acid (MW=256.43), oleic acid

© 2020 Tous droits réservés.

lilliad.univ-lille.fr

(MW=282.47) and stearic acid (MW= 284.48) were identified at 301.7, 327.7 and 329.7 m/z, respectively. Also the loss of the head group can be observed at 183 m/z, as a $[phosphate+choline+H]^+$ (data not shown). The proposed SALDI-MS-TOF method was, thus, also proved to have a good efficiency when it comes to detecting lipids and fatty acids in real samples.

Table II.5-1 Fragment and adduct attributions for the PC's SALDI-MS spectrum.

M=768 m/z	**Peak attribution**	**Palmitic acid**	**Oleic acid**
		m/z	
$[M + Na]^+$	Sodium adduct of PC	791	
$[M – H + 2Na]^+$	Sodium adduct of the sodium salt	815	
$[M - 183]^+$	Loss of phosphocholine + sodium adduct	585	
$[M + Na – RCH=C=O]^+$	Loss of neutral ketene from the sodiated adduct	551	525
$[M + H – RCH=C=O]^+$	Loss of neutral ketene from the protonated adduct	528	502
$[M - fatty\ acid]^+$	Loss of fatty acid	512	486
$[M - fatty\ acid^-Na^+]^+$	Loss of the fatty acid's sodium salt	490	464
$[M + Na - fatty\ acid]^+$	Loss of the fatty acid from sodiated PC	535	509

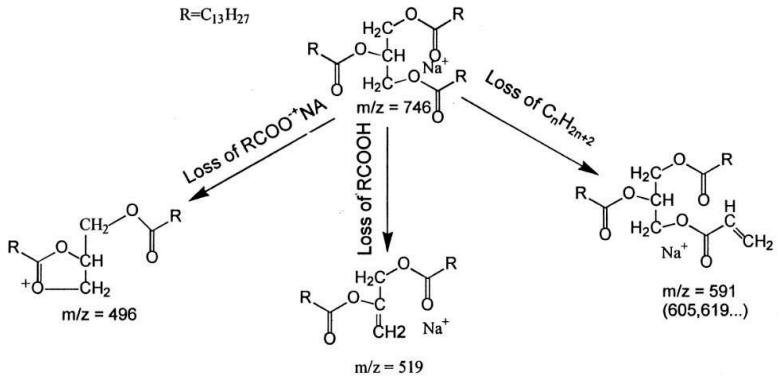

Scheme II.5-1 The major dissociative pathways for TAG's using high energy CID. Reproduced from reference[66] (TAG=triacylglicerides).

© 2020 Tous droits réservés.

lilliad.univ-lille.fr

II.6. Conclusions

The carbon nanowalls surfaces (CNWs) were found to be very efficient as SALDI-MS interfaces for the detection of saccharides, peptides up to 5800 m/z, carbohydrates, lipids, and other biomolecules/metabolic compounds. The proposed LDI method provided high MS signal intensities, good relative standard deviations (even less than 5% for sugars) and good detection limits.

Optimizations of SALDI-MS conditions with CNWs were investigated. Indeed, the presence of NaCl greatly increased the MS detection of sugars. In addition, all sugars are mainly detected as sodium adducts $[M+Na]^+$ and NaCl showed better ionization properties than LiCl, KCl or NaOH. Moreover, the laser power of 62% was found to give the best sensitivity for most of the molecules studied.

The dynamic range for glucose detection was from 5 to 400 pmol with a sensitivity of 36.58±0.58 pmol/0.5 µL and a calculated LOD of 0.32±0.02 pmol. Then, glucose was detected in real samples: 5.61 mM were detected in blood serum (in accordance with the normal glucose values) and 3.94 g/100mL in a soft drink. A conventional colorimetric carbohydrate detection method was used for comparison and low percentage errors (19%) were calculated between the colorimetric method and the proposed SALDI-MS method, for blood serum. The percentage error between the total sugar content in Coca-Cola present on the label and the one determined with the colorimetric method, is lower than 3%, but there is no possibility to distinguish between disaccharides and monosaccharides, empowering even more the feasibility of our proposed SALDI-MS method.

The high salt tolerance of the CNWs surface allowed the detection of melamine in urine, with an actual limit detection of 63±8.19 ng/µL. A paracetamol's metabolite (3-nitro-paracetamol) was also detected in the collected urine, as a consequence of oral uptake of 2 g, three days in a row. The proposed SALDI-TOF method can be used as a rapid screening tool for identification of paracetamol overdoses (>200mg/kg), in order to facilitate the treatment of the intoxicated patients. Other molecules contained in the urine were also identified (such as creatinine, that it is considered an important factor in the urine drug tests or in the kidney failure detection). Also, the entire lecithin fatty acids' source was analyzed from food supplements. Even the ionization is soft, the ion-source fragmentation of the lecithin occurred, and fatty acids were also detected.

Our work proved that the CNWs interfaces can be applied for the sensitive detection of various molecules (see **Table II.6-1**), outperforming the classical MALDI. Moreover, it can

© 2020 Tous droits réservés.

lilliad.univ-lille.fr

Thèse de Ioana Silvia Hosu, Université de Lille, 2020

provide a good opportunity for developing new methods for detection of metabolites, whenever MALDI is ineffective (such as urine, blood or other biological real samples).

In the next chapter, encouraged by these results, we will approach the main drawback of SALDI-MS: detection of bigger molecules, and more specifically, proteins.

All the presented results were published in Nanoscale, in 2017 (DOI: 10.1039/C7NR01069A) and it can be found in the references as ref. [67]

Table II.6-1 The variety of molecules studied in this chapter for detection with the SALDI MS method, in pure solution or in real sample.

Sample n.°	Analyte	Peak (m/z)	Solvent/Medium
1	Glucose	202.8 $[M+Na]^+$ 218.8 $[M+K]^+$	Water, NaCl 10 mM, Blood serum, Coca Cola
2	Gluconic acid	219 $[M+Na]^+$ 241 $[M+2Na-H]^+$	Water, NaCl 10 mM, Blood serum
3	Fructose	202.8 $[M+Na]^+$	Water, NaCl 10 mM, Coca Cola
4	Xylose	172.8 $[M+Na]^+$	Water, NaCl 10 mM
5	Sucrose	364.7 $[M+Na]^+$ 202.8 $[M-+Na]^+$	Water, NaCl 10 mM, Coca Cola
6	Galactose	202.8 $[M+Na]^+$	Water, NaCl 10 mM
7	Paracetamol	152 $[M+H]^+$	Water, urine
8	3 nitro-acetaminophen	197 $[M+H]^+$	Urine
9	Dopamine	154 $[M+H]^+$ 136 $[M-NH_3]^+$ 176 $[M+Na]^+$ 192 $[M+K]^+$	Water
10	Melamine	127 $[M+H]^+$ 149 $[M-NH_3]$	Water
11	Uric Acid	168.9 $[M+H]^+$ 142.8 m/z $[M-?]^+$	Water
12	Glycerol	114.8 $[M+Na]^+$	Water
13	Caffeine	194.9 $[M+H]^+$	Water
14	Lecithin	791 $[M+Na]^+$	Water/EtOH, Food supplement
15	Oleic acid	327.7 $[M-H+2Na]^+$	Water/EtOH, Food supplement
16	Stearic acid	329.7 $[M-H+2Na]^+$	Water/EtOH, Food supplement
17	Palmitic Acid	301.7 $[M-H+2Na]^+$	Water/EtOH, Food supplement
18	Creatinine	114 $[M+H]^+$, 136 $[M+Na]^+$	Urine
19	Insulin (bovine)	5734 $[M+Na]^+$	Ammonium citrate dibasic
20	Cytochrome C	-	Ammonium citrate dibasic
21	BSA	-	Ammonium citrate dibasic
22	Apomyoglobin (horse)	-	Ammonium citrate dibasic
23	Thioredoxin (E. coli)	-	Ammonium citrate dibasic
24	Dextran	-	Ammonium citrate dibasic
25	Cyano- benzylpyridinium	195 $[M+H]^+$, 116 $[M-pyridine+H]^+$	Water
26	Chloride-benzylpyridinium		Water
27	Flouride- benzylpyridinium		Water
28	Nitro-benzylpyridinium		Water

© 2020 Tous droits réservés.

lilliad.univ-lille.fr

II.7. References

1 Davami, K. *et al.* Synthesis and characterization of carbon nanowalls on different substrates by radio frequency plasma enhanced chemical vapor deposition. *Carbon* **72**, 372-380 (2014).

2 Hiramatsu, M. & Hori, M. in *Carbon Nanowalls: Synthesis and Emerging Applications* Ch. 1, 5 (Springer Vienna, 2010).

3 Krivchenko, V. *et al.* Carbon nanowalls: the next step for physical manifestation of the black body coating. *Scientific reports* **3**, 3328 (2013).

4 Tsvetkov, M. Y. *et al.* in *Photonics Prague 2014.* 94501V-94501V-94508 (International Society for Optics and Photonics).

5 Slobodian, P. *et al.* High sensitivity of a carbon nanowall-based sensor for detection of organic vapours. *RSC Advances* **5**, 90515-90520 (2015).

6 Ion, R., Vizireanu, S., Luculescu, C., Cimpean, A. & Dinescu, G. Vertically, interconnected carbon nanowalls as biocompatible scaffolds for osteoblast cells. *Journal of Physics D: Applied Physics* **49**, 274004 (2016).

7 Akhavan, O., Ghaderi, E. & Rahighi, R. Toward Single-DNA Electrochemical Biosensing by Graphene Nanowalls. *ACS Nano* **6**, 2904-2916, doi:10.1021/nn300261t (2012).

8 Karas, M., Bachmann, D. & Hillenkamp, F. Influence of the wavelength in high-irradiance ultraviolet laser desorption mass spectrometry of organic molecules. *Analytical chemistry* **57**, 2935-2939 (1985).

9 Tanaka, K. *et al.* Protein and polymer analyses up to m/z 100 000 by laser ionization time-of-flight mass spectrometry. *Rapid communications in mass spectrometry* **2**, 151-153 (1988).

10 Wei, J., Buriak, J. M. & Siuzdak, G. Desorption–ionization mass spectrometry on porous silicon. *Nature* **399**, 243-246 (1999).

11 Lewis, W. G., Shen, Z., Finn, M. G. & Siuzdak, G. Desorption/ionization on silicon (DIOS) mass spectrometry: background and applications. *International Journal of Mass Spectrometry* **226**, 107-116, doi:https://doi.org/10.1016/S1387-3806(02)00973-9 (2003).

12 Guinan, T. *et al.* Surface-assisted laser desorption ionization mass spectrometry techniques for application in forensics. *Mass Spectrometry Reviews* **34**, 627-640, doi:10.1002/mas.21431 (2015).

13 Chen, W.-T., Chiang, C.-K., Lin, Y.-W. & Chang, H.-T. Quantification of captopril in urine through surface-assisted laser desorption/ionization mass spectrometry using 4-mercaptobenzoic acid-capped gold nanoparticles as an internal standard. *Journal of the American Society for Mass Spectrometry* **21**, 864-867 (2010).

14 Trauger, S. A. *et al.* High sensitivity and analyte capture with desorption/ionization mass spectrometry on silylated porous silicon. *Analytical chemistry* **76**, 4484-4489 (2004).

15 Lim, A. Y., Ma, Z., Ma, J. & Rowell, F. Separation of fingerprint constituents using magnetic silica nanoparticles and direct on-particle SALDI-TOF-mass spectrometry. *Journal of Chromatography B* **879**, 2244-2250 (2011).

16 Law, K. P. & Larkin, J. Recent advances in SALDI-MS techniques and their chemical and bioanalytical applications. *Analytical and Bioanalytical Chemistry* **399**, 2597-2622, doi:10.1007/s00216-010-4063-3 (2011).

17 Tang, H.-W., Ng, K.-M., Lu, W. & Che, C.-M. Ion desorption efficiency and internal energy transfer in carbon-based surface-assisted laser desorption/ionization mass

© 2020 Tous droits réservés.

lilliad.univ-lille.fr

Thèse de Ioana Silvia Hosu, Université de Lille, 2020

spectrometry: Desorption mechanism (s) and the design of SALDI substrates. *Analytical chemistry* **81**, 4720-4729 (2009).

18 Law, K. P. & Larkin, J. R. Recent advances in SALDI-MS techniques and their chemical and bioanalytical applications. *Analytical and Bioanalytical Chemistry* **399**, 2597-2622, doi:10.1007/s00216-010-4063-3 (2011).

19 Coffinier, Y., Szunerits, S., Drobecq, H., Melnyk, O. & Boukherroub, R. Diamond nanowires for highly sensitive matrix-free mass spectrometry analysis of small molecules. *Nanoscale* **4**, 231-238 (2012).

20 Dupré, M. *et al.* Laser desorption ionization mass spectrometry of protein tryptic digests on nanostructured silicon plates. *Journal of proteomics* **75**, 1973-1990 (2012).

21 Coffinier, Y. *et al.* Affinity surface-assisted laser desorption/ionization mass spectrometry for peptide enrichment. *Analyst* **137**, 5527-5532 (2012).

22 Piret, G., Drobecq, H., Coffinier, Y., Melnyk, O. & Boukherroub, R. Matrix-free laser desorption/ionization mass spectrometry on silicon nanowire arrays prepared by chemical etching of crystalline silicon. *Langmuir* **26**, 1354-1361 (2009).

23 Piret, G. *et al.* Surface-assisted laser desorption–ionization mass spectrometry on titanium dioxide (TiO 2) nanotube layers. *Analyst* **137**, 3058-3063 (2012).

24 Dupré, M. *et al.* Investigation of silicon-based nanostructure morphology and chemical termination on laser desorption ionization mass spectrometry performance. *Analytical Chemistry* **84**, 10637-10644 (2012).

25 Lapierre, F. *et al.* High sensitive matrix-free mass spectrometry analysis of peptides using silicon nanowires-based digital microfluidic device. *Lab on a Chip* **11**, 1620-1628, doi:10.1039/c0lc00716a (2011).

26 Canham, L. T. Silicon quantum wire array fabrication by electrochemical and chemical dissolution of wafers. *Applied Physics Letters* **57**, 1046-1048 (1990).

27 Hiramatsu, M. & Hori, M. in *Carbon Nanowalls: Synthesis and Emerging Applications* 78 (Springer Vienna, 2010).

28 Tang, Y.-B. *et al.* Tunable Band Gaps and p-Type Transport Properties of Boron-Doped Graphenes by Controllable Ion Doping Using Reactive Microwave Plasma. *ACS Nano* **6**, 1970-1978, doi:10.1021/nn3005262 (2012).

29 Nayak, R. & Knapp, D. R. Matrix-Free LDI Mass Spectrometry Platform Using Patterned Nanostructured Gold Thin Film. *Analytical chemistry* **82**, 7772-7778, doi:10.1021/ac1017277 (2010).

30 Wang, Y., Li, J. & Song, K. Study on formation and photoluminescence of carbon nanowalls grown on silicon substrates by hot filament chemical vapor deposition. *Journal of Luminescence* **149**, 258-263 (2014).

31 Achour, A. *et al.* Thermal properties of carbon nanowall layers measured by a pulsed photothermal technique. *Applied Physics Letters* **102**, 061903 (2013).

32 Wang, K. *et al.* Effects of elemental doping on the photoluminescence properties of graphene quantum dots. *RSC Advances* **6**, 91225-91232 (2016).

33 Ni, Z., Wang, Y., Yu, T. & Shen, Z. Raman spectroscopy and imaging of graphene. *Nano Research* **1**, 273-291 (2008).

34 Polyakov, S. *et al.* Formation of Boron-Carbon Nanosheets and Bilayers in Boron-Doped Diamond: Origin of Metallicity and Superconductivity. *Nanoscale research letters* **11**, 1 (2016).

35 Sobaszek, M. *et al.* Optical and electrical properties of ultrathin transparent nanocrystalline boron-doped diamond electrodes. *Optical Materials* **42**, 24-34 (2015).

36 4th, F. P. *et al.* - Determination of internal energy distributions of laser electrospray mass. - *J Am Soc Mass Spectrom. 2014 Sep;25(9):1572-82. doi: 10.1007/s13361-014-0936-6.*, T - ppublish.

© 2020 Tous droits réservés.

lilliad.univ-lille.fr

Thèse de Ioana Silvia Hosu, Université de Lille, 2020

37 Flanigan IV, P. M. *et al.* Determination of internal energy distributions of laser electrospray mass spectrometry using thermometer ions and other biomolecules. *Journal of the American Society for Mass Spectrometry* **25**, 1572-1582 (2014).

38 Luo, G., Marginean, I. & Vertes, A. Internal energy of ions generated by matrix-assisted laser desorption/ionization. *Analytical Chemistry* **74**, 6185-6190 (2002).

39 Dreisewerd, K. The Desorption Process in MALDI. *Chemical Reviews* **103**, 395-426, doi:10.1021/cr010375i (2003).

40 Yagnik, G. B. *et al.* Large Scale Nanoparticle Screening for Small Molecule Analysis in Laser Desorption Ionization Mass Spectrometry. *Analytical Chemistry* **88**, 8926-8930, doi:10.1021/acs.analchem.6b02732 (2016).

41 Mohr, M. D., OlafBörnsen, K. & Widmer, H. M. Matrix-assisted laser desorption/ionization mass spectrometry: Improved matrix for oligosaccharides. *Rapid communications in mass spectrometry* **9**, 809-814 (1995).

42 Guinan, T. *et al.* Surface-assisted laser desorption ionization mass spectrometry techniques for application in forensics. *Mass Spectrom Rev* **34**, 627-640 (2015).

43 Cancilla, M. T., Penn, S. G., Carroll, J. A. & Lebrilla, C. B. Coordination of Alkali Metals to Oligosaccharides Dictates Fragmentation Behavior in Matrix Assisted Laser Desorption Ionization/Fourier Transform Mass Spectrometry. *Journal of the American Chemical Society* **118**, 6736-6745, doi:10.1021/ja9603766 (1996).

44 Lee, S.-Y. *et al.* Analysis of arginine, glucose, sucrose, and polyethylene glycols using a wood charcoal matrix for MALDI-MS. *Mass Spectrometry Letters* **1**, 33-36 (2010).

45 Sobaszek, M. *et al.* Diamond Phase (sp3-C) Rich Boron-Doped Carbon Nanowalls (sp2-C): Physicochemical and Electrochemical Properties. *The Journal of Physical Chemistry C* **121**, 20821-20833 (2017).

46 Wang, H.-C. & Lee, A.-R. Recent developments in blood glucose sensors. *Journal of Food and Drug Analysis* **23**, 191-200, doi:https://doi.org/10.1016/j.jfda.2014.12.001 (2015).

47 Wang, Q. *et al.* Non-enzymatic glucose sensing on long and short diamond nanowire electrodes. *Electrochemistry Communications* **34**, 286-290, doi:https://doi.org/10.1016/j.elecom.2013.07.014 (2013).

48 Wang, Q. *et al.* Electrophoretic Deposition of Carbon Nanofibers/Co (OH) 2 Nanocomposites: Application for Non-Enzymatic Glucose Sensing. *Electroanalysis* **28**, 119-125 (2016).

49 Shih, Y. H. *et al.* Nanoporous Carbons Derived from Metal-Organic Frameworks as Novel Matrices for Surface-Assisted Laser Desorption/Ionization Mass Spectrometry. *Small* **12**, 2057-2066, doi:10.1002/smll.201502817 (2016).

50 Chen, S. *et al.* Carbon Nanodots As a Matrix for the Analysis of Low-Molecular-Weight Molecules in Both Positive- and Negative-Ion Matrix-Assisted Laser Desorption/Ionization Time-of-Flight Mass Spectrometry and Quantification of Glucose and Uric Acid in Real Samples. *Analytical Chemistry* **85**, 6646-6652, doi:10.1021/ac401601r (2013).

51 Wang, C.-h., Li, J., Yao, S.-j., Guo, Y.-l. & Xia, X.-h. High-sensitivity matrix-assisted laser desorption/ionization Fourier transform mass spectrometry analyses of small carbohydrates and amino acids using oxidized carbon nanotubes prepared by chemical vapor deposition as matrix. *Analytica Chimica Acta* **604**, 158-164 (2007).

52 Yang, H.-J., Lee, A.-R., Lee, M.-K., Kim, W. & Kim, J.-K. Detection of small neutral carbohydrates using various supporting materials in laser desorption/ionization mass spectrometry. *Bulletin of the Korean Chemical Society* **31**, 35-40 (2010).

© 2020 Tous droits réservés.

lilliad.univ-lille.fr

Thèse de Ioana Silvia Hosu, Université de Lille, 2020

53 DuBois, M., Gilles, K. A., Hamilton, J. K., Rebers, P. A. & Smith, F. Colorimetric Method for Determination of Sugars and Related Substances. *Analytical Chemistry* **28**, 350-356, doi:10.1021/ac60111a017 (1956).

54 Augustin, M. & Khor, K. Determination of sugars in soft drinks by high performance liquid chromatography. *Pertanika* **9**, 119-123 (1986).

55 Han, M. & Sunner, J. An activated carbon substrate surface for laser desorption mass spectrometry. *Journal of the American Society for Mass Spectrometry* **11**, 644-649 (2000).

56 Pan, C. *et al.* Using Oxidized Carbon Nanotubes as Matrix for Analysis of Small Molecules by MALDI-TOF MS. *Journal of the American Society for Mass Spectrometry* **16**, 883-892 (2005).

57 Tang, H.-W. *et al.* Analysis of melamine cyanurate in urine using matrix-assisted laser desorption/ionization mass spectrometry. *Analytical Chemistry* **81**, 3676-3682 (2009).

58 Wu, H.-P., Yu, C.-J., Lin, C.-Y., Lin, Y.-H. & Tseng, W.-L. Gold nanoparticles as assisted matrices for the detection of biomolecules in a high-salt solution through laser desorption/ionization mass spectrometry. *Journal of the American Society for Mass Spectrometry* **20**, 875-882 (2009).

59 Kraj, A., Jarzebinska, J., Gorecka-Drzazga, A., Dziuban, J. & Silberring, J. Identification of catecholamines in the immune system by desorption/ionization on silicon. *Rapid communications in mass spectrometry* **20**, 1969-1972, doi:10.1002/rcm.2546 (2006).

60 Trettin, A. *et al.* LC–MS/MS and GC–MS/MS measurement of plasma and urine di-paracetamol and 3-nitro-paracetamol: proof-of-concept studies on a novel human model of oxidative stress based on oral paracetamol administration. *Journal of Chromatography B* **959**, 71-81 (2014).

61 Liu, Y., Liu, J., Deng, C. & Zhang, X. Graphene and graphene oxide: two ideal choices for the enrichment and ionization of long-chain fatty acids free from matrix-assisted laser desorption/ionization matrix interference. *Rapid communications in mass spectrometry* **25**, 3223-3234 (2011).

62 Ham, B. M., Jacob, J. T. & Cole, R. B. MALDI-TOF MS of Phosphorylated Lipids in Biological Fluids Using Immobilized Metal Affinity Chromatography and a Solid Ionic Crystal Matrix. *Analytical chemistry* **77**, 4439-4447, doi:10.1021/ac058000a (2005).

63 Murphy, R. C. in *Tandem Mass Spectrometry of Lipids: Molecular Analysis of Complex Lipids* Ch. 5 Glycerophospholipids, 130-193 (The Royal Society of Chemistry, 2015).

64 Calvano, C. D. & Zambonin, C. G. MALDI-Q-TOF-MS ionization and fragmentation of phospholipids and neutral lipids of dairy interest using variable doping salts. *Advances in Dairy Research*, 2-8 (2013).

65 Ayorinde, F. O., Garvin, K. & Saeed, K. Determination of the fatty acid composition of saponified vegetable oils using matrix-assisted laser desorption/ionization time-of-flight mass spectrometry. *Rapid communications in mass spectrometry* **14**, 608-615 (2000).

66 Asbury, G. R., Al-Saad, K., Siems, W. F., Hannan, R. M. & Hill Jr, H. H. Analysis of triacylglycerols and whole oils by matrix-assisted laser desorption/ionization time of flight mass spectrometry. *Journal of the American Society for Mass Spectrometry* **10**, 983-991 (1999).

© 2020 Tous droits réservés.

lilliad.univ-lille.fr

67 Hosu, I. S. *et al.* Carbon nanowalls: a new versatile graphene based interface for the laser desorption/ionization-mass spectrometry detection of small compounds in real samples. *Nanoscale* **9**, 9701-9715, doi:10.1039/c7nr01069a (2017).

© 2020 Tous droits réservés.

lilliad.univ-lille.fr

Chapter II. Carbon nanowalls for matrix-free laser desorption/ionization mass spectrometry detection of small compounds in real samples

Blank page

© 2020 Tous droits réservés.

lilliad.univ-lille.fr

Chapter III

Carbon nanowalls for matrix-free laser desorption/ionization mass spectrometry detection of ricin in complex media

© 2020 Tous droits réservés.
lilliad.univ-lille.fr

Thèse de Ioana Silvia Hosu, Université de Lille, 2020

Chapter III. Carbon nanowalls for matrix-free laser desorption/ionization mass spectrometry detection of ricin from complex media

III.1 Introduction 101
III.1.1 Detecting proteins with SALDI-MS 104
III.2 Optimization of CNWS for SALDI-MS. Detection of cyt C and ricin B chain 106
III.2.1 Surface characterization of boron doped CNWs 106
III.2.1.1 Morphological characterization of CNWs 107
III.2.1.2 Optical properties of carbon nanowalls 112
III.2.1.3 Other physical characteristics of CNWS important in SALDI-MS 114
III.2.1.4 Comparison of physical characteristics of CNWs with literature 117
III.2.1.5 Surface characterization of *ex-situ* boron doped CNWs. 119
III.2.2 Optimization of SALDI-MS parameters using cyt C on B-CNWs 122
III.2.2.1 Sample deposition methods for SALDI-MS 122
III.2.2.1.a Incubation of the analyte with CNWS SALDI-MS platform. 122
III.2.2.1.b Buffer in CNWS SALDI-MS procedure. 124
III.2.2.2 Boron doping levels and heights of CNWs in SALDI-MS 125
III.2.2.3 Correlation between SALDI-MS signals of Cyt C and internal energies. 128
III.2.2.4 Sensibility of the CNWs method towards Cytochrome C 129
III.2.3 Optimization of parameters using ricin B chain on *in-situ* doped CNWs 134
III.2.3.1 Sample deposition methods for SALDI-MS 134
III.2.3.1.a Incubation of the analyte with CNWS SALDI-MS platform. 134
III.2.3.1.b Buffer in CNWS SALDI-MS procedure 135
III.2.3.2 Boron doping levels and nanowalls' heights of CNWs in SALDI-MS 136
III.2.3.3 Sensitivity of the CNWs method towards ricin B chain 138
III.3 Affinity strategies for detection of ricin B chain on in-situ boron doped CNWs .. 139
III.3.1 Optimization of SALDI-MS, using non-covalent galactosamine moieties 140
III.3.2 Optimization of SALDI-MS, using covalent binding of galactosamine 141
III.3.3 Surface characterization of NH_2GAL *in-situ* boron doped CNWs surfaces 145
III.4 Detection of ricin B chain in real samples, using NH_2GAL-CNWS 147
III.4.1 Detection of ricin B chain in Coca-Cola® samples 147
III.4.2 Detection of ricin B chain in blood serum samples 148
III.5 Conclusions 150
III.6 References 153

© 2020 Tous droits réservés.

lilliad.univ-lille.fr

III.1. Introduction

We have already presented the MALDI and SALDI-MS procedures and the available literature related to the methods of detection of ricin-like proteins. In this chapter, we will present the challenges that we propose to overcome (both related to protein detection, in general, and/or to ricin-like proteins) and the methods and experiments we did perform in order to achieve the proposed goals.

Even though in Chapter II we did overcome some of the challenges (detection of a variety of small molecules using SALDI-MS methods, from buffered and real samples), we did only use one type of surface available at that moment (CNWS 2.0 K, 2.6 µm height). For further optimization of the parameters needed to be tuned for SALDI-MS's protein detection, we did characterize and describe various types of surface in order to better understand which parameters are more important to achieve our goals.

As we discussed in the first chapter, all the tedious steps described in MALDI-MS procedures are to be eliminated and the simplest solution would be to use SALDI-MS and to detect the direct intact protein, from the biological samples. Of course, some sample preparation will be needed, but in comparison with the steps needed for MALDI, this would be less complex.

Table III.1-1 presents some of the representative MALDI and SALDI-MS procedures used in the detection of proteins. The section "Material" refers to both inorganic or organic matrix used in the procedures (distinguishing between MALDI and SALDI) and the section "drawbacks" presents the challenges that are to overcome. The section "proteins" offers information about the protein detected, its molecular weight and if the protein was intact or fragmented.

The first thing to overcome in proteomics, in general, is the time consuming and the tedious sample preparation and manipulation before, during and after MALDI-MS. Indeed, usual step-by-step complex procedures including 2D-electrophoresis, crosslinking, enzymatic or nonenzymatic digestion, mass fingerprinting in known databases, with the reconstruction of protein sequences and analysis of the tertiary and quaternary structures are often required. These typical procedures are better described in Chapter I. Therefore, all the literature presented in **Table III.1-1,** that does not have the mention "intact" protein, is subjected to all or some of these tedious steps.

Another drawback comes from further modification of the MALDI-MS instrument (frequently modification of the ion sources) in order to have an IR ion source, because water

© 2020 Tous droits réservés.
lilliad.univ-lille.fr

can be used as matrix, as it absorbs IR wavelengths. Nevertheless, water offers a low sensitivity, and glycerol is still added. Also, even if most of the complex steps are not required, the intact protein is not detected as single charged ion.[1,2] One of the main reason is that IR ion sources induce an even more soft ionization of the proteins, so bigger the molecular weight and smaller the number of charges, lower the possibility of identifying the single charged ion.

Glycerol/graphite-like combined matrix improves the LDI comparing to glycerol itself, but the sensitivity is still poor and the ion source contamination and discharge effects may appear.[3] This method, where nanostructured powders are suspended in glycerol, is referred to as the "wet" method, but it brings the following drawbacks: "sweet spot" phenomena (which give raise to irreproducible MS spectra and limits in sensitivity), vacuum deterioration in the ion source, degradation of the instrumental device, reduced ionization efficiency.[4] Ion source contamination and discharge effects are also observed in "dry" graphite-like composed SALDI-MS, as the powders tend to fly and stick to the electrodes or other critical ion source components.[5]

There are several matrix-free method using inorganic surfaces of nanostructures like titania sol-gel films,[6] porous silicon, [7,8] porous alumina,[9] modified quantum dots (like CdSe)[10], AuNPs[11], that were used for detection of few proteins, overcoming therefore few of the MALDI-MS drawbacks (salt intolerance, "sweet spots", high costs, irreproducibility and low sensitivity). Anyway, most of them use the enzymatic or non-enzymatic digestion, making these methods time and reagent consuming, as described above.

There are only few exceptions among these methods that do not use any kind of protein digestion, and intact proteins are detected. Chen et al.[6] detected 8.5 pmol trypsinogen (24kDa), in 200 mM ammonium citrate solutions (as proton donor), using titania sol-gel film deposited on aluminium sheets. Nevertheless, the authors do not characterize the surface to try to explain why the detection was possible or to establish if other parameters could be optimized to increase the upper mass range or to increase sensitivity. Also, they do not describe any statistical validation parameters as RSDs of the measurements.

The most impressive inorganic material used as SALDI-MS platform are the HgTe nanoparticles. Chiang et al.[12] detected 5 pmol of Immunoglobulin G (150 kDa) as intact single charged ion, using 300 mM ammonium citrate (pH 5.0). They do not apply this method for biological samples and, surprisingly, there are no other reports of this material as a SALDI-MS platform. The main reason could be the high toxicity of HgTe nanoparticles. In order to better understand which are the most important parameters for the efficiency of the

© 2020 Tous droits réservés.
lilliad.univ-lille.fr

LDI process, we will compare this material (physical and morphological characteristics) as well as other SALDI-MS platforms, with our carbon nanowalls, which will be optimized and described in this chapter.

So, the most important challenge is to be able to optimize the carbon nanowalls surface and experimental conditions in order to be able to detect proteins, as only few important examples (the ones described above and presented in **Table III.1-1**) have been reported in literature.

Table III.1-1 MALDI-MS procedures for the detection of proteins larger than 8 kDa and the drawbacks to overcome.

Year an reference	Instrument	Material (in red mixture of inorganic matrix with/without organic matrix)	proteins	drawbacks
1995 [3]	UV MALDI-MS 337 nm	liquid matrix (glycerol and diethanolamine) + graphite	cytochrome C (12 kDa) and myoglobin (18 kDa)	enzymatic digestion, contamination of ion source, discharge effects, poor reproducibility and sensibility, as protein desorbs from dry state mainly.
2002 [1]	in-house built single-stage linear time-of-flight (LIN-TOF) IR MS of 3.5 m equivalent flight length (3 µm).	glycerol matrix	BSA (66 kDa)	prototype IR Mass Spectrometer inaccessible for the open market, only multiple charges detected, not single charged ion, use of glycerol, as matrix
2003 [7]	UV MALDI MS	**desorption/ionization on porous silicon (DIOS)**	adenovirus penton protein (72 kDa)	enzymatic digestion, time consuming, reconstruction of protein sequence
2004 [8]	UV MALDI Tof MS, delayed extraction period of 250 ns	**desorption/ionization on porous silicon (DIOS)**	BSA (66 kDa)	enzymatic digestion, time consuming, mass fingerprinting,
2004 [6]	UV MALDI Tof MS (337 nm)	**Titania sol-gel films, using diammonium citrate (200mM)/ citric acid (200mM)= 5:1.1 (v/v); pH 4.5)**	**intact** Trypsinogen (24 kDa)	this is the **upper mass range** ever detected.
2005 [13]	UV MALDI Tof/Tof MS, delayed extraction period of 400-700 ns	organic matrix CHCA (alpha-Cyano-4-hydroxycinnamic acid)	thioredoxin (12 kDa)	optimization of internal parameters of the MS spectrometer, nonenzymatic digestion, reconstruction of protein sequence, still time consuming
2007 [11]	MALDI-TOF MS (337 nm)	4-aminothiophenol-capped AuNPs, in 0.1% trifluoroacetic acid (TFA)	**intact** cytochrome C (12 kDa)	**limited upper mass range**, as usual in Au based materials

© 2020 Tous droits réservés.
lilliad.univ-lille.fr

2007 [9]	MALDI-TOF MS (337 nm)	**porous alumina**	BSA (66 kDa)	tryptic digest, time consuming, identification of peptide fragments in MS database
2009 [10]	337 nm	**Quantum dots: MUA modified CdSe**	lysozyme (14 kDa), myoglobin (18 kDa)	enzymatic digestion, time consuming, reconstruction of protein sequence, toxic
2010 [12]	MALDI-Tof MS, nitrogen laser (337 nm) delayed extraction period of 900 ns	**HgTe**	**intact IgG (150 kDa)**, proteina G and their complexes	toxic, no other references about this material used in SALDI-MS
2012 [14]			**intact** trypsin (23 kDa), α1-antitrypsin (54 kDa) and their complexes	
2013 [15]	UV MALDI-Tof MS, delayed extraction period of 500 ns	organic matrix CHCA (alpha-Cyano-4-hydroxycinnamic acid), SA (sinapinic acid), DHB (2,5-Dihydroxybenzoic acid),	**intact** Cytochrome C (12 kDa), **intact** IgG (150 kDa)	time consuming: recrystalization of matrix, protein purification through buffer exchange as MALDI is intolerant to salts, sweet spots
2018 [2]	Remote IR-MALDI MS	glycerol/water matrix	**intact** ubiquitin (8.6 kDa)	prototype IR Mass Spectrometer inaccessible for the open market, only multiple charges detected, not single charged ion, use of glycerol, as matrix

III.1.1. Detecting proteins with SALDI-MS

The LDI performance should be much higher than that of direct laser desorption (ablation) for a process to be categorized and considered suitable for SALDI-MS. A simple ablation would just fragment the protein, and as mentioned above, this is not our goal. LDI process requires improved energy-transfer efficiency. If the surface is not suitable for this process, the molecule deposited on the surface will not be able to form ions in the plume. A bigger molecule will absorb more energy. So bigger the molecule, the bigger the amount of energy required for the LDI. That is why, one of the greatest drawbacks of MALDI and SALDI-MS is an upper limit mass range.

The last and the most important goal of this chapter is to be able to detect ricin-like toxins in real samples (like soft drinks or blood serum). All the work and the optimizations steps described above should give rise to this final achievement if all the steps are treated accordingly. The real life application of our boron doped CNWS modified sensor is our final challenge and goal, due to the importance of ricin in criminal and bio-terroristic activities. It is to point out again that there is not SALDI-MS platform described in literature for ricin-like

© 2020 Tous droits réservés.
lilliad.univ-lille.fr

proteins. Our results are of great importance to the research world for all the challenges described in this introduction.

© 2020 Tous droits réservés.
lilliad.univ-lille.fr

III.2. Optimization of CNWS for SALDI-MS. Detection of cytochrome C and ricin B chain

Boron doped carbon nanowalls were used in chapter II to detect small biomolecules. We are not able to work with the entire ricin protein, as the laboratory doesn't meet the requirements of working with this toxic analyte. Carbon nanowalls were chosen for some of the features that are suitable for SALDI-MS: nanostructured morphology, high conductivity, high mechanical robustness, tunable band gap, tunable height and doping level, hydrophobicity, high absorbance of UV light, low photoluminescence.

Boron doping can tune different features as the band gap, electrical conductivity and surface morphology. Tuning these features, can influence the LDI-process for detection of bigger molecules, as proteins. As in Chapter II we did only study one doping level and one height of carbon nanowalls (2.0 K, 2.6 µm), in this chapter we will characterize different physical and chemical properties of the different tuned parameters during the synthesis and the post-synthesis of carbon nanowalls and correlate the changes in the properties with SALDI-MS signals for proteins. Initially cytochrome C will be used as model protein, as it has a lower molecular weight and it has been used previously in SALDI-MS (see **Table III.2-10**). After some parameters will have been optimized (doping level, height, of nanowalls, salt concentration, salt type etc) we will continue with ricin B chain, starting from similar parameters.

III.2.1. Surface characterization of boron doped CNWs

As explained in the Introduction, we want to study all the important morphological and physical characteristics of the boron doped carbon nanowalls in order to have a systematic picture of how specific parameter can influence the LDI process. Indeed, surface morphology plays an important role in the laser desorption/ionization processes. A paper from Vertes's group presents an interesting overview concerning the laser-nanostructures interactions. This review highlighted that interactions between UV laser radiation and nanostructured materials, with dimensions below 500 nm, result in enhanced desorption and ionization of organic compounds.[16] In fact, it was noticed that when critical dimensions of the nanostructures are below characteristic lengths *i.e.* phonon mean free path, thermal dissipation length, optical absorption length, modes of transport of the corresponding materials e.g., ballistic *vs* diffusive, energy confinement (phonon scattering), plasmon resonances, and local field are

© 2020 Tous droits réservés.
lilliad.univ-lille.fr

enhanced.[16] Thus, by controlling the nanostructures' dimension/physical properties, we can expect to better control the LDI performances.

III.2.1.1. Morphological characterization of CNWs

Morphology of SALDI-MS platforms influence the LDI-MS processes, as nanostructuration increases surface-area-to-volume ratio, enlarging the direct contact of the analyte with the surface/particles, and favoring the energy transfer, thus the desorption and ionization of the molecules. Small sized nanoparticles (NPs) lower the laser's threshold and increases desorption due to the increase of the number of molecules per mass of NPs. However, if the NPs are too small, the aggregation occurs and the reproducibility is poor. Similar morphological characteristics influence the LDI-MS efficiencies when it comes to CNWs SALDI-MS interfaces.[17] The verticality of the stacked graphene nanosheets, have a great impact on the physical properties, especially mechanical stability and the effect of a thermal sink.[18]

We did study morphological characteristics, after tuning doping levels and growth times, during CNWs synthesis. Morphological characterization was realized using SEM top views/cross sections of the different doped interfaces and different growing periods and AFM for the same surfaces. **Figure III.2-1** presents the top views SEM monographs of CNWs synthesized using different doping levels, at similar height (cca. 2.4 µm). Nanostructuration can only be observed in CNWs 1.2, 5.0 and 10.0 K, as maze-like structures change to a heterogeneous distribution of nearly straight walls. The pores become smaller, for doping levels until the 5.0 K. The pores size increases a little bit for the CNWs 10.0 K.

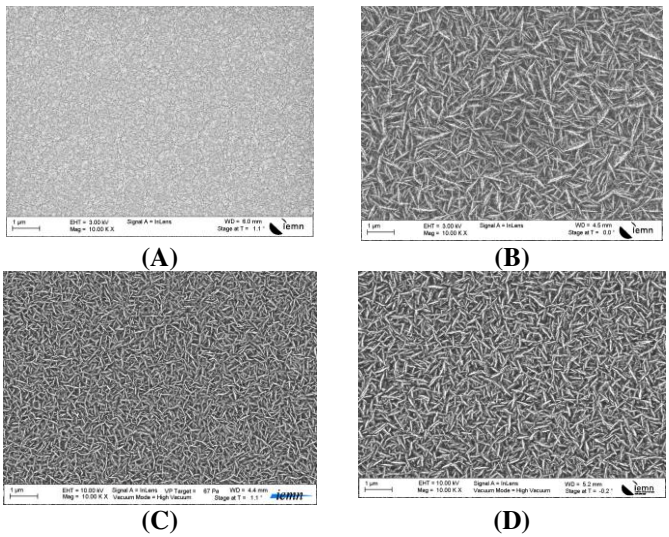

Figure III.2-1 SEM top-view monographs of CNWs with different doping levels, at similar height (cca 2.4 µm): **(A)** 0.0 K, **(B)** 1.2 K, **(C)** 5.0 K and **(D)** 10.0 K CNWs.

© 2020 Tous droits réservés.
lilliad.univ-lille.fr

The same tendency was observed by our collaborators in their work in The Journal of Physical Chemistry C, Sobaszek et al.[19], for carbon nanowalls, with different doping levels (1.2, 2.0 and 5.0 K). The amount of small pores/voids between nanowalls increases and contributes to the increasing of the specific surface area. Also, the sizes of the pores are important because they can trap the analyte inside, if they are too big, or they will not enhance the energy transfer, if the pores are too small, by correlation to the surface-area-to-volume ratio. Also, more voids mean more heat confinement.

They also described by using XPS analysis that elemental boron atoms are mainly located at the surface of the carbon nanowalls (**Figure III.2-2C**). They used the CNW surfaces as electrochemical electrodes and they found that boron doped CNWs 5.0 K is the best for transferring the charging current, because of the increasing of surface roughness and the area available for electrolyte ions penetration alongside with the improved sample conductivity.

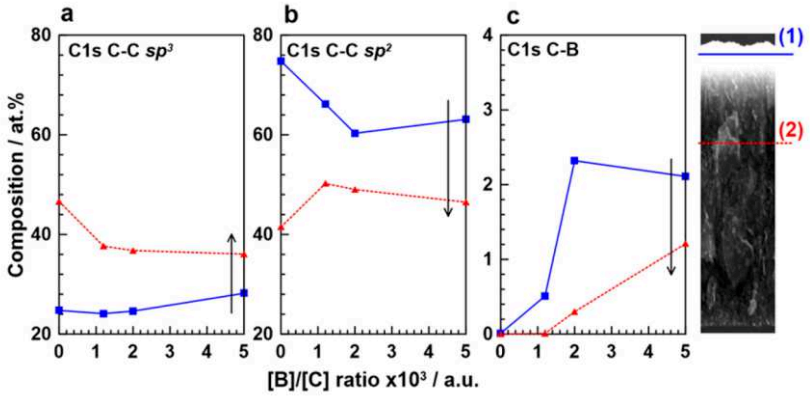

Figure III.2-2 Influence of B dopant concentration and the depth of sampling on the chemistry of B-CNW electrodes. High-resolution XPS analysis was carried out in the C 1s energy range (1) before and (2) after Ar+ ion sputtering for 240 s (3000 V): (a) C−C sp3 peak at 285.1 eV, (b) C−C sp2 peak at 284.5 eV, and (c) C−B peak at 283.1 eV. Reproduced from Sobaszek et al.[19]

The same previous studies[19] showed that increasing the doping level, decreases the height of the vertical standing graphene nanosheets. The strong morphological influence of BH_x is mainly attributed to the renucleation and twinning surface processes, as illustrated in **Figure III.2-3**. The renucleation processes that shorten the walls are a positive effect, resulting in the higher specific surface area. They also present a growing mechanism of the nanowalls. The mechanism is presented in 4 steps: (I) surface-bonded hydrogen abstraction; (II) nanowall edge bonding of BH and HCN toward the nanowall formation process; (III) nitrogen abstraction *via* CH_3 bonding toward the diamond formation mechanism; (IV) twin formation nucleation of the next layer of nanowall.

© 2020 Tous droits réservés.
lilliad.univ-lille.fr

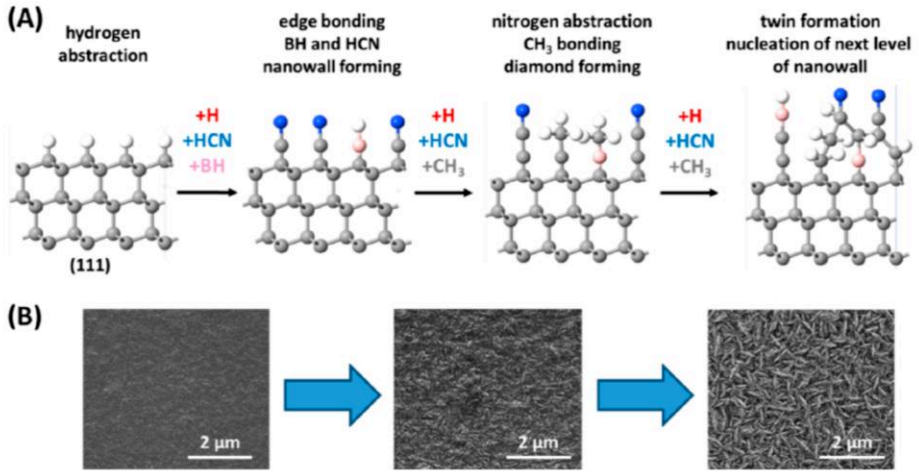

Figure III.2-3 Scheme of **(A)** the most favorable growth mechanism of boron-doped carbon nanowalls in the microwave plasma and **(B)** SEM microimages revealing the morphology of the subsequential steps of nanowall growth. Reproduced from Sobaszek et al.[20]

Agnoli et al.[21] described the possible defects induced by boron doping of graphene-materials: substitutional boron, to boronic and borinic esters, and organo-boranes. We have studied these species by XPS (**Figure III.2-4**), and we did found out the following energies: 187.8 (organo-borane), 189.2 (substitutional), 190.38 (borinic) and 191.8 eV (boronic).

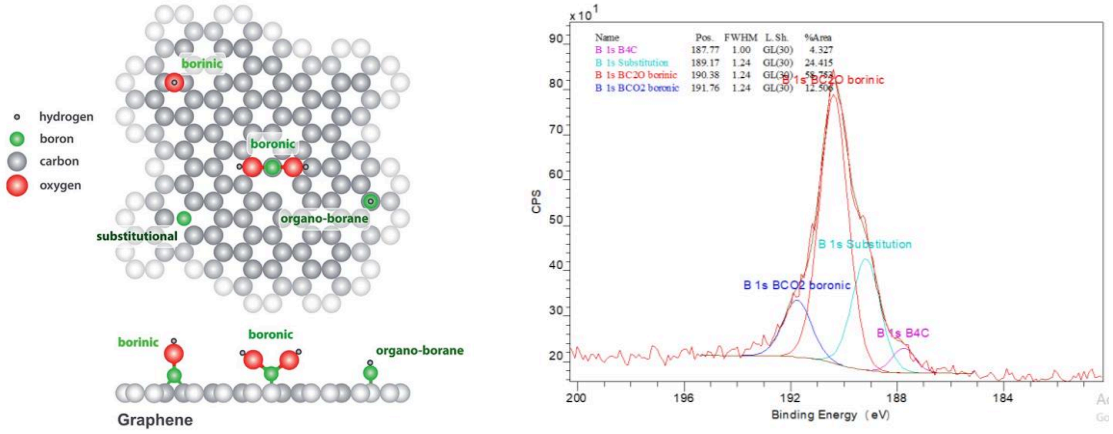

(A) **(B)**

Figure III.2-4 **(A)** Ball model of B-G showing some of the most common boron induced defects. **(B)** High resolution of XPS spectra of CNWs 5.0 K (8 hours) in the B1s energy range (190.28 eV)

In our case, for example, after 8 hours of growth, by increasing the doping level from 5.0 K to 10.0 K, the length decreases from 4.65 µm to 2.9 µm. In general, the walls become less dense for the same doping level, by varying the growth time, creating bigger pores (**Figure III.2-5**). The wall density difference is more important as the doping level is higher. However, for 2.0 K CNWs, it was observed that the density of the walls, as well as the length, is comparable no matter the growth period. Thus, the growth time, will also influence the quality of the LDI-MS process, as it influences the size of the pores.

© 2020 Tous droits réservés.
lilliad.univ-lille.fr

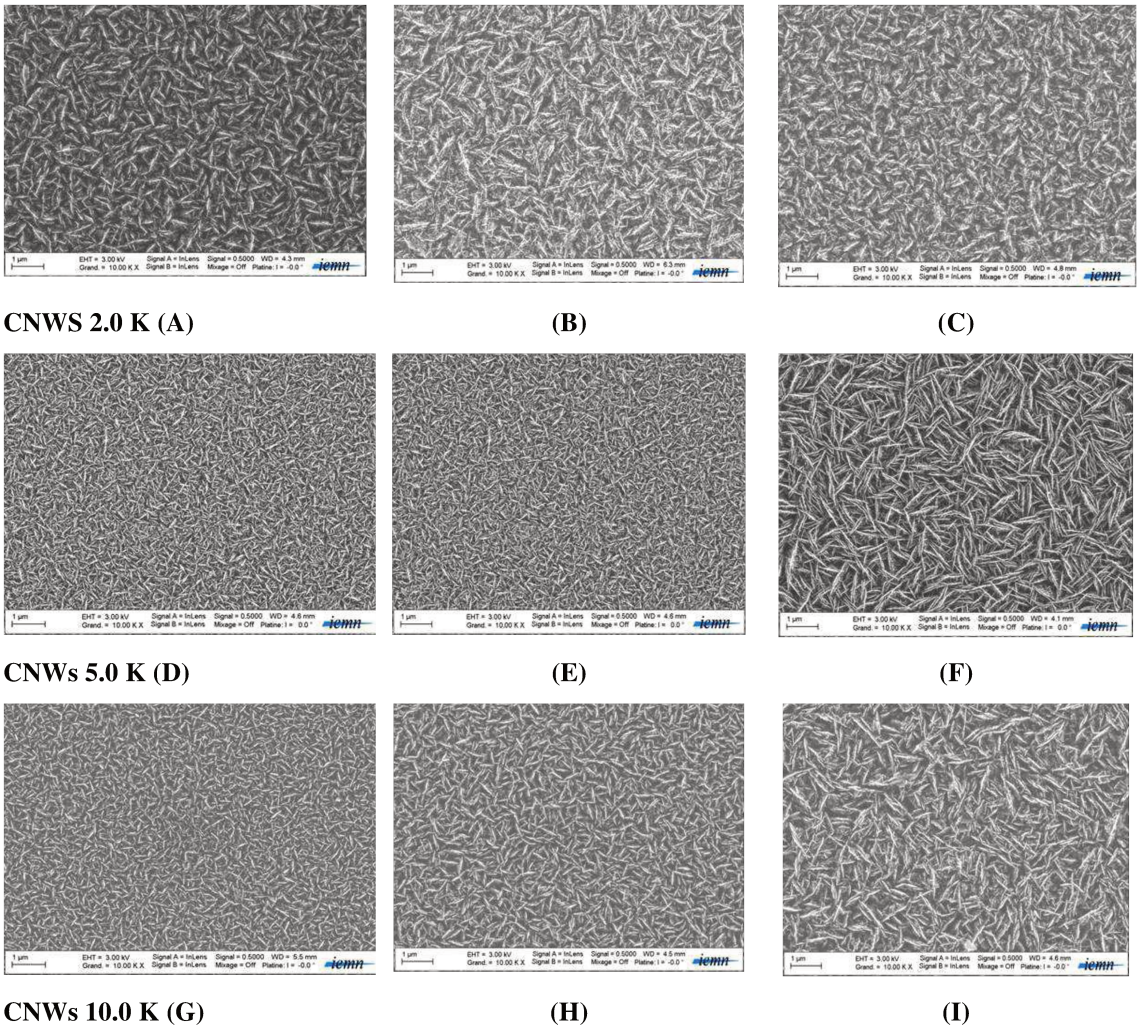

CNWS 2.0 K (A) **(B)** **(C)**

CNWs 5.0 K (D) **(E)** **(F)**

CNWs 10.0 K (G) **(H)** **(I)**

Figure III.2-5 SEM top view monographs of different boron doping levels at different growing periods: 2.0 K CNWs at (A) 2h (B) 4h and (C) 8h, 5.0 K CNWs at (D) 2h (E) 4h and (F) 8 h, 10.0 K CNWs at (G) 2 h (H) 4h and (I) 8h.

Figure III.2-6 presents the AFM monographs of the CNWs synthesized at different doping levels: 0.0, 1.2, 2.0, 5.0 and 10.0K, that also have similar height (cca. 2.4 µm). Using the AFM images, RMS roughness values were calculated using WSxM software. The roughness increases until 2.0 K and decreases after this doping level. Other RMS values are presented in **Table III.2-2**. More visual representations of the RMS roughness values from the table are presented in **Figure III.2-7**. RMS values were plotted as a function of doping levels, for similar heights and there is no straight linear correlation, but the RMS values increases until 2.0 K and decreases after this doping level. Instead, direct correlation was observed for RMS values as a function of growth time, for the same doping level (5.0 K). This is in good accordance with SEM observation, that increasing the growth time, creates bigger pores on the carbon nanowalls.

© 2020 Tous droits réservés.
lilliad.univ-lille.fr

The kinetics of growth of the carbon nanowalls is still unknown, but clearly the growing mechanism, especially the twining of the next level of carbon nanowalls, influences the density of the pores. Again, somehow the comparison can be made at the same heights, as the twinning depends on the growth period, thus height of nanowalls. As an example, at the same height of 1.4 µm (but different growth periods) and different doping levels (5.0 and 10.0 K), the RMS (root mean square roughness) changes from 29 nm to 47 nm respectively, and the SEM monographs (**Figure III.2-1B and D**) confirm the AFM results.

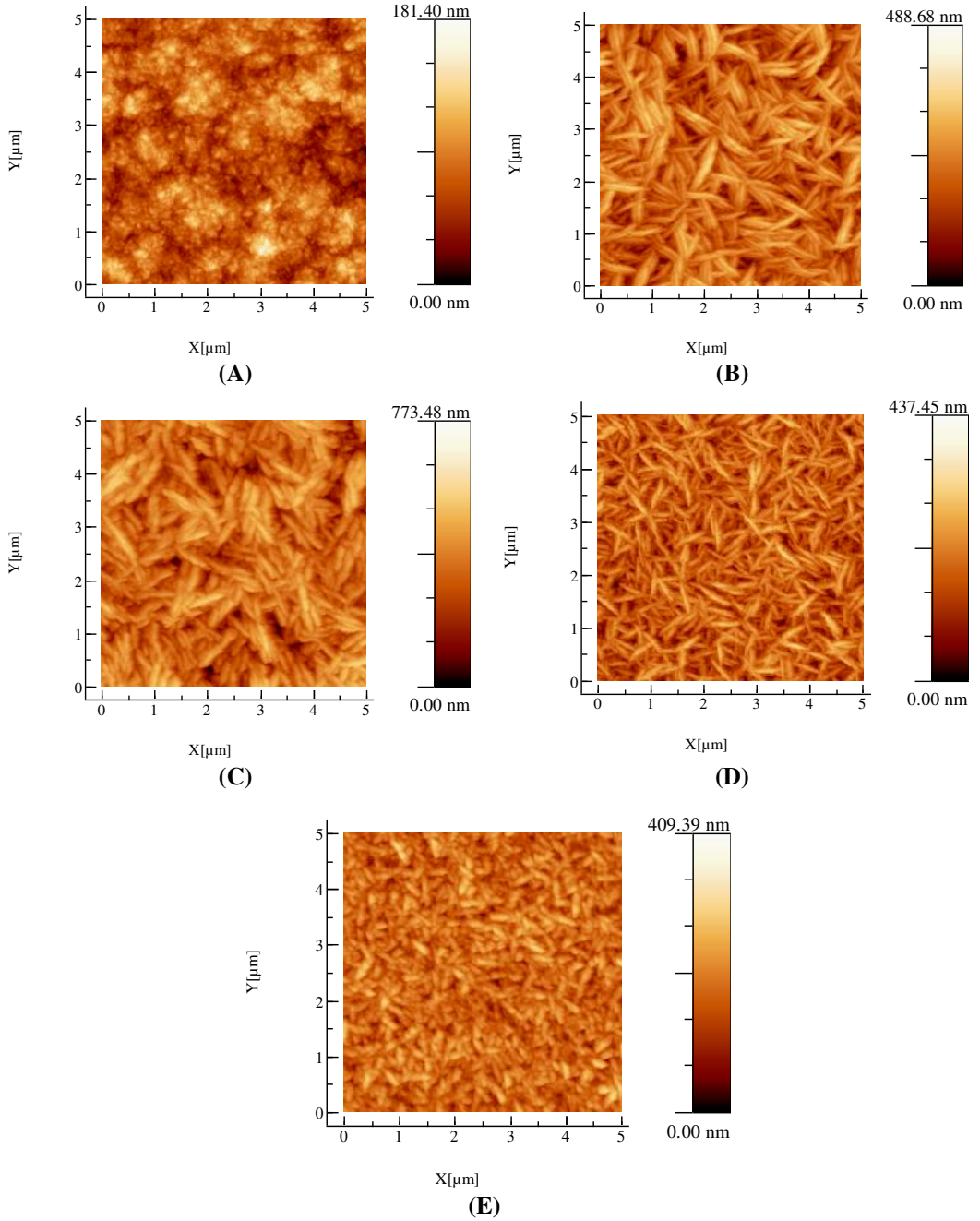

Figure III.2-6 AFM monographs of CNWs at different doping levels: **(A)** 0.0K **(B)** 1.2 K **(C)** 2.0 K **(D)** 5.0 K and **(E)** 10.0 K, similar height (cca. 2.4 µm)**.**

© 2020 Tous droits réservés.
lilliad.univ-lille.fr

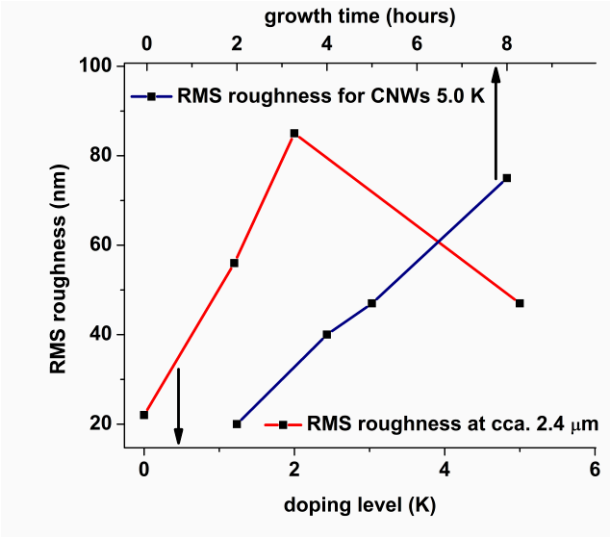

Figure III.2-7 RMS roughness as a function of the doping level at the similar height of the nanowalls (cca. 2.4 μm). Extracted from AFM data from **Figure III.2-6**.

III.2.1.2. Optical properties of carbon nanowalls

Absorbance of UV light beam at 355 nm is very important for SALDI-MS of our experiments, because this wavelength is used to desorb and ionize the sample in the ion source. Reflectivity spectra of CNWs 5.0 K and 10.0 K, at different heights, are presented in **Figure III.2-8A and B.** It can be observed that in all cases the reflectivity is below 10%, meaning that absorbance is high (in the 200-800 nm range). The main peak is observed around 315 nm, corresponding to the energy of 3.93 eV. We can observe that increasing different heights on the same doping level, the reflectivity decreases. As between absorbance and reflectivity there is an inverse proportionality, the reflectivity should decrease with increasing height in films. Boron doped carbon nanowalls were studied using XPS, by our collaborators. At the surface, the sp^2 carbon is predominant, as in depth, the sp^3 carbon is (**Figure III.2-2**).[19] It is expected that absorbance is similar to graphitic-like/graphene structures, because of the sp^2 structure. It is well known that graphene oxide absorbs energy around 230 nm (5.4 eV, π-π* transitions due to C=C conjugation system) and 300 nm (4.1 eV, n-π* transitions of the carbonyl groups, C=O). The reduced graphene oxide absorbs in the 250-275 (~5-4.5 eV) nm range, due to partial restoration of the sp^2 basal plane from the graphite-like structure, structural ordering and the increased density of electrons.[22] This energy is similar to the plasmon energy of graphene, where the real part of the dielectric function becomes negative.[23] Boron doping of graphene can red shift the necessary energy to produce the plasmonic effects,[24] and this red shift is observed even on our boron doped CNWs, towards 315 nm.

© 2020 Tous droits réservés.
lilliad.univ-lille.fr

Photoluminescence remains unchanged with increasing the height and the boron doping level during the synthesis of carbon nanowalls. The peaks that appear in photoluminescence (**Figure III.2-8C**) are the same as described in Chapter II, with the maximum emission around 700 nm, due mainly to defects band transition from oxygen atoms interfering with the electron transitions between π and π* bands.[25] As discussed in our previous paper [17] and in chapter II, the LDI mechanism is still unknown, but there are 2 main possible ways of transferring the energy from the SALDI interface to the analyte: thermal and non-thermal driven processes. As the photoluminescence of carbon nanowalls is small and mainly originated from the oxygen defects at the surface, the involving of the thermal mechanism is more suitable in this case, with the involving of phonons and non-radiative recombination mechanism.

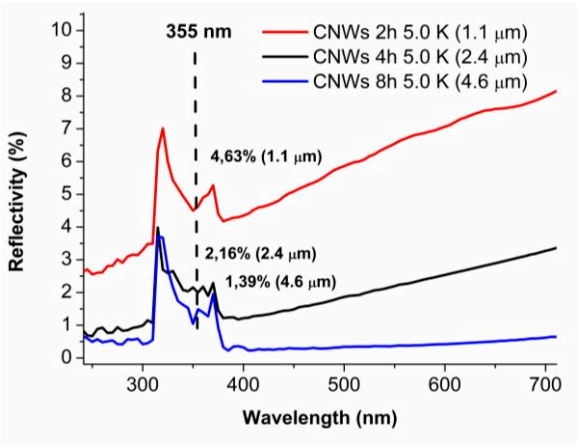

(A)

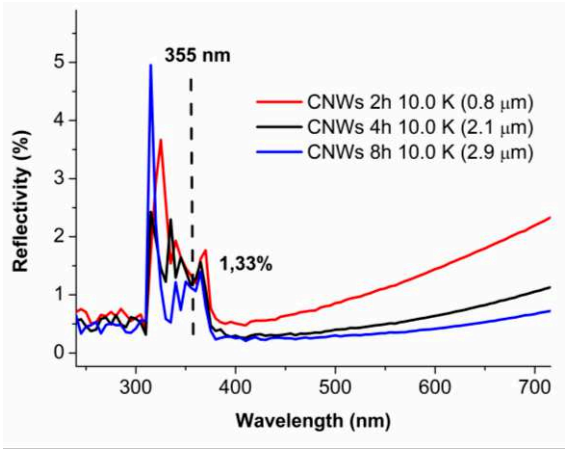

(B)

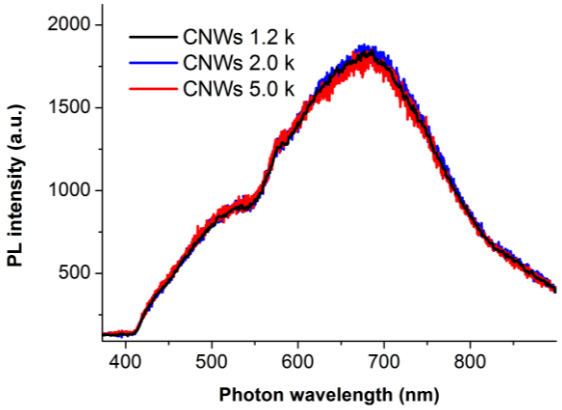

(C)

Figure III.2-8 (A) Photoluminescence spectra of different doping levels of boron, and different growth time of CNWs. Reflectivity spectra of the CNWs **(B)** 5.0 K and **(C)** 10.0 K interfaces.

© 2020 Tous droits réservés.
lilliad.univ-lille.fr

III.2.1.3. Other physical characteristics of CNWS important in SALDI-MS

Raman characterization (**Figure III.2-9**) shows the typical peaks around 1360 cm^{-1} (defects in the conjugated π system) and 1580 cm^{-1} (in plane vibrations of the sp^2 carbon atom constraints) corresponding to the D and G bands respectively. At the same growth time we can observe that lower doping levels (2.0 K and 5.0 K) also create some doping specific disorder shown in the Raman spectra as the D' band (at 1615 cm^{-1}).[26] Even though we initially believed that higher doping levels were expected to present higher D' bands,[19] the exact opposite trend is observed. It is mentioned in literature the D' band can be correlated to defects type, more than with concentration of defects, and that at high defect concentration, G and D' tend to merge together, so our findings are in good accordance with other's findings.[27] **Table III.2-1** presents the peak positions of D, G and D' bands, determined by fitting Lorenzian distribution, their correspondent intensities, as well as different important ratios. The I_D/I_G ratios, that describe the disorder in the graphitic structure, increase with increasing the doping level, meaning that the general disorder is also increasing, as dopants are inserted in the π conjugated system. The I_{2D}/I_G ratios are similar for all the samples and around 0.25, showing that many layers of graphene are present in the nanowalls. Second order Raman vibrations modes (**Figure III.2-9B**), as described before,[17] are encountered at 2700 and 2930 cm^{-1}. The shift of the G band occurs with increasing the doping level, meaning that strains are applied on the π conjugated systems, through hole doping (p-type semiconductor).[28] Low I_D/I_D' ratios in graphene are correlated to boundary-like defects in graphite.[27]

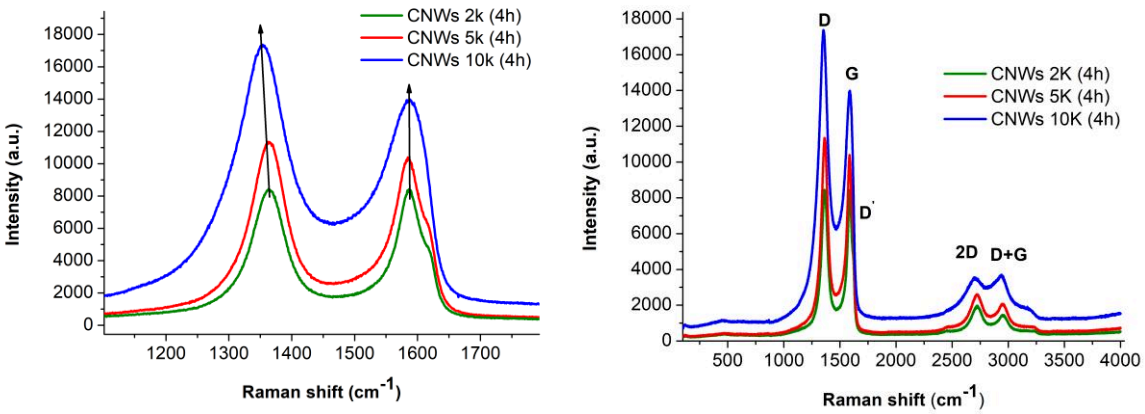

(A) **(B)**

Figure III.2-9. Raman spectra of different doping CNWs surfaces: 2.0, 5.0 and 10.0 K, after 4 hours of growth, **(A)** in the G and D bands region and **(B)** the extended region.

© 2020 Tous droits réservés.
lilliad.univ-lille.fr

Thèse de Ioana Silvia Hosu, Université de Lille, 2020

Table III.2-1 Values of peak frequencies (ν), relative intensities (I_D/I_G and I_{2D}/I_G) of D, G and D' band in Raman spectra of CNWs, at different doping levels and the same growing time. The peaks were fitted with Lorentzian distributions. * measured by SEM.

Samples (4h deposition time)	height of the walls (μm)*	ν_D (cm^{-1})	ν_G (cm^{-1})	$\nu_{D'}$(cm^{-1})	$I_{D/G}$	$I_{D/D'}$	$I_{2D/G}$
2.0 K CNWs	2.1	1364	1588	1615	1.0	1.70	0.23
5.0 K CNWs	1.7	1363	1584	1613	1.1	1.73	0.25
10.0 K CNWs	1.6	1351	1587	-	1.24	-	0.25

Other physical properties (length, height, RMS roughness and resistivity) are presented in **Table III.2-2**, as they play important roles in the SALDI-MS process. **Figure III.2-10** depicts the wetting properties and the roughness as a function of growth periods**.** For the CNWs 10.0 K surfaces the growth deposition periods did not affect greatly the water contact angles (WCA~127°), but a small increase was observed (2°). For the CNWs 5.0 K, the increase of average contact angle was of 10°. Hydrophobicity is known to increase SALDI-MS performances.[29] The hydrophobicity of CNWs comes from low C-O content (see XPS, from Chapter II) and the nonpolar hexagonal sp^2 carbon structures of the graphene vertically aligned nanosheets. As wettabillity usually depends on morphology, surface chemistry, crystallinity, surface roughness and other parameters. In our case, boron doping, roughness and morphology play the most important roles in the wettability properties. Non-doped carbon nanowalls have a water contact angle of 106±4° and lower nanostructuration (see SEM monographs). Increasing the boron doping level and surface roughness, the water contact angle also increases, in most cases until around ≈ 127°. The correlation between the growth time and wettabillity, is that by increasing the growth time, the roughness also increases together with the WCA (**Figure III.2-10**), so wettabillity decreases, creating more hydrophobic surfaces. Increasing roughness may increase the water contact angle, as literature describes.[30] Hydrophobicity is important in SALDI-MS, because it confines the analyte surface into small area, increasing sensitivity[31] and influences the interaction between the surface and the analyte.

© 2020 Tous droits réservés.

lilliad.univ-lille.fr

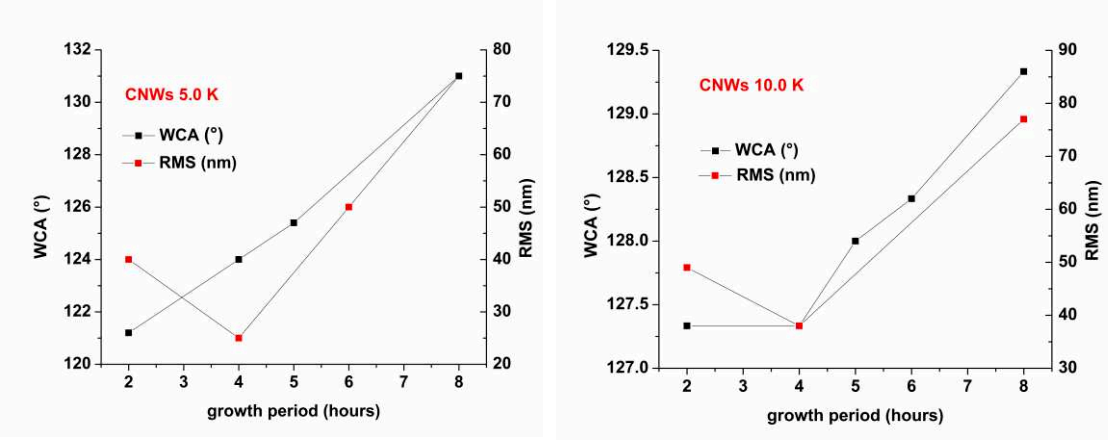

(A) **(B)**

Figure III.2-10. Correlation between WCA and RMS values as a function of growth time, for CNWS (**A**) 5.0 K and (**B**) 10.0 K.

Table III.2-2 Physical characteristics of CNWs with different doping levels at different growth time.

doping level /growth period (h)	Physical properties	2h	4h	**5h**	6h	8h
2.0 k	length nanowalls (µm)	-	550±37	**668±83**	573±35	-
	height nanowalls (µm)	-	2.1	**2.35**	3.05	4.7
	RMS roughness*(nm)	-	-	**85**	-	-
5.0 k	length nanowalls (µm)	540	460	**616**	728	700
	height nanowalls (µm)	1.1	1.45	**2.4**	2.6	4.65
	RMS roughness(nm)	26	40	**47**	-	75
	WCA (°)	120±5	121±3	**125±1**	126±1	131±3
10.0 k	length nanowalls (µm)	350	480	**583±56**	545±87	580
	height nanowalls (µm)	0.8	1.4	2.1	2.25	2.9
	RMS roughness*(nm)	49	38	-	-	77
	WCA (°)	127±2	127±3	**128±2**	128±2	129±2

*RMS= Root mean square of the roughness = $\sqrt{1/n}$ ($x_1^2+x_2^2+\ldots+x_n^2$), where x= h-h_{medium} and h represents the height of the pore.

In terms of electrical properties, boron doped CNWs are described as p-type semiconducting or semi-metallic materials[19] with high electrical conductivity. Resistivities are described in literature by our collaborators to be between 4.7-42.0*10^{-7} ohm/cm for samples boron doped CNWs with the height of ~ 3 µm at different boron doping levels (1.2, 2.0 and 5.0 K), using a Four-Point Probe.[19] In fact, vertically aligned graphene nanosheets are known to have similar electrical conductivities with horizontal graphene sheets, as the sheet-to-sheet resistance is avoided, due to the conductive substrate used for the nanowalls growth, and the high in-plane conductivity of graphene can be effectively used.[18] So, such low resistivities are usual for graphite-like materials. The same collaborators (Sobaszek et al.)

© 2020 Tous droits réservés.
lilliad.univ-lille.fr

described in the same study[19] that increasing the doping level on similar carbon nanowalls, decreases the resistivity, because of the increasing electrical conductivity due to hole carriers.

III.2.1.4. Comparison of physical characteristics of CNWs with literature

Table III.2-3 presents some other characteristics that are important in the LDI-MS processes. This table takes in consideration some of the metallic nanoparticles used in the detection of Cytochrome C. The experimental results obtained for the application towards detection of cytochrome C will be presented in the following sub-section, where there are summarized in **Table III.2-10.** Herein it is described only how these properties may influence the process, as a characterization method of the materials.

Taking in consideration the importance of the thermal mechanism, one of the important features of detecting higher molecular weight molecules is decreasing the heat capacity, thermal conductivity and melting point.[32] This way higher induced-laser temperatures are generated at the surface, and the energy transfer between the SALDI interface and analyte is much more efficient. The thermal conductivity of carbon nanowalls is described in literature[33] to be between 20-300 W/m*K. In comparison with graphene (>3000 W/m*K), CNTs (200 W/m*K) and the elemental thermal conductivities of HgTe (the best SALDI-MS platform described until this point for higher proteins with Hg 8.34 W/m*K and Te 2.35 W/m*K), we could see that our SALDI-MS platform stands between or near the lowest thermal conductivity values. These thermal conductivities depend on the height of the walls (so the growth period), doping level (as the band gap becomes tunable) and surface roughness (as voids disrupt thermal conductivity). The height of the nanowalls increases the thermal conductivity, by increasing the graphene nanosheets surface in vertical dimension, thus it may decrease the LDI-MS efficiency. This is one of the reason why tuning the height of the nanowalls is important. Usually, p-doping in carbon based materials decreases the thermal conductivity,[34] especially for carbon nanowalls, due to the transition from p-semiconducting characteristics to semi-metallic/metallic properties. Once again, the decrease of thermal conductivity favors the LDI-MS processes. So, it is normal that AuNPs (gold nanoparticles) can mostly detect smaller molecules, as thermal conductivity is 317 W/m*K, by comparison with the thermal conductivities of the material used for the highest mass range ever detected in SALDI-MS (HgTe) (**Table III.2-3**). In the case of AuNPs, heat cannot be contained in a small specific area and the energy transfer is less efficient.

© 2020 Tous droits réservés.
lilliad.univ-lille.fr

The melting point of carbon nanowalls should be probably close similar as graphene based materials (predicted graphene's melting point is between 4000-6000 K[35] and CNT's > 1300K), so very high values, that usually do not favor LDI-MS processes. But the real value of the melting point of CNWS is not described in literature. Still, metal nanoparticles that have a high melting point (like Au NPs with 1337 K), tend to limit the LDI-MS process. Low melting points, apparently, enhance the LDI-MS process through phase transition, that favors the ionization.[36] But, low melting points could create more easily clusters in the MS spectrum. Usually melting points are correlated with changes in thermal conductivities, and voids disrupt thermal conductivities, thus also influence melting points.

Molar heat capacity is another important characteristic for the LDI-MS process. Materials that need less energy for increasing the temperature of the material by one unit, are more efficient. Except Fe_3O_4 nanoparticles, that have molar heat capacity almost 6 times higher than the other nanoparticles, the average values is around 25 J/moles*K. By comparison with CNWs, the other values are higher, but the expression of the energy used for increasing the temperature with one Kelvin is presented per volume, thus making it difficult to compare it with number of moles (as done for the metal nanoparticles).

Electrical resistivity is also compared in **Table III.2-3** and it can be observed that gold having though the lowest value. Due to highest thermal conductivity (as usually high electrical conductivity, means high thermal conductivity) the LDI-MS efficiency from gold is not suitable for protein detection. Similar values are presented for carbon nanowalls, but as other desirable physical characteristics are in the good range, makes this material suitable for protein detection.

Table III.2-3 Physical characteristics of metal nanoparticles from **Table III.2-10** and our carbon nanowalls.

Physical characteristics	Au	TiO_2	Se	CdTe	Fe_3O_4	Pt	HgTe	CNWs	Desired tendance
thermal conductivity (W/m*K)	317[a)]	0.61	0.02-0.0052	0.075	0.6-0.8	71.6	8.34 and 2.35	20-300	low
melting point (K)	1337	1843	490	1092	1538-1597	2045	234 and 723	>973	low
molar heat capacity (J/ moles*K)	24.60	55.18	25.27	25.68	150.79	25.92	26.68	0.4-1.63 [b)]	low
electrical resistivity (Ω*cm)	227 $*10^{-8}$	0.08	0.106*10^{-3}	10-200	-	-	1.5 $*10^{-3}$	0.47-4.2 $*10^{-6}$	low
Maximum mass range detected (kDa)	1.3	12	12	12	25	25	150	64	high

a) The lowest values are highlighted in green and the highest values are highlighted in red.

b) Unit of measure is (J/K*cm^3) for the CNW surface.

© 2020 Tous droits réservés.
lilliad.univ-lille.fr

III.2.1.5. Surface characterization of *ex-situ* boron doped CNWs

We have observed in the previous headings that even if we can inject different flows of boron containing gas during CNWs synthesis and increase the growth time, we cannot control very well the height and morphology of the nanowalls, as different boron doping changes the growth kinetics. *In-situ* doping of boron is described in literature to have a crucial role on the growth kinetics and on the morphologies of CNWs.[19] For *ex-situ* boron doping, if we use a process as boron ionic implantation, the height of the CNWs is the same, and the doping can be tuned easier using different doses of dopant (up to 10^{21} boron atoms/cm^2). Implantation involves accelerating dopant ions towards a solid target (in our case the undoped CNWs), that will retain and integrate the ions in its structure, but the used energy can disrupt the crystalline structure of the target. Damage recovery is done using thermal annealing that will help rearranging the crystalline structure.

Ex-situ boron (boron ionic implantation) doping was performed on undoped CNWs growth (0.0 K) using the same growth period (4 hours). Indeed, we can easily see on (**Figure III.2-11A**) that 0.0 K CNWs doesn't have very well defined nanowalls. However, depending of the doping level, the morphology changed in the case of the highest doping, with platelets like morphology. Nanostructuration is created due to high energies used during the implantation process, which etches the surface of the graphene like structures.

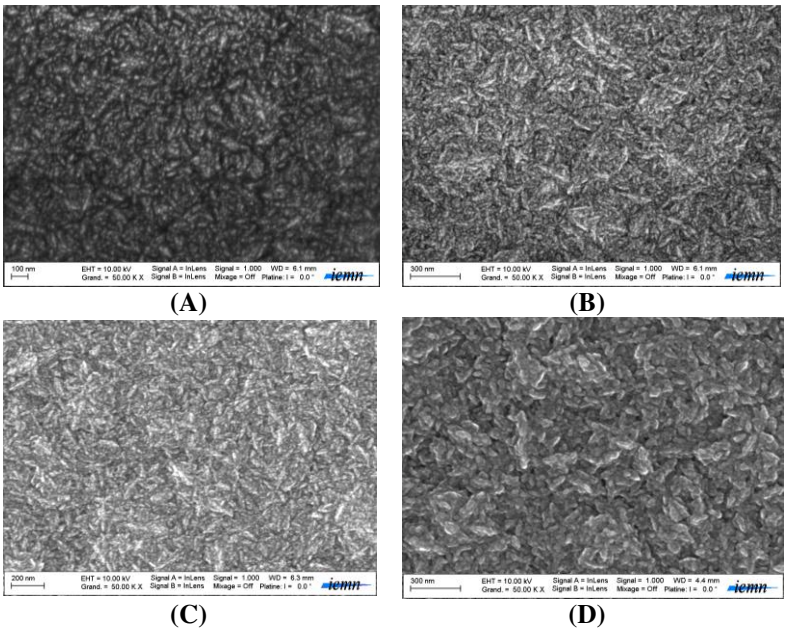

Figure III.2-11 SEM monographs of 0.0 K CNWs top view of different ion fluencies (per cm^2) during boron ion implantation: **(A)** 10^0, **(B)** 10^{15}, **(C)** 10^{18} **(D)** 10^{21}.

The Raman spectra are presented in **Figure III.2-12**. The D and the G band are present around 1339 and 1571 cm^{-1}, respectively. The red shift occurs in comparison with all *in-situ* boron doping levels, due to other possible strains in the system. No specific D' band is

© 2020 Tous droits réservés.
lilliad.univ-lille.fr

observed for the boron doping, as for *in-situ* lower doping levels of CNWs. The merging of the G and the D' can be observed when the doping is higher. The nanocrystalline diamond peak can be observed at 1150 cm^{-1}. Second order Raman vibrations modes are encountered at 2690 and 2938 cm^{-1}. Both $I_{D/G}$ and $I_{2D/G}$ have values around 0.95 and 0.33 respectively, for lower *ex-situ* doping fluencies (10^{15} and 10^{18} boron atoms/cm^2). For 10^{21} boron atoms/cm^2 implanted surfaces the $I_{D/G}$ is 0.64. This could mean that the highest *in-situ* doping level increases the disorder in the graphene layers. The number of stacked graphene layer seems to be similar in *ex-situ* and *in-situ* doping of CNWs, as well as in not doped ones, as $I_{2D/G}$ ratios are similar (0.25-0.33).

The position of D and G peaks as well as the $I_{D/G}$ ratios, are in correlation with the SEM images presented above. It could show that the graphitic/grapheme structure is being destroyed for higher fluencies of boron atoms (10^{21}). It is known that using higher doses in ionic implantation may destroy crystallization and the amount of crystallographic damage can be enough to completely amorphize. A large amount of the projectile kinetic energy is transferred to the atoms of the target displacing them from the lattice sites.[37] Therefore, the graphitic/graphene structures may have been destroyed in the case of 10^{21} boron atoms/cm^2, during the ion implantation.

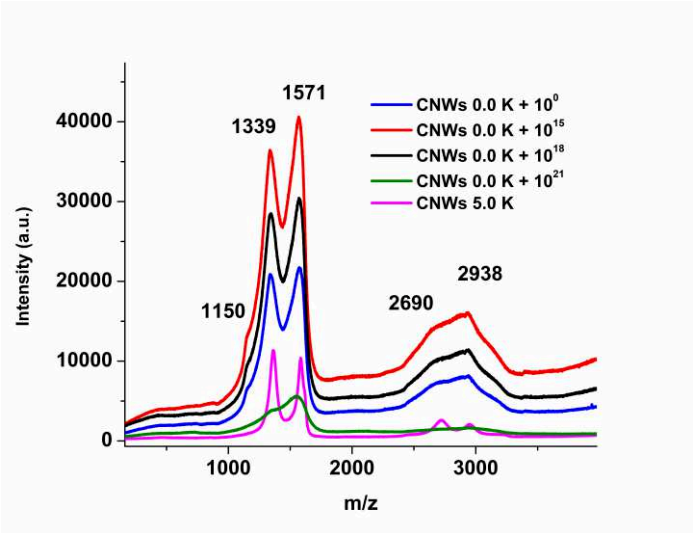

Figure III.2-12 Raman spectra of different *ex-situ* boron implanted surfaces.

Other physical characteristics of the *ex-situ* boron doped CWNs are presented in **Table III.2-4**. The resistivity of the highest doped CNWs has also the highest value. This trend was also observed for the *in-situ* doping level, and it is the opposite trend that we expected, because increasing the doping level, will increase the hole carries, and thus the electrical conductivity, with the electrical resistivity expected to decrease.

© 2020 Tous droits réservés.
lilliad.univ-lille.fr

The water contact angle remains between cca. 90 and 110°, thus allowing the drop of the analyte to confine in a small are. For the highest dose in ion implantation, the WCA seems to be lower, as oxidation of the nanostructures may have occurred. Also, similar lengths and heights are observed, with similar RMS values. Due to highest doping level, but other similar characteristics and better nanostructuration, we do expect that the CNWs 10^{21} to be a better SALDI-MS platform than the other *ex-situ* doped surfaces. Nevertheless, when we did measure XPS, the boron binding energy was not observed (**Figure III.2-13**), as the doping may be lower than the threshold detection of XPS.

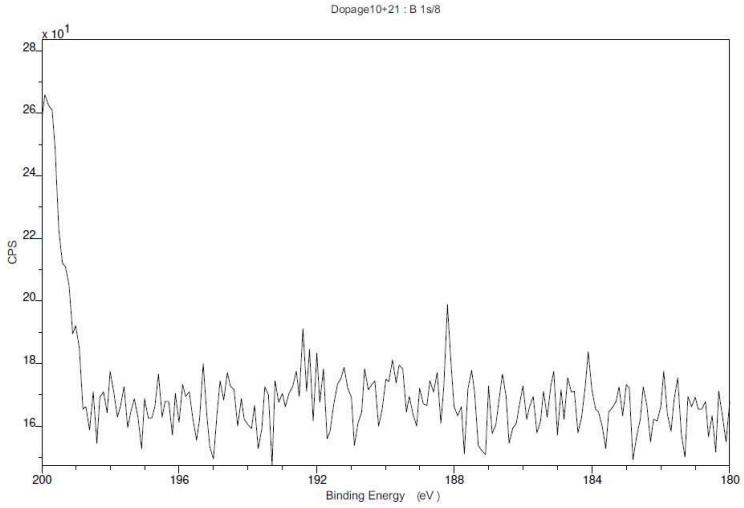

Figure III.2-13 High resolution of XPS spectra of CNWs 10^{21} ion implanted surface, in the B1s energy range (190.28 eV)

Table III.2-4 Different physical properties of boron doped CNWs via ionic implantation on CNWs 0.0 K.

doping level /growth period (h)	Physical property	10^0	10^{15}	10^{18}	10^{21}
CNWs 0.0 K					
	height (µm)	2.4±0.1	3.0±0.3	2.65±0.15	2.5±0.05
	length (µm)	167±35	166±21	130±14	160±40
	RMS*	22			
	WCA (°)	106±4	98±4	107±3	87±3

*RMS= Root mean square of the roughness = $\sqrt{1/n^*} (x_1^2+x_2^2+\ldots+x_n^2)$, where $x= h-h_{medium}$ and h represents the height of the pore.

© 2020 Tous droits réservés.
lilliad.univ-lille.fr

III.2.2. Optimization of SALDI-MS parameters using cyt C on B-CNWs

III.2.2.1. Sample deposition methods for SALDI-MS

Besides the surface itself (with the above measured and/or described morphological, electrical, optical characteristics), other parameters will also influence the LDI efficiency, especially the interaction between the surface and the analyte (through the deposition method) and the proton donors needed to ionize the analyte. To observe what is the most appropriate approach for protein detection, we will use cytochrome C as model protein, in order to optimize these parameters. After that, we will come back to the different doped CNWs surfaces, with the already optimized incubation method and buffer choice. We will also correlate the results obtained for cytochrome C with the internal energies deposited at the surface of CNWs. At the end of this subchapter we will describe the sensitivity of the method towards cytochrome C with a calibration curve and we will measure the RSDs.

III.2.2.1.a. Incubation of the analyte with CNWS SALDI-MS platform

Most of the SALDI-MS literature involves surfaces or nanoparticles co-deposited (inorganic matrix or analyte was deposited first on the MS target plate, and the other on the top) or pre-mixed (and deposited later on the MS target plate) with inorganic matrix (**Figure III.2-14**). As our SALDI-MS based platform is a surface, co-deposition is impossible. The CNWS surface is attached on the classical MALDI-plate with conductive material (usually double adhesive carbon tape).

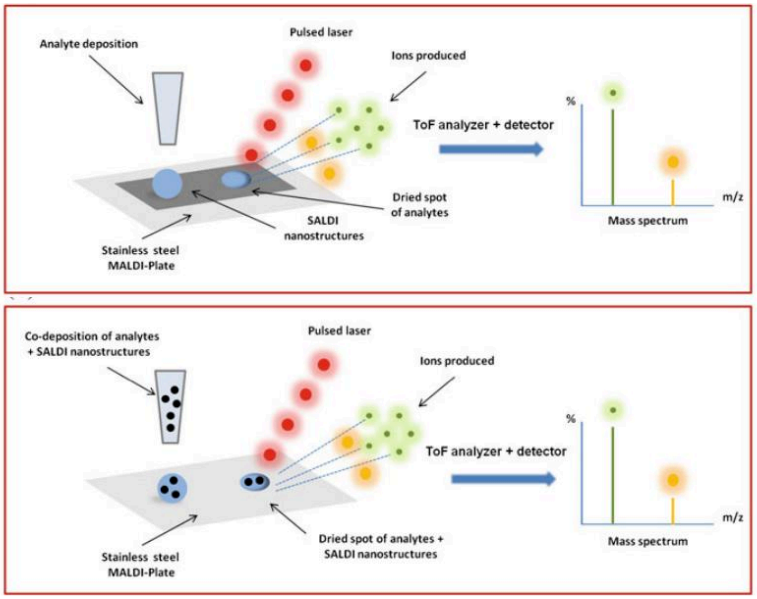

Figure III.2-14 Schematic representation of the principle of surface assisted laser desorption/ionization mass spectrometry (SALDI-MS): (A) LSD-MS process for analyte detection with analyte deposition on SALDI based nanostructures. (B) and co-deposition of analyte and SALDI-based material.[38]

© 2020 Tous droits réservés.
lilliad.univ-lille.fr

Ammonium salts (especially citrates or phosphates) or other H^+ donors help the ionization of the analytes. In the case of surfaces, the deposition method usually involves depositing (drop-casting) a solution of the analyte containing salts, on the MS target plate and drying them in air/vacuum. Even though we did try this approach for cytochrome C, no good results were obtained for carbon nanowalls. So, we decided to incubate the same drops with the surface and absorb them after a specific period of time with dustproof cleanroom papers tissues. To our knowledge, there is only one paper that describes a similar procedure (drop casting, incubating 3 s and reabsorbing the drop with pipette), using DIOS and BSA, as analyte.[8] The authors do explain this phenomenon as the ability for any molecule with a propensity for adsorption onto the surface to attach itself, yet any potential hydrophilic contaminants such as salts and buffers remain in solution, leaving the surface free of such contaminants.

Figure III.2-15 displays the SALDI-MS spectra of 10 pmol/µl of Cytochrome C sample, drop-casted and dried on a carbon nanowalls surface and incubated with the surface during 1 min. It can be clearly observed that drop casting provides no MS signal, while as the incubation gives rise to a MS signal to noise ratio of 40±10 (3 different counts). We did optimize the incubation time and we observed that incubating Cytochrome C with the surface, during 1 to 5 min, gives the best MS signal (**Table III.2-5**), with inter and intra-spots RSDs below 30%, with significant decrease of signal after 5 minutes incubation period.

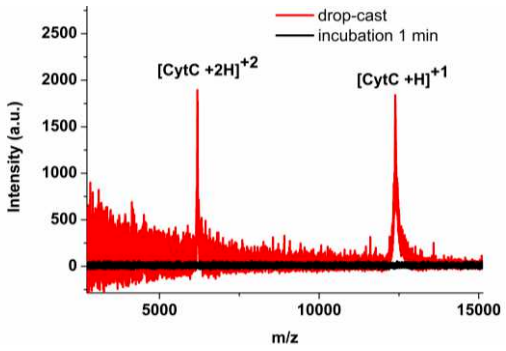

Figure III.2-15 SALDI-MS spectra for cytochrome C drop-cast vs incubation 1min (5 pmol/0.5 µl, ammonium citrate dibasic 50 mM), on CNWs 1.2 K, 2 hours of growth time.

Table III.2-5 Optimization of incubation time for the detection of cytochrome C (100 µM), using CNWs 5.0 K (8 hours of growth), ammonium citrate 150 mM.

Incubation time (min)	SALDI-MS intensity (a.u.)	S/N in SALDI-MS
0.5	407±60	2
1	5301±847	28
2	2483±1237	9
5	4525±1479	14
7	843±151	3
10	370±77	2
dry	-	-

© 2020 Tous droits réservés.
lilliad.univ-lille.fr

Taking into account that the morphology and the dimension of the nanostructures are important for SALDI-MS, we have considered that, there is the possibility that drop-casting and drying the spots with analytes and salts may fill in the pores of nanostructures of boron doped carbon nanowalls (B-CNWs), and the energy transfer may be inefficient. This statement was first brought to discussion for glucose, in Chapter II (with an approximate molecule dimension of 2.27 nm^2), where as the linear detection range for SALDI-MS using CNWs, had a maximum value of 800 pmol, that if we consider that the drop-casted spots is 2 mm in diameter and that glucose stacks after one over each other, after the first layer, (ideally in a layer-by–layer conformation) it corresponds to $4.817*10^{24}$ molecules (using Avogadro's number and taking into account the surface roughness, 50nm, and approximation of the nanostructures as pyramidal shapes distanced at approximatively 50 nm). This film has, by approximation, 88 nm height (not taking into account the salt's contribution, but only the glucose's), which may be difficult to desorb from the CNWs surfaces. These calculations are better described in the last chapter describing methods and experimental procedures. So, we thought that one of the most important parameters, generally ignored in literature, which allowed us to go from no MS signal at all to something, was the incubation time of the surface with the analyte. Similar case could be happening for cytochrome C, where the molecule dimension is 2.5 * 2.5 * 3.7 nm or for any other molecule, for that matter.

III.2.2.1.b. Buffer in CNWS SALDI-MS procedure

Proton donors are essentials for the ionization, so citric acid (or citric salts such ammonium citrate dibasic) or ammonium phosphates are usually employed to replace the original glycerol, simplifying the preparation steps and maintaining the vacuum in the mass spectrometer. Other SALDI-MS strategies do not use salts or inorganic acids as proton donors, as the acidic functional groups already exist at the surface of the nanoparticles or the surfaces.[39]

The quantity of proton donors is to be optimized. Also, ammonium citrate doesn't only play the role of a proton donor, but can also chelate alkali cations and thus prevent or greatly reduce their adduction to the analyte.[7] Too high salt concentrations are important, as the film of analyte may be too thick for the laser's energy to be able to be transferred to the surface, or on the contrary, if the salt concentration is too low, H^+ donors are not sufficient for cations formation. In **Table III.2-6**, the salt concentrations, that we did try experimentally, are presented. It can be observed that a salt concentration of 150 mM, gives rise to the best MS

© 2020 Tous droits réservés.
lilliad.univ-lille.fr

signal for cytochrome C. Salt concentration is also in good accordance with the data presented in literature.

Table III.2-6 Optimization of salt concentration for the detection of cytochrome C (50 pmol/0.5 µL), using CNWs 5K (8 hours of growth), incubation 5 min.

Salt concentration (ammonium citrate dibasic in mM)	SALDI-MS Intensity (a.u)	S/N in SALDI-MS
25	-	-
50	245±115	3
100	504±275	5
150	**5142±333**	**38**
200	1873±467	21
400	3478±1059	18
500	4684±2592	15

Another important parameter in the buffer choice is the pH, due to the appearance of charges, which will lead to formations of positive or negative ions (according to the isoelectric point of the protein). Thus in the case of cytochrome C (pI: 10.5) and ricin (pI: 6.91), a pH around 6 (that is below both isoelectric points) helps creating positive charges, thus the protonation is more likely to appear as well as affinity probing on the SALDI-MS surface (due to different negatively oxygen groups at the surface of the CNWs). The results are in good accordance with literature and our experimental data (data not shown).[12,40]

It can be observed that all the studies presented in **Table III.2-10** are using proton donors that have a pH around 5-6. For cytochrome C, as the charges on the surface are positive, at this pH value, favoring the cationic formation in MS positive modes. Another influence that pH can have is on the interaction between analyte and surface/nanoparticles: If is too strong, it offers specificity towards the analyte, if is too weak, desorption/ionization process may be hard to enhance.[32] Cytochrome C is a hydrophilic protein, exposing polar amino acids at the outer surface of the protein and partially unfolds at acidic pH, making it a good candidate for SALDI-MS preliminary experiments.

III.2.2.2. Boron doping levels and heights of CNWs in SALDI-MS

Boron doping of the graphene nanosheets transforms the nature of the material from p-type semiconducting to semi-metallic.[19] So, by increasing the boron doping level the conductivity of the material would increase and the MS efficiency as well. In **Figure III.2-16** we compared the MS spectra of Cytochrome C (50 pmol/0.5 µl) using different doping levels (0, 1.2, 5.0 and 10.0 K) at similar heights (cca. 2.4 µm). It can be clearly observed that increasing the doping level, increases the MS signal and the S/N ratios.

© 2020 Tous droits réservés.
lilliad.univ-lille.fr

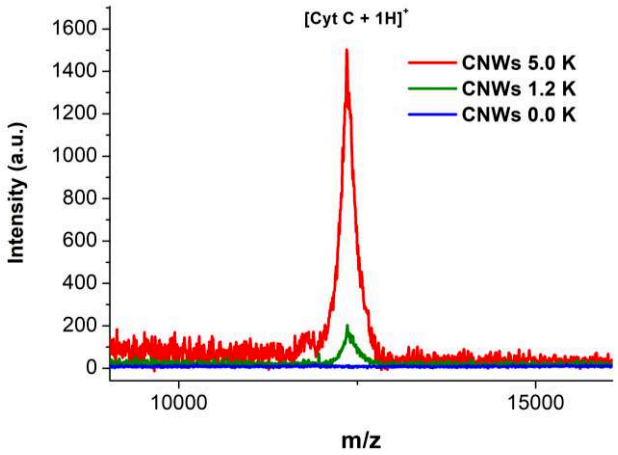

Figure III.2-16 SALDI-MS spectra of cytochrome C (5 pmol/0.5 µl, ammonium citrate dibasic 50 mM): incubation with the surface during 5 minutes, for 3 different boron doping levels for carbon nanowalls : 0.0, 1.2 and 5.0 K (for the same parameters in A, and 2.4 µm of height).

Other parameters to value in the case of SALDI-MS detection of Cytochrome C are the S/N values (**Table III.2-7**), which show even better that 5.0 K doping level, at a 4 hours growth period is the best surface to use for further detections, with a value of 90. In general, all the values for the 5.0 K doping are higher than for the other doping levels.

Table III.2-7 S/N values for SALDI-MS peaks at 12384 m/z, for cytochrome C (50 pmol/0.5 µL, in ammonium citrate 150 mM, incubation 5 min), using different doping levels of CNWs, at different growth periods.

Doping level/growth period	0.0 K	2.0 K	5.0 K	10.0 K
2 H	2	11	25	9
4 H	3	3	92	10
6 H	4	14	56	10
8 H	2	17	3	8

As it is difficult to control the height of the CNWs, during *in-situ* boron doping of CNWs, we did also perform similar SALDI-MS experiments to check if the *ex-situ* boron doped CNWS are suitable for detection of proteins and peptides. To do so, mixture 1 (MIX1) and mixture 2 (MIX2) from the calibration MS kit were used (for concentrations **Table V.7-1**, in Appendix). It can be observed in **Figure III.2-17** that no MS signal was obtained for the lower doping levels. For MIX 1, it can be observed that the signal/noise ratios are, at least, one order of magnitude lower for *ex-situ* boron doped CNWs in comparison with *in-situ* boron doped ones (**Table III.2-8**). For MIX 2, the situation is similar.

© 2020 Tous droits réservés.
lilliad.univ-lille.fr

Table III.2-8 Performances of *in-situ* and *ex-situ* boron doped CNWs, using MIX 1 and MIX 2peptides solution.

	Signal/noise (S/N)	
MIX 1	**In-situ doped CNWs (2.0 K, 2.6 µm)**	**Ex-situ doped CNWS (10^{21})**
DAB	465	6
A1	77	31
FBP	71	7
NT	10	4
MIX 2		
A1	160	11
ACTH1	66	6
ACTH18	72	11
ACTH7	493	4
INS	18	2

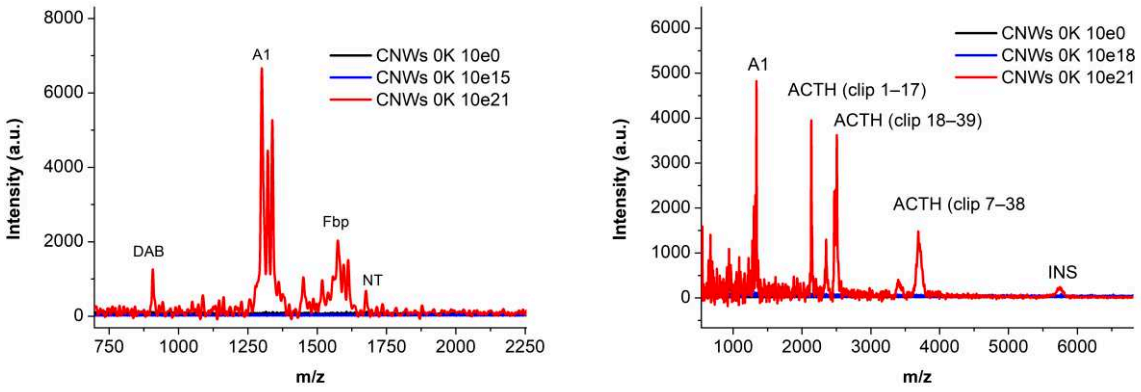

(A) **(B)**

Figure III.2-17 SALDI-MS spectra of MIX 1 **(A)** and MIX 2 **(B)**, in ammonium citrate 1mM, using *ex-situ* boron doping of CNWS.

We also have tried cytochrome C and ricin B chain with the already optimized parameters for *in-situ* boron doped (**Figure III.2-18**). In the case of cytochrome C, the detection was possible, but in the ricin B chain case, it was not. Nevertheless, the S/N was only 3, so it could barely be detected, and, as expected, only for the highest boron doping level. The impossibility of obtaining higher efficiency for cytochrome C may result from the lost of graphitic/graphene structuration, due to high energies that were used to bombard the surface with boron ions.

© 2020 Tous droits réservés.
lilliad.univ-lille.fr

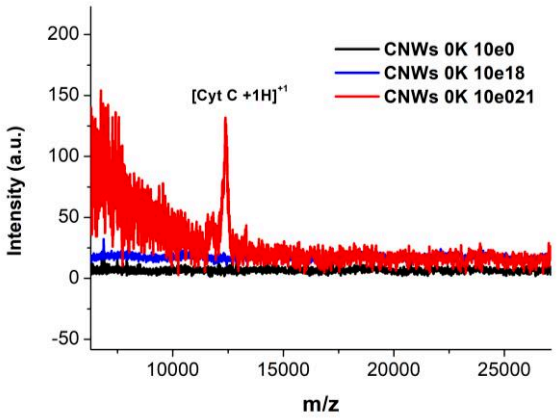

Figure III.2-18 SALDI-MS spectra of cytochrome C (50 pmols/0.5 µL), in ammoiunm citrate 150 mM, incubated 5 minutes on ex-situ boron doped CNWs.

III.2.2.3. Correlation between SALDI-MS signals of Cyt C and internal energies

Another way to characterize the potential of different interfaces as SALDI-MS platforms is measuring the internal energies deposited at the surface, as we already described.[17] Other extensive studies were done in order to observe if the 5.0 K doping level is the best for detection of cytochrome C, by comparing the internal energy deposited on the CNW's surface with the intensity of the SALDI-MS spectra, at the 12.385 m/z, for the other doping levels (**Figure III.2-19**). Herein, we did use CNWS surfaces synthesized during different growths periods, thus different nanowalls heights. When the surfaces were doped *in-situ* using the same boron level (during the synthesis step), there is a visible correlation between intensity and internal energies *vs* nanowalls height. The exception appears when the surface is not doped (**Figure III.2-19A)**, but both internal energies and intensities are much lower in comparison with the doped ones. In this case, the height of the nanowalls decreases the internal energies deposited because of the decreasing conductivity. For the doped surfaces, the higher the deposited internal energy, the higher the LDI-MS efficiency. The procedure and the theory of deposited internal energies are presented in the Appendix.

The conclusion was that a doping level of 5.0 K, having a height of 2.6 µm offers the best intensity in SALDI-MS, for the detection of cytochrome C, with a deposited internal energy of 2.1 eV.

© 2020 Tous droits réservés.
lilliad.univ-lille.fr

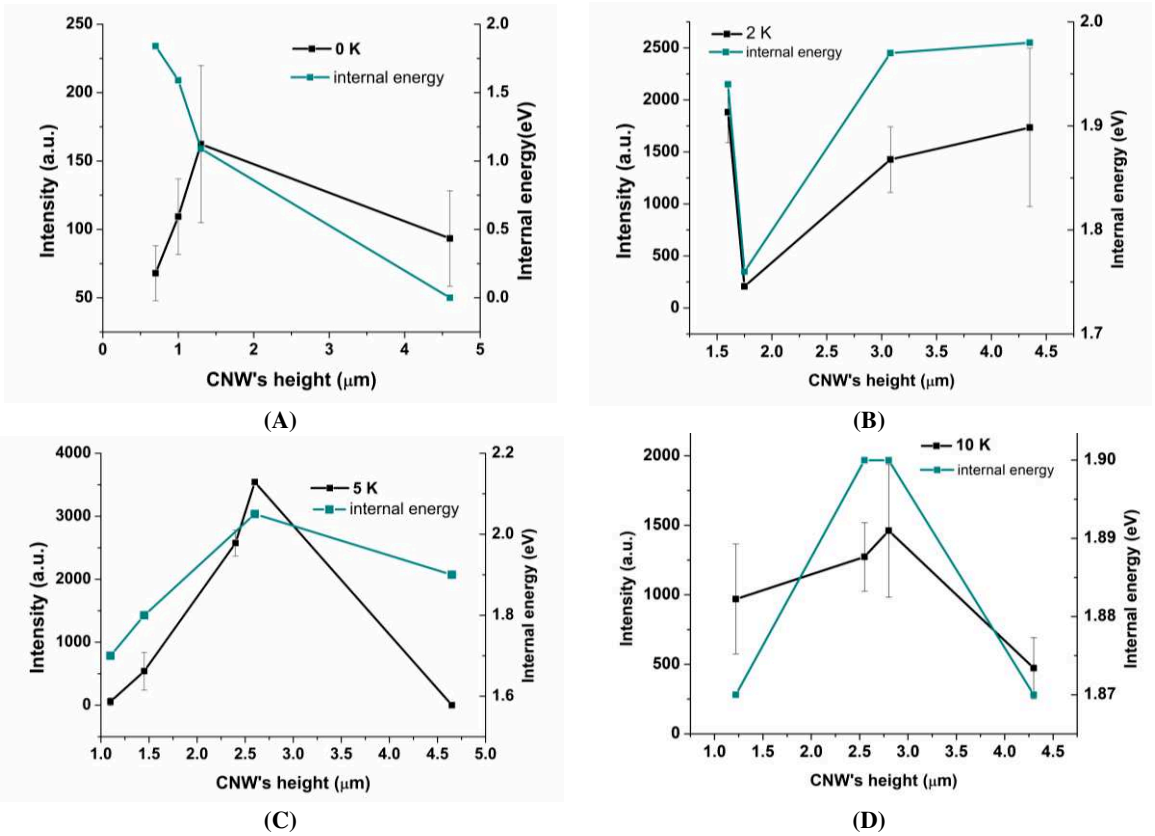

Figure III.2-19 The representation of Cyt C's MS signal depending on the height of CNWs with 0.0 **(A)**, 2.0 **(B)**, 5.0 **(C)** and 10.0 K **(D)** doping level (black) and internal energies corresponding to the specific heights (dark cyan).

III.2.2.4. Sensitivity of the CNWs method towards Cytochrome C

First, a strong recall is needed, in order to point out that in Chapter II, we were able to calibrate a method using a 2.0 K CNWs surface (2.6 µm) for the detection of glucose, for further usage of quantification in real samples. We did not study all the above presented parameters for the small molecules presented in Chapter II, because the performance of the available type of surface, at that time, was suitable for our purpose. In this Chapter, as our purpose it to detect proteins, the meticulousness required is higher.

© 2020 Tous droits réservés.
lilliad.univ-lille.fr

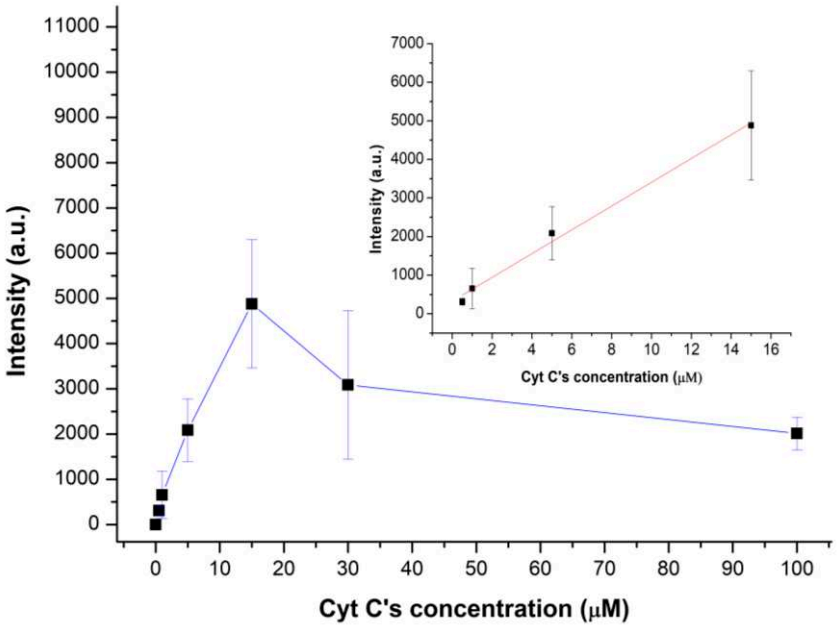

Figure III.2-20 Dynamic range of the SALDI-MS procedure used for the calibration of Cytochrome C, in ammonium citrate, 150 mM. Zoom in: linear range.

Using the 5.0 K CNWs we have determined that the LOD is 250 fmol/0.5 µL. The calculated LOD = 200 fmol/0.5 µL (with the mathematical formula LOD = 3*noise/slope of the calibration curve), which is very similar with the actual LOD that we were able to actually measure (356±39, RSD=10%. S/N=3). The linear range for the calibration curve is 0.25-7.00 pmol/0.5 µL, with R^2=98.761 and according to our knowledge, this is the first procedure, ever described in the literature, to use a SALDI-MS method for the quantification of a protein (**Figure III.2-20**). Even though this method could be optimized, quantification of Cytochrome C is not of real interest, so we just present this method as a proof of concept. All the RSDs (inter and intra-spots) values were smaller than 33%, making this method, with further adjustments, suitable for quantitative measurements, as no actual methods in literature were found for such purpose. The decrease of the MS signal after 20 µM can be explained by the fact mentioned above: as the analyte thickness is bigger, the LDI-MS can be less efficient, as the energy will not be transferred as efficiently to the analyte (laser energy doesn't reach the catalytical sites for CNWS that helps enhancing the LDI-MS process). All the measured intensities or S/N values are presented in **Table III.2-9**.

© 2020 Tous droits réservés.
lilliad.univ-lille.fr

Table III.2-9 SALDI-MS intensities and S/N of the Cytochrome C (50 pmols/0.5 µL) detected using CNWs 5K (8 hours of growth), incubated 5 min, in ammonium citrate (150 mM). Average and SDs of 3 different measurements.

Cytochrome C in ammonium citrate 150 mM (µM/0.5 µL)	SALDI-MS intensity (a.u.)	S/N in SALDI-MS
0.1	x	x
0.5	**356±39**	**3**
1	354±50	8
5	2085±691	59
15	4879±1417	47
30	3839±1405	14
100	2012±361	14

Our results were also compared to the available literature regarding the detection of cytochrome C, using SALDI-MS methods. Chen et al. presented the silanized Fe_3O_4, that being negatively charged, were used as affinity probes to capture tryptic digests of cytochrome C, at pH 5. This lead to a LOD down to 10 nM (in a 0,2 ml solution), corresponding to 5 pmol/0.5µL.[41] In the same paper, silanization with TEOS (tetraethoxysilane) of Fe_3O_4 nanoparticles increased the sensitivity 10 times in the case of ubiquitin.

Tang et al.[42] use Hummer's graphene oxide and a few graphene sheets synthesized by lithium ion intercalation by high power sonication of graphite flakes. In this case graphene based materials play a multirole: proton donors and inorganic matrix for indirect energy transfer to the analyte. Even though they achieved remarkable LODs ($5*10^{-10}$ and $5*10^{-7}$ pmol/0.5 µL), they use graphene based materials mixed to organic matrix (sinapinic acid) to enrich the MALDI-MS detection of proteins and to pre-concentrate the samples, so the protons also come from the classical H^+ donors in the organic matrix (sinapic acid). Also, no statistical errors (RSDs) are calculated for the results, not talking about reproducibility.

Another carbonic materials is used for the detection of cytochrome C, but again, the diamond nanoparticles are used to enrich the classical MALDI-MS method.[40] The mass limit range in this case (66KDa) is the same as in the case of graphene based materials described before. The only carbon material that was able to detect cytochrome C by itself, without adding organic matrix, were the carbon nanotubes (CNTs) synthesized by Chen et al.[43] They do use citric acid in the buffer and in the analyte solutions, as they prefer the co-deposition method on the MALDI-MS plate (matrix was deposited first on the MS target plate, and the

© 2020 Tous droits réservés.
lilliad.univ-lille.fr

analyte solution on the top, after drying of the first layer). Citric acid is not used to absorb UV light, thus is not considered to be a matrix, but it is an important extra proton donor. Also, it was observed that the presence of citric acid can suppress the analyte signal if the lower mass region ions are not deflected. This is the only carbonic based material that was used to obtain similar results as in the presented work: LOD (2 pmol/0.5µL) is almost 10 times lower than CNWs LOD (0.25 pmol/ 0.5µL), but no reproducibility parameters are presented, in the case of CNTs.

Nanoparticle based detection of cytochrome C is the most extended part of SALDI-MS. In **Table III.2-10** we do describe the following ones: AuNPs, TiO_2 NPs, SeNPs, CdTe quantum dots (QDs), Fe_3O_4 NPs, and Pt nanosponges.[14,32,44] Because they have low heat capacitance, thermal conductivity and melting points they are better platforms for SALDI-MS. That is why we did describ them in the "Morphological characterization of CNWs" subchapter and compared them to our CNWs. HgTe nanoparticles were used for the highest mass range ever detected (150 kDa) and also for cytochrome C detection. Their LOD is 10 times better than in our case, with a value of 0.025 pmol/ 0.5 µL and RSDs lower then 25%. Nevertheless, this material was not used in other SALDI-MS experiments, because of their high toxicity. AuNPs used in a layer-by-layer technique, on a Si wafer have and LOD of 5 pmol/ 0.5 µL. It is expected that Au cannot detect higher molecules due mainly to high thermal conductivity, that cannot be confined under the analyte, so that the energy trasnfer is not efficient. The lowest LOD was described for Pt nanosponges (0.0015 pmol/ 0.5 µL), even though it has the highest melting point and it is followed by Fe_3O_4 NPs (0.0056 pmol/ 0.5 µL). The highest LOD was obtained for CdTe QDs(25 pmol/ 0.5 µL), because of their poor electrical conductivity. From this general picture, we could figure that for our CNWs, the upper limit of detection could be between 25 and 150 kDa, if we are to judge from the LODs. As ricin B chain has a molecular weight of 32 kDa and ricin itself 64 kDa, it seems that they are suitable for our purpose.

© 2020 Tous droits réservés.
lilliad.univ-lille.fr

Table III.2-10 Literature study for SALDI-MS detection of cytochrome C (and other proteins).

ref	SALDI substrate	Other conditions	Method of deposition	Dimension	Solvent	Analytes	Highest mass range	LoD (pmol/ 0. 5 µL)	RSDs
41	bare Fe_3O_4 magnetic particles		rinsed and enriched particles are resuspended in 0.2 µL buffer (premixed:particle suspension in analyte solution)	25 nm	citric acid (150 mM) and DHC (150 mM), pH 5	Ubiquitin	16 kDa	17.4	-
	[a)] silanized Fe_3O_4 magnetic particles					Ubiquitin		0.174	-
	bare Fe_3O_4 magnetic particles	Entire molecule				Cytochrome C		1.2	-
	silanized Fe_3O_4 magnetic particles	Tryptic digest				Cytochrome C		5	-
	bare Fe_3O_4 magnetic particles	Entire molecule				Myoglobin		0.89	-
42	GO	Usage of organic matrix (sinapic acid)	GO/G solutions were mixed witht the analyte solution, centrifuged and washed several times with water. 1 µl was added to the plate	-	Phosphate saline buffer	Cytochrome C	66 kDa	$5*10^{-10}$	-
	G							$5*10^{-7}$	-
40	carboxylated/oxidized diamond nanoparticles	Usage of organic matrix (4HCCA)/considers possible binding adsorption sites of NPs	pre-mixed (particle suspension in analyte and matrix solution)	100 nm	20 mM phosphate buffers controlled pH	Cytochrome C, myoglobin, albumin	66 kDa	0.34	-
43	CNTs	CNTs dispersed in ethanol/citrate buffer solution (vol/vol,4/1)	co-deposition (0.2 µl of CNTs + 0.2 µl analyte solution in 50mM citric acid)	250nm/ 60 µm	50 mM ammonium citrate dibasic and 50 mM citric acid, pH 4	Insulin, Cytochrome C	12kDa	2	-
32	Au NPs	-	co-deposition (1 µl NPs solution + 1 µl analyte solution)	14±2 nm	ammonium citrate buffer (0.5–50 mM; pH 4.0)	Cytochrome C Insulin	1.3 kDa	no detection	-
	TiO_2 NPs	concentration of NPs: 24 µM		5±1 nm			12 kDa	15	20%
	Se NPs	concentration of NPs: 1 nM		100±10 nm				2.3	27%
	CdTe NPs	concentration of NPs: 25 µM		3±0.5 nm				25	26%
	Fe_3O_4 NPs	concentration of NPs: 800 nM		13±3 nm		Insulin, Cytochrome C, Chymotrypsin	25 kDa	**0.0056**	16%
	Pt NSPs	concentration of NPs: 8 nM		37±6 nm			25 kDa	**0.0015**	35%
12	HgTe NPs		Pre-mixed	20 nm	300 mM ammonium citrate pH 5	Cytochrome C	**150 kDa**	**0.025**	<25%
						IgG		**5**	
44	Si/SiOx wafer covered layer by layer AuNPs/PAHC	best MS signal $(AuNPs/PAHC)_5$	co-deposition (layers AuNPs/PAHC + 1 µl analyte solution)	RMS 100	200mM ammonium citrate dibasic/ 200 mM citric acid	Cytochrome C	12 kDa	**5**	-
					PFOS-H, replacing citrate buffer	Angiotensin		**0.0007**	-
This work	CNWs	Incubation 5 min with the surface	Drop-casted	2.6 µM	150mM ammonium citrate dibasic, pH 6	Cytochrome C	**64 kDa**	**0.25**	<30%
						Ricin B chain			

III.2.3. Optimization of parameters using ricin B chain on *in-situ* doped CNWs

After the optimization of different parameters with Cytochrome C, it has become much easier to have an approximate idea how we could try to detect ricin B chain. As a reminder, this protein is a big protein (having 64 kDa) as compared to cytochrome C (12 kDa) and the highest molecule to be detected ever by SALDI-MS had 150 kDa. So, similar experiments were performed for ricin B chain, as for cytochrome C the following parameters were found to be the best: height of the nanowalls (2.6 µm), incubation time (5 min), salt concentration (150 mM), buffer's pH, doping level (5.0 K).

III.2.3.1. Sample deposition methods for SALDI-MS

III.2.3.1.a. Incubation of the analyte with CNWS SALDI-MS platform

As discussed in previous headline, the first parameter to optimize is the incubation time of ricin B chain, on the carbon nanowalls surface, in correlation with the salt concentration. Incubating 15 µM (7.5 pmol/0.5 µL) of ricin B chain during 5 min, in ammonium citrate (150 mM), on different a CNWs 2.0K surface, the best intensity was obtained 467±55, with S/N= 4 (**Figure III.2-21**). Similar results were obtained for incubation times 0.5, 1 and 2 minutes (**Table III.2-11**).

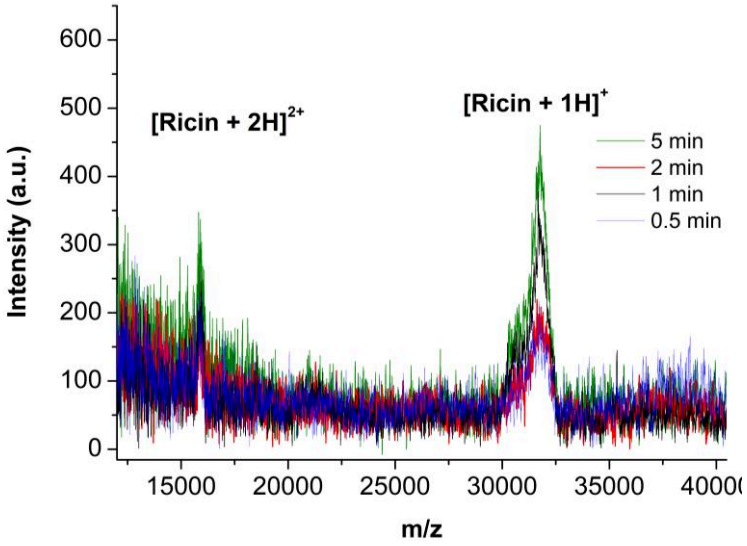

Figure III.2-21 SALDI-MS spectra of different incubation times of ricin B chain (7.5 pmol/0.5 µl), in 150 mM ammonium citrate, on CNWs 2 K (4.7 µm).

© 2020 Tous droits réservés.
lilliad.univ-lille.fr

Table III.2-11 Optimization of salt concentration and incubation time, for the detection of ricin B chain, using CNWs 5K (4 hours of growth).

Salt concentration (ammonium citrate dibasic in mM)	Measured value	incubation time (min)				
		0.5	1	2	5	10(dry)
10	intensity	X	X	X	X	X
	S/N	X	X	X	X	X
25	intensity	X	X	X	X	X
	S/N	X	X	X	X	X
50	intensity	100	226	175	87	185
	S/N	3	3	3	3	2
100	intensity	X	X	530	511	X
	S/N	X	X	3	3	X
150	intensity	**541**	**547**	**449**	**701**	**291**
	S/N	**3**	**4**	**3**	**4**	**3**
200	intensity	X	132	342	427	X
	S/N	X	3	2	4	X

III.2.3.1.b. Buffer in CNWS SALDI-MS procedure

For the pH study, we have used 3 different values (6, 7 and 11) using ammonium citrate, as for cytochrome C, TRIS and sodium carbonate-bicarbonate buffer **(Figure III.2-22A)**. The provider of the ricin B chain specifies that the powder shouldn't be exposed to acidic pH, probably due to structural stability. As ricin has the pI: 6.91, a pH below this limit would create positive charges on the surface of the protein. Thus, both the method that we did establish using Cytochrome C and the ricin B chain stability suggest that the pH to be used in the detection of ricin should be close to neutral or basic. Once again, the suitable buffer was found to be the ammonium citrate, as the pH is neutral enough not to affect the stability of ricin B chain, but acidic enough to create positive charges on the surface of the lectin, enhancing the protonation, and the LDI process. Both SALDI-MS spectra of negative and positive mode and different buffers are presented in **Figure III.2-22B**. We did decide to start with examining the MS mode, using linear methods, in order to observe if negative ions could be observed for ricin B chain. This was not the case: no MS peak could be observed in negative mode.

Incubation time of the analyte solution was studied and presented above in **Table III.2-11** in correlation with salt concentration. A concentration of 150 mM of ammonium citrate was found to be appropriate for ricin B chain, also. This concentration is particularly interesting, as it is also the concentration of sodium chloride in physiological medium (as blood serum), making our method even more

© 2020 Tous droits réservés.
lilliad.univ-lille.fr

suitable for ricin B chain determination in serum, despite the classical MALDI-MS, that is not salt-tolerant, and 150 mM of sodium chloride from serum inhibits the MS signal.

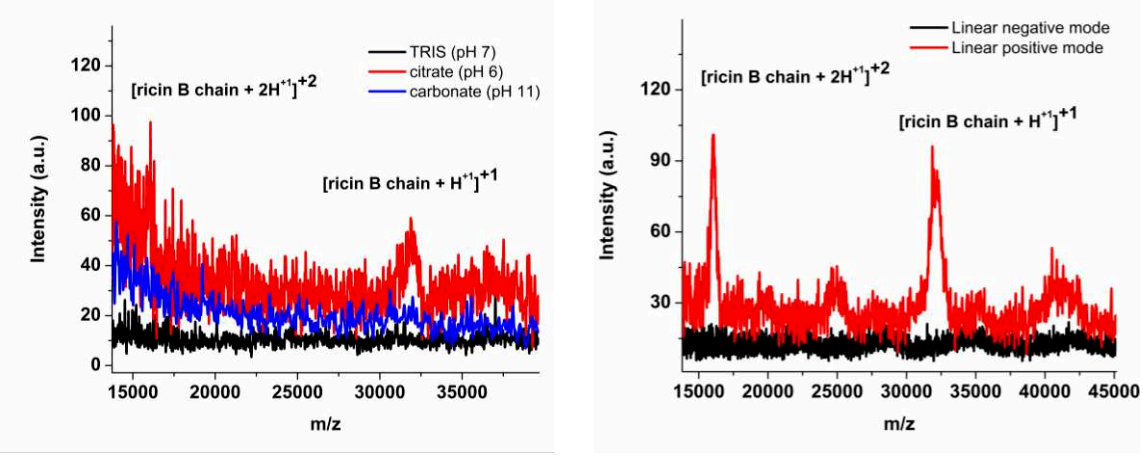

(A) **(B)**

Figure III.2-22 SALDI-MS spectra of ricin B chain (15 pmol/ 0.5 µL) **(A)** at different pHs, in different buffers: ammonium citrate dibasic for pH 6 (black), TRIS for pH 7 (blue), sodium carbonate for pH 11 (red), 50 mM, and incubated for 5 min. CNWs 2K (height of the walls: 4.7 µm). **(B)** using both linear negative and linear positive mode, using ammnoum citrate dibasic at pH 6.

III.2.3.2. Boron doping levels and nanowalls' heights of CNWs in SALDI-MS

When it comes to see how height of the walls can influence the MS signal of both ricin B chain and Cytochrome C, we have chosen two different doping levels that we would keep constant (5.0 and 10.0 K), and varied the growth time (2, 4 and 8 hours). As the growth kinetics of the nanowalls are different from a doping level to another, the heights were not the same for the same growth time, for both doping levels. As stated before,[17] the height of the walls can influence greatly desorption/ionization processes of molecules. In **Figure III.2-23**, the SALDI-MS spectra for both cytochrome C and ricin B chain are presented for CNWs 5.0 and 10.0 K (2, 4 and 8 hours of PECVD growth). It was already described and observed as for cytochrome C that for the 10.0 K the MS intensities were lower when comparing to 5.0 K doping level. In the case of ricin B chain, there is no real improvement for the MS intensities, when we compare 5.0 K with 10.0 K.

© 2020 Tous droits réservés.
lilliad.univ-lille.fr

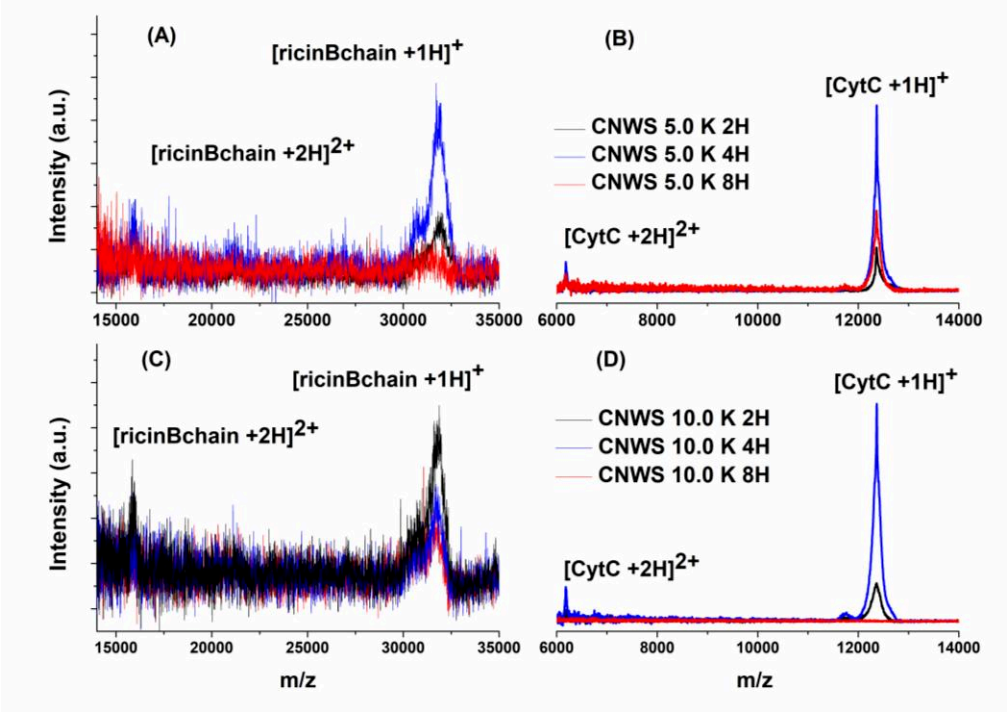

Figure III.2-23 SALDI-MS spectra of **(A, C)** ricin B chain (15 pmol/0.5 µL) and **(B, D)** cytochrome C (50 pmol/0.5 µL) in ammonium citrate 150 mM, incubation 5 min, on different CNWs growing periods using 5.0 and 10.0 K boron doping level.

Nevertheless, the same trend is observed when we do compare SALDI-MS intensities for both cytochrome C and ricin B chain, on boron doped CNWS 5.0 K. A growth period of 4 hours seems to give the best sensitivity towards both proteins (**Figure III.2-24**). To conclude, the optimization steps for both proteins offered us the possibility to conclude that similar parameters have to be used for further detection: CNWs surfaces with a doping level of 5.0 K, grown for a period of 4 hours are to be used for further incubation (during 5 min) of the analyte dissolved in ammonium citrate dibasic (150 mM).

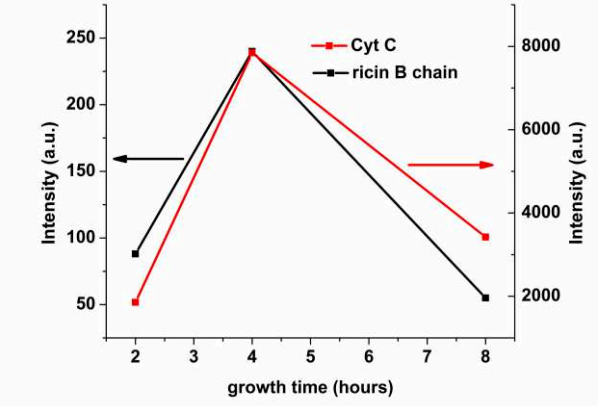

Figure III.2-24 Representation of SALDI-MS intensities in the case of cytochrome C (100 µM) and ricin B chain (30 µM), incubated 5 min on the surface of CNWs 5.0 K, for different growth periods (2, 4 and 8 hours).

© 2020 Tous droits réservés.
lilliad.univ-lille.fr

III.2.3.3. Sensitivity of the CNWs method towards ricin B chain

Different ricin B chain concentrations were also evaluated to see if some kind of calibration curve could be determined. This was not possible, in the available concentration range (limited by the producer's stock solution of 30 µM). Nevertheless, the lowest concentration detected (LOD) on the surface of unmodified CNWs was 5 µM, corresponding to 2.5 pmol/0.5 µL (thus to 80 ng/0.5 µL) (**Table III.2-12**). This limit of detection is sufficient to detect the lowest amounts of ricin that are able to bring death to the persons that interact with the toxin, even if the sample has to be diluted 10 or 20 times (samples like soft-drinks or blood serum), because this would mean 1.6 µg. Injection of ricin has the highest lethal statistical percentage even if the LD_{50} = 10 µg/kg[45] is comparable to LD_{50} = 5-10 µg/kg for inhalation and the least dangerous is the oral ingestion, with LD_{50} = 1-20 mg/kg.[46] We can observe that our limit of detection is more than 3 times lower than the lowest median lethal dose. **Figure III.2-25** depicts the SALDI-MS spectra of different ricin B chain concentrations. The MS signal saturation can be observed after the concentration of 15 µM (7.5 pmol/ 0.5 µL) of ricin B chain.

Table III.2-12 SALDI-MS values (signal intensity and signal to noise ratio) obtained for different ricin B chain concentrations (µM) in ammonium citrate 150 mM, on unmodified CNWs.

Incubation time →	Incubation 2 min		Incubation 5 min	
Ricin B chain in ammonium citrate 150 mM (µM/0.5 µL) ↓	SALDI-MS intensity (a.u.)	S/N in SALDI-MS	SALDI-MS intensity (a.u.)	S/N in SALDI-MS
0.1	x	x	x	x
0.5	x	x	x	x
1	x	x	x	x
5	**214**	**3**	**124**	**2**
15	407	4	204	2
30	295	3	177	2

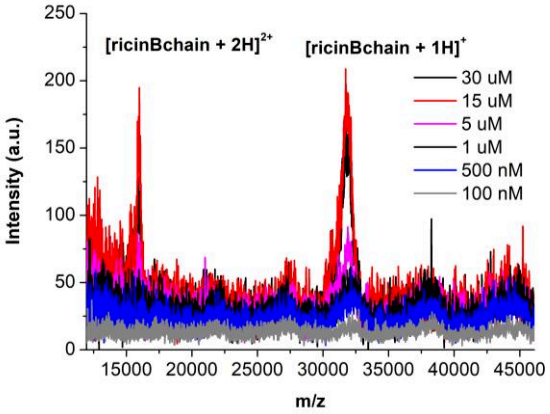

Figure III.2-25 SALDI-MS spectra of ricin B chain different concentrations, on unmodified CNWs, using 150 mM of ammonium citrate, as proton donor, incubation 5 min.

© 2020 Tous droits réservés.
lilliad.univ-lille.fr

III.3. Affinity strategies for detection of ricin B chain on *in-situ* boron doped CNWs

The specificity of any SALDI-MS method can be achieved by conjugation of the material with a recognition element.[32] One of the characteristic to be avoided is that the interaction between the recognition element and the analyte not be too strong, because desorption from the SALDI-MS substrate can be impossible in this case. Nevertheless, a too weak interaction could not offer enough specificity. For real application, we also needed to think about a selectivity strategy towards ricin-like proteins. For this purpose, the toxicity mechanism of ricin-like proteins (described in Chapter I) will be used as inspiration for chemical surface modification. Shortly, ricin B chain (a lectin) will be covalently attached to a specific amino-sugar (galactosamine), previously attached to the surfaces through the carboxylic groups of the carboxylic pyrene modified CNWs surface, through amide bonds. This also represents an important challenge that we will need to overcome by optimizing all the reaction steps in the surface modification.

The CNWs surface may possibly have carboxylic groups present on the surface, but the amount is too low to be able to bind the amine groups. For this purpose, we will physically adsorb 1-pyrenecarboxylic acid on the graphene based nanowalls. We describe the affinity strategy in **Figure III.3-1**, with all the summarized steps in the detection of ricin B chain using our SALDI-MS method.

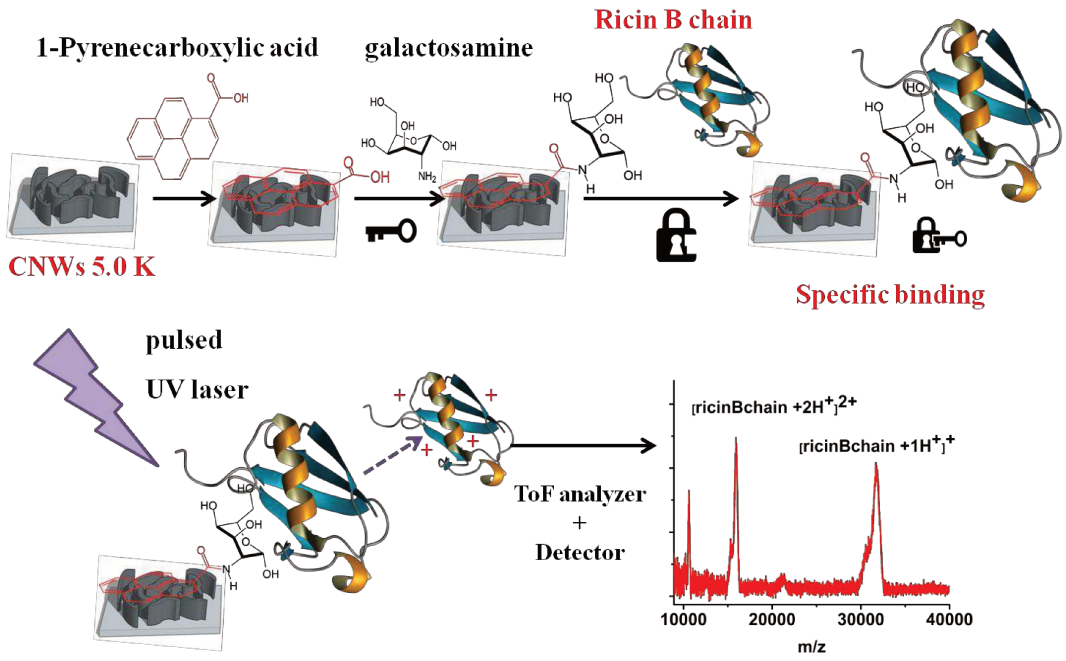

Figure III.3-1 Scheme of the affinity strategy in the modification of CNWs for the detection of ricin B chain, for the detection in SALDI-MS.

© 2020 Tous droits réservés.
lilliad.univ-lille.fr

III.3.1. Optimization of SALDI-MS, using non-covalent galactosamine moieties

One of the studies we performed is incubating three different sugars with ricin, on the same interface in order to observe if the incubation with specific sugars (galactose, GAL and lactose, LAC) may increase the adsorption of ricin, thus the MS signal, by comparison with the non-specific sugar (glucose, GLC). The way this experiment was performed: drop casting a cca. 1 mm spot of sugar (in water), let it dry and incubating a drop of ricin (150 mM ammonium citrate) during 2 and 5 minutes (as in the experiments described before). Even though the MS signal was increased 2 times by comparison with no sugar modification on the surface (**Figure III.3-2A**), no important differences were observed between the specific (GAL and LAC) and non-specific sugars (GLC) (**Table III.3-1**). No selectivity was insured because no rinsing step was possible because of non-covalent bonding. Also, the S/N values almost double by the previous addition of the sugar on the surface. Another important achievement while performing the above experiment was that the 64 kDa peak of the dimeric form of the ricin B chain was detected by enriching the surface with the sugar (in this case, the best was observed for lactose, **Figure III.3-2B**)

Drop-casting galactosamine and glucosamine (10 mM) in order to see if the MS signal enhancing occurrs, proved that the ricin B chain signal increased 2 times in comparison with no modified CNWs surface,

Literature study may reveal the binding kinetics of sugar-ricin interaction, in order to optimize such specificity experiments. Such optimization may include incubation time of ricin with the sugar. Before grafting the recognition element on the surface of the CNWs (by covalent bonding), we should establish what is the appropriate incubation time of specific sugars with ricin B chain moieties.

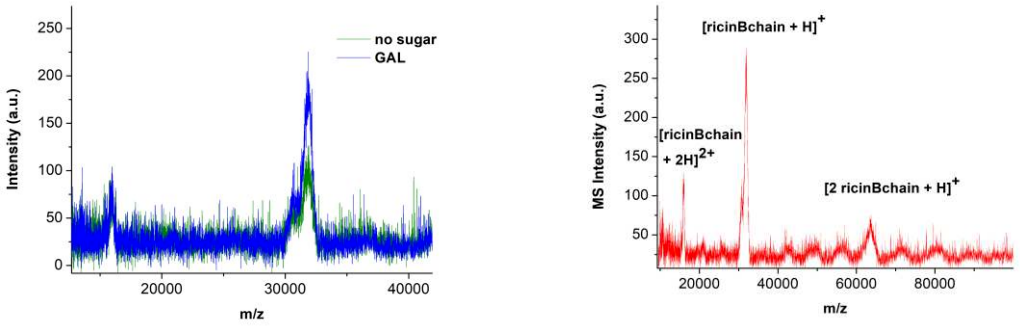

(A) **(B)**

Figure III.3-2 SALDI-MS spectra of ricin B chain: **(A)** drop-casted with the specific sugar, galactose (blue) and without surface modification (green) and **(B)** in the presence of lactose, using CNWS 1.2 K (8 hours), incubation 5 min, ammonium citrate 150 mM.

© 2020 Tous droits réservés.
lilliad.univ-lille.fr

Table III.3-1 SALDI-MS performances of for ricin B chain, at 32 kDa, using non-covalently modified sugar CNWs surfaces.

Surface modification	incubation time → measured values ↓	2 min	5 min
no sugar	Intensity (a.u.)	237	255
	S/N	3	3
GAL	Intensity (a.u.)	377	287
	S/N	5	4
GLC	Intensity (a.u.)	298	375
	S/N	4	5
LAC	Intensity (a.u.)	404	242
	S/N	5	3

III.3.2. Optimization of SALDI-MS, using covalent binding of galactosamine

In order to assure the possibility to covalently bond the galactose moiety to the CNWs, we have used galactosamine for further experiments. The amine group could be used to form amide bond with carboxylic moieties from the carbon nanowalls or from physically adsorbed carboxylic modified pyrene (through π-π stacking).

Once we have established which the affinity recognition element is, we need to answer the following questions:

- Which is the most rapid, but still optimal incubation time of NH_2GAL with the modified COOH CNWs?
- Which is the appropriate solvent to bond amine from galactosamine with the carboxylic groups from COOH pyrene?
- Which is the solvent for the grafting of NH_2GAL that we should used in order to create enough proton donors for the LDI-MS process? If the solvent from the previous step is not ammonium citrate, how could we ensure the donors in the capture of ricin from the samples we should measure?
- Should we use water based procedure or organic based procedure to obtain the amide bond?

To answer our questions we have proposed 2 protocols: Protocol 1 (a water based process) and protocol 2 (an organic based process). Both protocols are largely described in the “Experimental conditions” chapter. The difference is that in water based process we dissolved galactosamine in water and in organic based process we did dissolve it in DMSO and the activation of carboxylic groups is done in PBS (in protocol 1) and in DMF (in protocol 2).

© 2020 Tous droits réservés.
lilliad.univ-lille.fr

So, in order to try to simplify the process, we did try to use ammonium citrate dibasic as solvent to create the amide bond, so we did choose a water based amide formation. EDC (N-(3-Dimethylaminopropyl)-N'-ethylcarbodiimide hydrochloride)/NHS (N-Hydroxysuccinimide) strategy was first applied, as described in the Appendix chapter. As XPS results did not show any increase in nitrogen (**Figure III.3-3**), we did suppose that the modification was not complete or not too efficient. Huge amount on nitrogen coming from CNWs was observed, so we cannot distinguish lower amounts on nitrogen (coming from the amide bond) after the modification.

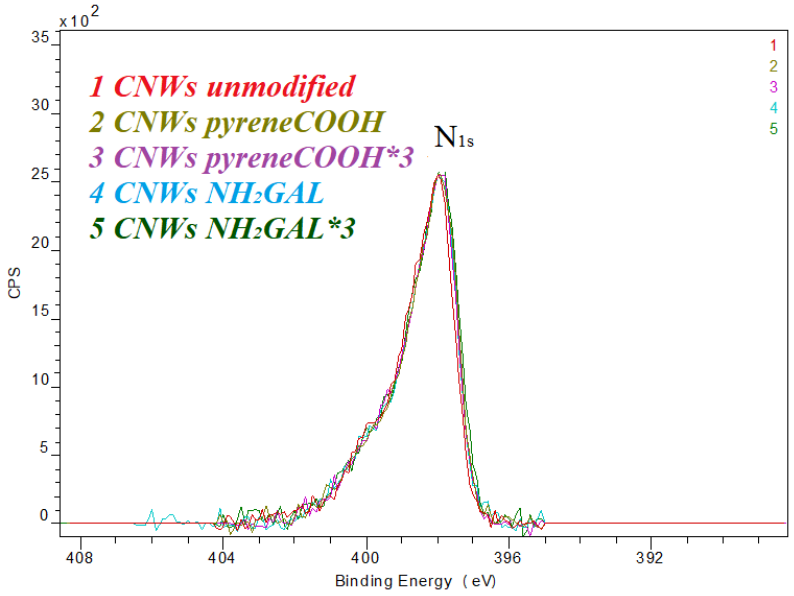

Figure III.3-3 High-resolution XPS analysis was carried out in the N1s energy range (397.9 eV).

Also, SALDI-MS detection of ricin B chain was unsuccessful, using Protocol 1 modified surfaces. So we did add sinapinic acid, as organic matrix, over the drop casted of ricin on modified CNWs, to observe if ricin could be detected (**Figure III.3-4**). It can clearly be observed that the modified surface gave rise to a more intense MS peak, for ricin B chain. It means that the modification enhanced the MS signal, but the LDI-MS process, without the organic matrix, was not initiated. Ricin was still captured by the galactosamine, so the modification of the surface should have been working. The lack of an enhanced LDI-MS process, without the organic matrix could have appeared because of the following parameters: too much salt, and the NH_2GAL film became either too high, or the proximity of NH_2GAL with the pyrene modified surface was unsuccessful for proper binding (again, because of too much salt). As after the rinsing, we have proven that ricin is still present, we were wondering if we should add the proton donor, later. Literature showed that, HEPES (10

© 2020 Tous droits réservés.
lilliad.univ-lille.fr

mM) can be used for efficient capture of ricin, using specific sugar moieties, during 2 hours of incubation and 1 hour of centrifugation with AuNPs (gold nanoparticles).[47]

Also, the pH of the reaction was unsuitable, probably, as ammonium citrate has a pH value of 6, a little bit too acidic in comparison with PBS (pH 7.4), that is usually used in a water based amide formation. As PBS is known to be a very important blocker of the LDI-MS process in SALDI-MS, we did decide to switch to organic based solvent amide formation.

EDC was replaced with DCC (N,N′-Dicyclohexylcarbodiimide) and ammonium citrate dibasic should be replaced with an organic solvent. We did try to dissolve galactosamine in DMF, but after 24 hours of π orbital stirring, the dissolution was not possible. We replaced DMF, with DMSO, because the solubility of galactosamine was proven to be higher (1 hour of π orbital stirring and vortexing). DMF was still used for the activation step of the carboxylic groups.

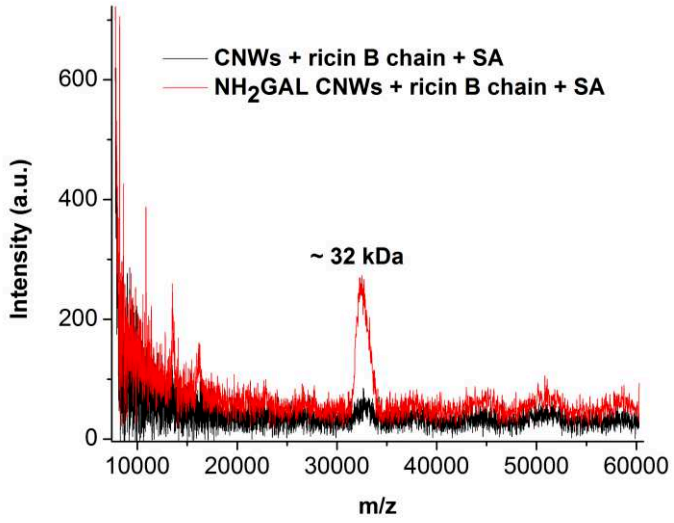

Figure III.3-4 MALDI-MS spectra of ricin B chain, on top of unmodified and Protocol 1 modified CNWs (10.0 K 4H), using sinapic acid as organic matrix.

Ammonium citrate dibasic (150 mM) was still the best choice for incubation of ricin B chain with the NH_2GAL CNWs surface, after the organic based solvent procedure was applied for the surface modification. The incubation time was one hour. MS signal for HEPES (10 mM) was not reached (data not shown). Rinsing was also to be performed with ammonium citrate.

Similar results were obtained for the drop-casted glucosamine CNWs surface. The galactosamine modified surface through covalent bond increased the signal 5 times in comparison with no modified carbon nanowalls surface (**Figure III.3-5**). Surface modification also decreased the RSDs values from 30% to 20%.

© 2020 Tous droits réservés.
lilliad.univ-lille.fr

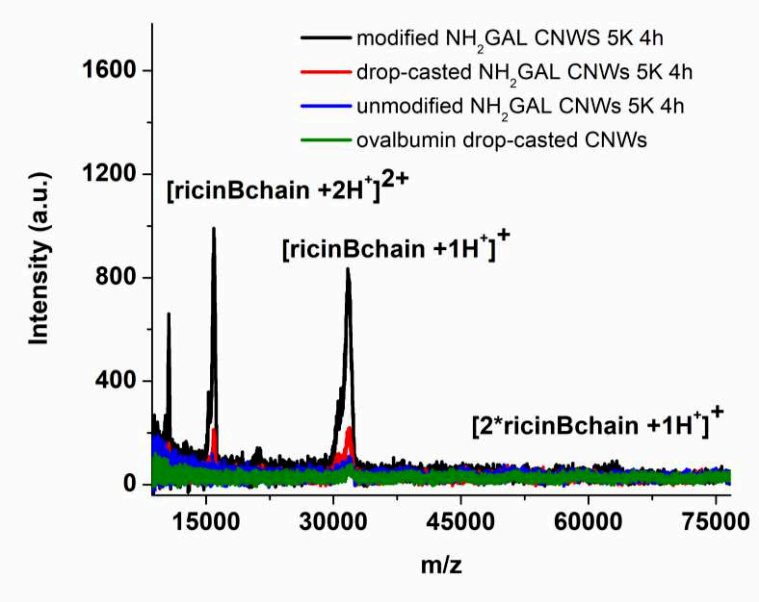

Figure III.3-5 SALDI MS spectra of ricin B chain (30 µM, ammonium citrate 150 mM, incubated 5 min), using unmodified, modified and drop-casted galactosamine (10 mM, water) CNWs 5 K 4h.

Another strategy could be applied, by replacing galactosamine with ovalbumin, as a naturally occuring glycoprotein, with sugar moieties that can selectively bind to the ricin B chain. This strategy was used as ricin sensing probes using ovalbumin-encapsulated gold nanoclusters.[48] Using the conditions that we tried (described in the last subchapter), the ricin B chain signal was observed but it was not enhanced (**Figure III.3-5**). Maybe this could be resolved with trying other conditions. But, as the NH_2GAL strategy works, this will be used in further studies.

Even more, our method is able to detect down to 1.5 µM of the ricin B chain, whereas classical MALDI-MS (with sinapinic acid, 10 mg, dissolved in 30% ACN + 0.3% TFA in water, as recommended by producer in a mass calibration kit, from SCIEX) did not give rise to any peak and, of course the background noise is bigger, especially in the lower region, but also in the region of interest (**Figure III.3-6**).

© 2020 Tous droits réservés.
lilliad.univ-lille.fr

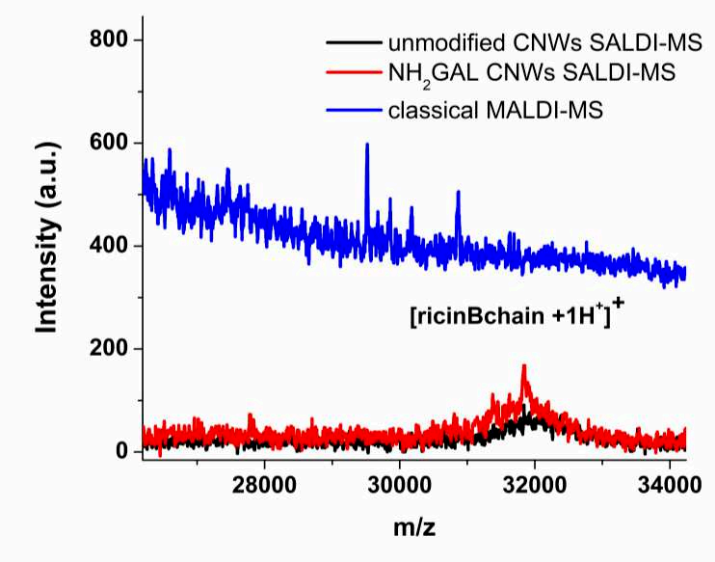

Figure III.3-6 MS spectra of ricin B chain (1.5 µM, in ammonium citrate 150 mM) using classical MALDI-MS and SALDI-MS with unmodified and NH_2GAL CNWs.

III.3.3. Surface characterization of NH_2GAL *in-situ* boron doped CNWs surfaces

To prove that the modification of the CNWs surfaces was successful we did use MALDI-TOF as characterization method for the surface. Galactosamine (Mw=179.17) and 1-pyrenecarboxylic acid (Mw=246.26) can be used to observe the modification. [galactosamine + 1H]$^{1+}$ should be found around 180 m/z, but as described in the previous chapter, carbohydrates tend to form sodium [galactosamine + Na]$^+$ and potassium [galactosamine + K]$^+$ adducts at 202.16 and 218.17 m/z, respectively (**Figure III.3-7A**). The main problem is that pyrene-COOH can also lose the carboxylic acid functional group and pyrene (Mw=202.25) could be detected at 203.25 as [pyrene + H]$^+$. Even though the mass spectrometer is one of high resolution, this very small peak separation of 1.09 Da is hard to observe exactly (**Figure III.3-7B**). Nevertheless, it can be observed a peak separation of 0.1 Da between [pyrene + H]$^+$ and [galactosamine + Na]$^+$. Anyway, the modification with 1-pyrene carboxylic acid is well observed at 246.5 m/z for [1-pyrenecarboxilic acid + H]$^+$. Other unidentified adducts are observed for galactosamine modified surfaces. When ricin is incubated with the modified surface, two new peaks occur at 207.5 and 225.5 m/z. Attribution of these peaks was still not succeeded, but it may suggest that structural modification occurred of the galactosamine, during bonding of ricin. Even though we tried to identify the entire pyreneCO-NHGAL (Mw=407.5 Da), no peak was observed in that region, using the positive reflectron mode.

© 2020 Tous droits réservés.
lilliad.univ-lille.fr

We have also tried Raman and FTIR characterization of the modified surfaces, but apparently the quantity of both 1-pyerenecarboxylic acid and galactosamine were insufficient for the detection.

A very simple method to prove the modification of the surfaces with both pyrene-COOH or NH_2GAL is to measure the water contact angle (**Table III.3-2**). Before the modification the studied surface had a WCA of 127±3°. As expected after pyrene-COOH modification the surface became hydrophilic (with WCA less than 10°). Wettability changed again after the NH_2GAL modification and the WCA was 93±7°. This WCA is suitable for MS detection, as we already talked that concentration of the analyte in a small area of the SALDI-MS substrate is important.

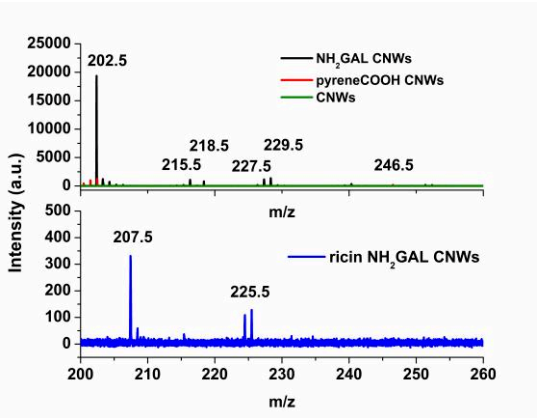

(A)

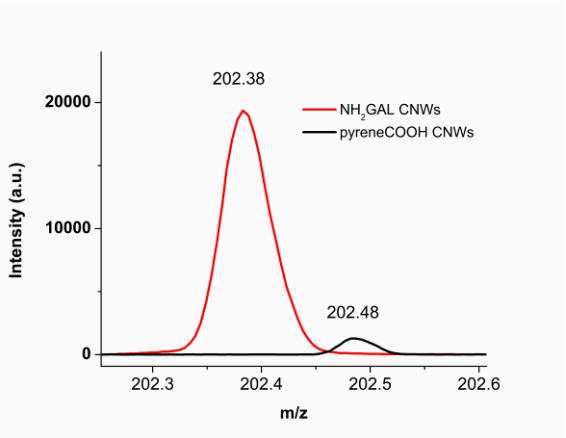

(B)

Figure III.3-7 SALDI-MS spectra of **(A)** modified CNWs surfaces: pyrene-COOH CNWs (red) and NH_2GAL CNWS (black) and control CNWs (green), in the small region, using reflectron mode. **(B)** zoom-in for the 202 m/z peak.

Table III.3-2 Resistivity and water contact angle for unmodified CNWs (5.0 K grown for 8 H) and the same surfaces modified with pyrene-COOH and NH_2GAL.

doping level /growth period (h)	Physical property	unmodified	1Pyrene-carboxilic acid	NH_2GAL
CNWs 5.0 K 8h				
	WCA (°)	127±3	<10	93±7

© 2020 Tous droits réservés.
lilliad.univ-lille.fr

III.4. Detection of ricin B chain in real samples, using NH_2GAL-CNWS

III.4.1. Detection of ricin B chain in Coca-Cola® samples

The detection of ricin is more helpful if is detected before assimilated in the body, as a prevention method against deathly bioterrorism weapon. For this purpose, we have tried to consider that the uptake of the toxin could be realized by drinking poisoned liquids. The easiest way to do it is to poison water or different juices, as soft drinks. Usually soft drinks have an acidic pH that really was a problem in our first experience of detecting ricin B chain, as the method that works needs a quite neutral pH. The high concentration of ammonium citrate present in the established method neutralized the acidic conditions, and the detection of ricin in Coca-Cola® was possible.

For this purpose, modified NH_2GAL CNWS were used (as described in Appendix chapter). Prior to drop-casting, ricin B chain was incubated 5 minutes to Coca Cola samples. Different dilutions of Coca Cola were used and the lowest one was used (10 times), in order to establish the most reliable method when it comes to real samples of Coca Cola that might be poisoned with ricin, and not to dilute to much the real concentration. **Figure III.4-1A** presents the SALDI-MS spectra of ricin B chain (15 µM, in ammonium citrate 150 mM) spiked in Coca Cola soft-drink, using modified NH_2GAL CNWs. It can be observed that even the Coca Cola is a complex medium, with other possible sugars present, that could interfere with the ricin B chain (like fructose, sucrose, glucose), 55% of the MS signal was still obtained when ricin B chain was spiked in Coca Cola. Taking in consideration that this is not, yet, a quantitative method, the results are very good for screening of ricin in real samples. Taking in consideration that NH_2GAL CNWs surfaces could be prepared prior to the analysis and kept at room temperature several months, the entire detection method, approximately 1 hour, and the most time consuming step is the decarbonization of Coca Cola, a step that could be further optimized, for an even more rapid analysis.

© 2020 Tous droits réservés.
lilliad.univ-lille.fr

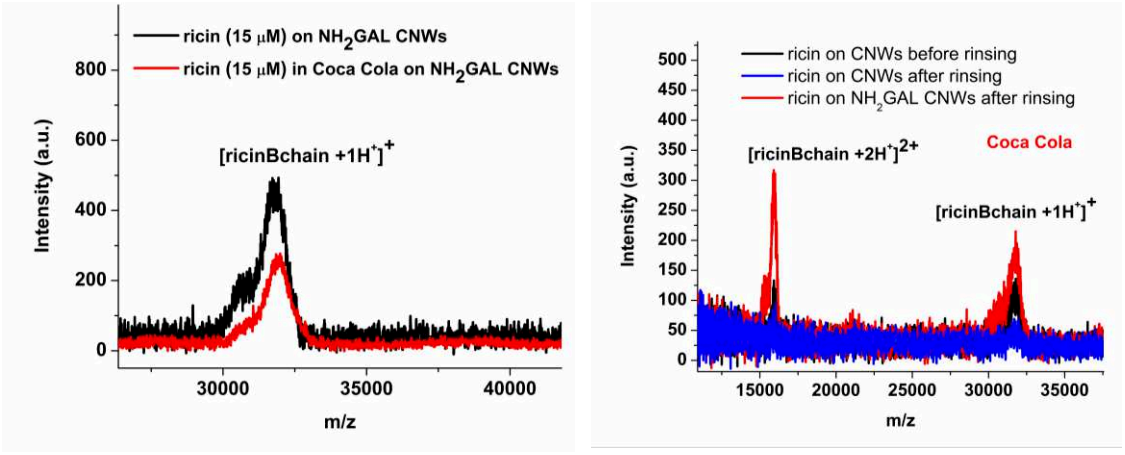

(A) **(B)**

Figure III.4-1 (A) SALDI-MS spectra of ricin B chain (15 µM, in ammonium citrate 150 mM) on NH_2GAL CNWs (5 K 4 h), in Coca Cola, diluted 10 times in ammonium citrate 150 mM (red) and control (no Coca Cola). **(B)** SALDI-MS spectra of ricin B chain (15 µM, in ammonium citrate 150 mM) on NH_2GAL CNWs (5 K 4 h), in Coca Cola, diluted 10 times in ammonium citrate 150 mM, after rinsing with citrate (red) and unmodified CNWs, before (black) and after rinsing (blue).

The selectivity of the method, using galactosamine was proven by rinsing the drop-casted ricin B chain-spiked Coca Cola spot, with ammonium citrate 150 mM, 2 times, during 15 min, by π orbital stirring (150 rpm). In **Figure III.4-1B** it can be observed how rinsing influences that MS signal of ricin B chain. NH_2GAL CNWs surface maintained almost 80% of MS signal in contrast with the unmodified CNWs, which almost lost the MS signal, making the S/N below 3, thus impossible to identify. This is a perspective worthy for study, even though Coca Cola itself doesn't contain any protein and spiking soft drinks for criminal purposes wouldn't gain any advantage by contamination with other proteins.

III.4.2. Detection of ricin B chain in blood serum samples

This method could also be used to determine if ricin is present in blood serum, after an eventual contamination. Galactosamine was drop-casted on the surface to enhance the signal and capture ricin B chain, on CNWs 5.0 K 4h, as they were the best surfaces for ricin B chain detection. In can be observed in **Figure III.4-2** that control samples (blood serum diluted 20 times) did not give rise to a MS peak at 32 kDa and the spiked ricin B chain blood serum did. By comparison, the MS signal for ricin B chain sample analyzed without spiking it to blood serum is bigger than when spiked in serum. As stated for Coca Cola this could be because of the complex media, that could interfere with the LDI desorption of the ricin. Almost 50% of the MS signal was still

© 2020 Tous droits réservés.
lilliad.univ-lille.fr

recovered when ricin B chain was spiked in blood serum. Not being a quantitative method, more a screening method, the results are suitable for real sample analysis.

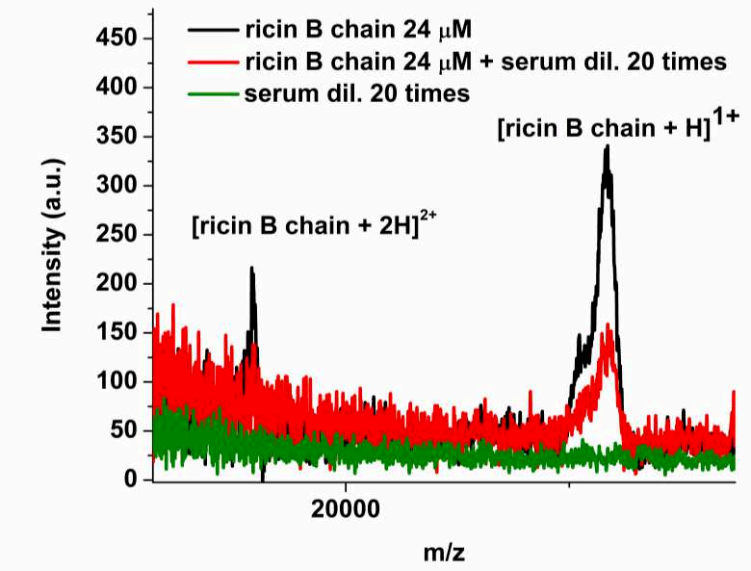

Figure III.4-2 SALDI –MS spectra of ricin B chain (24 μM), ricin B chain (24 μM) spiked in serum (diluted 20 times) and control serum samples (diluted 20 times), in ammonium citrate 150 mM. drop-casted NH_2GAL CNWs 5k 4h were used.

© 2020 Tous droits réservés.
lilliad.univ-lille.fr

III.5 Conclusions

This chapter can be divided in the following main goals and their subsequent consequences:

1. We have extensively studied our surfaces to observe how different characteristics evolve and how can we use them to be able to detect proteins, in general, with our boron doped CNWs, using SALDI-MS, as this is a real drawback in our society nowadays, as only few examples are presented in the SALDI-MS literature.

The important factors we did take in consideration were: morphology of the surface (roughness of the surface, length and height of the nanowalls), optical properties (reflectivity and photoluminescence), other physical characteristics (as resistivity, melting point, heat capacitance, thermal conductivity, vibration modes, wetting properties) and the presence of the boron doping in the graphene-like structure of the nanowalls. We have discussed the importance of these characteristics in the LDI-process.

The maze-like structures change to a heterogeneous distribution of nearly straight walls, as the doping is increased. The pores become smaller until the 5.0 K doping. The amount of small pores between nanowalls increases and contributes to the increasing of the specific surface area. Roughness increases with the length of the nanowalls, because of the twining of the nanowalls. Thus, nanostructuration increases also. The sp^2 graphene-like structures are found mostly at the surface of nanowalls, and they do absorb UV-light, the light beam used in the LDI process. As photoluminescence is low and absorbance is high, together with the low thermal conductivity, low melting point and low heat capacitance, the energy in confined in a small area, enhancing desorption and the ionization of the proteins. Also, the hydophobicity confines the drop-casted analytes in small areas (cca. 1.5 mm^2), so the energy from the laser is even more efficiently transferred to the analyte (as laser has a diameter of only 100 μm). Except the morphological influence, the boron doping level makes the transition from p-type semiconductor to semi-metallic/metallic properties, thus increasing electrical conductivity. Proton donors were extrinsically available from the ammonium citrate dibasic and as well from acid groups at the surface of the nanowalls. We did also study the concentration of proton donors in the solution of analyte and a concentration of 150 mM was found to be the best. Incubation of the analyte (around 5 minutes) with the surfaces seemed to be the threshold between being able to detect cytochrome C or not.

© 2020 Tous droits réservés.
lilliad.univ-lille.fr

2. The correlation of the SALDI-MS intensities of the model protein used (cytochrome C) with the internal energy efficiency in order to understand how we can have another systemic check-up method for efficiencies in LDI-MS process.

SALDI-MS intensities of cytochrome C were measured for all the doping levels and all the growing periods and compared with internal energies. The conclusion was that a doping level of 5.0 K, having a height of 2.6 µm offers the best intensity in SALDI-MS, for the detection of cytochrome C, with a deposited internal energy of 2.1 eV. Using the 5.0 K CNWs we have determined that the LOD is 250 fmol/0.5 µL. The calculated LOD = 200fmol/0.5 µL (with the mathematical formula LOD = 3*noise/slope of the calibration curve), which is very similar with the actual LOD that we were able to actually measure (356±39, RSD=10%. S/N=3). The linear range for the calibration curve is 0.25-7.00 pmol/0.5 µL, with R^2=98.761 and according to our knowledge, this is the first procedure, ever described in the literature, to use a SALDI-MS method for the quantification of a protein.

3. After the systematic studies of several parameters that are important in SALDI-MS process, we did use the optimized method to detect the ricin B chain (one of the two chains in the ricin toxin) in real samples (soft drink and blood serum).

Before applying the method to real samples we did measure some semi-quantitative parameters for ricin. Different ricin B chain concentrations were also evaluated to see if some kind of calibration curve could be determined. This was not possible, in the available concentration range (limited by the producer's stock solution of 30 µM). Nevertheless, the lowest concentration detected (LOD) on the surface of unmodified CNWs, was 5 µM/0.5 µL, corresponding to 2.5 pmol/0.5 µL and to 80 ng/0.5 µL. This limit of detection is sufficient to detect the lowest amounts of ricin that are able to bring death to the persons that interact with the toxin, even if the sample are to be diluted 10 or 20 times (samples like soft-drinks or blood serum), because this would mean an initial ricin concentration of 1.6 µg. Injection of ricin has the highest lethal statistical percentage even if the LD_{50} = 10 µg/kg[45] is comparable to LD_{50} = 5-10 µg/kg for inhalation and the least dangerous is the oral ingestion, with LD_{50} = 1-20 mg/kg.[46] We can observe that our limit of detection is more than 3 times lower than the lowest median lethal dose. The MS signal saturation can be observed after the concentration of 15 µM (7.5 pmol/ 0.5 µL) of ricin B chain.

When we did spiked ricin in Coca-Cola (diluted 10 times with ammonium citrate), 55% of the SALDI-MS signal was recovered, even after the surface was rinsed intensively (2 times, using π stirring, 150 rpm, during 15 minutes). For blood serum we did use a 20 times

© 2020 Tous droits réservés.
lilliad.univ-lille.fr

dilution. 50% percent of the signal was recovered in blood serum, in comparison with the buffered ricin B chain solution, only. As this is not a quantitative method, it is perfect for a rapid screening of contaminated samples, as even if we do multiply the LOD values by 2 (as the recovery rate of the signal was 50%), we can still get an appropriate signal.

As a more general conclusion, we do report for the first time in this chapter the detection of ricin B chain using SALDI-MS. We study different parameters, in order to optimize the process and we mainly did so using, initially, a model protein (cytochrome C). As all these systematic studies seem to fit for ricin B chain, we use the carbon nanowalls sensors to detect the ricin B chain in serum blood samples. These results contribute greatly to the evolution of SALDI-MS designs, as we do try to correlate certain physical and chemical characteristics of the surfaces with the ability to give rise to protein's MS signals. It is to be remembered that, nowadays, SALDI-MS used for protein detection it is still unachievable to a great extent.

© 2020 Tous droits réservés.
lilliad.univ-lille.fr

III.6. References

1 Menzel, C., Dreisewerd, K., Berkenkamp, S. & Hillenkamp, F. The role of the laser pulse duration in infrared matrix-assisted laser desorption/ionization mass spectrometry. *Journal of The American Society for Mass Spectrometry* **13**, 975-984, doi:10.1016/s1044-0305(02)00397-5 (2002).

2 Fatou, B. *et al.* Remote Atmospheric Pressure Infrared Matrix-Assisted Laser Desorption-Ionization Mass Spectrometry (Remote IR-MALDI MS) of Proteins. *Molecular & Cellular Proteomics* **17**, 1637, doi:10.1074/mcp.TIR117.000582 (2018).

3 Sunner, J., Dratz, E. & Chen, Y.-C. Graphite surface-assisted laser desorption/ionization time-of-flight mass spectrometry of peptides and proteins from liquid solutions. *Analytical Chemistry* **67**, 4335-4342, doi:10.1021/ac00119a021 (1995).

4 Tarui, A. *et al.* Gold-nanoparticle-supported silicon plate with polymer micelles for surface-assisted laser desorption/ionization mass spectrometry of peptides. *J Nanosci Nanotechnol* **9**, 159-164 (2009).

5 Chen, S. *et al.* Carbon Nanodots As a Matrix for the Analysis of Low-Molecular-Weight Molecules in Both Positive- and Negative-Ion Matrix-Assisted Laser Desorption/Ionization Time-of-Flight Mass Spectrometry and Quantification of Glucose and Uric Acid in Real Samples. *Analytical Chemistry* **85**, 6646-6652, doi:10.1021/ac401601r (2013).

6 Chen, C.-T. & Chen, Y.-C. Desorption/ionization mass spectrometry on nanocrystalline titania sol–gel-deposited films. *Rapid Communications in Mass Spectrometry* **18**, 1956-1964, doi:10.1002/rcm.1572 (2004).

7 Lewis, W. G., Shen, Z., Finn, M. G. & Siuzdak, G. Desorption/ionization on silicon (DIOS) mass spectrometry: background and applications. *International Journal of Mass Spectrometry* **226**, 107-116, doi:https://doi.org/10.1016/S1387-3806(02)00973-9 (2003).

8 Trauger, S. A. *et al.* High Sensitivity and Analyte Capture with Desorption/Ionization Mass Spectrometry on Silylated Porous Silicon. *Analytical Chemistry* **76**, 4484-4489, doi:10.1021/ac049657j (2004).

9 Nayak, R. & Knapp, D. R. Effects of Thin-Film Structural Parameters on Laser Desorption/Ionization from Porous Alumina. *Analytical Chemistry* **79**, 4950-4956, doi:10.1021/ac062289u (2007).

10 Shrivas, K., Kailasa, S. K. & Wu, H.-F. Quantum dots laser desorption/ionization MS: multifunctional CdSe quantum dots as the matrix, concentrating probes and acceleration for microwave enzymatic digestion for peptide analysis and high resolution detection of proteins in a linear MALDI-TOF MS. *PROTEOMICS* **9**, 2656-2667, doi:10.1002/pmic.200800772 (2009).

11 Castellana, E. T. & Russell, D. H. Tailoring Nanoparticle Surface Chemistry to Enhance Laser Desorption Ionization of Peptides and Proteins. *Nano Letters* **7**, 3023-3025, doi:10.1021/nl071469w (2007).

12 Chiang, C.-K. *et al.* Detection of Proteins and Protein−Ligand Complexes Using HgTe Nanostructure Matrixes in Surface-Assisted Laser Desorption/Ionization Mass Spectrometry. *Analytical Chemistry* **82**, 4543-4550, doi:10.1021/ac100550c (2010).

13 Liu, Z. & Schey, K. L. Optimization of a MALDI TOF-TOF mass spectrometer for intact protein analysis. *Journal of The American Society for Mass Spectrometry* **16**, 482-490, doi:10.1016/j.jasms.2004.12.018 (2005).

© 2020 Tous droits réservés.
lilliad.univ-lille.fr

14 Chen, W.-T., Chiang, C.-K., Lee, C.-H. & Chang, H.-T. Using Surface-Assisted Laser Desorption/Ionization Mass Spectrometry to Detect Proteins and Protein–Protein Complexes. *Analytical Chemistry* **84**, 1924-1930, doi:10.1021/ac202883q (2012).
15 Au - Signor, L. & Au - Boeri Erba, E. Matrix-assisted Laser Desorption/Ionization Time of Flight (MALDI-TOF) Mass Spectrometric Analysis of Intact Proteins Larger than 100 kDa. *JoVE*, e50635, doi:doi:10.3791/50635 (2013).
16 Stolee, J. A., Walker, B. N., Zorba, V., Russo, R. E. & Vertes, A. Laser–nanostructure interactions for ion production. *Physical Chemistry Chemical Physics* **14**, 8453-8471, doi:10.1039/c2cp00038e (2012).
17 Hosu, I. S. *et al.* Carbon nanowalls: a new versatile graphene based interface for the laser desorption/ionization-mass spectrometry detection of small compounds in real samples. *Nanoscale* **9**, 9701-9715, doi:10.1039/c7nr01069a (2017).
18 Chen, J., Bo, Z. & Lu, G. in *Vertically-Oriented Graphene: PECVD Synthesis and Applications* (eds Junhong Chen, Zheng Bo, & Ganhua Lu) 11-18 (Springer International Publishing, 2015).
19 Sobaszek, M. *et al.* Diamond Phase (sp3-C) Rich Boron-Doped Carbon Nanowalls (sp2-C): Physicochemical and Electrochemical Properties. *The Journal of Physical Chemistry C* **121**, 20821-20833 (2017).
20 4th, F. P. *et al.* - Determination of internal energy distributions of laser electrospray mass. - *J Am Soc Mass Spectrom. 2014 Sep;25(9):1572-82. doi: 10.1007/s13361-014-0936-6.*, T - ppublish.
21 Agnoli, S. & Favaro, M. Doping graphene with boron: a review of synthesis methods, physicochemical characterization, and emerging applications. *Journal of Materials Chemistry A* **4**, 5002-5025, doi:10.1039/c5ta10599d (2016).
22 Marcano, D. C. *et al.* Improved Synthesis of Graphene Oxide. *ACS Nano* **4**, 4806-4814, doi:10.1021/nn1006368 (2010).
23 Houmad, M., Zaari, H., Benyoussef, A., El Kenz, A. & Ez-Zahraouy, H. Optical conductivity enhancement and band gap opening with silicon doped graphene. *Carbon* **94**, 1021-1027, doi:https://doi.org/10.1016/j.carbon.2015.07.033 (2015).
24 Hage, F. S. *et al.* Local Plasmon Engineering in Doped Graphene. *ACS Nano* **12**, 1837-1848, doi:10.1021/acsnano.7b08650 (2018).
25 Piret, G., Drobecq, H., Coffinier, Y., Melnyk, O. & Boukherroub, R. Matrix-free laser desorption/ionization mass spectrometry on silicon nanowire arrays prepared by chemical etching of crystalline silicon. *Langmuir* **26**, 1354-1361 (2009).
26 Achour, A. *et al.* Electrochemical anodic oxidation of nitrogen doped carbon nanowall films: X-ray photoelectron and Micro-Raman spectroscopy study. *Applied Surface Science* **273**, 49-57 (2013).
27 Eckmann, A. *et al.* Probing the Nature of Defects in Graphene by Raman Spectroscopy. *Nano Letters* **12**, 3925-3930, doi:10.1021/nl300901a (2012).
28 Tang, B., Guoxin, H. & Gao, H. Raman Spectroscopic Characterization of Graphene. *Applied Spectroscopy Reviews* **45**, 369-407, doi:10.1080/05704928.2010.483886 (2010).
29 Tang, H.-W., Ng, K.-M., Lu, W. & Che, C.-M. Ion desorption efficiency and internal energy transfer in carbon-based surface-assisted laser desorption/ionization mass spectrometry: Desorption mechanism (s) and the design of SALDI substrates. *Analytical chemistry* **81**, 4720-4729 (2009).
30 Shirtcliffe, N. J., McHale, G., Atherton, S. & Newton, M. I. An introduction to superhydrophobicity. *Advances in Colloid and Interface Science* **161**, 124-138, doi:https://doi.org/10.1016/j.cis.2009.11.001 (2010).

© 2020 Tous droits réservés.
lilliad.univ-lille.fr

31 Dupré, M. *et al.* Investigation of Silicon-Based Nanostructure Morphology and Chemical Termination on Laser Desorption Ionization Mass Spectrometry Performance. *Analytical Chemistry* **84**, 10637-10644, doi:10.1021/ac3021104 (2012).
32 Chiang, C.-K., Chen, W.-T. & Chang, H.-T. Nanoparticle-based mass spectrometry for the analysis of biomolecules. *Chemical Society Reviews* **40**, 1269-1281, doi:10.1039/c0cs00050g (2011).
33 Achour, A. *et al.* Thermal properties of carbon nanowall layers measured by a pulsed photothermal technique. *Applied Physics Letters* **102**, 061903 (2013).
34 Chien, S.-K., Yang, Y.-T. & Chen, C. o.-K. The effects of vacancy defects and nitrogen doping on the thermal conductivity of armchair (10, 10) single-wall carbon nanotubes. *Solid State Communications* **151**, 1004-1008, doi:https://doi.org/10.1016/j.ssc.2011.04.025 (2011).
35 Ganz, E., Ganz, A. B., Yang, L.-M. & Dornfeld, M. The initial stages of melting of graphene between 4000 K and 6000 K. *Physical Chemistry Chemical Physics* **19**, 3756-3762, doi:10.1039/c6cp06940a (2017).
36 Chu, H.-W., Unnikrishnan, B., Anand, A., Mao, J.-Y. & Huang, C.-C. Nanoparticle-based laser desorption/ionization mass spectrometric analysis of drugs and metabolites. *Journal of Food and Drug Analysis* **26**, 1215-1228, doi:https://doi.org/10.1016/j.jfda.2018.07.001 (2018).
37 Rimini, E. in *Ion Implantation: Basics to Device Fabrication* Ch. 4, 131 (Springer US, 2013).
38 Coffinier, Y., Boukherroub, R. & Szunerits, S. in *Carbon Nanoparticles and Nanostructures* (eds Nianjun Yang, Xin Jiang, & Dai-Wen Pang) 331-356 (Springer International Publishing, 2016).
39 Amini, N., Shariatgorji, M. & Thorsén, G. SALDI-MS Signal Enhancement Using Oxidized Graphitized Carbon Black Nanoparticles. *Journal of The American Society for Mass Spectrometry* **20**, 1207-1213 (2009).
40 Kong, X. L. *et al.* High-Affinity Capture of Proteins by Diamond Nanoparticles for Mass Spectrometric Analysis. *Analytical Chemistry* **77**, 259-265, doi:10.1021/ac048971a (2005).
41 Chen, W.-Y. & Chen, Y.-C. Affinity-based mass spectrometry using magnetic iron oxide particles as the matrix and concentrating probes for SALDI MS analysis of peptides and proteins. *Analytical and Bioanalytical Chemistry* **386**, 699-704 (2006).
42 Tang, L. A. L., Wang, J. & Loh, K. P. Graphene-based SELDI probe with ultrahigh extraction and sensitivity for DNA oligomer. *Journal of the American Chemical Society* **132**, 10976-10977 (2010).
43 Chen, W.-Y., Wang, L.-S., Chiu, H.-T., Chen, Y.-C. & Lee, C.-Y. Carbon nanotubes as affinity probes for peptides and proteins in MALDI MS analysis. *Journal of The American Society for Mass Spectrometry* **15**, 1629-1635 (2004).
44 Kawasaki, H. *et al.* Layer-by-Layer Self-Assembled Mutilayer Films of Gold Nanoparticles for Surface-Assisted Laser Desorption/Ionization Mass Spectrometry. *Analytical Chemistry* **80**, 7524-7533, doi:10.1021/ac800789t (2008).
45 Fetter, L. *et al.* Electrochemical aptamer scaffold biosensors for detection of botulism and ricin toxins. *Chemical Communications* **51**, 15137-15140 (2015).
46 Schieltz, D. M. *et al.* Analysis of active ricin and castor bean proteins in a ricin preparation, castor bean extract, and surface swabs from a public health investigation. *Forensic Science International* **209**, 70-79 (2011).
47 Selvaprakash, K. & Chen, Y.-C. Detection of ricin by using gold nanoclusters functionalized with chicken egg white proteins as sensing probes. *Biosensors and bioelectronics* **92**, 410-416, doi:https://doi.org/10.1016/j.bios.2016.10.086 (2017).

© 2020 Tous droits réservés.
lilliad.univ-lille.fr

48 Selvaprakash, K. & Chen, Y. C. Detection of ricin by using gold nanoclusters functionalized with chicken egg white proteins as sensing probes. *Biosens Bioelectron* **92**, 410-416 (2017).

© 2020 Tous droits réservés.
lilliad.univ-lille.fr

Thèse de Ioana Silvia Hosu, Université de Lille, 2020

Chapter IV
Dual surfaces: SPR-MS and other bimodal techniques. Preliminary results and perspectives

© 2020 Tous droits réservés.
lilliad.univ-lille.fr

Thèse de Ioana Silvia Hosu, Université de Lille, 2020

Chapter IV. Dual surfaces: Preliminary results and perspectives

IV.1 Introduction....160
IV.2 SPR-MS using gold/graphene-based interfaces....162
IV.2.1 Important parameters when we combine SPR with MS……...162
IV.2.2 LSPR-MS…….……166
IV.2.2.1 Different methods for gold particles' network fabrication....168
IV.2.2.1.a Deposition of citrated gold nanoparticles (suspension, 20 nm) 168
IV.2.2.1.b Creating AuNPs through metallization and annealing (dewetting) ...170
IV.2.2.1.c Dots on the Fly....171
IV.2.2.2 LSPR-MS conclusions....172
IV.2.3 Graphene-SPR-MS……...174
IV.2.3.1 Graphene and graphene-like (graphene oxid/reduced graphene oxide) methods of deposition on glass/gold surfaces....176
IV.2.3.1.a Drop-casting....176
IV.2.3.1.a.1 Drop casting conclusions....178
IV.2.3.1.b Electrophoretic deposition (EPD)....179
IV.2.3.1.b.1 Sample deposition method....183
IV.2.3.1.b.2 Electropheoretic deposition conclusions....183
IV.2.3.1.c The transfer of CVD graphene through wet-transfer method....184
IV.2.3.1.c.1 Insulating layer between gold and graphene....188
IV.2.3.1.c.2 Use of pyrene-COOH....192
IV.2.3.1.c.3 CVD graphene wet transfer – conclusions....193
IV.2.3.1.d Layer by layer (LBL)....195
IV.2.3.1.d.1 Layer by layer conclusions....199
IV.2.3.1.e Bubble method....200
IV.2.3.1.e.1 Bubble method conclusions....201
IV.3 SERS-MS using CNWs....202
IV.3.1 Carbon nanowalls - Plasmon-free substrate for SERS/MS for ricin B chain detection……..206
IV.4 EC-MS using CNWs....209
IV.4.1 EC and detection of ricin……..217
IV.5 Conclusions and perspectives....218
IV.5.1 LSPR-MS graphene based dual surfaces……..218

© 2020 Tous droits réservés.
lilliad.univ-lille.fr

IV.5.2 SPR-MS graphene based dual surfaces……218
IV.5.3 SERS-MS graphene based dual surfaces……..220
IV.5.4 EC-MS dual surfaces……220
IV.5.5 Dual surfaces conclusion and perspectives……...220
IV.6 References.....224

© 2020 Tous droits réservés.

lilliad.univ-lille.fr

IV.1. Introduction

The detection of ricin with a better sensitivity, no matter the environment (water, air or in poisoned food), remains an important research domain of interest. We have described in Chapter I the fact that the most important classical methods for detecting ricin are ELISA or other immunoassay methods, SPR, optical methods and MS. Combined techniques (such as SPR and MS) can give rise to very interesting new type of analytical tools.

The role of a dual surface is to detect an analyte or a chemical interaction using two characterization methods, starting from the same interface and the same experiment/sample. There are several examples described in literature,[1-7] but to our knowledge, no comprehensive review of bimodal analytical techniques has been written. Generally, reviews or articles focus on specific combination of two techniques. Most of the methods described are used off-line, but on-line coupling is the final purpose. When it comes to MALDI-MS, on-line coupling is even harder to obtain, as one of the main principles it that molecules need to be desorbed and ionized in vacuum, to avoid contamination and ionic collisions, for high sensitivity and high resolution. Nevertheless, in this chapter we will limit ourselves to off-line combination of complementary techniques, as this is not the main goal of this thesis.

The main reasons why SALDI-MS is one on the method suitable for further development of dual surfaces for bimodal techniques are the followings:

1. Complementary information can be obtained. One classical well know mutual assistance in the analytical characterization tools is FT-IR and Raman, as one offers information about polar molecules and the other offers information about non-polar ones. Combining this kind of complementary techniques one can achieve unequivocal conclusions. This simple concept can be extended for other more quantitative analytical techniques, such as Surface Plasmon Resonance (that can provide binding kinetics and capacity, affinity constants between surface-ligand or ligand-analyte, real-time monitoring of molecular interactions, quantification, but may require further identification of the molecules),[5,8,9] Electrochemistry (that can study electrochemical reactions, achieve quantification, but may require redox mechanism oxidation, by-products elucidation)[6,7] and Surface Enhanced Raman Spectroscopy (that can offer information about the nature of functionalization, especially for non-polar molecules, chemical nature, but may require more precise identification and structural identification).[10,11] MS can offer complementary information to all these three methods. Better perspective over the complementarity will be offered in this chapter.

© 2020 Tous droits réservés.

lilliad.univ-lille.fr

2. On-field experiments are starting to appear, as some miniature and fieldable mass spectrometers are already developed.[12] Explosives and chemical warfare agent (CWA) stimulants have been some of the most commonly studied chemicals with miniature mass spectrometers. Even so this is not for usual use, so further on-field experiments are needed.[13]

3. MALDI-MS can be a technique easy to use, if all the steps of the procedures are well established. Once you have placed the MALDI-MS steel plate inside the spectrometer, all can be fully automated, again, if the methods are well established. The performances of MALDI-MS are up to the challenges of proteomics (that are brought to the analytical field) and it offers high resolution, high sensitivity and it can be applied on an extremely vast category of molecules, with different functional groups and different molecular weights.[14,15]

4. Some methods may require calibration, and this can be performed with LDI-MS. A recent example was given by Haick et al. that developed noise sensors (using CNTs and gold particles for resistor devices), but there is the need of GC-MS for the calibration of these devices.[16]

5. Nowadays, nanoparticle based analytical fields are well developed and this is the common background for many analytical principles in the detection field.[15,17,18] For example, optical properties, such as exhibiting surfaces Plasmon resonance, is common ground for SPR, SERS, MS and other techniques.

In this chapter we will focus mostly on SPR-MS, as it was already proven to be efficient in proteomics, together with MS.[9] Except the SPR-MS combination for detection of ricin, using a glass surfaces covered with gold and graphene-like materials (that is the main focus of this chapter), we will also describe the evolution and some perspectives for:

- combination with LSPR (localized SPR), using a cystein peptide on gold network nanoparticles.

- combination with surface enhanced mass spectrometry (SERS) for detecting ricin B chain itself, using CNWs.

- combination with electrochemistry (EC) for detection of glucose, using CNWS.

As stated in the previous chapters, the most difficult part of the thesis is to be able to detect entire proteins using SALDI-MS, as they are difficult to desorb and ionize without organic matrices. In fact, there are only few reports presented in literature related to detection of proteins using SALDI-MS based sensors, and the usual upper mass is around 12 kDa (where usually Cytochrome C is used as model protein for detection). Except the fact that we want to present new proof-of-concepts for these bimodal approaches, the main perspective is still to develop methods that are suitable for ricin sensitive detection.

© 2020 Tous droits réservés.
lilliad.univ-lille.fr

IV.2. SPR-MS using gold/graphene-based interfaces

The main goal of this section is to show how a dual SPR-MS surface could create an important tool, using an ultrasensitive carbon-based sensor for real-time detection of ricin. **Figure IV.2-1** presents a schematic representation of the SPR-MS dual surface preparation and use towards ricin. The graphene will enhance both SPR and MS signal (without adding of label or organic matrix). The ligand to be used is a sugar (galactose or galactose-based moieties), being specific for ricin B chain (lectin). SPR methods for ricin have already been extensively described in Chapter I. Nevertheless, MS methods are quite scarce, and there is no real presentation of SPR-MS dual technique for ricin detection.

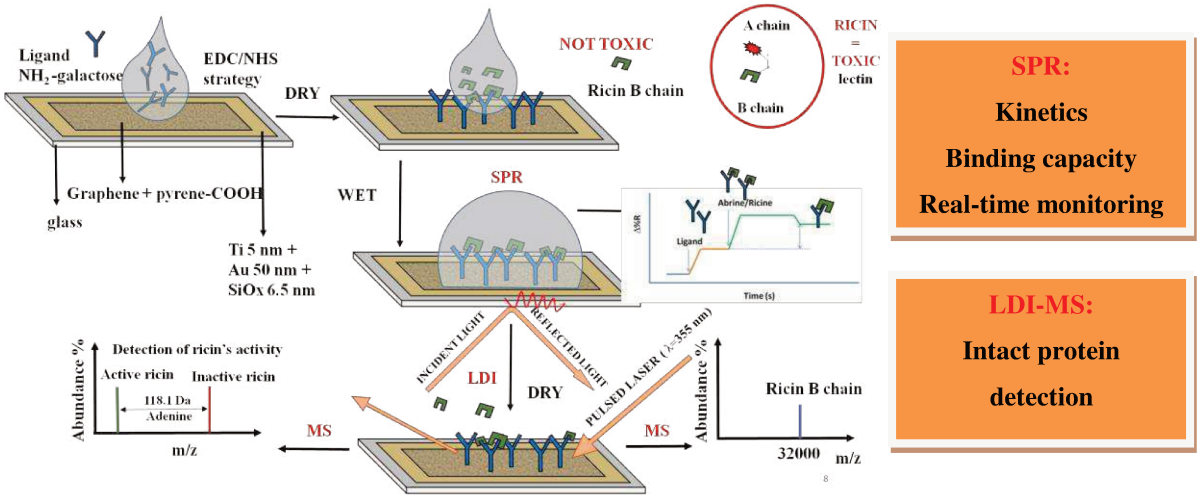

Figure IV.2-1 Schematic representation of combination of SPR-MS for the detection of ricin.

Quantitative (SPR) and structural identification of the analytes (MS), determination of the surface-ligand and ligand-analyte interactions, kinetics, real-time monitoring of affinity purification, binding capacity (SPR), and enzymatic activity (MS), are the main complementary benefits obtained by the development of such a powerful analytical tool. SPR is one of the few applicable techniques that allows monitoring dynamic interactions within a fluid environment that is similar to conditions encountered *in vivo*.[19] We have described mass spectrometry in detail. Herein we will describe SPR/LSPR and we will present why it is important to combine these techniques and what parameters are important to succeed to do so.

IV.2.1. Important parameters when we combine SPR with MS

In order to combine MS to some other techniques, the surface of the sensor has to be designed to suit both techniques, and the best strategy, from our point of view, it

© 2020 Tous droits réservés.
lilliad.univ-lille.fr

was starting to develop the SALDI-MS (surface assisted laser desorption/ionization mass spectrometry) sensors.

Even though carbon nanowalls (CNWs) are very efficient in the detection of ricin B chain in SALDI-MS, it is impossible to use them the way we described in the previous chapter, for both SPR or LSPR, as the graphene sheets are aligned vertically and the thickness is very unsuitable for SPR signal (the resonant material has to be lower than 300 nm, and our surfaces have more than 1 µm). Even the substrate that was used for the growth of the CNWs (silicon wafer) is impossible to use for SPR and LSPR, as it is not transparent and cannot act as a high-refractive index prism, to refract light. Electrical conductivity of the substrate is also an important factor. If the substrate is glass, it is important that the contacts are made with the electrical conductive surface (for example gold or silver, because these metals exhibit Surface Plasmon Resonance). The metal MALDI-MS plate is conductive, so the adhesive double carbon tape used in the experiments was overlapped to the gold surface, not only to the glass substrate.

A review written in 2019 describes different approaches for coupling SPR with MS.[5] The schematic representation of this review is presented in **Figure IV.2-2**. As for the SPR the most used is the classical Kretschmann configuration. The coupling with MS can be done either on-line or off-line.

For the off-line method the most used MS technology is MALDI-MS and there are 2 ways to use the SPR chips for such analysis: directly on the chip or eluting analytes from the chip and further analyze them with MS. For the direct analysis in the SPR chip there are also 2 ways: adding organic matrix on top (but the background peaks of matrix hinders the analytes peaks) or using the gold on the SPR chip as surface assisted laser desorption ionization (but mostly for small molecules). Bimodal imprinted chips were developed using photocleavable peptide on the silver-sputtered chip, which can be imprinted on another gold-coated chip to perform SPR analysis and the sample left on the silver-sputtered chip is detected by MALDI MS.[20] This process is anyway complicated and needs several organic synthesis (peptides were also biotinylated, the photocleavable linker at C terminal and cystein at N terminals etc). Using elution of the analytes from the SPR chip was combined with MALDI-MS or ESI-MS. Especially for ESI concentration or desalting steps can be introduced in between (as ESI is less tolerant to salts), but this introduces differences between MS and SPR results, as disruption of analytes interactions and separating the two analyzing techniques.

© 2020 Tous droits réservés.
lilliad.univ-lille.fr

As for the on-line method, many attempts to achieve real-time analysis of molecular interactions were done using SPR, but the results were a success for small molecules.[21-23] Valve package was used to transfer the SPR flow to an LC-MS system, without taking the SPR chip out[23] or connecting the SPR flow to a nebulizing gas tip that sprays the sample between the MS inlet and a direct analysis in real time (DART) ion source (on an ESI-MS equipment).[22] Desalting steps were skipped and ambient environment was used. Nevertheless, this is only possible for small compounds and the equipment modification is an important step in on-line measurements, even though real-time measurements have been achieved.

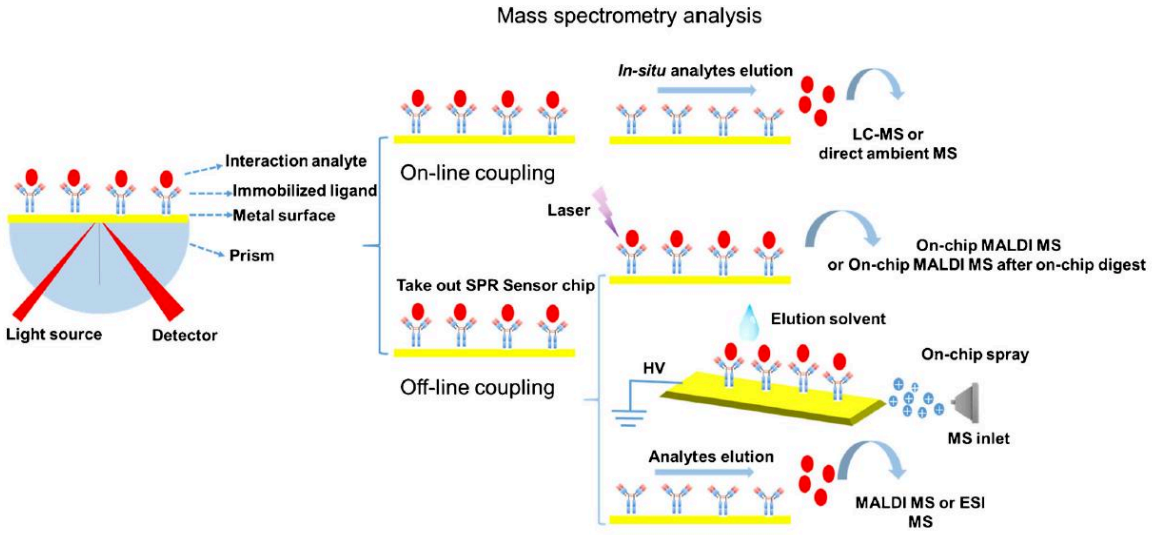

Figure IV.2-2 Different approaches for coupling SPR to MS.[5]

Some other SPR-MS literature is also presented in **Table IV.2-1**. An early example of combination of SPR with MS is described by Bujis, in 2005. A classical Biacore® gold chip is modified with calmodulin-binding domain (CBD) of myosin and to capture calmodulin from bovine brain extract, followed by recovery and identification of the captured material. They used an MS-compatible buffer (50 mM NH_4HCO_3) to wash and recovered around 300 fmol of calmodulin. Trypsin for digestion was also flowed using the SPR equipment, followed by CHCA (ethanol/acetone (2:1) with TFA 0.5%). After drying the gold chip was introduced in MALDI-TOF-MS and the recovered MS peaks were compared to a peptide digested database. This work is a good example of ligand fishing (identification and optimization of the interaction process between the recognition elements and the analyte), with automatization using very small amounts of samples (few µL) and rapid throughput. The combination with MS can also enable the role of post-translational modifications in protein function to be studied in the context of proteomics approaches.[24]

© 2020 Tous droits réservés.
lilliad.univ-lille.fr

Thèse de Ioana Silvia Hosu, Université de Lille, 2020

A relatively recent report presented the combination of SPR and MS. Brush Border Membrane Protein (BBMP) was used to create a biosensor, using a carboxymethylated dextran layer (present on the gold surface), which was further activated with EDC/NHS and coupling with BBMP was followed using SPR. Injections of ricin at different concentrations were performed. For the HPCE-ESI-MS, the ricin was physisorbed on the SPR sensor and BBMP was injected, using the SPR microfluidic system of the equipment. Due to the fact that ricin was not immobilized covalently on the surface of the sensor, when BBMP is injected, ricin-BBMP complex is formed and eluting with the solvent in the cleaning injection step. This complex is recovered at the waste exit and further studied with HPCE-ESI-MS.[19] Then, 28 proteins (contained in BBMP) known to interact with ricin were identified.

Remy-Martin[25] created a SPR gold etched prism (1.48 mm radius), using on chip digestion and matrix deposition for MALDI-MS. Identification and characterization of tryptic digest were used using a specific database and software. As we described in chapter III, this digestion of proteins is time and reagent consuming.

Table IV.2-1 Literature study presenting combination of SPR-MS of ricin and other molecules

year	MS technology	analyte	Recognition element	Buffer
2005 [24]	MALDI-MS	calmodulin	calmodulin-binding domain (CBD) of myosin	50 mM NH_4HCO_3, 2 mM $CaCl_2$
2009 [19]	HPCE-ESI-MS	Proteins that bind to ricin	dextran	HBS-EP
2012 [25]	MALDI-TOF MS	Monoclonal IgGs against lymphocyte-activation protein	rat serum albumin	sodium acetate buffer, pH 5.2 and 5.5.
2014 [20]	MALDI-TOF MS	Peptides (hemagglutinin A)	antibody AHA	PBS

Herein we propose to use gold to develop the SPR chip as enhancer of LDI-MS process, with the help of graphene, with unmodified MALDI-TOF-MS equipment, using the affinity strategy described **Figure IV.2-1** in for ricin-like proteins. Nevertheless, the proof of concept from preliminary results of the combination technique is done using cytochrome C, without any affinity step. But as we will present our results, we can emphasize the compatibility of the proposed strategy is feasible.

© 2020 Tous droits réservés.

lilliad.univ-lille.fr

IV.2.2. LSPR-MS

We have seen in Chapter I that gold nanoparticles can be used for the SALDI-MS detection of small compounds, peptides and even several small proteins as cytochrome C, BSA, insulin, with or without tryptic digest,[26] due to the ability of Au nanoparticles to absorb UV laser light.[27] As gold nanoparticles exhibit L-SPR properties, they will be further used in our experiments. Coating gold surfaces (plain and nanoparticles) with graphene will enhance the sensitivity of SPR signal.[28-31] In addition, due to its high surface to volume ratio, graphene sheets will promote high adsorption of organic compounds due to the π conjugated system properties that will also increase the MS signal and its ability to perform LDI-MS of proteins without organic matrix.[32]

LSPR is a non-specific technique because the signal is only dependent on the refractive index around the metal particle, and the specificity is only achieved through biomolecular recognition elements such as antibodies, ssDNA.[33] [34] Combining LSPR with MS is one solution to this problem. In this combined technique, the amount of analyte bound is quantitated by LSPR and the analyte is identified by MS.[35] The combination with MS can expand applications as it can identify and improve limits of detections, more likely in the lower mass region.

McLean et al.[36] detected peptides and small proteins (as bovine insulin) using different sizes of Au particles suspensions (2, 5 and 10 nm). Au particles sizes of 2 nm are not appropriate for LSPR, due to quantum sized effects for particles <3 nm. MALDI-TOF-MS presents peaks for Au^{3+} and Au^{5+} for 2 nm sized particles and the ionization order of Au from the background increases with size. The abundance of peptide peaks to Au ions is better for 2 nm than for 5 and 10 nm in the positive mode, but less sensitive in the negative mode. They did not try to deposit the gold nanoparticles in a repetitive network, that may have given more stability of the nanoparticles and less background peaks, but that the particles themselves could have been used for co-deposition in SALDI-MS. They did not use them for LSPR detection of the peptides detected in MS.

Microhole arrays have both SPR and LSPR properties, if diameter of the hole is equal to half of the periodicity.[37] Nanosphere lithography was used to attach silver nanospheres on glass slides. The slides were used for both LSPR and MS for the detection of amyloid beta oligomers (important for Alzheimer's Disease). Nevertheless, they did still used organic matrix for MALDI-MS.[34]

© 2020 Tous droits réservés.
lilliad.univ-lille.fr

Nevertheless, the literature and the studies for the combination of LSPR-MS is scarce, leaving place for many improvements and optimizations.

For the LSPR-MS purpose, we also need a substrate that has to be transparent and conductive. To do so, glass slides were covered by a conductive aluminum-doped zinc oxide thin film (AZO) and used for further modification with gold nanoparticles (AuNPs) in order to obtain a substrate that could combine both SALDI-MS and LSPR. First crucial point is to control the gold particle network. Several methods can be used for the formation of such LSPR surfaces. One of these methods is the deposition of thin metallic films (such as Ag and Au, because they exhibit LSPR properties) on a glass slide covered with a transparent electric thin film (300 nm of AZO, by PVD) and annealing at 500°C, during 1 min. **Figure IV.2-3** presents such a surface, in comparison with a similar surface that could be used for SPR. Other options to be considered: e-beam lithography (which is high-cost, but could create a very symmetrical arrangement of nanoparticles). A particular e-beam lithography, named Dot on the fly technique was developed in IEMN.[38] Another method is the self-assembled monolayer of nanoparticles. PECVD (SiOx), could protect the nanoparticles from the environment and increase the thermal confinement. As perspective, the deposition of a high *K* dielectric material using ALD (Al_2O_3, ZrO_2, HfO_2), could be used to replace SiOx. These materials are usually used in electronics for better performances. Herein we will use only SiOx, as it is transparent. Graphene can be also used both to protect enhance SPR/LSPR and MS. The role of graphene will be explained and exemplified later on.

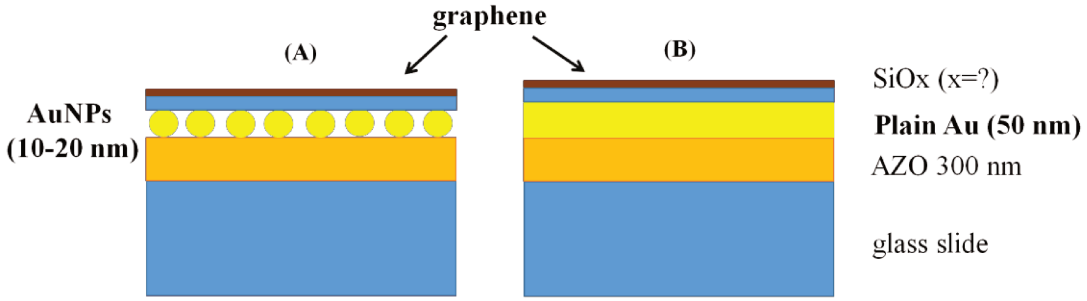

Figure IV.2-3 Representation of the desired surface for the dual applications: (A) LSPR-MS and (B) SPR-MS. Surfaces without AZO were also used.

Until this moment, we were not able to obtain an optimal network for the detection of proteins (only cysteine-terminated peptide) but we have strong beliefs that optimization of the density of the AuNPs on the surface, the SALDI-MS detection could be possible, as AuNPs were already used for the detection of cytochrome C.[39] We will describe in the following paragraphs the progress that we made and the further perspective of our preliminary results.

© 2020 Tous droits réservés.
lilliad.univ-lille.fr

IV.2.2.1. Different methods for gold particles' network fabrication

IV.2.2.1.a. Deposition of citrated gold nanoparticles (suspension, 20 nm)

Initially, we did deposit citrated gold nanoparticles over a glass surface modified with 3(aminopropyl)trimethoxysilane (through electrostatic interactions). We did replace glass slides with glass covered with aluminum-doped zinc oxide, to be sure that surface is electrically conductive. Citrate gold modified nanoparticles were also replaced with alkyl thiol modified gold nanoparticles, to have different suface modification and to observe if LSPR and MS experiments are influenced by these changes.

SEM top view images (**Figure IV.2-4A and B**) show how gold citrated nanoparticles cover the glass/AZO surface. The main problem is that the space between the particles is larger or equal to the particle size (20 nm), but the network is quite homogenous. LSPR experiments (shown in **Figure IV.2-4C)** were performed to establish what is the best incubation time of the citrated gold nanoparticles with the glass slides modified with APTMS, as increasing incubation time of AuNPs/glass increases the LSPR signal. Also, the preparation steps are presented in this figure.

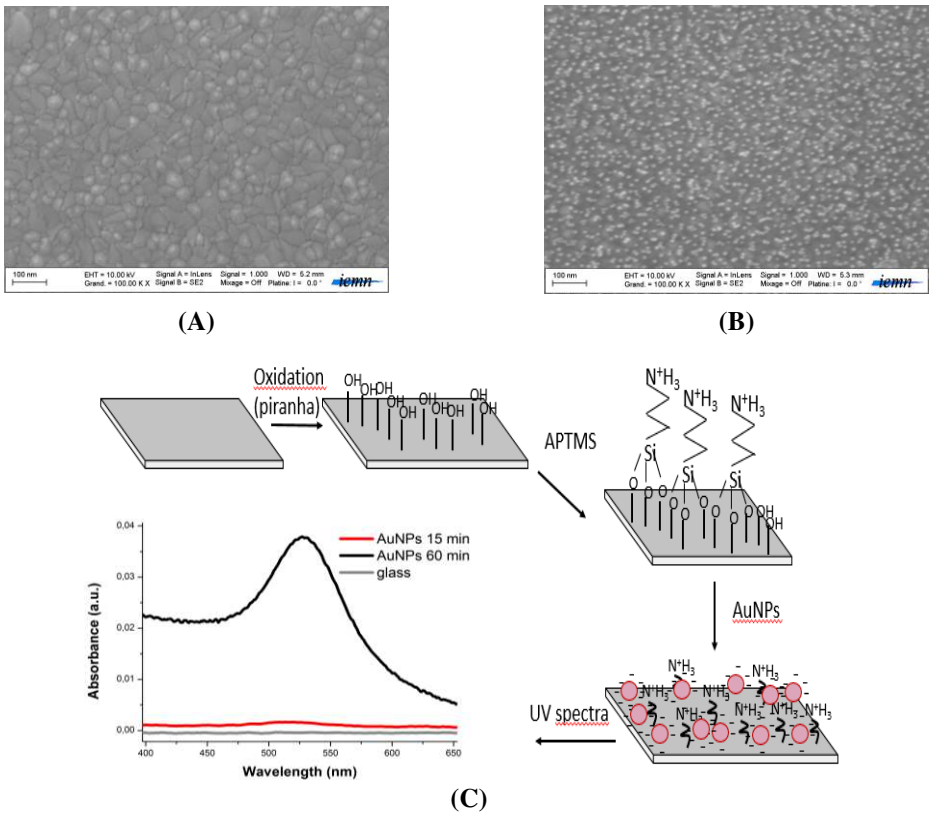

Figure IV.2-4 **(A)** SEM image of AZO/glass surface before **(A)** and after **(B)** citrated deposition AuNPs and **(C)** Schematic representation of AuNPs deposition (electrostatic) and UV spectra of the resulting AuNPs/glass interfaces for different incubation times: (red) 15 min and (black) 60 min.

© 2020 Tous droits réservés.
lilliad.univ-lille.fr

After establishing the incubation time (60 minutes) on glass slide, we have covered the glass slide with aluminum-doped zinc oxide thin films (~300 nm), to make the substrate electrically conductive, as SALDI-MS uses applied voltages on the ion source to obtain a gradient acceleration depending on the mass of the analyte. Regarding the LSPR signal, it is observed using UV-Vis spectrometry, that particles (20nm) absorb light at the 550 nm (**Figure IV.2-5**), even after citrate exchange with alkyl thiols (1-dodecanethiol, 1 mM) for increasing the hydrophobicity of the surface. The absorbance was increased from less than 0.2 arbitrary units (**Figure IV.2-4C**) to almost 0.7 arbitrary units (**Figure IV.2-5**), by evaporation of solvent, and increasing the initial AuNPs (20 nm) concentration 40 times. Also, incubation time of the nanoparticles was increased to 60 minutes, under a thin cover slide. Nevertheless, no difference in absorbance was observed after changing the ligand.

Ligand exchange changes the surface functionalization (**Figure IV.2-6**) and it should influence interaction with proteins, as citrate renders the surface covered with negative charges and alkyl thiols bind to gold through Au-S and create a self-assembled monolayer through Van der Waals interactions. WCA was measured before (WCA=60°) and after (WCA=90°) ligand exchange. Even though alkyl thiols are known to create hydrophobic surfaces (>100°), depending on nanostructuration and the alkyl chain, but in our case this doesn't happen, because of the fact that our AuNPs network is not well organized, and the space between the particles is larger than the particles themselves. We did not observe differences in morphology (using SEM, data not shown). There was no change in absorbance, when comparing citrated nanoparticles with thiol-modified ones. This is as expected, as alkanes do not absorb light in this region of wavelength.

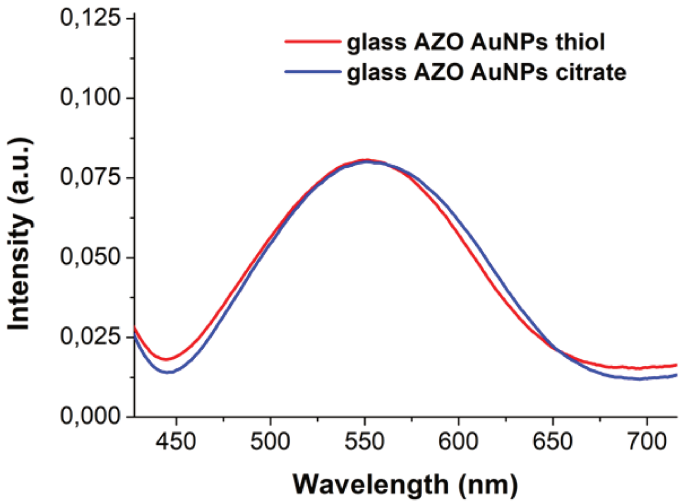

Figure IV.2-5 LSPR curves of glass/AuNPs with citrate ligand and alkyl-thiol ligand.

© 2020 Tous droits réservés.
lilliad.univ-lille.fr

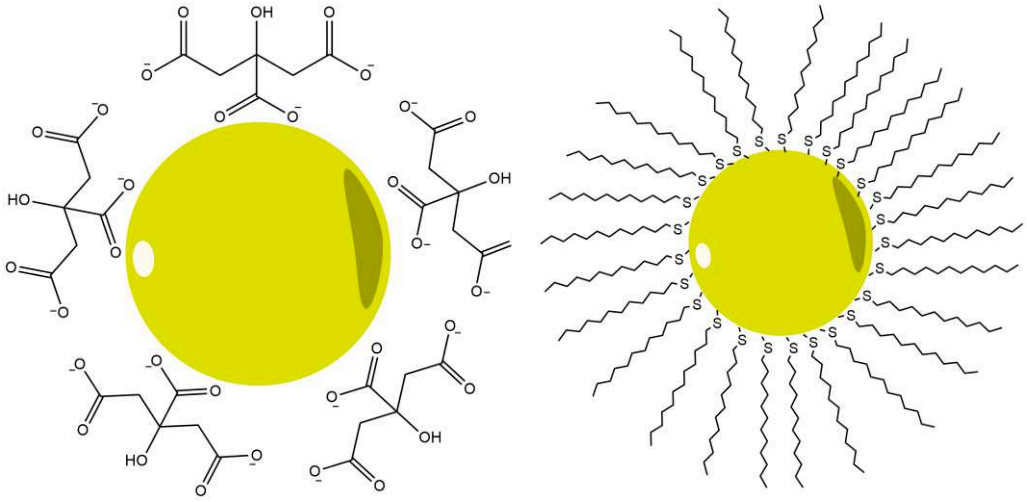

(A) **(B)**

Figure IV.2-6 Representation of gold nanoparticles with different ligands: **(A)** citrate and **(B)** alkyl thiol.

IV.2.2.1.b. Creating AuNPs through metallization and annealing (dewetting)

Deposition of 2, 4 or 6 nm-thick Au layers on glass slides and annealing (dewetting) at 500°C during 1 minute, to obtain Au nanoparticles. **Figure IV.2-7A** presents the SEM monograph of a 4 nm annealed Au film. It can be observed that the AuNPs created have around 10 nm in diameter. The increase of gold layer thickness creates a red shift, as expected, when LSPR is measured near 500 nm (**Figure IV.2-7B**).

To prove that the binding of some molecules may change the refractive index, we drop-casted and incubated a cysteine-terminated peptide (CysPol), that created a 8 nm red shift comparing with the sensor by itself or with the sensor incubated with solvent (EtOH:H_2O at 1:1 ratio). These results were represented in **Figure IV.2-7C**. Even if the shift is small, similar strategies were described in the literature, as the one using Au nanoparticles incubated with anti-biotin antibodies, which exhibited a 13 nm red shift or 11 nm shift, after binding biotin.[40] The problem of these surfaces is the stability of the AuNPs on glass. This issue is to be addressed in the following subchapters.

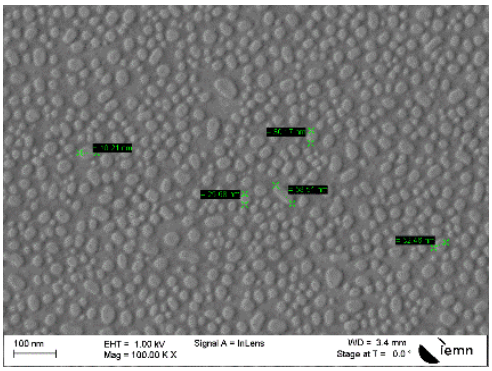

(A)

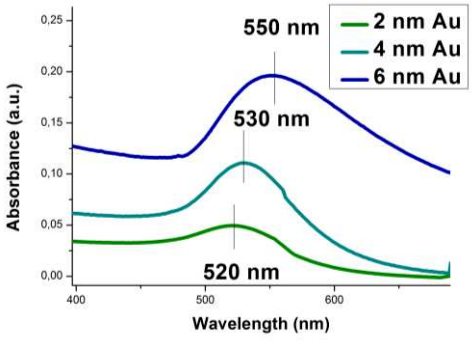

(B)

© 2020 Tous droits réservés.
lilliad.univ-lille.fr

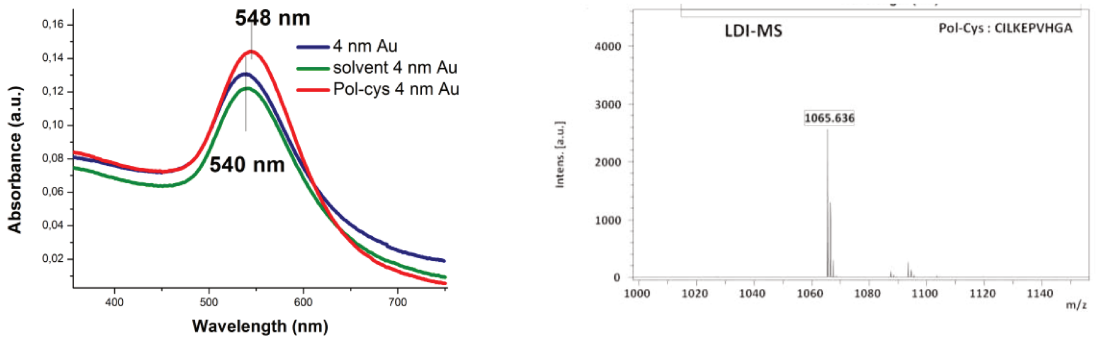

(C) **(D)**

Figure IV.2-7 (A) SEM monograph of AuNPS (4 nm) annealed on glass slide, at 500°C during 1min. **(B)** LSPR spectra of AuNPs/glass for different Au layer thicknesses after annealing at 500°C during 1 min, **(C)** LSPR spectra before incubation with CysPol peptide (blue), after incubation with solvent (green) and after incubation with CysPol peptide (red), **(D)** SALDI-MS (1065 m/z) spectrum of CysPol peptide studied with LSPR, using glass AZO/AuNPs.

IV.2.2.1.c. Dots on the Fly

This is a technique based on e-beam lithography writing using a continuous flow of electrons that will follow a pre-established pattern (mask). This technique was developed in the institute to make easier and faster (10 times faster) the writing of small patterns on huge area.[38] In our case, the substrate is a glass surface covered with hexamethyldisilazane (HDMS) acting as adhesion coating and poly(methyl methacrylate) PMMA 4% 950K diluted 5/3 (E-Beam positive resist). In **Figure IV.2-8**, is represented a gold particle network on Si surface. To do this type of network on both glass and ITO surfaces, we did dose tests to find the best writing parameters first. However, Au particles network that we designed was not obtained, mainly because of the bad adhesion properties of gold onto glass/ITO (**Figure IV.2-9**).

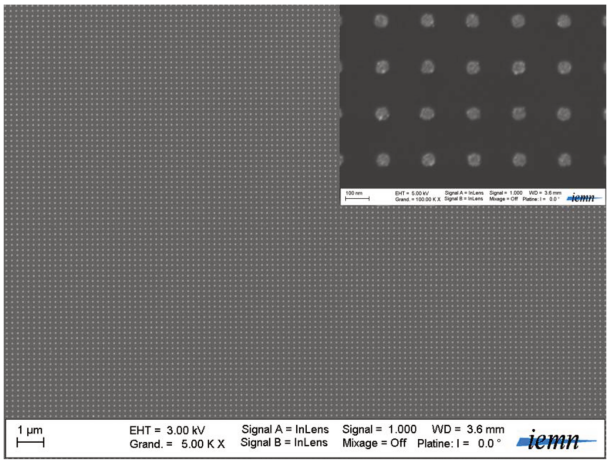

Figure IV.2-8 SEM images of gold nanodots on Si surface made *via* DoT technique with diameter of 50 nm and interspacing of 100 nm.

© 2020 Tous droits réservés.
lilliad.univ-lille.fr

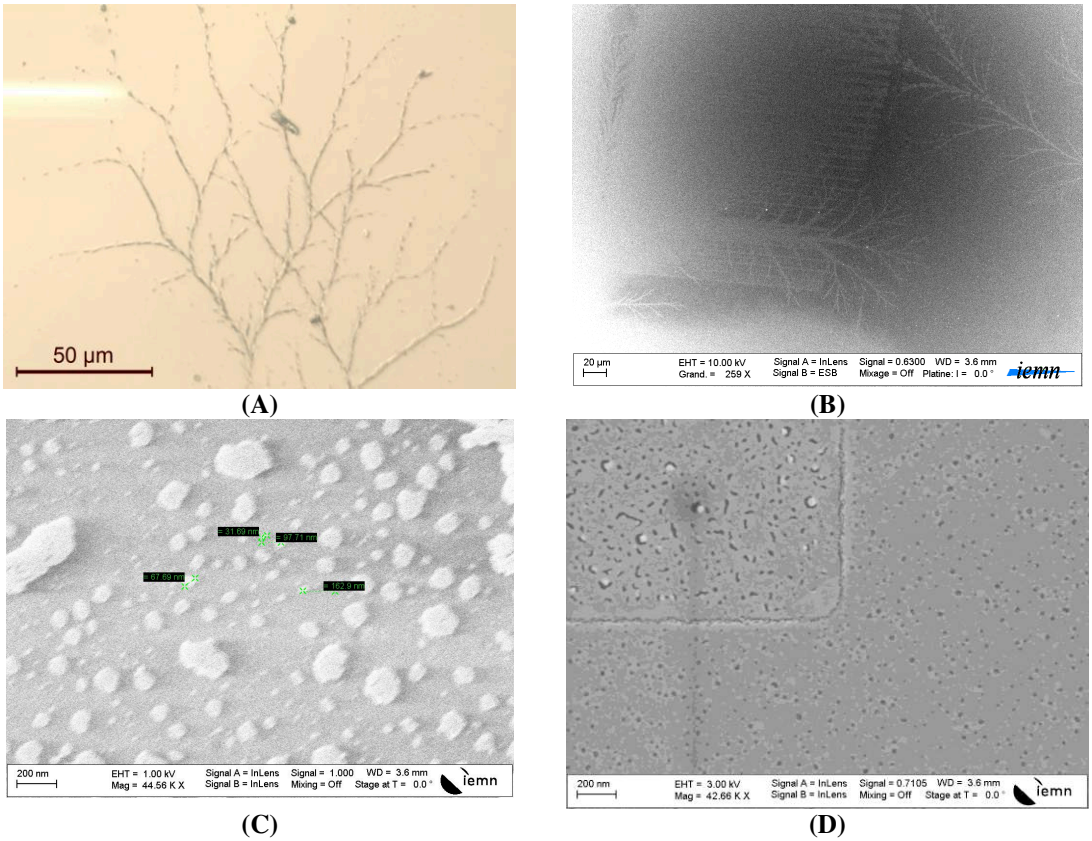

Figure IV.2-9 (**A**) Optical microscope image and **(B)** SEM for ITO dose tests for Au dots of 10 nm, (C) glass dose test for Au dots of 50 nm (245 uC) and (D) ITO dose test for Au 100 nm (225 uC)

IV.2.2.2. LSPR-MS conclusions

We did used 3 methods in order to create a gold nanoparticle network suitable for LSPR measurements: deposition of gold citrated nanoparticles, dewetting thin films of Au and e-beam writing of Au networks (Dots on the Fly method).

The least feasible, taking into account our experiments, is the Dots on the Fly method as several steps are involved and the bad adhesion of gold on glass was not even suitable to find the right current dose for creating a decent network. This method is expensive and requires e-beam writing.

We did succeed to obtain decent networks and LSPR-based absorbance shift using the dewetting method and gold citrated nanoparticles depositions. Even though dewetting method showed more potential in creating reproducible sized AuNPs, the stability is poor. This problem could be solved by following the graphene transfer or SiO_x deposition on top of the AuNPs network. AuNPs on AZO surfaces were more stable, and tuning ligand exchanges, deposition times and different sized AuNPs could influence greatly the sensitivity of the LSPR method.

© 2020 Tous droits réservés.
lilliad.univ-lille.fr

Thèse de Ioana Silvia Hosu, Université de Lille, 2020

Nevertheless, we did succeed to obtain a nice detection for binding cystein based peptide (3.2 mM) on the dewetted AuNPs, with both LSPR and MS, but the same procedure could be used for the citrated (or other ligand) deposited AuNPs.

From these perspectives, the best method would be using citrated gold nanoparticles, as more parameters could be optimized to obtain a stable LSPR signal (shift of absorbance).

© 2020 Tous droits réservés.

lilliad.univ-lille.fr

IV.2.3. Graphene-SPR-MS

Graphene also plays an important role on different ways: stability of citrated nanoparticles on the glass surface (for LSPR) and enhancing the SPR/LSPR effect because of the: high surface-to-volume ratio and π stacking interaction (efficient adsorption of biomolecules compared with gold), passivation of the surface against oxidation, controlling of the sensitivity with the number of graphene layers.[41-43]

Although graphene based materials are used in literature (usually graphene oxide,[44,45] reduced graphene oxide,[46,47] carbon nanotubes and other composite materials[47,48]), not actual reports of pristine monolayers of graphene are described in literature for SALDI-MS. Graphene absorbs UV-light (at 355 nm, MS's laser wavelength). The absorbed energy can be transformed in heat/photons and can desorb/ionize different molecules that stay in contact with the graphene layer. Graphene as a substrate material avoids the fragmentation of analytes, achieves good reproducibility and it has high salt tolerance.[49] It can act as a trap and transfer energy to the analyte, that will be desorbed and ionized, enhancing SALDI-MS. In the case of graphene oxide, the carboxylic groups act as proton donors in the LDI process also, and electrical conductivity is also lower. In fact, thermal conductivity of graphene oxide is 2-3 orders of magnitude lower than in pristine graphene, and this could be an advantage.

Graphene oxide and reduced graphene oxide are usually used to replace organic matrix in SALDI-MS, but usually the thickness of the deposited layer is too big for SPR. On the contrary, CVD graphene was used for SPR in our group and worldwide (as only one or few graphene layers are transferred on the surface), but it was not used in SALDI-MS.

Low stability of proteins and rapid degradation tendency determines soft ionization mass spectrometry to be a desirable tool for simple protein analysis. Even though graphene oxide and reduced graphene oxide were widely used in SALDI-MS for a variety of molecules, when it comes to proteins, the literature studies are quite scarce. When it comes to proteins detection, graphene-like materials as usually use for probing samples. Tang et al.[45] compared graphene oxide (GO) and few-layered graphene flakes (G, more comparable to reduced graphene oxide, rather than pristine graphene) for SALDI-MS detection of cytochrome C and single stranded DNA. Few-layered graphene flakes has a higher loading capacity for ssDNA, because of the hydrophobic and π-π interactions and was also used as extraction method in a mixed solution with cytochrome C. As the interaction between G and Cyt C is weaker (as hydrophobic G requires reorientation of hydrophilic cytochrome C, thus denaturation), the SALDI-MS spectra were better in comparison with GO, with lower fragmentation. Once

© 2020 Tous droits réservés.
lilliad.univ-lille.fr

again, we observe that the interaction between SALDI-MS substrate and the analyte is important.

The compatibility of graphene for enhancing both methods becomes one of the ways to achieve our goal: to create dual surfaces. For this purpose, in this section we will describe different methods of deposition for different graphene based materials and analyze them as SALDI-MS platforms for proteins (especially for cytochrome C) or peptides (mixtures MIX 1 and MIX 2 of peptides presented in the "methods and procedures chapter") and also check their compatibility with SPR. These are the real challenges of this part: to create depositions compatible with both techniques and to be able to detect proteins (as there is no actual report where SALDI-MS was combined with SPR for the detection of ricin).

© 2020 Tous droits réservés.
lilliad.univ-lille.fr

IV.2.3.1. Graphene and graphene-like (graphene oxid/reduced graphene oxide) methods of deposition on glass/gold surfaces

With these studies we do try to offer a more extended understanding of the LDI mechanism by conducting a systematic comparison within different graphene based deposition methods (drop-casting, layer-by-layer, bubble-surfactant deposition, electrophoretic deposition or wet transfer of CVD pristine graphene) using peptides, proteins and benzylpyridinium molecules (which are used to calculate the deposited internal energy, due to their ability to breakdown into known compounds with specific critical energies). The deposited internal energy is compared with the MS signal, signal-to-noise ratio and other characterization techniques, such as SEM, Raman, ellipsometry, AFM and profilometry.

IV.2.3.1.a. Drop-casting

The most easy and most used method in literature, when it comes to depositing graphene oxide (GO) and reduced graphene oxide (rGO) is drop-casting from solutions and drying of the drop-casted materials (**Figure IV.2-10**). This usually creates thick and not homogeneous films of material on gold surfaces or any other surfaces (this is not suitable for SPR, as we already described above) and the film is not so stable for LDI-MS, as GO/rGO on thick films can fly and form different carbon plumes and contaminate the ion source or the electrodes and also discharge effects may appear.[50] Even though, when it comes to MS, different mixtures (*e.g.* GO and rGO in glycerol mixtures or hybrid materials, such as polymers or metal based) were used during time and decreased this effects, but the problem was not solved.

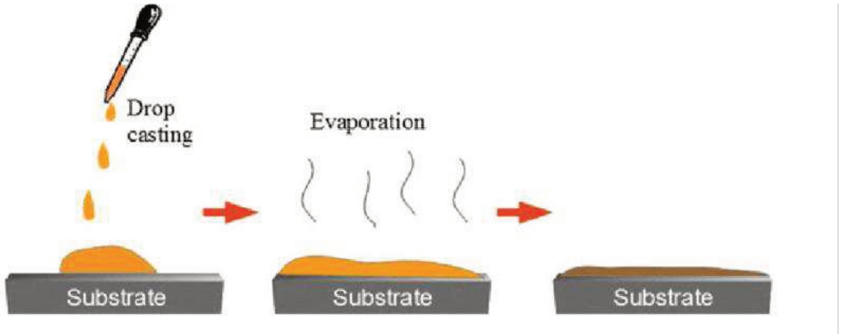

Figure IV.2-10 Schematic representation of drop-casted method.[51]

As observed by SEM (**Figure IV.2-11**) the homogeneity of drop casted graphene oxide (0.5 mg in water) and reduced graphene oxide (0.5 mg in DMF) is not very good, as graphene sheets crumple one over each other. This crumpling will affect both SPR and LDI-MS process. Especially SPR will be impossible, as the sheets are few µm of thickness.

© 2020 Tous droits réservés.
lilliad.univ-lille.fr

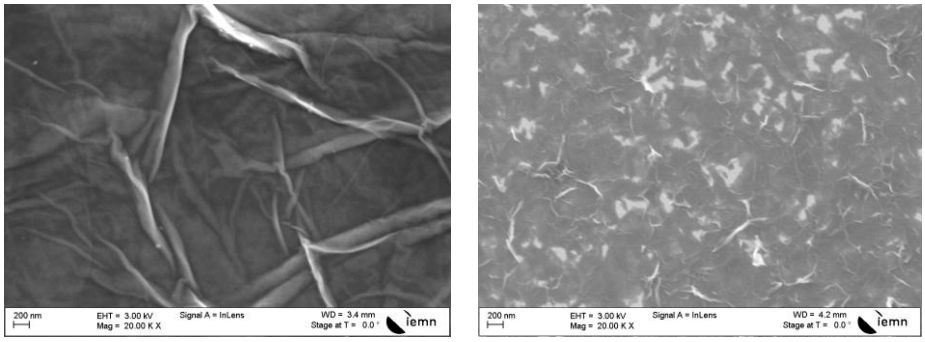

(A) **(B)**

Figure IV.2-11 SEM of **(A)** glass/Au/GO and **(B)** glass/Au/rGO.

The drop-casted GO or rGO solution (0.5 mg/ml water or DMF, respectively) on glass/Au surfaces were used for LDI-MS for the mixture of calibration peptides. The results in LDI-MS presented a lot of background peaks (as carbon ions dominate the MS spectra), especially for GO, where no peptide peaks were present (**Figure IV.2-12**). In the case of glass/Au/rGO, 3 peaks out of 4 peptides were identified for MIX 1 (but with barely 3 as signal-to-noise ratio value in the case of the lowest mass peptide) and 2 peaks out of 5 peptides were identified for MIX 2 (but the signal-to-noise ratio value was lower than 2). No peaks were identified in the case cytochrome C for either GO or rGO drop-casted surfaces. Graphene oxide presents various oxygen groups (–COOH, –OH, and –C(O)H) that interferes with the analyte peaks, in mass spectrometry. The hydrophobicity of the surfaces is also related to the oxygen groups and oxidized surfaces present usually better adhesion of hydrophilic analytes (as cytochrome C) and laser/desorption appears more often for the material-analyte together. As reduced graphene oxide has lower oxygen groups on the surfaces, the oxygen group related peaks are lower, with lower interference in the LDI-MS spectra. Also, the interaction of peptides may be stronger in the case of graphene oxide and may render the flight of the peptides by themselves more difficult.

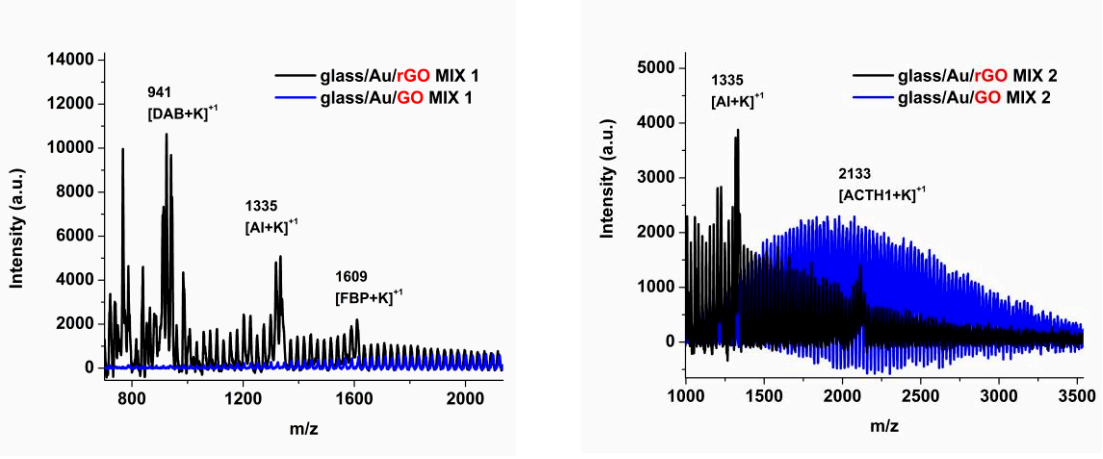

(A) **(B)**

Figure IV.2-12 SALDI-MS spectra of **(A)** MIX 1 and **(B)** MIX 2 using either glass/Au/GO or glass/Au/rGO drop-casted surfaces.

© 2020 Tous droits réservés.
lilliad.univ-lille.fr

IV.2.3.1.a.1. Drop casting conclusions

As expected, this method is not suitable for SPR, as the thickness of the deposited layer is too big. As for SALDI-MS, no protein was detected. 3 or 2 peptides were detected in the peptide mixtures (MIX 1 and MIX 2), but only in the case of reduced graphene oxide. This is mainly due to the low background noise, because of the lack of oxygen groups on the surface, that could be ionized and can be detected by MS. Wetability of the surfaces is also different, as the water contact angle of GO is around 50° and of rGO around 130°.[52] Hydrophobicity (in the case of rGO) was already described in Chapter II to enhance LDI-MS processes.

The main advantages of this method: simple, rapid, low-cost. The main disadvantage is that this method is not suitable for thin film depositions, especially for rGO deposition, which has higher electrical conductivity and may enhance better the SALDI-MS signal, as well as SPR. Another disadvantage of this method is the thick layers deposited on the surface could fly and stick to the ion source and contaminate it, together with other important parts such as electrodes.

© 2020 Tous droits réservés.
lilliad.univ-lille.fr

IV.2.3.1.b. Electrophoretic deposition (EPD)

Electrophoretic deposition (EPD) is a two-step process in which charged particles in suspension move toward an electrode of opposite charge due to the influence of an electric field and then deposit to form a compact film.[53] A schematic representation of the method is presented in **Figure IV.2-13**.

Graphene oxide has zeta potential of around -35 mV so it will move toward the anode (positively charged electrode). Different positive voltages have been used in literature for EPD of graphene, but higher ones create a thinner film of partially reduced graphene oxide on the gold surface. The problem is that high voltages also strip the gold film from the glass surface, so a compromise has to be made.

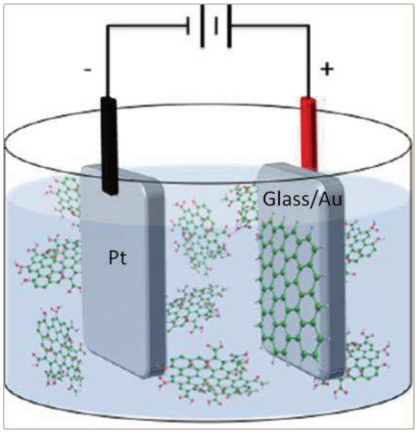

Figure IV.2-13 Electrophoretic deposition of graphene, adapted from reference.[53]

In **Figure IV.2-14A** it can be observed that 1 min of electrophoretic deposition (using 15 V and GO solution of 1mg/ml) creates less homogenous and less compact rGO film on the gold surface, by comparison with a 2 min deposition **(B)**. The transformation of GO into rGO, thorough electrophoretic deposition, was shown in our group.[54] The electrophoretically deposited GO shows a significant change in the C1s core level spectrum (**Figure IV.2-15**) with three dominant bands at 283.8, 285.5 and 287.3eV. The band at 283.8 eV, due to sp2-hybridized carbon, became predominant, suggesting the reconstitution of the graphitic network under the applied DC voltage.[54]

After the MS laser was used to shot the Au/EPD surfaces, it can be observed that holes and the melting of the Au (**Figure IV.2-14C and D**) occurs depending on the laser power. Also, different Au ions (Au^{1+}, Au^{2+} and Au^{3+}) start to appear at the laser power of cca. 56% (m/z=197). This is the laser power from which also Cyt C gets desorbed/ionized.

© 2020 Tous droits réservés.
lilliad.univ-lille.fr

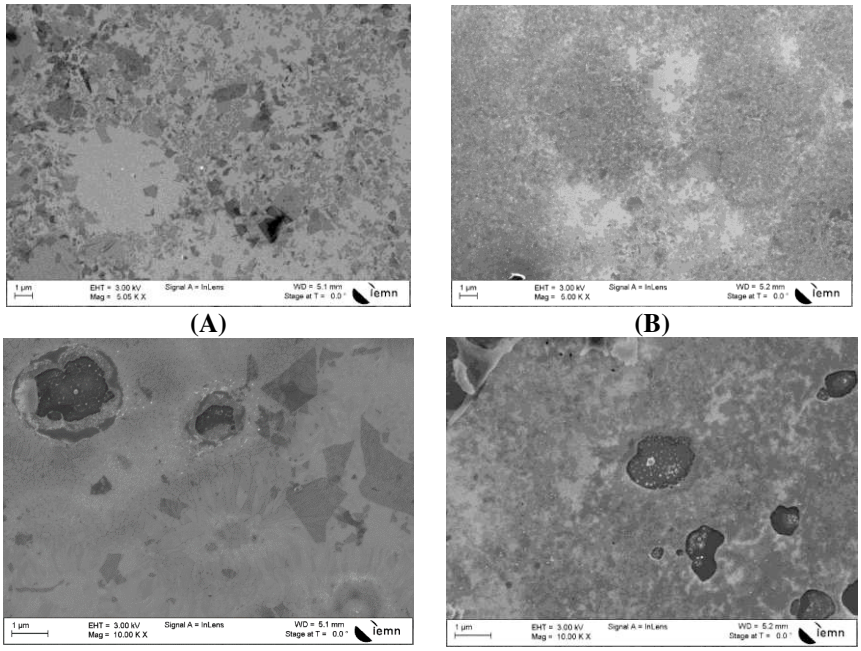

Figure IV.2-14 SEM images of EPD GO (1 mg/ml, 15 V) on gold during 1 min **(A,C)** and 2 min **(B,D)**, before and after laser shooting (70%).

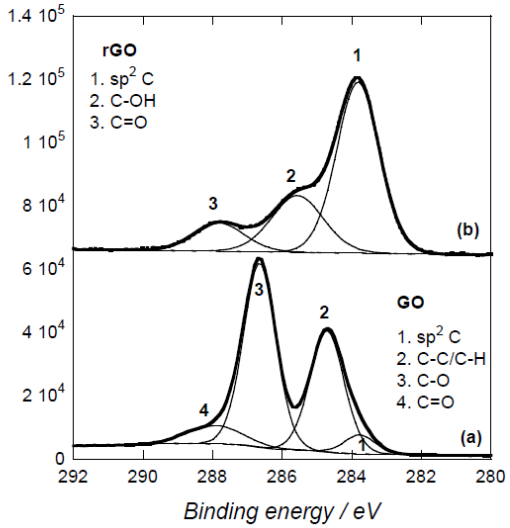

Figure IV.2-15 C1s core-level XPS spectra of GO before (a) and after (b) electrophoretic deposition onto the glass/Au interface.[54]

Even though several spots were drop casted (and dried in air) on both 1 and 2 min EPD surfaces, only one particular spot was efficient in detecting Cytochrome C, on the 2 min deposition. These results, as well as SEM images, are in accordance with the internal energies deposited on the surfaces (1.95 eV for 1 min deposition and 2.05 eV for 2 min deposition, in comparison with control gold sample, 1.94 eV). The MS spectra presented in **Figure IV.2-16A and B**, before and after re-hydration (after 24 H) of the drop casted spot, just before measuring the MS spectra. It can be observed that rehydration of the spot, increased significantly the MS signal, raising questions about the role of water in desorption of the

© 2020 Tous droits réservés.
lilliad.univ-lille.fr

protein and in the surface-protein interaction. Liu et al.[55] proved that both solvents and functional groups on the surface of DIOS are important for the LDI-MS process, as they used deuterated water in the preparation of analytes and their conclusion was that $[M+D]^+$ peaks (+1 uma) were present in the MS spectra, detrimental to the $[M+H]^+$. Residual solvent molecules, trapped in the nanostructuration of graphene, in our case, act as protonation species in the condensation phase of the LDI-MS process.

As the protein is hydrophilic, and the surface water contact angle is around 80° (due to partially reduced graphene oxide sheets), thus more hydrophobic.

This particular spot was studied with SEM, and it could be observed that the detection was possible where the deposition of Cyt C was not homogenous and the graphene sheets did not form a very thick layer, as on the drop casted Cyt C spots that did not give rise to any MS signal. (**Figure IV.2-16C**). Mechanical profilometer was used to estimate the thickness of the deposited Cyt C on the surface. It could be observed that the only drop casted spot that worked has many defects in the homogeneity of the protein layer, glass/Au interfaces are directly available for laser contact (**Figure IV.2-17**).

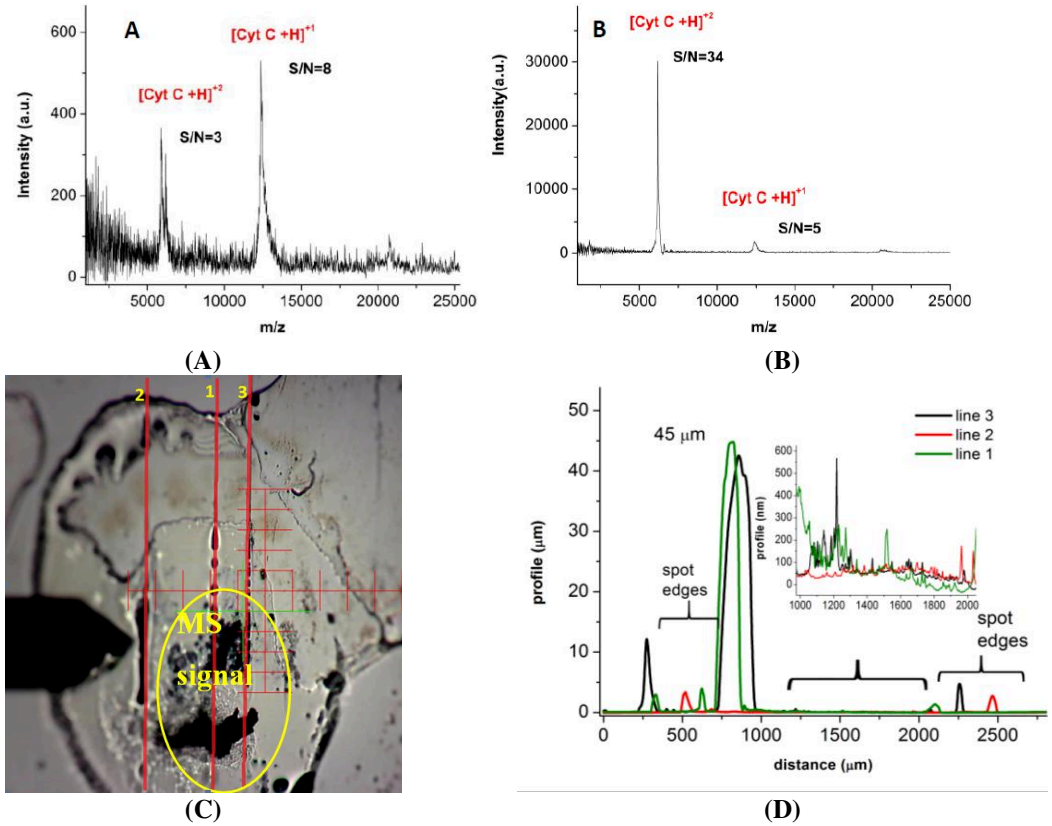

Figure IV.2-16 MS spectra of Cyt C (100 µM, in ammonium citrate 50 mM), drop casted on Au/EPD graphene oxide 15 V (2 min) before **(A)** and after re-hydration, after 24 H **(B)**. Microscope image of the Cyt C spot that give rise to MS signal **(C)**. Mechanical profiles registered for 3 different lines on the Cyt C spot from **(D)**.

© 2020 Tous droits réservés.
lilliad.univ-lille.fr

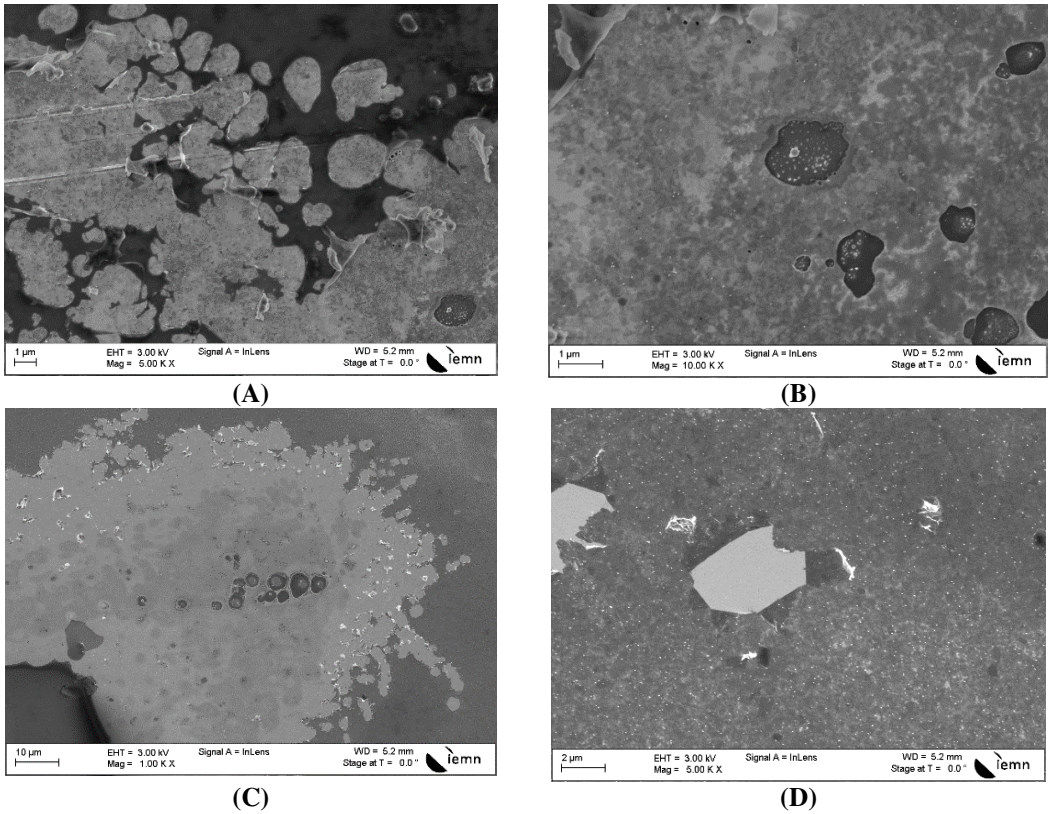

Figure IV.2-17 SEM images of Cyt C (100 µM, in ammonium citrate 50 mM), drop casted on Au/EPD graphene (1 mg/ml, 15 V, 2 min), on the spot with MS signal **(A, B)** and on the spot without MS signal **(C,D)**, laser fluence of 70%.

As EPD was proven above to be suitable in MS detection, we have also checked the SPR angle shift after the modification of the gold surfaces (**Figure IV.2-18**). As expected, the surfaces were suitable for obtaining a nice SPR peak, even though quite broad.

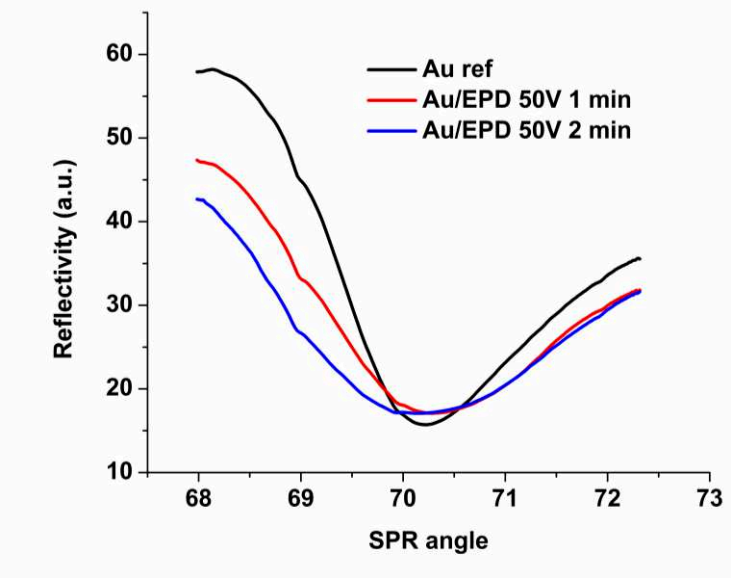

Figure IV.2-18 SPR curves for the glass/Au, glass/Au/GO deposited 1 and 2 minutes, using electrophoretic deposition at 15 V.

© 2020 Tous droits réservés.
lilliad.univ-lille.fr

IV.2.3.1.b.1. Sample deposition method

Different parameters for the detection of Cyt C, such as analyte concentrations (10, 50 and 100 µM Cyt C dissolved in 50mM ammonium citrate dibasic) and salt concentrations (5, 25, 50 and 100 mM ammonium citrate dibasic) were assessed (**Figure IV.2-19**). In all cases the Cyt C solution was simply drop-casted and let dried under ambient atmosphere. Unfortunately, we had to face a lack of reproducibility for getting MS signal of Cytochrome C. To try to improve our LDI-MS detection, we have chosen to incubate (during 1 min) the solution containing the analyte with the surface. The remaining liquid was absorbed with a clean room tissue by capillarity. The MS signal for single charged Cytochrome C appeared as expected, at 12384 m/z $[Cyt\ C+H]^+$ and the double charged molecule at 6193 m/z $[Cyt\ C+2H]^{2+}$. Even though the thickness of the EPD deposition was not too homogeneous (thick deposition up to ~800 nm, thin deposition1~up to 300 nm and thin deposition2~up to 200 nm), the MS signal was obtained for all 3 cases.

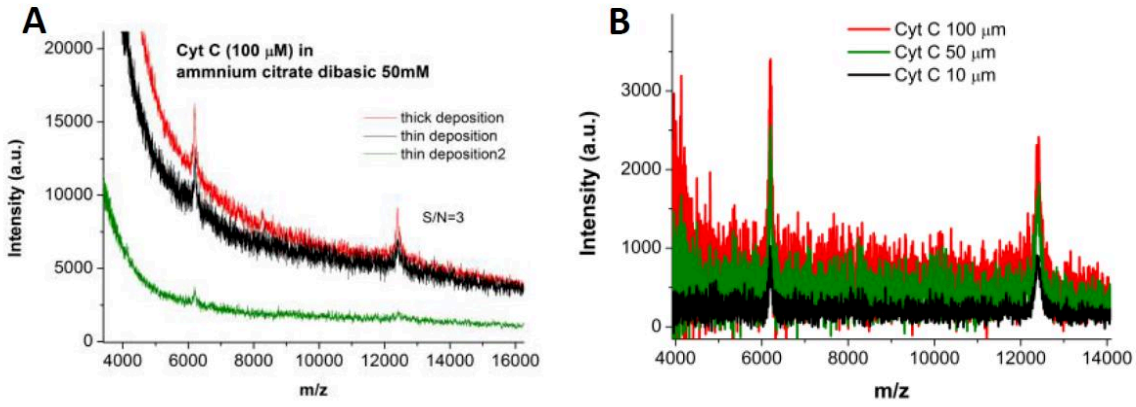

Figure IV.2-19 SALDI-MS spectra of Cytochrome C (50 pmol) using glass/Au/EPD surface, on different thickness depositions of rGO **(A)** and SALDI-MS spectra of different concentrations of Cyt C (B) (ammonium citrate dibasic 50 mM, laser power of 70%, linear positive mode). Deposition method: incubation during 1 min.

IV.2.3.1.b.2. Electrophoretic deposition conclusions

Incubation of the EPD (15V) surfaces with protein solutions seems to enhance the MS signal of Cyt C, probably due to smaller thickness of the protein layer and the increased possibility of the heat transfer from the surface to the protein. Nevertheless, reproducibility was not so good, and it is highly dependent on the homogeneity of the deposition, that was not too good. Several other voltages and deposition periods have to be tested, to obtain a better homogeneity/reproducibility.

© 2020 Tous droits réservés.
lilliad.univ-lille.fr

IV.2.3.1.c. The transfer of CVD graphene through wet-transfer method

The greatest advantage of this method is that it can easily be used for SPR, as pristine graphene layer is very thin (lower than few nanometers), as described above. **Figure IV.2-20** shows the schematic representation of pristine graphene of glass/Au surfaces. The biggest challenge and disadvantage of using pristine CVD, is that it was not used for SALDI-MS as usually horizontally pristine graphene layer is hard to obtain (as several complicated steps are to be followed) and acts as a rapid thermal dissipater, mostly, in the 2D plane of the layer, because of huge thermal conductivity (5300 W m^{-1} K^{-1}) and the lack of defects in the surface. The energy can be dissipated furthermore through the thin Au film.

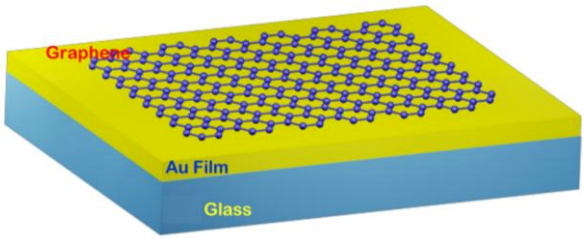

Figure IV.2-20 Schematic representation of pristine graphene on glass/Au surfaces.[56]

This problem could be solved partially by placing a thin layer of transparent insulator (with a refractive index similar to the prism, such as SiO_2/SiOx) between the gold layer and the graphene layer, as described earlier in **Figure IV.2-3**. This could also confine the heat, that will help LDI process and would enhance the SPR signal. The graphene CVD transfer was performed using the chemical wet method, using PMMA resist and H_2O_2/HCl/H_2O for the copper etching (see **Figure IV.2-21**).[57]

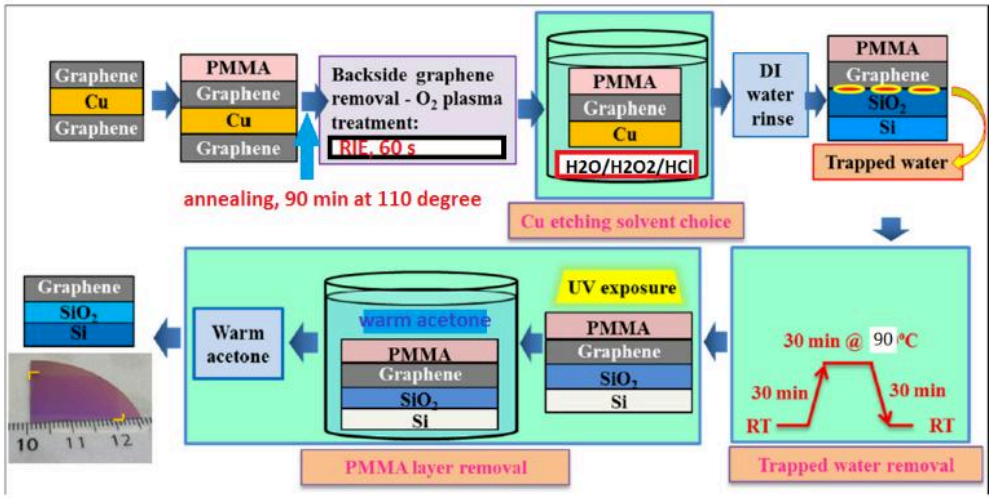

Figure IV.2-21 Wet graphene transfer process.[57] The backside graphene removal step was eliminated, for the work where Cyt C was detected by MS.

© 2020 Tous droits réservés.
lilliad.univ-lille.fr

Because we have tried several times (6 times) to detect cytochrome C using SALDI-MS based on the gold surfaces (with the transferred graphene on gold layer) and we only succeeded one time to detect cytochrome C using SALDI-MS, we made some presumptions of why this could have happened:

1. Some contamination of the graphene layer may have appeared, due to the Raman spectra (**Figure IV.2-22**), where the G band (1581 cm^{-1}) presents another peak at 1521 cm^{-1}, that initially it was considered a contamination. Nevertheless, this contamination doesn't seem to be residual copper, from unsuccessful removal (As EDX shows no copper contamination).
2. The Cyt C layer thickness may also be important, as the MS signal was obtained at the edge of the Cyt C spot. We have alredy discussed this problem in Chapter III and in the Appendix Chapter.
3. As ellipsometry studies of the glass/gold/graphene surface, which did function for SALDI-MS showed a thicker graphene layer than usual monolayer transfer (0.87±0.05 nm, corresponding to cca. 2 graphene layers).

The hypothesis where a contamination seems to be less probable, as EDX did not show any other traces of elements. Nevertheless, this method may not be sensitive enough to detect such contamination. The thickness of cytochrome C is important as well as re-hydration of the protein, as specified above in the electrophoretic deposition section. Finally, as ellipsometry showed us that 2 graphene layers may be the actual cause, we focused more on this specific case.

The surface obtained in this way was characterized by Raman (**Figure IV.2-22**). It is well known that the $I_{2D/G}$ for monolayers if above 2.0 and this ratio is related to the number of graphene layers. $I_{D/G}$=0.17 shows that we do not have many defects on the transferred surfaces, as it is similar to the $I_{D/G}$=0.10 for the copper/graphene surface used for the CVD growth of graphene (from the producer). It is stated in literature that Raman spectroscopy can clearly distinguish a single layer, from a bilayer from few (less than 5) layers, as for more than 5 layers is difficult to distinguish it from graphite.[58] The 2D band in a bilayer is up-shifted and broader than in monolayer graphene. Even though an up-shift is observed in our case from 1 monolayer (2697 cm^{-1}) to a bilayer (2706 cm^{-1}), no significant broadening is observed.

© 2020 Tous droits réservés.
lilliad.univ-lille.fr

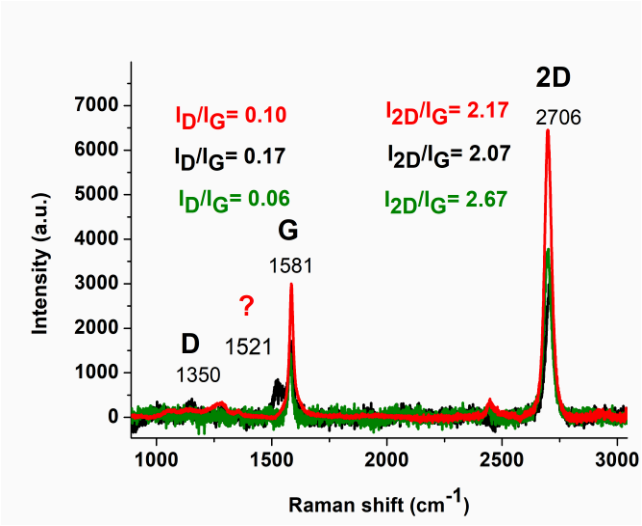

Figure IV.2-22 Raman spectra of glass/Au 1graphene layer (green) and glass/Au/ 2 graphene layers (black) and Cu/graphene from producer (red).

Cytochrome C (100 µM) and Insulin (200 µM) were drop casted (1µL) on the surface of the transferred pristine graphene (Au/CVD graphene), using both ammonium citrate (50 mM) and ammonium citrate dibasic (50 mM) + citric acid (50 mM) as solvents and ionizing salts.

Because, we observed that by using the buffer solution that contains citric acid (pH=4), insulin tends to precipitate (isoelectric point ~5). Even though the solvent containing citric acid did not precipitate Cytochrome C (isoelectric point 10.8), the MS signal was not better. So, we decided to only use ammonium citrate (50 mM) as buffer. **Figure IV.2-23** shows the SALDI-MS signal for Cytochrome C and Insulin, using ammonium citrate (50 mM). Only on some specific locations of the analyte dried spots gave MS signals. One of these locations were analyzed with SEM and EDX (**Figure IV.2-24A and B**) and compared to one location that did not work for SALDI-MS detection of Cytochrome C (**Figure IV.2-23C and D**). Copper contamination did not occur on EDX. It can be observed that no differences in morphology were found, except that the location where the MS signal was obtained, correspond to the edge of the Cyt C spot.

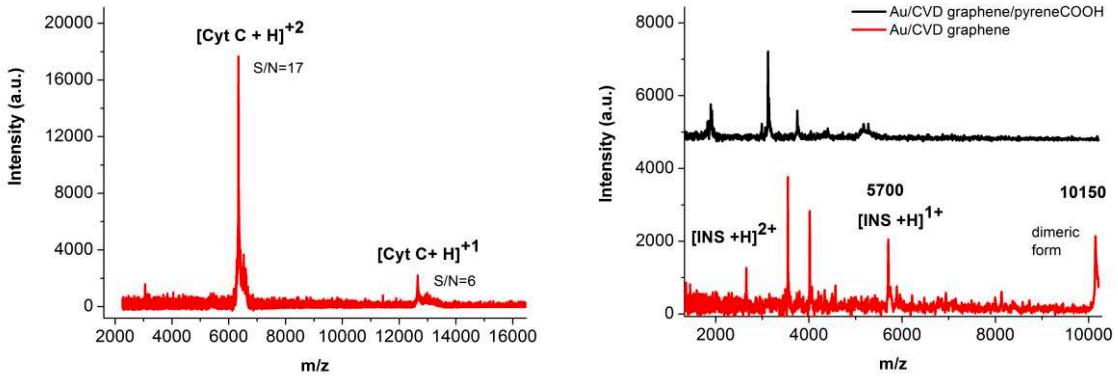

© 2020 Tous droits réservés.
lilliad.univ-lille.fr

(A) **(B)**

Figure IV.2-23 (A) Cytochrome C (50 pmol) using glass/Au/CVD graphene, and **(B)** insulin (100 pmol) detection by LDI-MS using glass/Au/CVD graphene with or without pyrene modification (ammonium citrate dibasic 50 mM, laser power of 70%, linear positive mode). Deposition method: drop cast and drying in air.

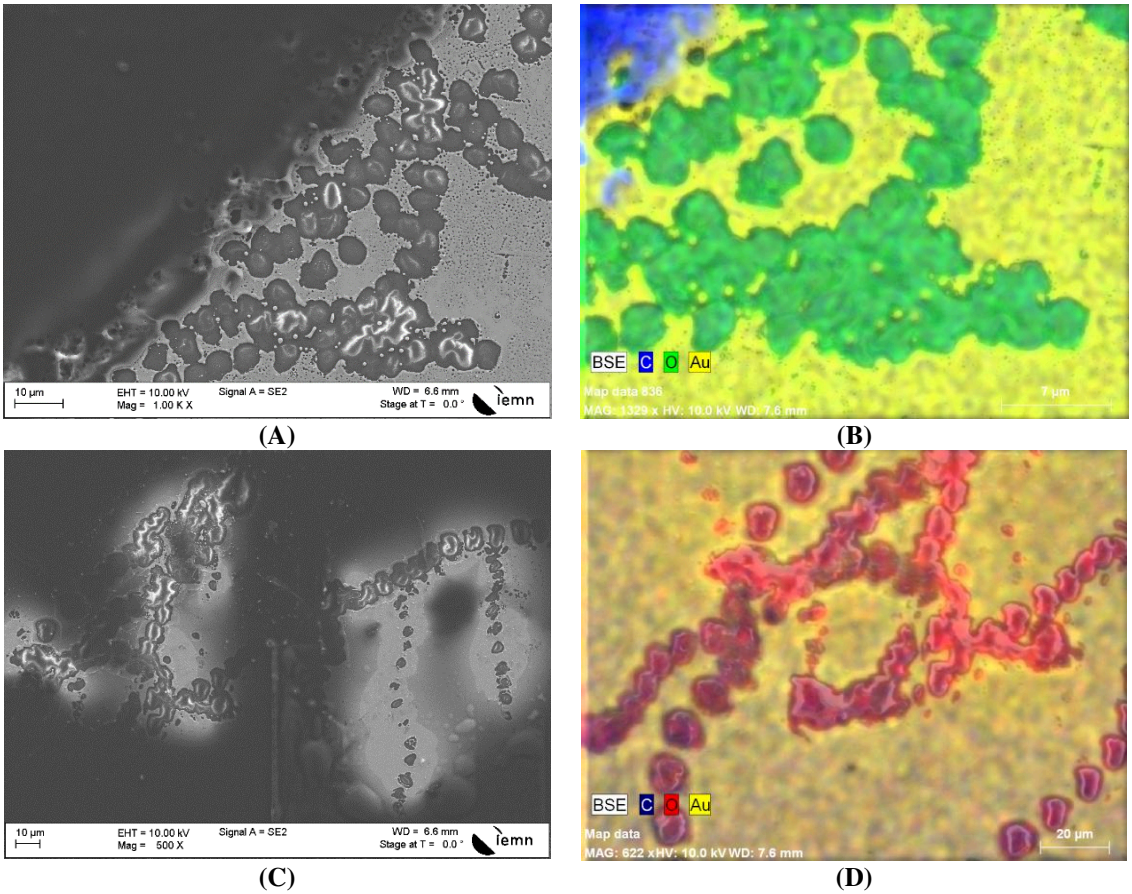

Figure IV.2-24 SEM images of drop casted Cyt C (50 pmol) on Au/CVD graphene surface, after the SALDI-MS analysis, **(A)** where Cyt C was detected and **(C)** where Cyt C was not detected. EDX mapping for the same spots (**B** and **D**).

As expected, the internal energy deposited on the Au/CVD graphene surface (1.83 eV) is lower than for the control sample (gold, 1.94 eV), due to the high conductivity of the plain sp^2 graphene layer. Using as received Cu/CVD graphene (not transfered and used as received) as control samples, did not result to MS peaks, even in the case of calibration peptides in MIX 1 and MIX 2. For this case (Cu/CVD graphene) the deposited internal energy was calculated to be 1.16 eV, apparently not enough for LDI-MS processes. Cu/CVD did not even permitted the desorption of benzyl pyridinium compounds, and calculation of survival yield was not possible. We did also try to detect Cytochrome C on Cu/CVD, but it did not work. From this point of view, copper contamination of the Au/CVD, seems less probable (not identified with EDX and not suitable for SALDI-MS).

Repeating the same CVD graphene transfer process, presented similar Raman peaks, telling us the idea that the 1521 cm^{-1} peak may be a contamination it is not standing and more

© 2020 Tous droits réservés.
lilliad.univ-lille.fr

related to the double layer graphene sheet. However, the MS signal for Cyt C was not found, after repeating again the experiment. Other deposition techniques were taken in consideration, for reducing the costs of the optimization process, as the thickness of the Cyt C layer may be very important, for the desorption/ionization process.

We did also try angular SPR mode for the above surfaces, as this could serve to goals: to establish if we did in fact transfer 2 layers of graphene (at least in some spots) and to observe if the surfaces could be used for SPR detection. The answer is yes in both cases. The results are presented in **Figure IV.2-25.** Simulations vs. measured SPR angular curves for glass/Au/ 1 layer of graphene show an overlap, as proof that the experiments were performed correctly. Measured SPR angular curves for surfaces with 1 and 2 graphene layers show that the difference in SPR angle is around 0.25 degrees and this is in accordance with literature.[41] Winspall software was used to simulate SPR curves, with the following parameters: (n_{prism}=1.52, n_{Ti}=2.36+i3.47 (d=5 nm); n_{Au}=0.197+i3.67 (d=50 nm); $n_{graphene}$=3.0+i1.216, at λ=670 nm, n_{SiOx}=1.48).[41,59] Good correlation was found between experimental and simulations.

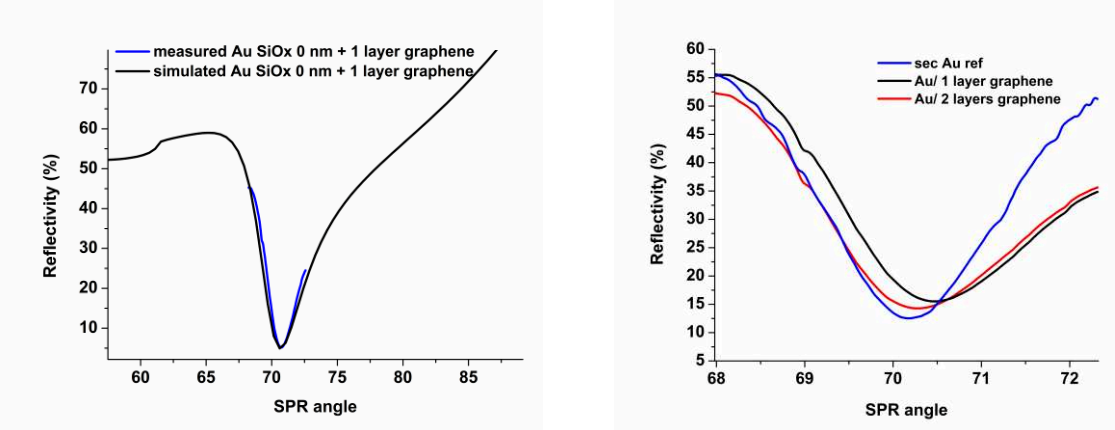

(A) **(B)**

Figure IV.2-25 (A) Simulated (black) and measured (blue) SPR angular curves for a glass/Au/1 graphene layer and **(B)** measured SPR angular curves for glass/Au (blue- reference), glass/Au/1 graphene layer (red) and glass/Au/2 graphene layers (black).

IV.2.3.1.c.1. Insulating layer between gold and graphene

The most attractive part of using gold coated silicon oxide surfaces was that silica may be easily modified due to the presence of the silanol groups, through silane coupling chemistry.[59] Beside this advantage, silica being an insulator may serve as a heat/energy entrapment at the surface, could enhance the laser desorption/ionization of molecules, thus improving the MS signal. High K refractive index materials are usually used as dielectric layers in electronic for insulating different materials. As we were only able to detect

© 2020 Tous droits réservés.
lilliad.univ-lille.fr

cytochrome C using glass/Au/ 2 layers of graphene only one time, we decided to add on top of gold thin layer (50 nm) a SiO_x layer. To determine the suitable thickness of this layer we took in consideration several parameters: suitability for SPR and sensitivity using SALDI-MS for peptides and cytochrome C.

In the case of SPR, SiO_x depositions of 3 and 6 nm only shifts the SPR angle with around 0.4 ° (for each 3 nm of deposition). These thicknesses seem to be suitable for SPR. (**Figure IV.2-26**).

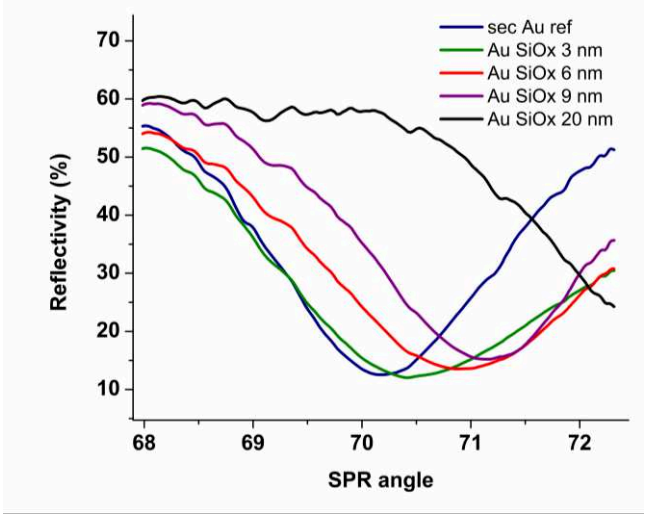

Figure IV.2-26 SPR curves for glass/Au and glass/Au with different thicknesses of SiO_x deposited on top: 3, 6, 9, 20 nm.

SALDI-MS was performed using MIX 1 and MIX 2. Angiotensin I was chosen as reference of comparison between several different thicknesses of SiO_x in glass/Au/SiO_x/graphene surfaces. Representations of signal-to-noise ratios for this peptide are shown in **Figure IV.2-27**. In both MIX 1 and MIX 2, the best results are obtained for a thickness of 6 nm (in terms of S/N and numbers of peptides detected from the mixtures). In the same figure the SALDI-MS spectra are also presented, for both mixtures.

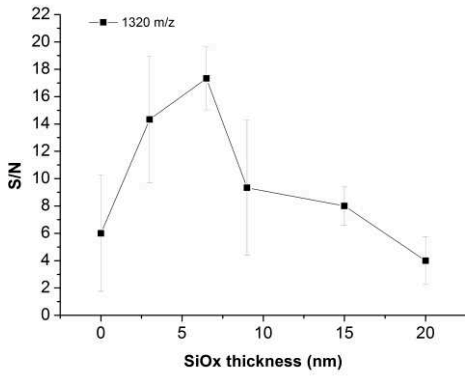

(A)

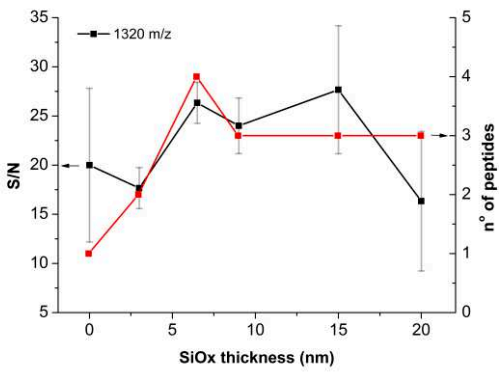

(B)

© 2020 Tous droits réservés.
lilliad.univ-lille.fr

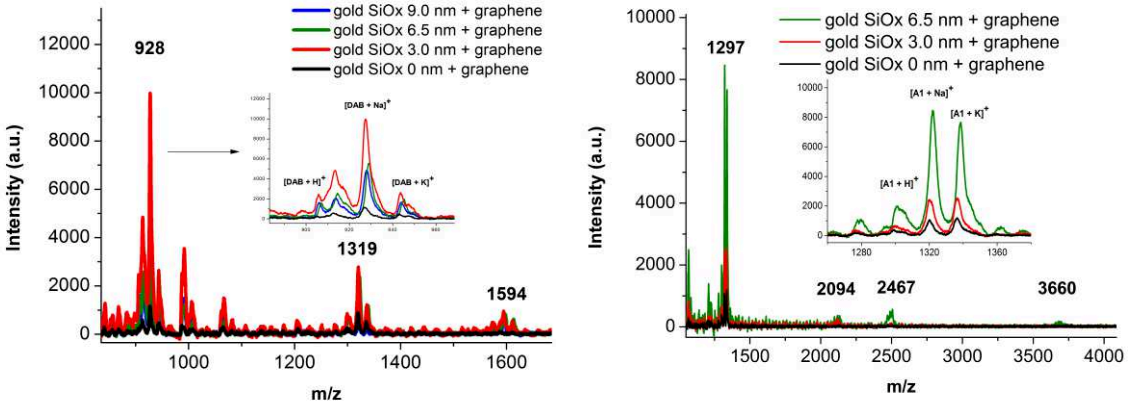

(C) **(D)**

Figure IV.2-27 Angiontensin 1 representation of signal-to-noise ratio from SALDI-MS spectra in **(A)** MIX 1 and **(B)** MIX 2 and SALDI-MS spectra of **(C)** MIX 1 and **(D)** MIX 2, using glass/Au/SiO_x of different thicknesses + CVD graphene.

For further characterization, we did also use SEM for top-views observation of glass/Au/graphene and glass/Au/SiOx graphene. It can be seen that adhesion of graphene on the SiOx layer is worse than in the case of gold, as several cracks appear on the graphene layer (**Figure IV.2-28A and B**). This could be also an advantage, as patterning graphene could stop the heat dissipation on horizontal large scale, and the deposition of thermal energy could be confined better. Raman spectra also presents typical G (1350 cm^{-1}), G (1580 cm^{-1}) and 2D (2706 cm^{-1}) bands, for 1 layer of graphene.

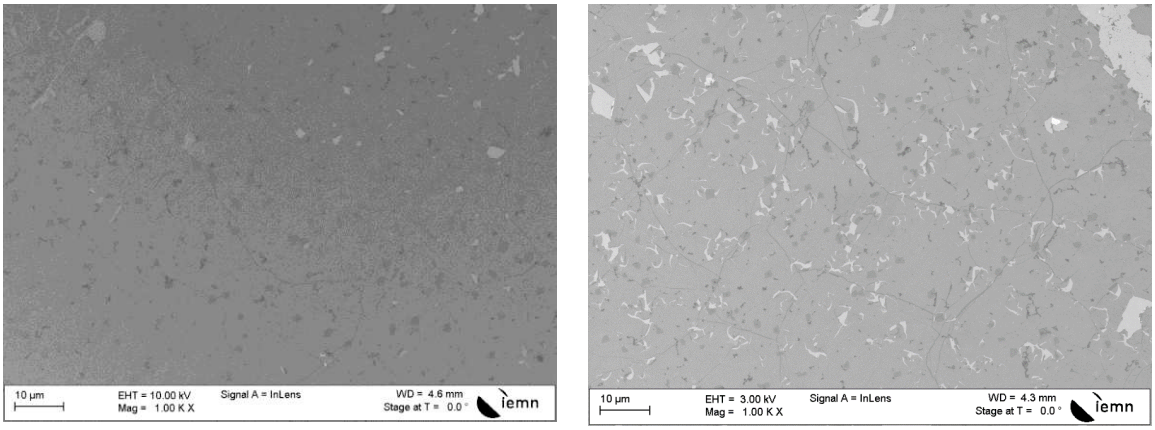

(A) **(B)**

© 2020 Tous droits réservés.
lilliad.univ-lille.fr

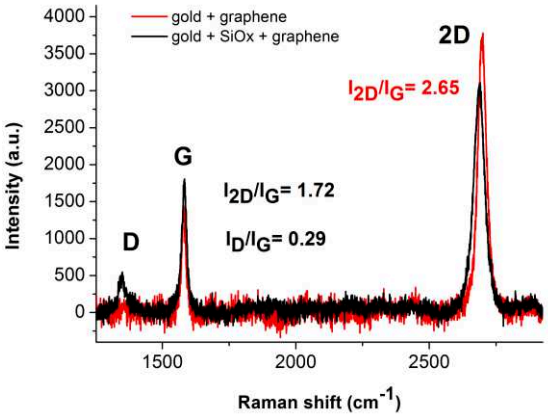

(C)

Figure IV.2-28 SEM top views of glass/Au/graphene **(A)** and glass/Au/SiO_x6nm/graphene **(B)**. Raman spectra of the same samples **(C)**.

Even if the WCA (**Figure IV.2-29**) of graphene on Au/SiO_x 0 nm is much higher compared to the WCA on Au/SiO_x 6 nm, the MS response is better in the case of the latter surface. Nevertheless, the water contact angle should increase as CVD pristine graphene is hydrophobic and uniformly transferred on the surfaces.

	Au SiOx 0 nm	Au SiOx 3 nm	Au SiOx nm 6,5	Au SiOx 9 nm	Au SiOx 15 nm	Au SiOx 20 nm
before transfer	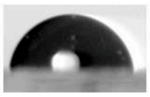	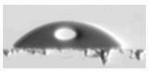	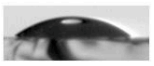	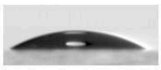		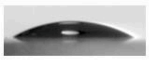
88°	46°	45°	33°	27°	32°	
after transfer	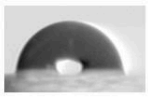		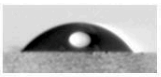			
95°	43°	52°	23°	21°	29°	

Figure IV.2-29 Water contact angle of different SiOx thicknesses on the glass/Au surfaces.

There are two possible reasons why the water contact angle is almost the same: wetting transparency of graphene (that is still quite controversial), but well described[60,61] or graphene instability on the SiO_x thin layer. We did study the stability of a drop of water on the glass/Au/SiO_x/graphene and we did observe that even a gentle nitrogen flow for removing the drop of water, destroys the graphene sheet (**Figure IV.2-30A**).

© 2020 Tous droits réservés.
lilliad.univ-lille.fr

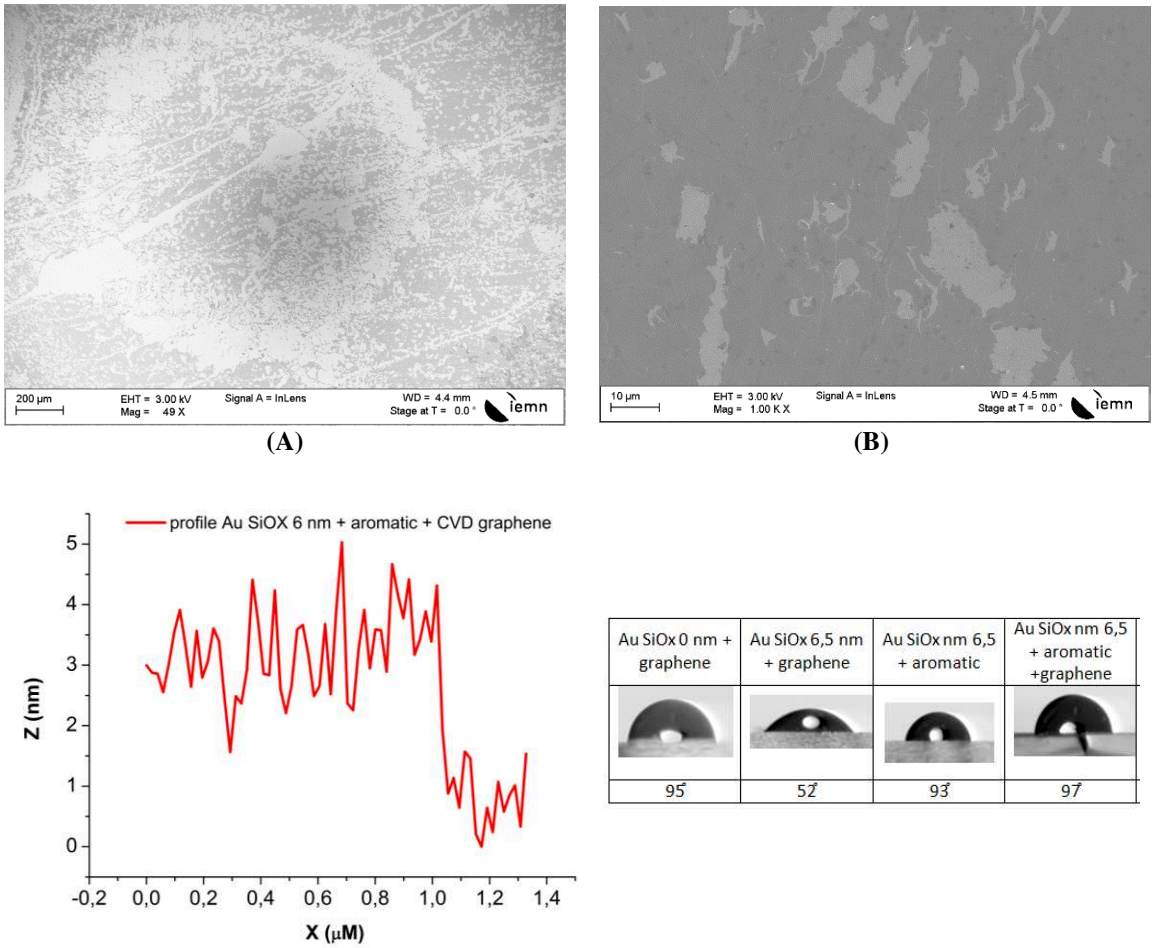

Figure IV.2-30 SEM monographs of the glass/Au/SiO_x/graphene after WCA, (A) before and after (B) modification with aromatic silane.

To improve the stability of graphene, we have modified the SiO_x layer, before graphene transfer, with an aromatic silane (Benzoyl propyl trimethoxysilane), through silanization technique. The π conjugated system of the silane can act as an adhesion layer for graphene. This improved the WCA (**Figure IV.2-30B**), as it can be observed using SEM. Also, the silane did not form a too thick film, as AFM confirmed (profile height 2.5 nm only). Apparently, the adhesion worked, as WCA angles also remained constant, when we compared glass/Au/graphene surface with the glass/Au/SiO_x/aromatic/graphene. (around 95°).

IV.2.3.1.c.2. Use of pyrene-COOH

Pyrene-COOH was used mainly for 3 reasons: because it can adsorb on the surface of graphene like materials, through π stacking, it provides extra carboxylic groups on the surface, which can be easily functionalized further forming amide bonds with galactosamine and also provides acidic hydrogen groups, which can act as proton donors in the LDI process.

© 2020 Tous droits réservés.
lilliad.univ-lille.fr

Pyrene was already used in literature for the preparation of graphene based SPR surfaces as non-covalent method of functionalization with nitrilotriacetic acid, which can chelate copper cations, that further coordinate with biotinylated cholera toxin. [42]

Even though Raman was used for surface characterization, after modification with pyrene, due to the great similarity of chemical structure of 1-pyrenecarboxilic acid with pristine graphene (π conjugated system), no differences were observed.[62] FT-IR showed only a slightly increase in intensity for the 817 (C-H out-of-plane deformation), 1263 (C-O stretching band), 2850 and 2925 (C-H stretching) cm^{-1}, in comparison to the pristine graphene.[63] Both FT-IR and water contact angle (≈90° before and <30° after 1–pyrenecarboxylic acid modification), presented in **Figure IV.2-31** show that pyerene-COOH is present on the surface of Au/graphene. Nevertheless, the peak at 1710 cm^{1} (C=O) was not identified, but this could be because of low intensities in FT-IR, due to low amounts of pyerene-COOH.

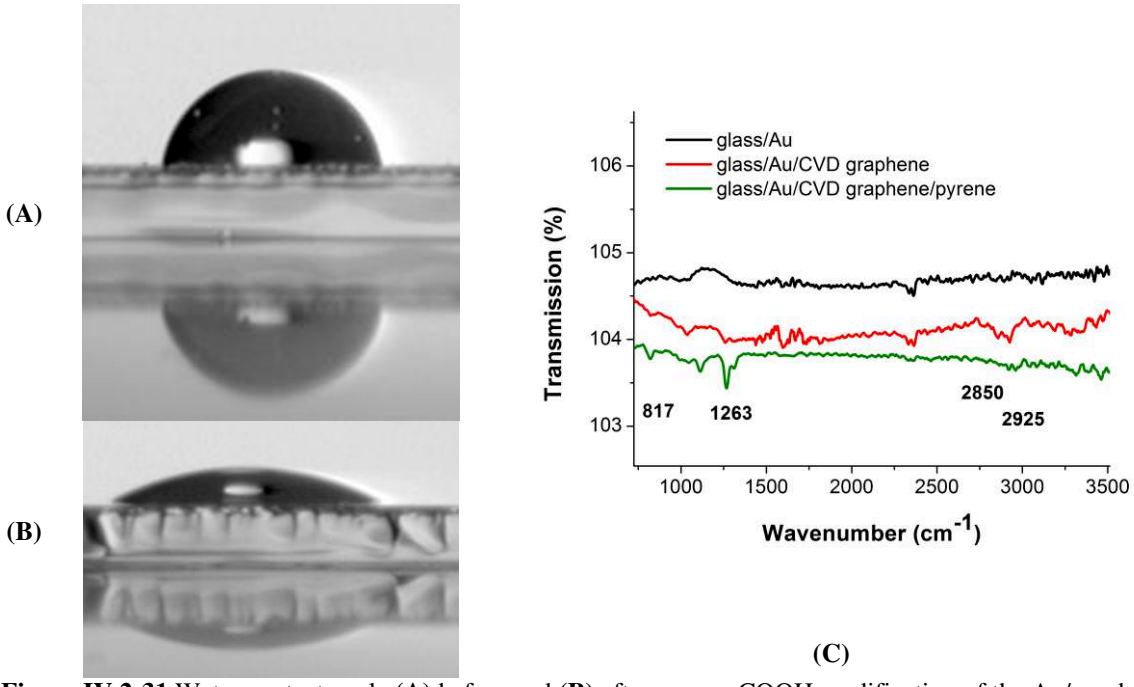

Figure IV.2-31 Water contact angle **(A)** before and **(B)** after pyrene-COOH modification of the Au/graphene surface. **(C)** FT-IR spectra of Au, Au/graphene and Au/graphene+pyreneCOOH surfaces.

IV.2.3.1.c.3. CVD graphene wet transfer – conclusions

Surprisingly enough, graphene deposited directly on gold allowed the detection of a model proteins (cytochrome C and insulin) without a thermal confinement layer. Another mechanism, except thermal desorption, may be involved in the LDI process. These results are very promising for the rest of the project. In addition, the detection was even better than for

© 2020 Tous droits réservés.
lilliad.univ-lille.fr

the analysis was made just after deposition (<3h) or after rehydration of the deposit (adding a drop of water, <10 min). This allows us to highlight the importance of the residual solvent on these surfaces during the LDI-MS analysis. It should be noted that the introduction of a carboxylic group (pyrene-COOH) did not make it possible to improve the performances.

Internal energies also confirmed that heat dissipation is higher in the case of glass/Au/graphene (1.83 eV) when compared to glass/Au (1.94 eV). Cu/graphene (provided by the producer) gives rise to an internal energy of 1.16 eV, that was not enough for LDI-MS process.

Insulating the glass/Au with a SiOx layer of 6 nm and transfer of graphene single layer on top, provided good MS results for peptides, but no results for cytochrome C. It should be taken into account the graphene deposition without any confinement layer that gave rise to MS signals, could have been, in fact, a double layer graphene. This double layer could act as thermal confinement by itself, as defects (such as cracks) can be introduced, providing a more patterned graphene surface.

Nevertheless, we do have to take into account the complexity and high cost of this method, along with the time required for the transfer (usually more than 1 day). As this method also did not present good reproducibility, further studies are to be performed in order to assess properly the potential use of this method as SPR-MS dual technique. The main perspective from this point of view is to transfer multiple layers of graphene, as this could also decrease heat dissipation by introducing several defects, but still be thin enough for SPR measurements. We did start this procedure, but we did not have enough time to measure MS and SPR signals.

© 2020 Tous droits réservés.
lilliad.univ-lille.fr

IV.2.3.1.d. Layer by layer (LBL)

Electrostatic interactions between polycations (such as poly(diallyldimethylamonium), PDDA) and graphene oxide (negatively charged) are used in literature to form thin films on the surfaces of gold and used for SPR.[64,65] Replacing polycations with multi-walled carbon nanotubes (MWCNTs, positively charged),[66] small molecules were detected using SALDI-MS. Another method used in MS replaced polycation with gold nanoparticles.[67] Schematic representation of the method is presented in **Figure IV.2-32**.

Nevertheless, even though both AuNPs and MWCNTs are good platforms for SALDI-MS, they are not suitable for SPR, mainly due to the high thickness of material. We will also use the alternation of PDDA with graphene for our experiments. The layer-by-layer (LBL) approach, based on the successive deposition of compounds with opposite charges is advantageous for developing graphene-based biosensors as it allows obtaining multilayer coatings with controlled composition, thickness and functionality.[64] This method is simple and can be prepared easily, but for a higher number of layers it may require some time, as each PDDA/GO layer requires 30 minutes.

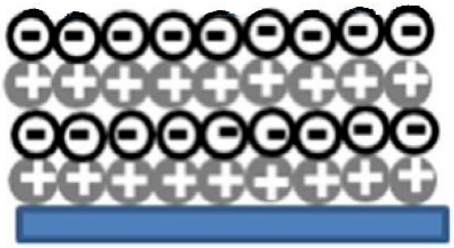

Figure IV.2-32 Representation of electrostatic interactions between polycation PDDA (+) and GO (-).[64]

The Raman spectra **(Figure IV.2-33)** displays the main features of graphene-based materials with a D-band at 1351 cm^{-1} and a G-band at 1595 cm^{-1} with a 0.9 D-to-G intensity ratio for GO and $I_{D/IG}$ 1.01 for GO deposited on gold-PDDA interfaces. The smaller ID/IG peak intensity ratio for GO corresponds to lower density of defects/disorder in the graphitized structure.[64] The presence of GO was in addition validated by contact angle measurements, where the water contact angle of gold (90±2°) changed to 27±2° after PDDA deposition, and to 40±2° after GO addition (**Figure IV.2-34**).

© 2020 Tous droits réservés.
lilliad.univ-lille.fr

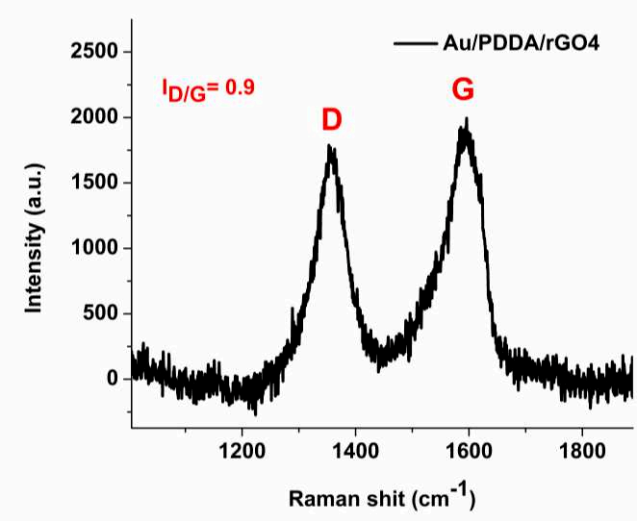

Figure IV.2-33 Raman spectra of Au/PDDA/rGO4.

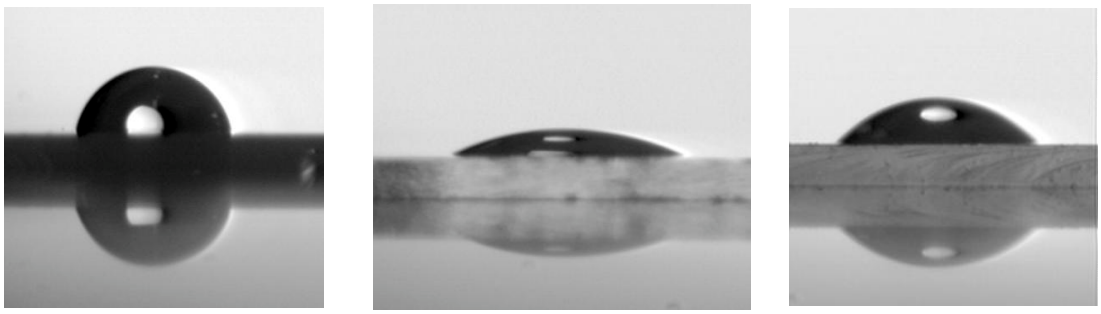

(A) **(B)** **(C)**

Figure IV.2-34 Water contact angle measurements of **(A)** glass/Au, **(B)** glass/Au/PDDA and **(C)** glass/Au/PDDA/GO.

As SEM images show (**Figure IV.2-35**), similar surfaces coverage is obtained in the case 2, 4 and 8 layers of PDDA/rGO.

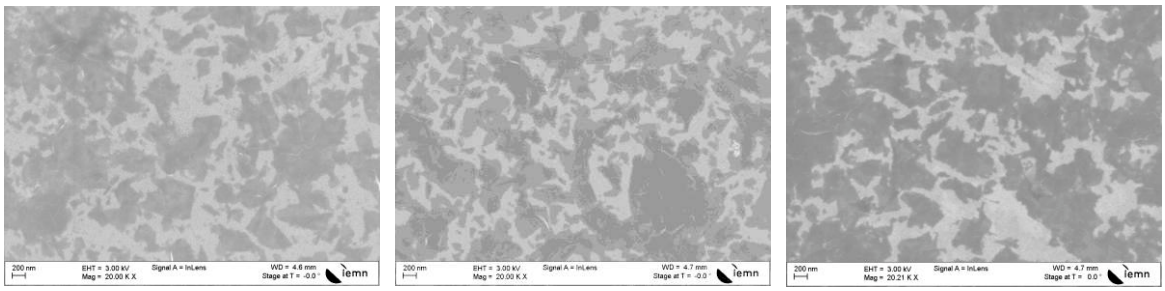

(A) **(B)** **(C)**

Figure IV.2-35 SEM monographs for Au/PDDA/rGO for different layers: **(A)** 4 layers, **(B)** 6 layers and **(C)** 8 layers.

Prior to MS measurements, the SPR curves were measured for all the layers (**Figure IV.2-36**). It can be observed that the dynamic range related to the SPR intensity, is decreased upon addition of more layers, and this trend can be particularly observed for the Au/PDDA/rGO surfaces. A still acceptable dynamic range can be obtained with around 4-6 layers of the polycation/GO or polycation/rGO (especially in the case of rGO).

© 2020 Tous droits réservés.
lilliad.univ-lille.fr

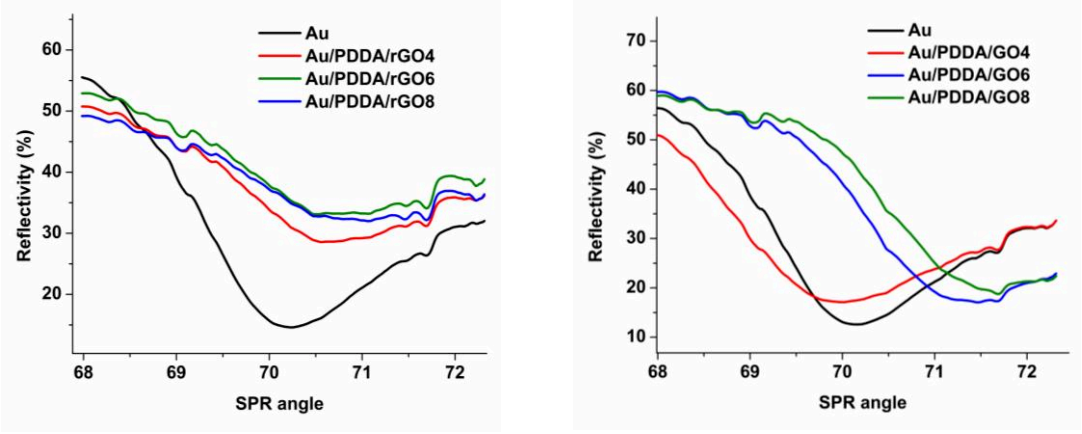

(A) **(B)**

Figure IV.2-36 SPR curves using reduced graphene oxide and graphene oxide for LBL.

For studying the MS performances of the surfaces, MIX 1, MIX 2 and MIX 3 are used. In the case of PDDA/GO, when MIX 2 of peptides is analyzed, only 2 peptides can be observed and the best results were obtained for 6 layers (**Figure IV.2-37**), in both terms of intensity of the signal and S/N ratio. The same number of peptides is observed for the MIX 1, but 4 layers seem to enhance desorption of Angiotensin I. The sensitivity for the potassium adducts is better than for sodium or protonated forms, even though no cations were added to the solutions.

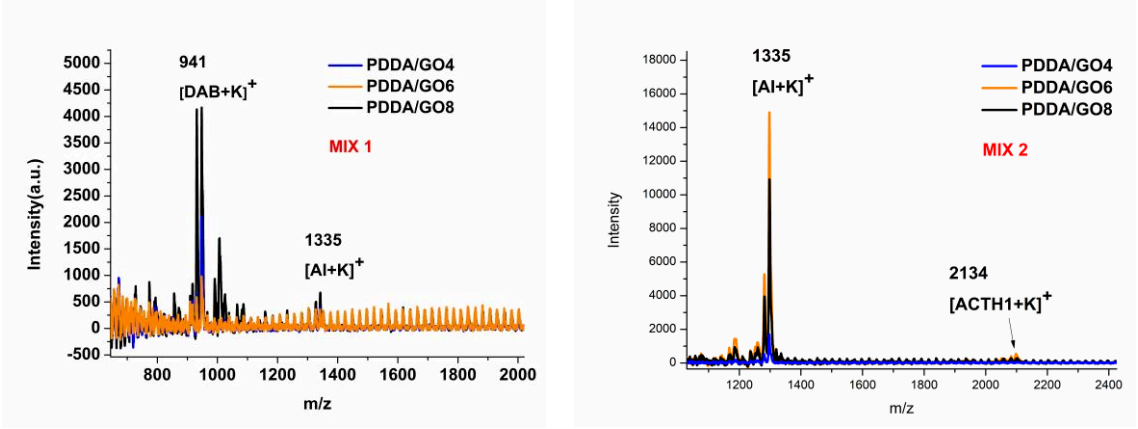

(A) **(B)**

Figure IV.2-37 SALDI-MS spectra for MIX 1 **(A)** and **(B)** MIX 2 using the Au/PDDA/rGO surfaces.

The sensitivity was better for PDDA/rGO and it becomes almost constant after 6 layers of PDDA/rGO for MIX 2. (**Figure IV.2-38**). The sensitivity towards Angiotensin I seems to be the best for 4-6 layers of PDDA/rGO, in MIX 1. Also 3 peptides out of 4 were observed for MIX1 and 4 out of 5 for MIX2 (insulin was not observed). The detection of peptides was achieved with a better sensitivity for the potassium adducts, than for sodium and the protonated form for both PDDA/GO and PDDA/rGO.

© 2020 Tous droits réservés.
lilliad.univ-lille.fr

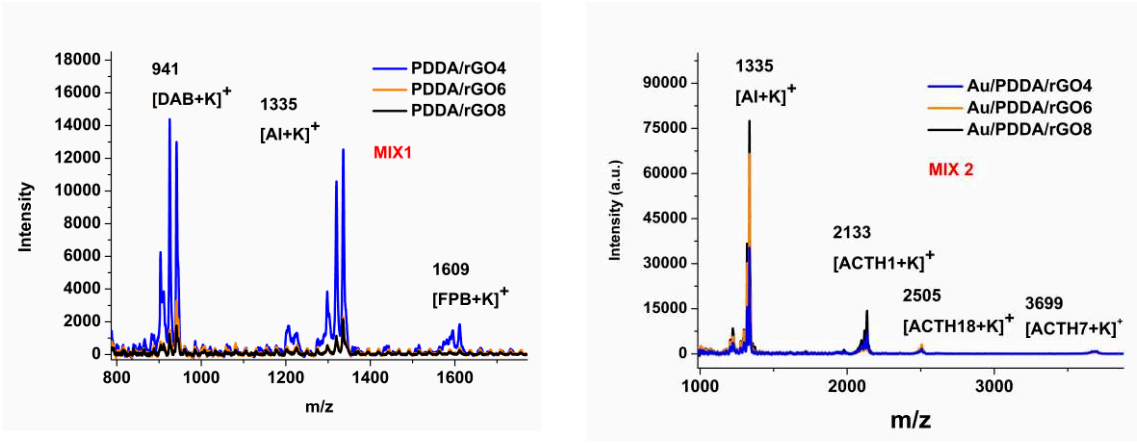

(A) **(B)**

Figure IV.2-38 SALDI-MS spectra for MIX 1 **(A)** and **(B)** MIX 2 using the Au/PDDA/rGO surfaces.

When the background noise is to be compared in the case of PDDA/GO and PDDA/rGO, it can be observed that PDDA/rGO sufaces have lower background signals/peaks (**Figure IV.2-39**), for the same number of layers. Moreover, for the PDDA/rGO surface, peaks originating for the Au surfaces, are still observed. The measurements for the Au/PDDA/GO are noisy in the 1000-4000 Da range (**Figure IV.2-39A**), but the noise seems to decrease with the number of layers. Only the glass/Au substrate presents the peaks specific for Au^+ and other Au ions aggregates (**Figure IV.2-39B**). All the MS spectra were measured in linear positive mode, with 10.000 shots and a frequency of 1000 Hz, and the laser power is 60 %, if is not stated in another way. When the background noise is to be compared in the case of PDDA/GO and PDDA/rGO, it can be observed that PDDA/rGO surfaces have lower background signals/peaks, for the same number of layers. Moreover, for the PDDA/rGO surface, peaks originating for the Au surfaces, are still observed.

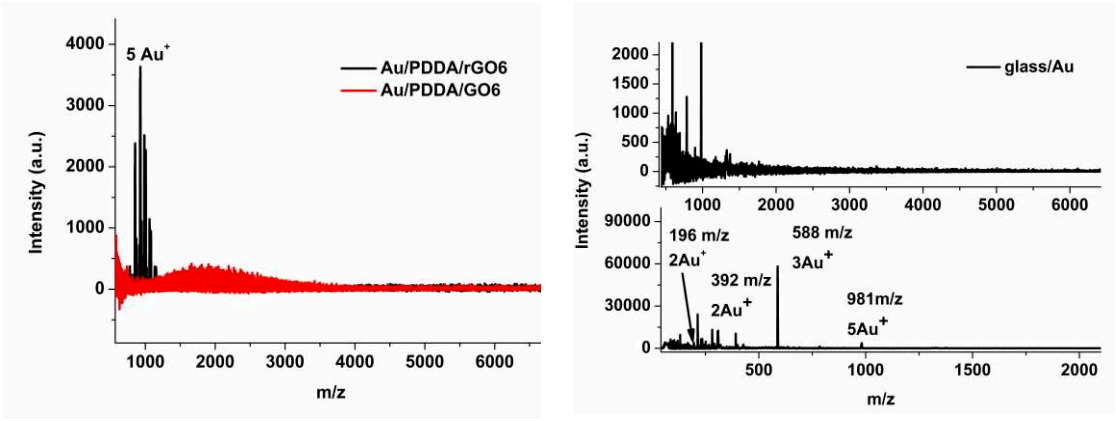

(A) **(B)**

Figure IV.2-39 The MS spectra of PDDA/GO in different layers (from top to bottom: 3, 4, 6 and 8 layers), when the substrate itself was exposed to a laser power of 60%. (B) the glass/Au substrate, when MIX 2 was analyzed**.**

© 2020 Tous droits réservés.
lilliad.univ-lille.fr

IV.2.3.1.d.1. Layer by layer conclusions

This method is simple and can be used to prepare SALDI-MS surfaces with low cost materials within an acceptable time window (2 hours). It can be concluded that SPR curves do not change drastically with the numbers of layers when rGO is being used, but the SALDI-MS spectra of peptides are much better in this case, as it was observed above for other methods. A good compromise is 4 layers in the case of PDDA/rGO. When it comes to GO, the SPR curves change sensitivity with the number of layers (4 layers surface has similar reflectivity intensity and SPR angle as gold), but the MS spectra are worse than in the case of rGO. The best compromise is to use rGO, with 4 layers of PDDA/rGO, as also rGO does not give rise to numerous background peaks (by contrast with PDDA/GO).

© 2020 Tous droits réservés.
lilliad.univ-lille.fr

IV.2.3.1.e. Bubble method

Azevedo et al.[68] presented a new strategy to form thickness adjusted and ultrasmooth films of very large and unwrinkled graphene oxide (GO) flakes through the transfer of both hemispherical and vertical water films stabilized by surfactants (**Figure IV.2-40**). As discussed above for drop-casting, the hydrophobic character and interaction of G or rGO are important. In this case the hydrophobic interaction with the aliphatic part of surfactants is often used to achieve an enhanced stability of G or rGO in water.[69] The main advantages of this method: simple, rapid, low-cost. The main disadvantage is that this method is not suitable for rGO deposition, which has higher electrical conductivity and may enhance better the SALDI-MS signal, as well as SPR.

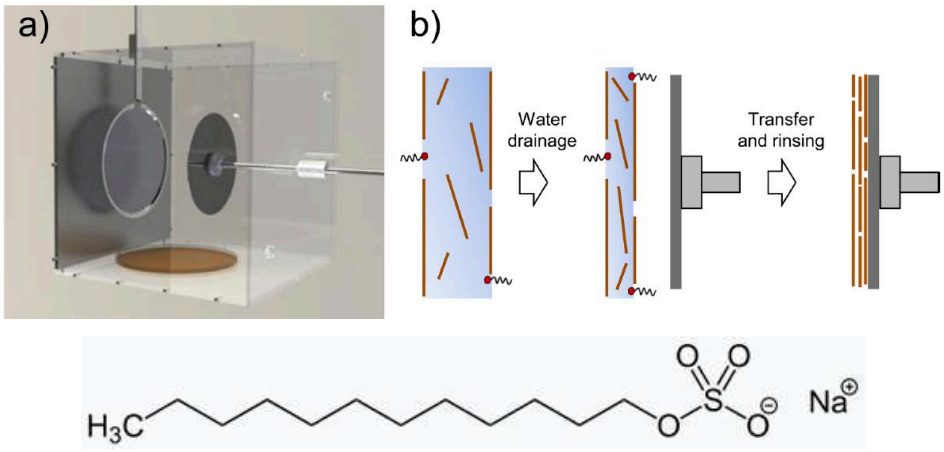

Figure IV.2-40 Scalable approach with large vertical surfactant films. **(A)** Principle of vertical film transfer with a metal ring of 220 mm in diameter. **(B)** Schematic representation of the process steps leading to GO film formation.[68] Inset of the SDS chemical structure.

Surfactant (SDS, sodium dodecyl sulfate, 0.5mg/ml) was used in order to create thin bubble layers and deposit several thin layers of graphene oxide, from different concentration solutions (0.1, 0.5 and 1.0 mg/ml).[70] The method of preparation is described thoroughly in the Appendix chapter.

Also, surfactants are known to help in desorption/ionization in SALDI MS (e.g. methylephedrine).[71] We could suppose that due to this synergetic effect, GO/SDS give rise to MS signal for Cyt C (**Figure IV.2-41**). Control surfaces cannot be prepared, as GO cannot create bubbles by itself, so it is hard to have a comparison.

Deposited internal energies were calculated for these 3 concentrations of GO solutions, and the results were in good accordance with the SEM images and the MS signal for Cyt C. The best surface (0,5 mg/ml GO) was found to have a deposited internal energy of 2.12 eV,

© 2020 Tous droits réservés.
lilliad.univ-lille.fr

in comparison with 2.08 eV (for 1,0 mg/ml GO), 1.87 eV (for 0,1 mg/ml GO), and 1.94 eV for control sample (just gold).

Profilometer was used to measure the thickness of the 3 different GO concentrations in the case of bubble deposition, and it was confirmed that ultrathin layers are obtained (8±2 nm for 0.1 mg/ml, 10±3 nm 0.5 mg/ml and 43±5 nm for 1.0 mg/ml).

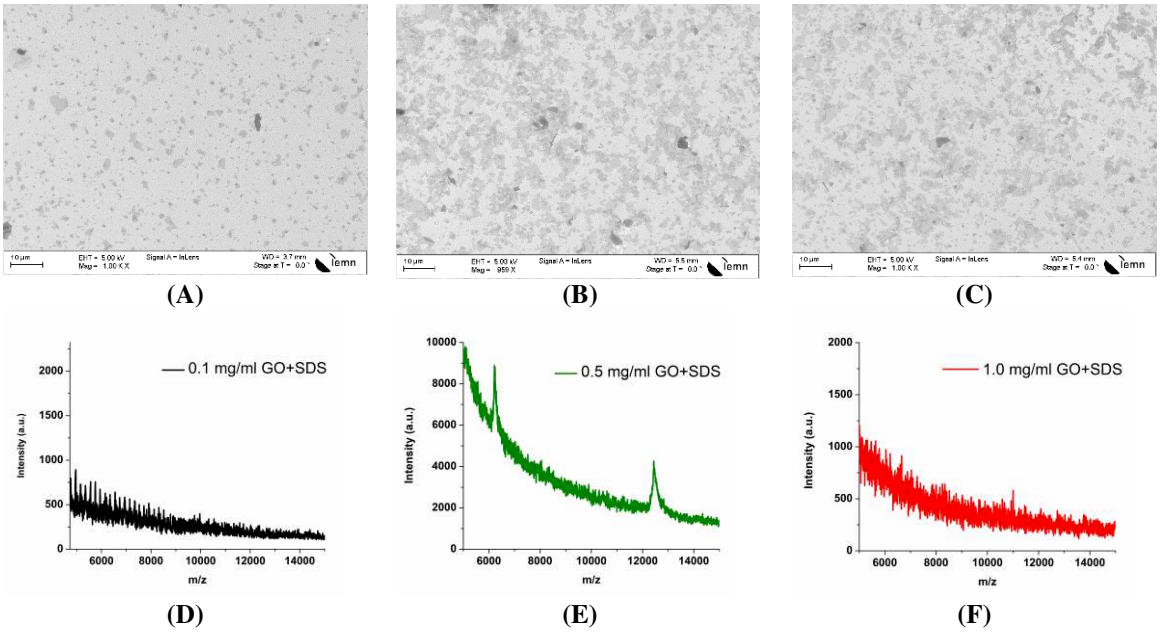

Figure IV.2-41 SEM images of Au/bubble SDS/GO deposited at different concentrations of GO: **(A)** 0,1 mg/ml **(B)** 0,5 mg/ml and **(C)** 1,0 mg/ml, and their correspondent SALDI-MS spectra using 50 pmol cytochrome C (ammonium citrate dibasic 50 mM, laser power of 70%, linear positive mode, deposition method: drop cast and drying in air).

IV.2.3.1.e.1. Bubble method conclusions

Even though SPR was not performed, the ultrathin film prepared this way should render the surface compatible with SPR, as there are several references in literature that can attest this hypothesis.[72] When 0.5 mg/ml of GO was used, Cyt C was detected. This could also be explained by the fact that surfactants can change the absorption capacity of graphene,[69,73] even though we do have only a thin layer around 10 nm deposited on the glass/gold surface. As this method is simple, rapid (20 minutes), low cost and reproducible, it seems to be one of the best approaches in detecting proteins using SPR-MS bimodal technique.

© 2020 Tous droits réservés.
lilliad.univ-lille.fr

IV.3. SERS-MS using CNWs

SERS (Surface Enhanced Raman Spectroscopy) is a rapid and nondestructive method which allows obtaining information over the chemical nature of the absorbed compounds to analyze (especially the nature of functionalization), their orientation and their interactions. However, the assignation problems of the Raman bands take time and it is not all obvious. SALDI-MS could confirm the identification of compounds, allowing the distinction in the analyzed sample. **Figure IV.3-1** presents the schematic representation of CNWS used as SERS/MS platform.

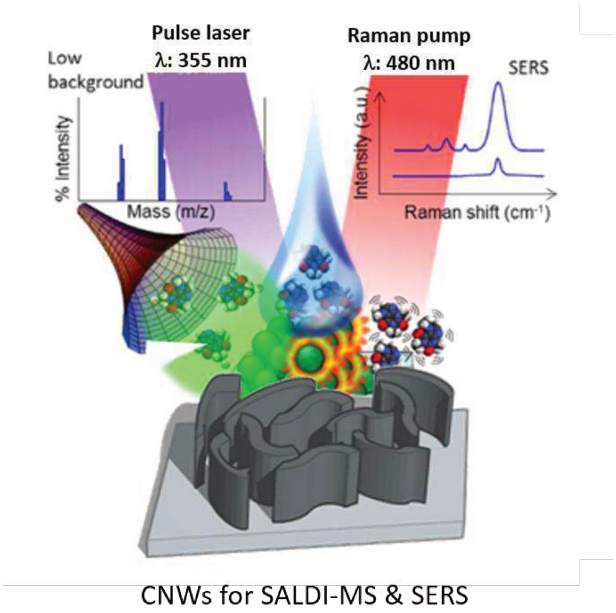

Figure IV.3-1 Schematic representation of SERS-MS using CNWs.[74]

The combination of SERS and SALDI-MS was recently described for small molecules (4-aminothiphenol and methylene blue). In this study, glass fibers were covered with plasmonic silver nanoparticles (20-50 nm).[2] The best SERS/SALDI activity was obtained in the closely-spaced Ag NPs, with the inter-particle nanoscale gaps <10 nm. As glass/silver substrates have low thermal conductivity (1.05 $W*m*K^{-1}$ in bulk glass, 429 $W*m*K^{-1}$ in bulk silver), heat confinement contributes to the closed packs AgNPs, creating localized "thermal hot spots". Like for LSPR surfaces, the deposition of Al_2O_3 or other high K materials, which will limit the decay of SERS performances (increasing the lifetime) and reinforce the performances of SALDI-MS (by heat confinement).[75] Nevertheless, plasmonic nanoparticles can disrupt the molecular systems especially when dynamic processes are to investigate.[74] Most of the SERS/MS dual platforms are based on Ag or Au plasmonic nanoparticles.

© 2020 Tous droits réservés.
lilliad.univ-lille.fr

Later, the same year, a multimodal assay technique called "RaMassays" was described, using SiO_2/TiO_2 core/shell (T-rex) beads (SiO_2 core, a 100 nm shell layer of TiO_2) for caffeine, cocaine and other drugs and conversion of L-tyrosine to L-DOPA.[74] They prove mutual assistance of SERS/MS showing how regio-isomers (theophylline and theobromine) can be distinguished by SERS, as they have the same molecular weight. This method (**Table IV.3-1**) is plasmonic-free, as is based on dielectric material platform, being less invasive and more reproducible. Besides avoiding aggregation due to salts present in biological samples, this dielectric shells provides the possibility of new functionalizations.[10]

Table IV.3-1 Literature study presenting combination of SERS-MS for different molecules.

year	MS technology	Analyte	Recognition element	Buffer/solvent
2016 [74]	MALDI-TOF-MS	Caffeine, cocaine, theophylline and theobromine, L-tyrosine, L-DOPA	-	methanol
2016 [20]	MALDI-TOF MS	4-aminothiphenol and methylene blue	-	ethanol

In our group there is a method that describes deposited AgNPs, on SiNWs, that allowed the detection of rhodamine 6G (R6G) using SERS, with a limit of detection of 10^{-4}.[76] The morphology of these electroless nanoparticles deposited by the method described in the work of Galopin et al., it's suitable for SERS because of the creation of "hot spots". This work can be continued for coupling SERS with SALDI-MS for detection of small compounds. Different nanoparticles (Ag, Au, Cu) created by evaporation (5 nm of Ag or Au) or using the electroless method, were proven to be useful for detection of peptides, and this is presented in **Figure IV.3-2.** It can be observed in SALDI-MS spectra when Ag or Au were evaporated, that peaks appear at 970 m/z and 1772 m/z corresponding to Ag_9^+ and Au_9^+ clusters respectively. These clusters could be used for *in-situ* re-calibration of MS spectra as shown by the group of Voelcker. In this study, they analyzed illicit drug presence on a thumb fingerprint obtained by contact with a porous silicon surface covered by an Ag film.[77]

© 2020 Tous droits réservés.
lilliad.univ-lille.fr

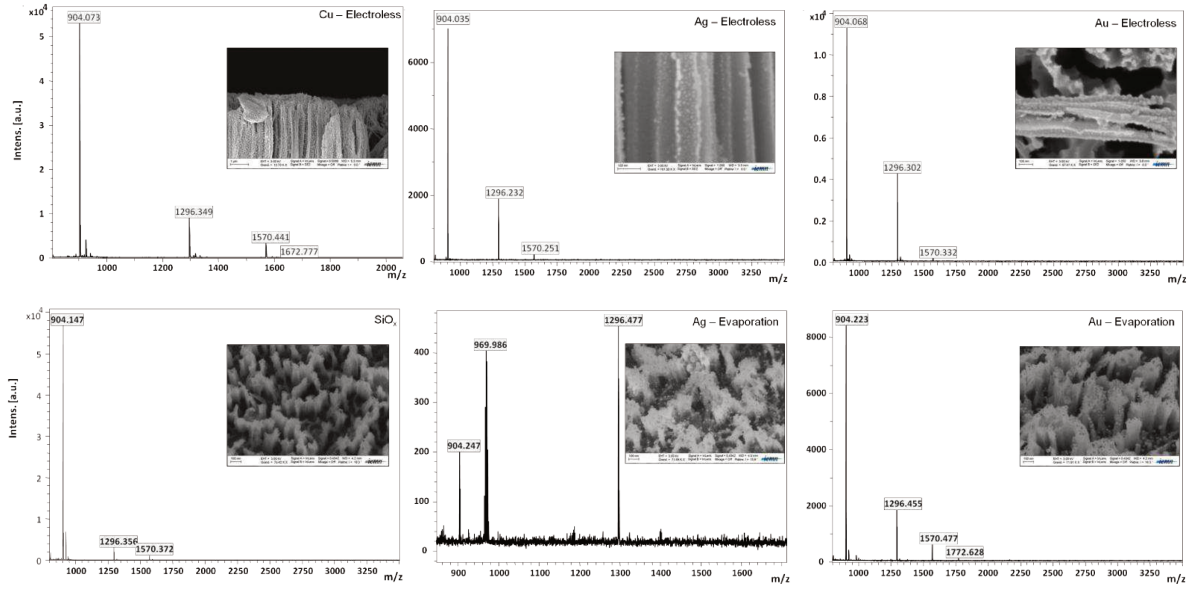

Figure IV.3-2 Silicon nanowires decorated with metallic nanoparticles for the detection of peptides in MS.

When it comes to ricin B chain, Szlag et al.[78] have developed and SERS method using N-Acetyl-Galactosamine glycopolymers as affinity target-capture elements. Silica nanospheres were self-assembled on a silicon wafer, followed by vacuum deposited gold. A chain transfer agent (CTA) is used to promote radical polymerization of N-acetyl-galactosamine, that is the specific sugars that can bind ricin. The CTA used here is trithiocarbonate, that is also able to chemisorb to gold, making this a convenient anchoring chemistry for SERS. **Figure IV.3-3A** presents the SERS spectra for ricin using the Au coated silicon nanoparticles modified with the glycopolymers. Different concentration of ricin were used and the peak at 700 cm^{-1} (corresponding to peak to tyrosine and tryptophan vibrations) was used for calibration, as this peak also does not interfere with the peaks from the glycopolymer (**Figure IV.3-3B and C**).

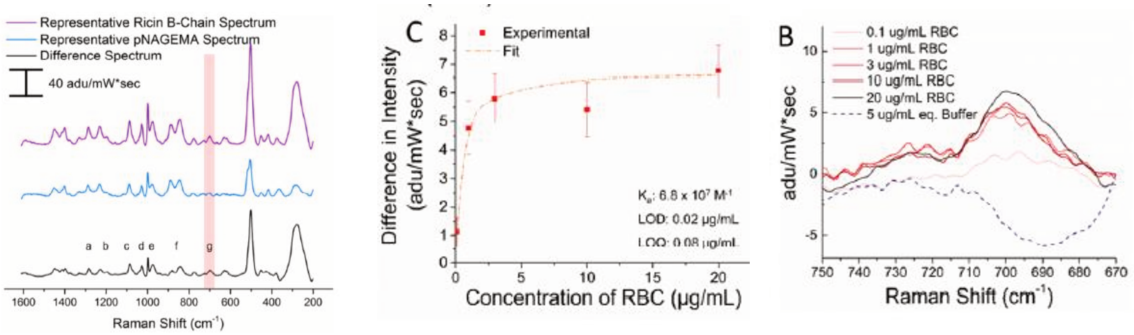

(A) **(B)** **(C)**

Figure IV.3-3 Spectral differences due to the presence of RBC: **(A)** representative difference spectrum demonstrating changes (a–g) due to ricin B chain; **(B)** difference spectra of varying concentrations of RBC in the 670–750 cm^{-1} shift region; **(C)** quantification of the increased amplitude at 700 cm^{-1} shift with increasing RBC concentration, including the calculated association constant (Ka), and limits of detection (LOD) and quantification (LOQ).[78]

© 2020 Tous droits réservés.
lilliad.univ-lille.fr

Thèse de Ioana Silvia Hosu, Université de Lille, 2020

Table IV.3-2 presents a literature study adapted from Szlag et al.[78] Different plasmonic nanostructures are described for detection of ricin derivated proteins (ricin or ricin B chain). In this table the wavelengths at which the detection was possible are depicted. Usually the laser is chosen close the wavelength at which the LSPR effect is observed and this is size dependent, as described in the LSPR section of this chapter. As usually the nanoparticles chosen are ranging from 15 to100 nm, lasers are usually in the orange-red region (600-800 nm). In our case, the CNWS substrate absorbs all wavelengths (being a black material), but in the UV-visible region the absorption is higher (as all graphene-like materials).[79] As the available Raman spectrometer we had access to, is composed of a blue colored laser (463 nm), we considered it appropriate for our experiments.

Table IV.3-2 Comparison of recent SERS sensing ricin work.[78]

Author	SERS Substrate	Target	Bands (cm^{-1}) (laser wawvelength)	Capture Agent	LOD	Sample Prep and Detection Time	Spectral Distinction	Complex Matrices
He [80]	Ag dendrites	Ricin B chain	985, 621 (780 nm)	Aptamer	10 ng /mL (PBS), 50 ng/mL (orange juice), 100 ng/mL (milk)	< 40 min	Spectra, 2nd derivative, PCA	Orange juice, milk (PBS)
He [11]	Ag dendrites	Ricin	900, 915 (780 nm)	Immuno-magnetic separation	4 µg/mL (milk)	20 min	2nd Derivative, PCA	Milk (PBS)
Wang [81]	deposited Ag 80 nm nanoparticles on inverted pyramidal nanovoids	Ricin	major: 1204, minor: 642, 1209, (785 nm)	None	Concentration not stated	Not stated	Spectra	PBS
Zengin.[82]	Ag 15 nm nanoparticles	Ricin B chain	1610 (785 nm)	Aptamer	10.2 fg/mL	~1 hr	Raman tag of 4,4'-bipyridyl	Orange juice, milk, blood, urine (PBS)
Tang [83]	Au 100 nm nanoparticles immobilized on Si wafer, covered in a silver shell post-ricin attachment	Ricin	735 compared to Si 520 signal. (633 nm)	Single-stranded oligodeoxy-nucleotides	8.9 ng/mL	~90 min	Spectra peak ratio	Apple juice, human serum
Szlag [78]	Au 80 nm film over nanospheres	Ricin B chain	700, 1088, 1280, (785 nm)	N-Acetyl-galactosamine glycopolymer	20 ng/mL	6 hr	Difference spectra, PCA	Apple Juice, orange Juice (2-mercaptoethanol)

Authors usually described how the Raman bands of ricin could seem to overlap with the ones of the substrate or the buffer (usually salt based ones, especially PBS, pH 7.5). In order to obtain these distinctions, they also used some data processing (like 2nd derivative, PCA or spectra differentiation)[11,80] or they used a tag (4,40-bipyridyl).[82] He et al.[80] described that ricin B chain can exhibit Raman vibrations at 633 cm^{-1} (Cystine,

© 2020 Tous droits réservés.

lilliad.univ-lille.fr

cysteine , C–S stretching), 716 cm^{-1} (Cystine, cysteine, C–S stretching) and 1001 cm^{-1} (Phenylalanine-ring breathing) and Szlag et al.[78] described, in addition, band at 1088 cm^{-1} (C−C and C−N stretching vibrations) and 1280 cm^{-1} (unstructured coil of RBC) but these bands can shift with the influence of substrate, salts, wavelength of laser etc, as they also have shifts to 985 and 621 cm^{-1}, in their work.

Nevertheless, plasmonic-free approaches were not described in literature up to now, to our knowledge. In the following section we will describe preliminary results and perspectives for detection of ricin B chain using CNWs.

IV.3.1. Carbon nanowalls - Plasmon-free substrate for SERS/MS for ricin B chain detection

CNWs were already used in as SERS platforms, but they are decorated with gold nanoparticles, so plasmonic approach is used.[84] Au sputtering is used for creating 30 nm gold nanoparticles (similar to the average surface roughness of CNWs) on top of CNWs. Detection of BSA, tryptophan, guanine, keratin, rhodamine 6G. They have detected concentrations of 1 µM for the first three mentioned molecules and 1 nM for the last one. CNWs were used here more as a support than the enhancement SERS material. As they have high surface area, low thermal conductivity and absorbs UV and visible light they have potential to be used as plasmonic-free SERS platforms.

As we have studied extensively MS detection of ricin B chain using SALDI-MS (Chapter III), herein we will only describ the SERS experiments we performed for detection of ricin B chain, using CNWs. For this purpose, we did use the same optimized parameters described in Chapter III (ammonium citrate dibasic, 150 mM, incubation during 5 minutes or drop casting) and compared them with ricin B chain desalted, at the same concentrations (30 and 15 µM). Apparently salt plays an important role in the SERS detection, as when water was used as solvent, no peaks were detected (**Figure IV.3-4**). It is described that salts aggregate nanoparticles and enhance the SERS signal, in plasmonic silver approach. This is done by bridging the gap between nanoparticles.[85,86]

When we compare the ricin B chain Raman spectrum with the control spectrum (the one obtained for CNWs), we can identity peaks at: 607, 793, 831, 898, 1048, 1721, 2082 and 2300 cm^{-1}. Szlag et al.[78] used the peak at 700 cm^{-1} (using a diode laser of 785 nm) for quantification of ricin B chain. This peak is attributed to tyrosine and

© 2020 Tous droits réservés.
lilliad.univ-lille.fr

tryptophan vibrations. As our laser has a wavelength of 473 nm, a shift of the peak is expected.

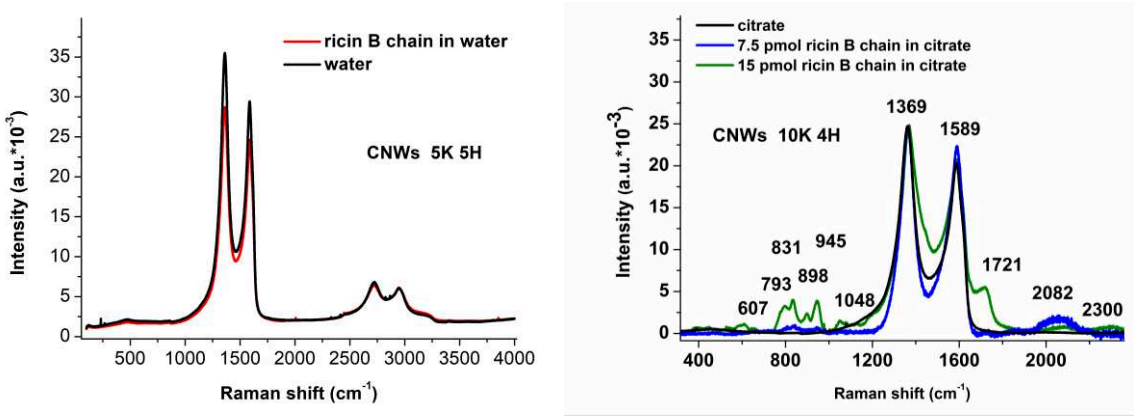

(A) **(B)**

Figure IV.3-4 SERS spectra of ricin (30 and 15 µM) dissolved on water (A) and (B) ammonium citrated dibasic (150 mM) and incubated during 5 minutes on the surfaces of CNWs 5.0 K 5 H.

Also, we did rule out the possibility of confusing Raman vibrations of trapped water with the one of ricin, by measuring the controls. Also, literature shows vibrations of water can be found in the region of 300-1000 cm^{-1}, but as broad peaks (430, 650, out-of-plane 795 cm^{-1}). Nevertheless, this is not our case as the peaks are not broad and the typical vibration peak for water around 3000 cm^{-1} (OH stretching) is not present (as a strong band should observed, data not shown).

Main interfering Raman shifts could be from ammonium citrate dibasic. To be sure that we do not measure ammonium citrate peaks only, we did compare the spectra with ammonium citrate dibasic powder (to be described in the next section) or ammonium citrate deposited in the same way as the analyte (as in **Figure IV.3-4**).

For the ammonium citrate dibasic powder, the analyte (ricin 30 µM) was drop casted and dried several days, as the Raman peaks were more intense in this way (**Figure IV.3-5A**). Ricin B chain is known to be stable at room temperature during several days, so this should not influence our experiments. We could observe that the resolution of the peaks is better in the raw Raman spectra and some of the peaks of the ammonium citrate overlap with the ones for ricin B chain. Second derivatives of the Raman peaks are used for the enhancing the resolution of some peaks, as the peaks full widths at the half maximum is decreased by a factor of three. The negative obtained peaks enable the locations of overlapped peaks in the absorption spectra, elucidating broad peaks. Also, it eliminates the background offset and the slope.[87] This second derivative method made things more clear: 758, 965 and 910 cm^{-1} bands are

© 2020 Tous droits réservés.
lilliad.univ-lille.fr

exclusively from the ammonium citrate bands. The 797 cm^{-1} and 945 cm^{-1} bands can be attributed to ricin B chain only and the band at 831 cm^{-1} is common for both, but always higher in the ricin B chain case. When differentiation of average spectra is used (at least 3 measurements performed for both citrate and citrate-ricin) the more intense band of 831 cm^{1} for ricin B chain can be observed easier (**Figure IV.3-6**). This band should appear due to common groups in both ricin B chain and ammonium citrate, but with higher contribution in ricin B chain. In the region 1300-1600 cm^{-1} it is impossible to observe any peak of ricin, as the D and the G band of the CNWS are strong and predominant.

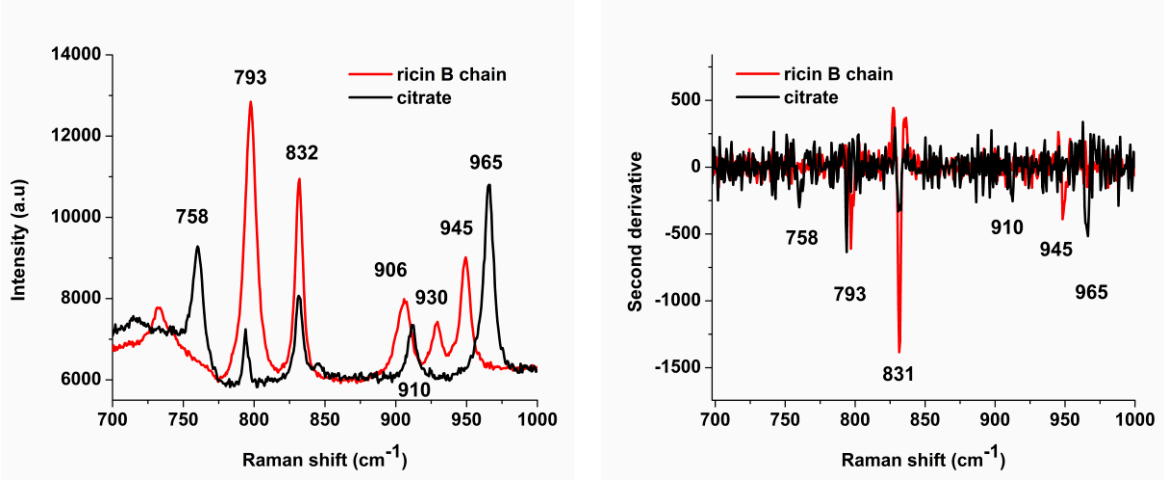

(A) **(B)**

Figure IV.3-5 **(A)** Raman spectra of ammonium citrate dibasic in powder and ricin (30 µM, in ammonium citrate dibasic 150 mM, drop casted and dried several days) **(B)** Second derivative of Raman spectra of ammonium citrate dibasic and ricin B chain, on CNWs 5K 5H.

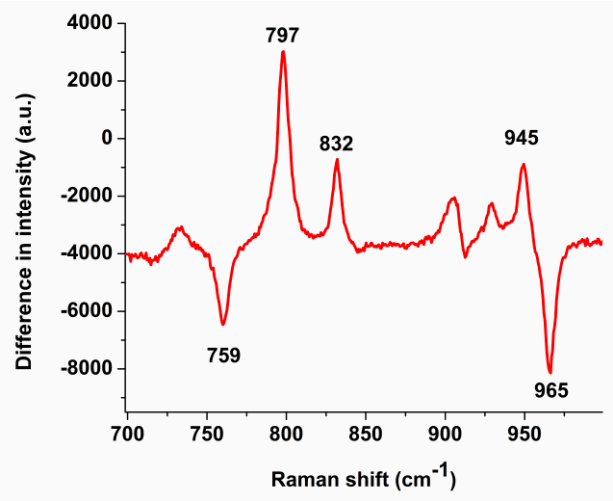

Figure IV.3-6 Difference spectra obtained after subtraction of ammonium citrate spectra from the ricin B chain analyzd in ammonium citrate (150 mM), on CNWs 5.0 K 5H.

© 2020 Tous droits réservés.
lilliad.univ-lille.fr

IV.4. EC-MS using CNWs

The combination of electrochemistry (EC) and MS represents a suitable analytical tool especially when it is difficult to elucidate the redox chemical reactions, to identify some products/by-products and the interfering species (that will lead to false-positives responses) with the help of MS.[88] As a model molecule we used glucose, as we already described the SALDI-MS detection of this molecule in chapter II, as of all various saccharide-related diseases, diabetes has the most important impact on human, social, and economic fields and the number of patients with diabetes is thought to reach 700 million in 2030.[89] The idea is that, for example, in the oxidation of glucose, MS could distinguish between glucose (Mw=180 Da) and gluconic acid (Mw=196 Da), the oxidized product.

In this section, we propose an original approach for the detection of glucose (GLC) by non-enzymatic EC means combined to surface-assisted laser desorption ionization MS (SALDI-MS) methods. We have already extensively described the SALDI-MS detection of glucose in chapter II. Herein, we will show how, the same CNWs surface can be used for both detection of glucose, by EC and by SALDI- MS. The schematic representation of this strategy is presented in **Figure IV.4-1.** The redox mechanism is also presented in this figure. This mechanism could be elucidated using SALDI-MS.

As the CNWs surface is hydrophobic, an oxidation voltage should be used to create hydroxyl groups at the surface of the electrode, so that contact of the surface with the aqueous solution (NaOH 100 mM) is ensured and to create an electrical double layer (and increase mass and electron transfer), by making the surface hydrophilic. Water contact angle was measured before (127°) and after polarization (13°). Also, creating hydroxyl groups could enhance the interaction of glucose with the surface, through hydrogen bonds.

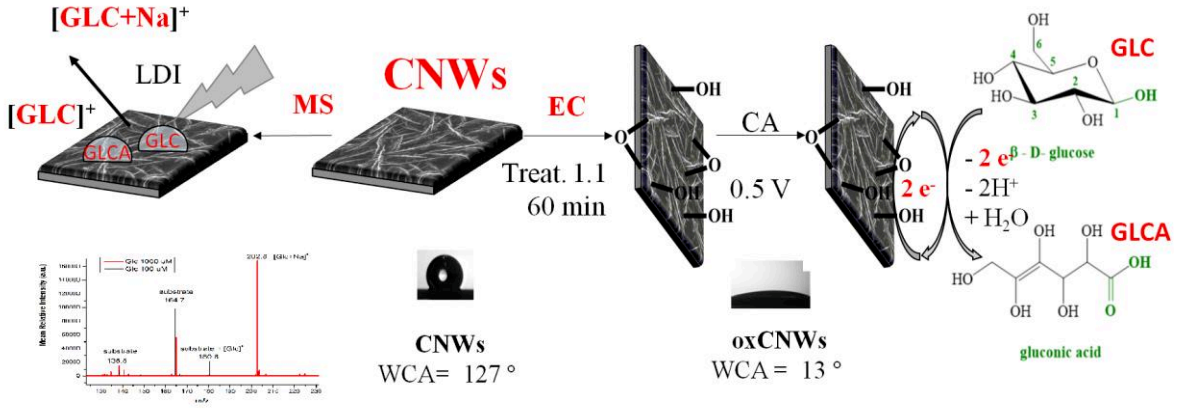

Figure IV.4-1 Schematic representation of combination of EC-MS using CNWs as dual interface.

© 2020 Tous droits réservés.
lilliad.univ-lille.fr

A study of sensitivity and response time is presented in **Figure IV.4-2A**. Polarization during 1 h is chosen for further measurements, as detection of 200 µM of glucose gives the best response as compared to lower polarization periods, increasing the sensitivity 5 times and decreasing the response time 10 times (from chronoamperometry experiments at 0.5 V).

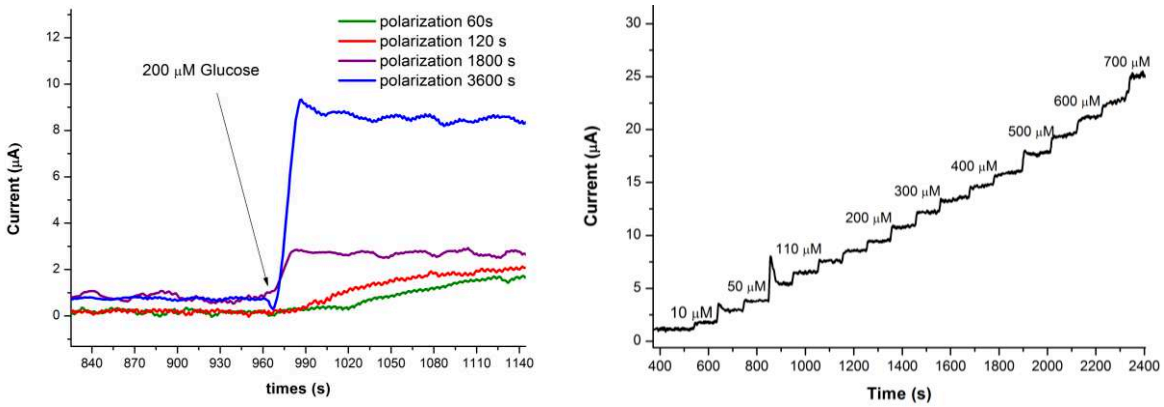

(A) **(B)**

Figure IV.4-2 (A) Chronoamperometry at 1.1. V during different periods of time for polarization and **(B)** Chronoamperometry at 0.5 V using increasing glucose concentration onpolarized CNWs (60 min).

Using CA at 0.5 V (**Figure IV.4-2B**), the calibration curve was plotted (**Figure IV.4-3A**), before and after polarization. The characteristics of the electrodes are presented in **Table IV.4-1**, for the electrodes used after polarization at 1.1 V. The polarization increased sensitivity due to hydrophilic groups created on the surface and the facilitated access of GLC to the catalytic sites. The calibration curve obtained after the polarization is I/µA= 2,914+ 0,026*[glucose]/µM. As we have already studied and published our results for the detection of glucose using CNWs in SALDI-MS,[90] we can observe that the linear ranges are similar (10-550 µM for EC and 10-800 µM in SALDI-MS). This means that the same samples can be used for dual detection and quantification using the same kind of surface, but mutual assistance of SALDI-MS can be also achieved over EC, with the extended linear range.

© 2020 Tous droits réservés.
lilliad.univ-lille.fr

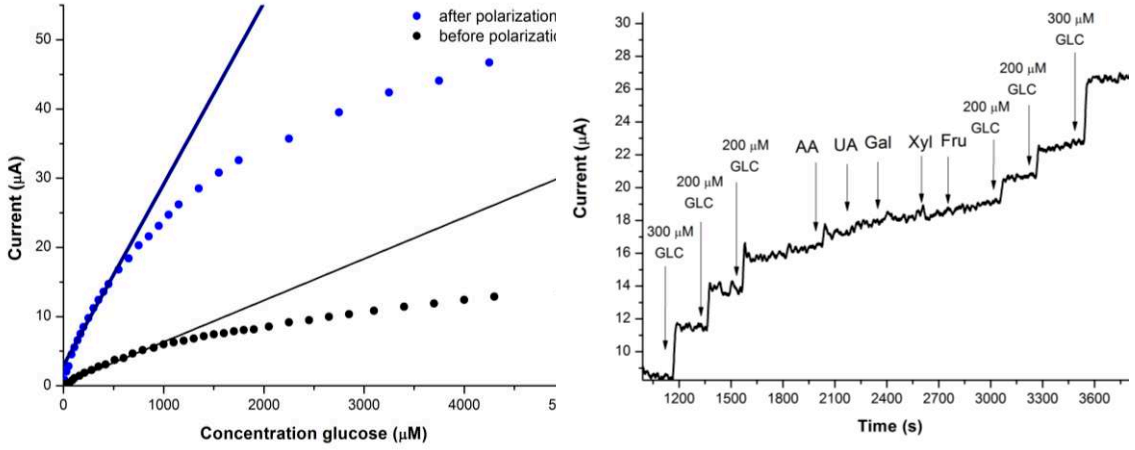

(A) **(B)**

Figure IV.4-3 (A) Calibration curves using CA at 0.5 V after and before polarization at 1.1 V and **(B)** CA at 0.5 with injecting different interfering species : AA (ascorbic acid), UA (uric acid), Gal (Galactose), Xyl (Xylose), Fru (fructose), each 600 µM.

An interference study was performed for different EC active molecules at physiological concentrations (**Figure IV.4-3B**). It can be clearly observed that even the concentration of the interfering species was 3 times higher and the signal for glucose remained unchanged. This makes our method suitable for detection of glucose in real samples (especially in blood serum).

Non-enzymatic approaches of EC methods were already described in our group and around the world. We can observe that the performances of our EC method is competitive with the ones described in **Table IV.4-1**, but improvements could be done by studying different doping levels (as we did in Chapter III), as this improves electrical conductivity, thus influences directly electrochemical performances. The surfaces we tried here had a lower doping level (2.0 K, as in Chapter II), as in Chapter III we already determined that 5.0 K or 10.0 K doping levels exhibit better performances in SALDI-MS.

The CNWs surfaces were used to detect glucose with both MS (LOD= 0.7 µM) and EC (LOD= 10 µM). These LOD is in the normal range described in EC, and one order of magnitude better in MS.

© 2020 Tous droits réservés.

lilliad.univ-lille.fr

Table IV.4-1 Short literature study for the electrochemical non-enzymatic detection of glucose and our work.

	Linear range	Sensitivity	Specific sensitivity	LOD	Response time	reference
Our EC method (CNWs)	10 - 550 µM	0.026 µA/µM	0.065 µA/µM per cm^2	10 µM	20 s	This work
Our SALDI-MS method (CNWs)	10-800 µM	36.58 a.u. /µM (per $1mm^2$)	3658/ µM per cm^2	0.7 µM	10 s	Hosu et al.[90]
graphene oxide/Cu nanoparticle (EPD)	10-1200 µM	-	0.44 µA/µM	3.4 µM	-	Wang et al.[91]
BDD (diamond nanowires)	60-8000 µM	0.50 µA/µM (0.1 cm^2)	5 µA/µM per cm^2	60 µM	-	Wang et al.[92]
Cu nanoparticles modified as-grown CVD graphene	20–2300 µM	-	0.379.31 µA/µM per cm^2	1.39 µM	< 5 s	Wang et al.[93]

Also, we can observe, the sensitivity using SALDI-MS method is by far the best, because MS is a high-sensitive tool. The best advantage that EC can bring in creating a complimentary dual technique is studying electrochemical reactions, which can be further elucidated with MS. The simple case of glucose was also studied by us. When EC produces a mixture of isomeric or isobaric molecules (like glucose, galactose, mannose, fructose), one makes use of a separation method combined with MS [mostly liquid chromatography (LC)]. [6]

First thing to mention is that we described in Chapter II that NaOH can be used as ion proton donor, but the sensitivity towards glucose was smaller than in the case of NaCl, due to higher ionicity in the salt. Nevertheless, as the electrolyte in electrochemistry for the above described method is NaOH (100 mM), it is suitable for performing MS on the same surfaces, which was here in EC, for detection of glucose.

Gluconic acid (M_w= 196.15 g/mol), the product of EC (oxidation of glucose), was studied with MS. As the molecular weight is different than in the case of glucose (M_w= 180.16 g/mol) it could be distinguished by MS. We did study first if gluconic acid MS signal is enhanced by NaCl (10 mM), but the intensity of the main peak (219 m/z assigned $[GlcA+Na]^+$) remains the same, as the peak at 241 m/z (assigned to $[GlcA-H+2Na]^+$) (**Figure IV.4-4**) increases. This happens because increasing the Na^{+1}ions in the solution increases the peak at 241 m/z with a factor larger than 2, as sodium adduct of the gluconate is formed. Also, the ability of gluconate to complex metal cations in alkaline solutions is well known.[94] Gluconic acid being a weak acid, it is partially dissociated in solution, as both associated and dissociated species can be found in solutions.

© 2020 Tous droits réservés.
lilliad.univ-lille.fr

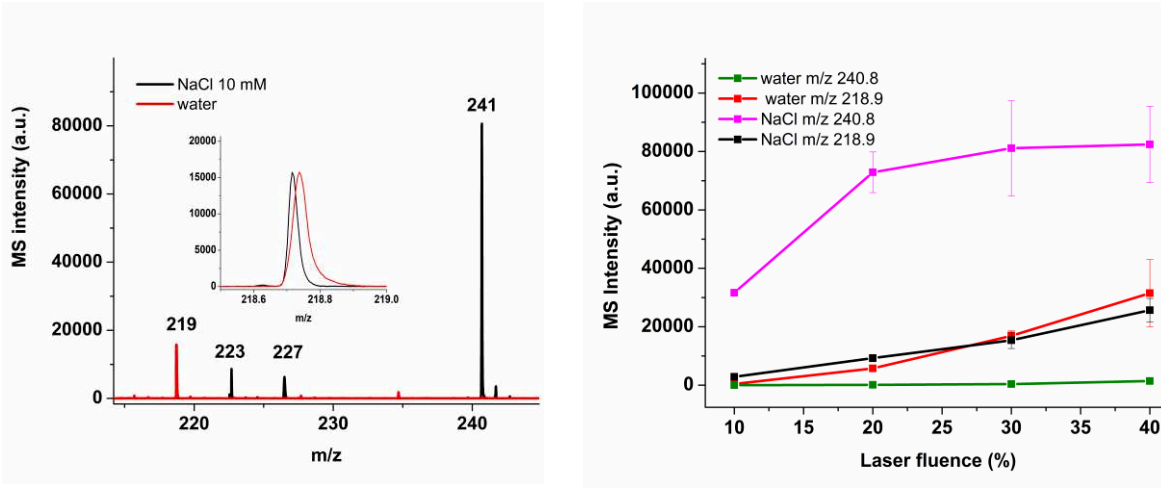

(A) **(B)**

Figure IV.4-4 (A) SALDI-MS spectra of gluconic acid in water and in NaCl (10 mM) and **(B)** representation of MS intensities as a function of laser fluence (relative percentage), in both water and NaCl (10 mM), using CNWs 2.0 K (3.95 µM), SALDI-MS substrate.

Glucose in alkaline solution undergoes auto-oxidation, during time, and it can decompose to gluconic acid also.[95] So, peaks corresponding to gluconic acid in the NaOH glucose solutions are expected. It can be observed in **Figure IV.4-5A** that glucose (Glc) in NaOH solution presents 2 peaks: at 203 (assigned to $[Glc+Na]^+$) and 241 (assigned to $[GlcA-H+2Na]^+$) m/z, as we already mentioned that gluconic acid (GlcA) could be an auto-oxidation product of glucose, in alkaline medium. Gluconic acid itself presents 2 peaks: at 219 m/z (assigned to $[GlcA+Na]^+$) and at 241 m/z (assigned to $[GlcA-H+2Na]^+$). Other secondary peaks are present at 218, 379 and 395 m/z corresponding to: $[GlcA-H+Na]^+$, $[2GlcLa+Na]^+$ or $[2GlcLa+K]^+$, respectively. So, after electro-oxidation of glucose, if we are able to observe the peaks for gluconic acid, it means that gluconic acid is a by-product of the process.

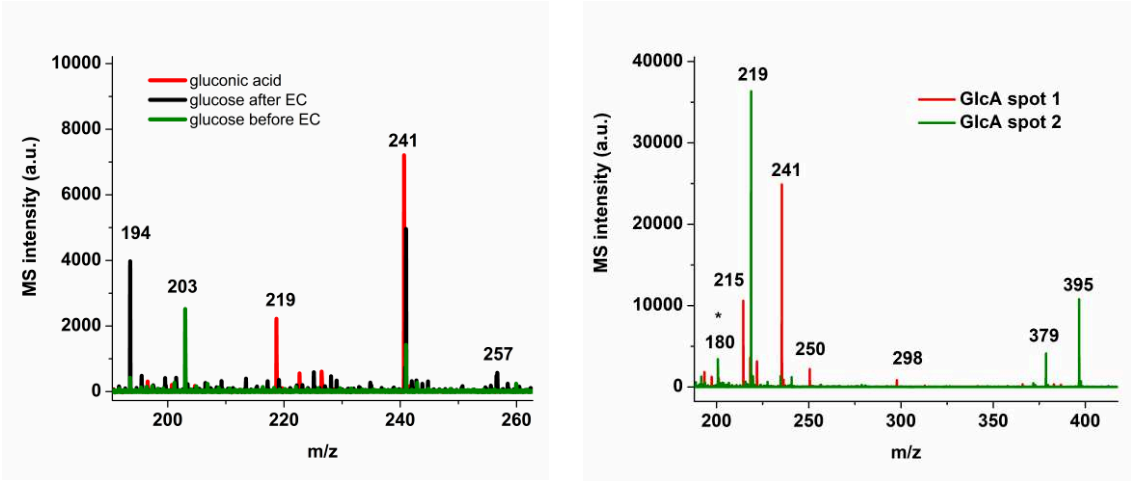

(A) **(B)**

Figure IV.4-5 SALDI-MS spectra presenting gluconic acid and glucose **(A, B)** before and **(A)** after electro-oxidation, in NaOH (100 mM), using CNWs as EC-MS dual surface.

© 2020 Tous droits réservés.
lilliad.univ-lille.fr

In the same figure, we can observe that after electrochemistry the peak at 241 m/z is observed but not the one at 219 m/z. The peak at 219 m/z is in strong correlation with the peaks at 379 and 395 m/z (correlated to β-Glucono-δ-lactone species, GlcLa). When these peaks increase, the peak at 241 m/z is decreasing (in **Figure IV.4-5B** along with a smaller peak at 218 m/z assigned to $[GlcA-H+Na]^+$). These peaks were measured in water samples, not to complicate more the spectra with the peaks from the auto-oxidation process and there are mostly dependent of the spot to which we apply the laser, so the position of these species.

This is another proof than more species are involved in both auto-oxidation and electro-oxidation processes. **Figure IV.4-6** shows the oxidation of glucose to both gluconic acid and lactone. So, depending on the mutarotation of the cyclic form to open-chain form, we could obtain through oxidation the mentioned products, with the main product being gluconic acid, as the equilibrium is shifted to this form.[96]

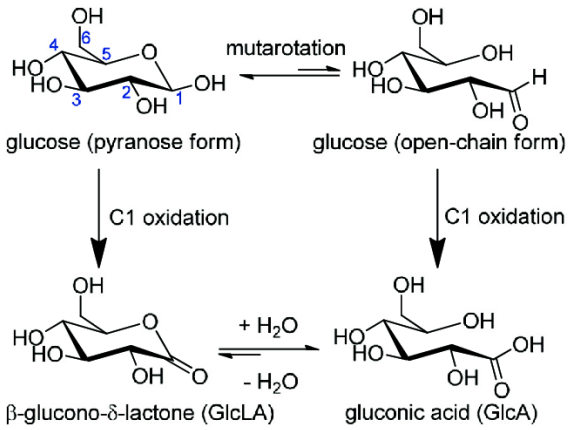

Figure IV.4-6 Oxidation of glucose to gluconic acid and β-Glucono-δ-lactone from reference [96]

Table IV.4-2 presents different glucose oxidation related species that could be determined in MS. This table presents their chemical and structural formulas, and the calculation of MS signals, together with the assigned peaks. **Table IV.4-3** instead, presents the peaks we already found in MS, using the CNWs surface, for glucose before and after electro-oxidation and for gluconic acid. We can observe that here is a series of peaks we can found in both gluconic acid and after EC, meaning that we can conclude that one by-product is, indeed, gluconic acid. This helps us establish that the mechanism we proposed in **Figure IV.4-1** is correct.

© 2020 Tous droits réservés.
lilliad.univ-lille.fr

Table IV.4-2 Different species related to oxidation of glucose and their chemical structure and formula, together with their molecular weight and MS assigned peaks.

analyte	M_w	Detected in MS	Chemical structure	Chemical formula
glucose	180	-	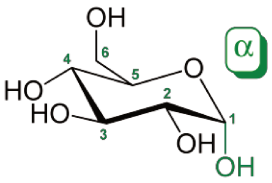	$C_6H_{12}O_6$
glucose sodium adduct	180+23= **203**	$[Glc+Na]^+$	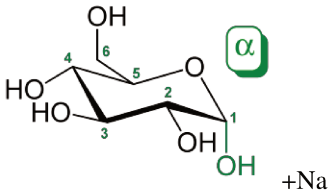	$C_6H_{12}O_6$+Na
glucose potassium adduct	180+39= **219**	$[Glc+K]^+$	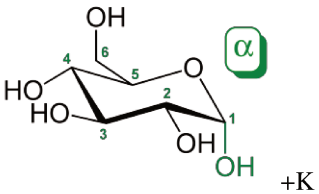	$C_6H_{12}O_6$+K
gluconic acid	196	-	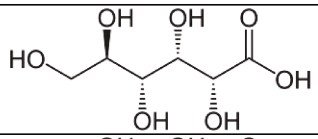	$C_6H_{12}O_7$
gluconic acid sodium adduct	196+23= **219**	$[GlcA+Na]^+$	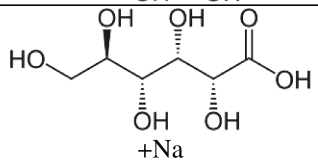	$C_6H_{12}O_7$+Na
gluconic acid potassium adduct	196+39= **235**	$[GlcA+K]^+$	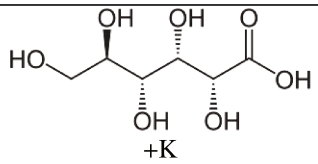	$C_6H_{12}O_7$+K
2*gluconic acid molecules sodium adduct	196*2+23= **415**	$[2GlcA+Na]^+$	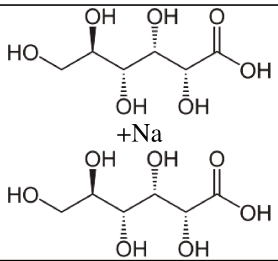	$C_{12}H_{24}O_{14}$+ Na
2*gluconic acid molecules potassium adduct	196*2+39= **431**	$[2GlcA+K]^+$	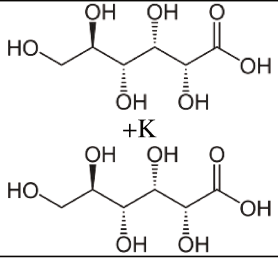	$C_{12}H_{24}O_{14}$+ K
sodium gluconate	196-1+23= **218**	$[GlcA-H+Na]^+$	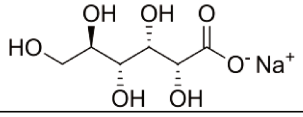	$C_6H_{11}NaO_7$

© 2020 Tous droits réservés.
lilliad.univ-lille.fr

sodium gluconate sodium adduct	196-1+23+23= **241**	[GlcA-H+2Na]$^+$	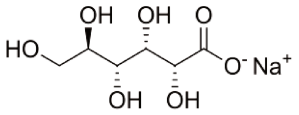 +Na	$C_6H_{11}NaO_7$ +Na
sodium gluconate sodium adduct	196-1+39+39= **273**	[GlcA-H+2K]$^+$	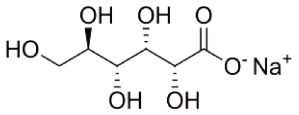 +K	$C_6H_{11}NaO_7$ +K
β-Glucono-δ-lactone	178	-	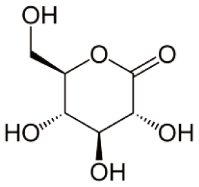	C_7O_6
2*β-Glucono-δ-lactone sodium adduct	178*2+23= **379**	[2GlcLa+Na]$^+$	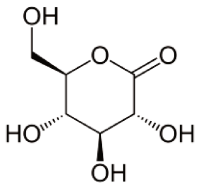 +Na	2*$C_6H_{10}O_6$ +Na= $C_{12}H_{20}O_{12}$+Na
2*β-Glucono-δ-lactone potassium adduct	178*2+39= **395**	[2GlcLa+Na]$^+$	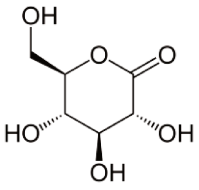 +K 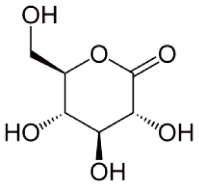	

Table IV.4-3 Comparison of the MS peaks, found for gluconic acid and glucose before and after electrochemistry. Highlighted the common peaks that help us prove that gluconic acid is a by-product of the electro-oxidation of glucose, using CNWs as EC-MS dual surface.

Background MS peaks in NaCl	Background MS peaks in NaOH	Gluconic acid (water) MS peaks (M_w= 196)	Glucose before EC MS peaks (M_w= 180)	Glucose After EC MS peaks
139	132	132 ?	NaCl 203 [Glc+Na]$^+$	203 [Glc+Na]$^+$
165	165	168 ?	NaCl 219 [Glc+K]$^+$	**176 ?**
175	180	218 [GlcA-H+Na]$^+$	NaOH 203 [Glc+Na]$^+$	**193 ?**
180	201	**219** [GlcA+Na]$^+$	NaOH **241** [GlcA-H+2Na]$^+$	228?
223	**214**	235 [GlcA+K]$^+$		**241** [GlcA-H+2Na]$^+$
307	**242**	228 ?		338
449	378	**241** [GlcA-H+2Na]$^+$		353
	392	**379** [2GlcLa+Na]$^+$		367
		395 [2GlcLa+K]$^+$		**379**[2GlcLa+Na]$^+$
		423 ?		**395**[2GlcLa+K]$^+$
		557 ?		
		575 ?		

© 2020 Tous droits réservés.
lilliad.univ-lille.fr

IV.4.1. EC and detection of ricin

Our next goal is to extend the above presented advantages, the preliminary results and mutual assistance of EC-MS for proteins, especially for ricin-like molecules. As we discussed in detail the SALDI-MS detection or ricin B chain, here we will talk mostly of electrochemical detection of ricin-like proteins.

Electrochemical DNA biosensors are used for detection by relaying on changes in the conformational dynamics of synthetic DNA (that is also modified with an aptamer or a recognition element for the specific target). Daniel et al. used gold sensors modified with methylene blue-DNA specific sequence for ricin, in PBS, pH 7.4, 100 mM. Square wave voltammetry was used to detect the methylene blue peak at -0.3 V, and when the analyte was added, due to conformational changes of the DNA, the efficiency of the electron transfer is assured, so the current is increased.[97] They were able to detect ricin A chain down to nM levels (100 fmol, in 100 µL). This limit of detection is similar to the one we determined using SALDI-MS for ricin B chain (250 fmol/0.5 µL).

Aluminium nanostructures were also used to detect ricin using an electrochemical impedance immunosensor.[98] The transducer was an anti-ricin polyclonal antibody. APTES (3-aminopropyltriethoxysilane) was used to render the surface hydrophilic and further modified with the antibody through glutaraldehyde cross-linking. Impedance was used to detect ricin, in acid pH, down to 500 ng/ml (15 pmol in 1 ml), in 20 minutes.

Glassy carbon electrode was also used for detection of ricin, in PBS (pH 7.0), using square wave voltametry, at a scan rate of 50 mV/s and 53 pM LOD was determined, at 0.72 V oxidation potential, using electrochemically active tryptophan amino acid in the ricin structure.[99] No modification of the glassy carbon was performed and no interfering studies were performed, but this work is interesting because of the simplicity.

These studies allow us to conclude that we could use our galactosamine modified CNWs surfaces for detection of ricin-like molecules, using electrochemistry, as carbon nanowalls were proven above to be a suitable platform for electrochemistry, due to their good electrical conductivity, robust mechanical resistance, high specific surface area and nanostructuration.

© 2020 Tous droits réservés.

lilliad.univ-lille.fr

IV.5. Conclusions and perspectives

IV.5.1. LSPR-MS graphene based dual surfaces

We did used 3 methods in order to create a gold nanoparticle network suitable for LSPR measurements: deposition of gold citrated nanoparticles, dewetting thin films of Au and e-beam writing of Au networks (Dots on the Fly method).

The least feasible, taking into account our experiments, is the Dots on the Fly method as several steps are involved and the bad adhesion of gold on glass was not even suitable to find the right current dose for creating a decent network. This method is expensive and requires e-beam writing.

We did succeed to obtain decent networks and LSPR-based absorbance shift using the dewetting method and gold citrated nanoparticles depositions. Even though dewetting method showed more potential in creating reproducible sized AuNPs, the stability is poor. This problem could be solved by following the graphene transfer or SiO_x deposition on top of the AuNPs network. AuNPs on AZO surfaces were more stable, and tuning ligand exchanges, deposition times and different sized AuNPs could influence greatly the sensitivity of the LSPR method. Nevertheless, we did succeed to obtain a nice detection for binding cystein based peptide (3.2 mM) on the dewetted AuNPs, with both LSPR and MS, but the same strategy could be used for the citrated (or other ligand) deposited AuNPs.

From these perspectives, the best method would be using citrated gold nanoparticles, as more parameters could be optimized to obtain a stable LSPR signal (shift of absorbance).

IV.5.2. SPR-MS graphene based dual surfaces.

As expected, drop casting method of both graphene oxide and reduced graphene oxide, is not suitable for SPR, as the thickness of the deposited layer is too big. As for SALDI-MS, no protein was detected. 3 or 2 peptides were detected in the peptide mixtures (MIX 1 and MIX 2), but only in the case of reduced graphene oxide. This is mainly due to the low background noise, because of the lack of oxygen groups on the surface, which could be ionized and can be detected by MS. Another disadvantage of this method is the thick layers deposited on the surface could fly and stick to the ion source and contaminate it, together with other important parts such as electrodes. From our studies, this is the worse method to create a dual SPR-MS graphene based surface.

In the case of layer by layer, that is a simple, low cost and not time consuming method, the best compromise is to use rGO with the polcation (PDDA), with 4 layers of PDDA/rGO,

© 2020 Tous droits réservés.
lilliad.univ-lille.fr

as also rGO does not give rise to numerous background peaks (by contrast with PDDA/GO), even though SPR is not the best, as a reflectivity lost of 15% can be observed. Nevertheless, there is enough dynamic range for the detection of compounds.

As the entire purpose of this thesis it to detect proteins using graphene based surfaces with MS and other bimodal MS techniques, the best method are considered to be the ones that can detect a model protein (cytochrome C). From this point of view, using bubble method, where a surfactant is used to deposit a ultrathin layer around 10 nm on the glass/gold surface, we were able to detect 50 pmol of cytochrome C. As this method is simple, rapid (20 minutes), low cost and reproducible, it seems to be one of the best approaches in detecting proteins using SPR-MS bimodal technique. We were not able to use this method for reduced graphene deposition, as the surfactant was not able to create the thin suspension layer of the bubble, as in the case of graphene oxide.

The second best method is wet transfer of CVD pristine graphene, which gave rise to peaks for both cytochrome C and insulin. The method that worked seems to be a double layered graphene enhancement of LDI-MS process. Confinement of heat dissipation could be achieved apparently using a double layer graphene, as multiple attempts of using single layered graphene were not successful. Other insulating technique was used: deposition of high refractive index $SiO_{x,}$ followed by deposition of graphene. This gave rise to detection of peptides in mixtures MIX 1 and MIX2 and the conclusion that a layer of 6 nm is the best for both SPR and MS. As there are many records of graphene enhancing SPR signal, this could be a very interesting way to combine it with MS. Nevertheless, we do have to take into account the complexity and high cost of this method, along with the time required for the transfer (usually more than 1 day). As this method also did not present good reproducibility for single layered graphene, but preliminary results showed very promising results for double layered method, further studies are to be performed in order to assess properly the potential used of this method as SPR-MS dual technique.

The third best deposition method seems to be electrophoretic deposition. This method was used previously in SPR, but, to our knowledge, never in SALDI-MS. We were able to detect cytochrome C, on thin depositions of the same electrophoretic graphene oxide surface. It is known that this method reduces slightly the graphene oxide, so an intermediate state is obtained, between graphene oxide and reduced graphene oxide. For further studies other parameters have to be optimized (voltage, deposition time).

© 2020 Tous droits réservés.
lilliad.univ-lille.fr

IV.5.3. SERS-MS graphene based dual surfaces

In this section we did used CNWs as plasmonic-free enhancer of the SERS signal of ricin B chain. Raman bands were clearly assigned to ricin B chain after second derivate or difference average spectra were studied. Peaks at 797, 832 and 945 cm^{-1} can be used for further studies over ricin samples. At this moment we were able to detect 7.5 pmol/0.5 µL of ricin solutions (ammonium citrate dibasic, 150 mM, incubation 5 minutes, using a CNWs 5k 5H surface). The experimental conditions used here are the same we used in Chapter III for detection of ricin B chain in soft drinks and blood serum, using SALDI-MS. This is compatible for dual detection of ricin B chain using SERS/MS bimodal CNWS, as the same surface and analyte spot studied with SERS, can be further analyzed with MS, or the inverse. As mutual assistance of SERS and MS was already described above, in our case this surfaces could be used to differentiate between other molecules with similar molecular weight, or to distinguish, maybe, between ricin B chain and ricin A chain, using the same affinity strategy used for SALDI-MS. Improvements can be done studying the same parameters we studied for SALDI-MS optimization (height of the nanowalls, doping level, salt concentration).

IV.5.4. EC-MS dual surfaces

We did manage to use the same CNWs surface for detection of glucose with both techniques, using similar optimized parameters. SALDI-MS was largely discussed in Chapter III, and the performances of CNWs as EC electrode are described and compared to other references for glucose detection described in literature. Our method is competitive and SALDI-MS is far more sensitive, as this is the advantage of high resolution mass spectrometry. The EC method can be improved by studying different doping levels and tuning different morphological characteristics (like we did in Chapter III for the detection of ricin B chain). This will improve the sensitivity, as CNWs change electrical conductivity with the doping level.

The most important part is that we did succeed to prove the mutual assistance of EC-MS of our surface: quantification of the same analyte (glucose) with both techniques, but the same surface, studying electrochemical reactions with EC and further clarification of the EC redox mechanism, identification of by-products (in our case gluconic acid) of the electro-oxidation of glucose, with MS.

IV.5.5. Dual surfaces conclusion and perspectives

The combination of complementary technique is desired as it can create powerful analytical tools. In this chapter we show how SPR, SERS and EC can be combined with MS,

© 2020 Tous droits réservés.
lilliad.univ-lille.fr

using SALDI-MS graphene based surfaces. For each bimodal technique the most important parameters are described and characterizations and different studies are performed to obtain optimized surfaces to suit the combination purpose.

Our final goal, for this section was to show how these techniques could be used for the detection of ricin B chain, and in general for ricin-like toxins. Our approaches are quite original, detailed and the preliminary results are promising. This chapter only mentions the SALDI-MS results that were described in detail in Chapter II (small molecule detection) and Chapter III (protein and ricin B chain detection). In all cases SALDI-MS plays an important role in the detection and quantification, as well identification of products, with high sensitivity.

Different model molecules are being used: mainly cytochrome C and/or insulin (SPR-MS) or cystein based peptides (LSPR-MS), or glucose for the EC/MS. Ricin B chain was used for the SERS-MS studies.

For LSPR-MS, the best method was deposition of citrated gold, as we can exchange the ligand, play with incubation periods and obtain more stable LSPR signals. As for SPR-MS, graphene like materials are known to enhance SPR and MS signals, so different deposition techniques were also studied, to ensure a good surface coverage of the substrate: 1)bubble surfactant method of graphene oxide, 2) wet transfer of CVD pristine graphene, 3) electrophoretic deposition of graphene, 4) layer by layer using a polycation and graphene oxide, 5) drop casting of both graphene and reduced graphene. The mentioning order is in correlation with decreasing SALDI-MS efficiency towards proteins.

Another perspective that we did not approach in any of these above sections is the following: an SPR system, in the constant angle mode, can actually help to improve the sensor, because the concentrations of ligands (amino modified sugars) are to be optimized, and a maximum binding concentration can be assessed. Only after these steps are achieved, we can fully say that our SPR-MS bimodal surfaces are fully optimized for to the detection of ricin B chain/ricin-like molecules. A schematic representation of the optimization flow is presented in **Figure IV.5-1**. For this purpose, the above described glass/Au/graphene-like-material surfaces, are to be modified with pyrene-COOH (as described in Chapter III) and then, the amino modified sugars will be immobilized on the sensor, using the SPR microfluidic system for real-time assessment of the binding. Only after the ligand binding is correctly achieved (**Figure IV.5-1A**), different concentrations of a ricin B chain can be used to observe the change in refractive index using an SPR/LSPR system. The sensor will be calibrated and different other characteristics will be determined (kinetic constants, detection

© 2020 Tous droits réservés.
lilliad.univ-lille.fr

limit, linear range, sensitivity, reproducibility). The incorrect sensor development means that the detection of the analyte cannot be achieved in the optimal conditions.

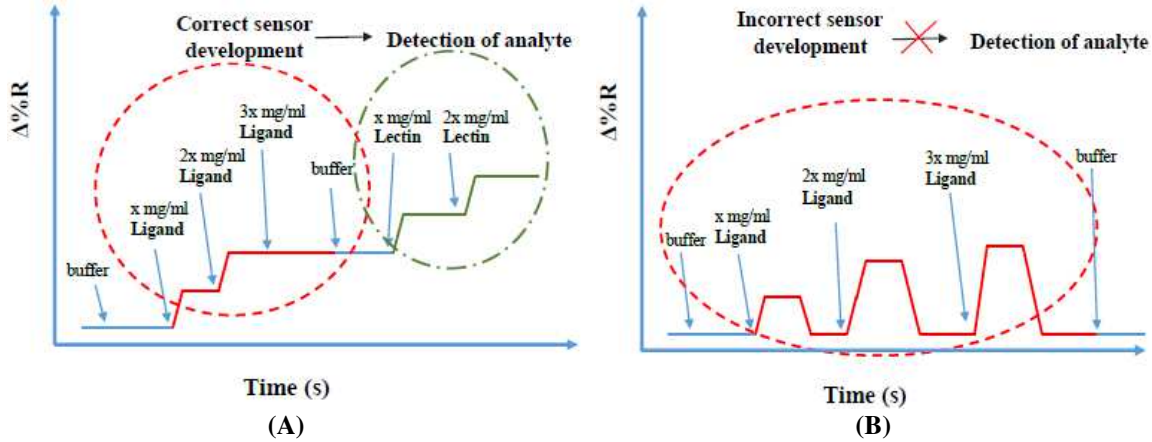

Figure IV.5-1 Schematic representation of **(A)** successful and **(B)** unsuccessful binding of ligand (galactosamine or other amino modified sugar), using SPR, in the constant angle mode.

In the SERS/MS part we did actually use ricin B chain, and the results are interesting as we were able to select specific Raman bands at which ricin B chain vibrates. For data processing we used two spectral distinctions: second derivatives of both control and analyte spectra and average difference of the same spectra. As it can be seen, SERS usually requires more data manipulation, so the SALDI-MS method comes with rapid and clearer distinction for the ricin detection. This being a plasmonic-free SERS platform, it can be used for molecular interaction, orientation and functionalization of ricin. All these complimentary characteristics make SERS-MS a powerful tool. To the best of our knowledge, this is the first plasmonic-free method optimized and described for ricin-like proteins.

For EC-MS part we did characterize the performances of our electrode CNWS and compared it to the literature. We used the similar parameters for both methods. The protonation of glucose is assured but the sodium ions in MS, and NaOH used as electrolyte in electrochemistry was good enough to apply our SALDI-MS method, even though better detection of glucose was achieved in Chapter III, using NaCl. Our method is in good accordance with other literature methods, and the SALDI-MS method is by far more sensitive than the electrochemical methods. Interfering species study showed that we could used our surface for further detection in real samples, as blood serum or soft drinks, as it was already proven very efficient for the same purpose using SALDI-MS (Chapter III). As the most important feature of EC is to study electrochemical reactions and to quantify specifically different analytes, the SALDI-MS can help a lot with the elucidation of the redox mechanism. We did show here the gluconic acid is a by-product in the electrochemical oxidation of

© 2020 Tous droits réservés.
lilliad.univ-lille.fr

glucose, by comparing the MS peaks before and after oxidation with the MS peaks of gluconic acid. As the proof of concept regarding the combination of EC with MS was described in detail for glucose, a literature study showed the approaches used for ricin detection using EC, thus the possibility to further couple it with our SALDI-MS method described in Chapter III.

We succeeded to show the proof-of-concept of all bimodal methods (SPR-MS, SERS-MS and EC-MS) and we did describe further approaches to transfer these methodologies to detection of ricin-like proteins. The affinity strategy used in Chapter III is suitable for assuring the specificity of the further to develop methods.

From our studies, we can state that SPR-MS is the best method that someone can develop, due to huge amount of information that one can obtained from it (quantitative and qualitative analysis, very good approach for sensor formation, high throughput, as micro-arrays can be developed, enzymatic activity of ricin and detection of entire molecule, specifically extracted from real samples). Micro-fluidic format of SPR is low cost and low reagent consuming, but it can require some time for SPR signal stabilization and equipment preparation. Also, this method is usually compatible for neutral pH approach, and SALDI-MS is high salt tolerant, making it suitable for real sample applications (as we already showed in Chapter III).

SERS-MS is the second best, as we used plasmonic-free approach and one method completes the other. Another advantage is the rapidity of both methods (similar necessary time for data acquisitions, 10 minutes), but a little bit more complicated for data manipulation and band interpretation, in the case of SERS.

EC-MS is the third best method, in our opinion and according to our preliminary results, as we did not yet approach the ricin electrochemical detection. Nevertheless, this dual tool can offer information about molecular interaction, group functionalizations and determination of electrochemically obtained by-products (proof-of-concept for glucose case).

All methods require calibration, and this requires time. But a well establish method can reduce the detection time. In our opinion, all three methods deserve further optimizations for ricin detection, as for all three proof-of-concepts were shown. The same affinity strategy (amino modified sugar specific for ricin, in our case galactosamine) can be applied to all three, making them comparable for future development steps.

© 2020 Tous droits réservés.
lilliad.univ-lille.fr

IV.6. References

1 Breault-Turcot, J., Chaurand, P. & Masson, J.-F. Unravelling Nonspecific Adsorption of Complex Protein Mixture on Surfaces with SPR and MS. *Analytical Chemistry* **86**, 9612-9619, doi:10.1021/ac502077b (2014).

2 Kurita, M., Arakawa, R. & Kawasaki, H. Silver nanoparticle functionalized glass fibers for combined surface-enhanced Raman scattering spectroscopy (SERS)/surface-assisted laser desorption/ionization (SALDI) mass spectrometry via plasmonic/thermal hot spots. *Analyst* **141**, 5835-5841, doi:10.1039/c6an00511j (2016).

3 Marshall, D. D. & Powers, R. Beyond the paradigm: Combining mass spectrometry and nuclear magnetic resonance for metabolomics. *Progress in Nuclear Magnetic Resonance Spectroscopy* **100**, 1-16, doi:https://doi.org/10.1016/j.pnmrs.2017.01.001 (2017).

4 Nitta, S., Yamamoto, A., Kurita, M., Arakawa, R. & Kawasaki, H. Gold-Decorated Titania Nanotube Arrays as Dual-Functional Platform for Surface-Enhanced Raman Spectroscopy and Surface-Assisted Laser Desorption/Ionization Mass Spectrometry. *ACS Applied Materials & Interfaces* **6**, 8387-8395, doi:10.1021/am501291d (2014).

5 Xue, J., Bai, Y. & Liu, H. Hybrid methods of surface plasmon resonance coupled to mass spectrometry for biomolecular interaction analysis. *Analytical and Bioanalytical Chemistry* **411**, 3721-3729, doi:10.1007/s00216-019-01906-y (2019).

6 Bruins, A. P. An overview of electrochemistry combined with mass spectrometry. *TrAC Trends in Analytical Chemistry* **70**, 14-19, doi:https://doi.org/10.1016/j.trac.2015.02.016 (2015).

7 Faber, H., Vogel, M. & Karst, U. Electrochemistry/mass spectrometry as a tool in metabolism studies-a review. *Anal Chim Acta* **834**, 9-21 (2014).

8 Williams, C. & Addona, T. A. The integration of SPR biosensors with mass spectrometry: possible applications for proteome analysis. *Trends in Biotechnology* **18**, 45-48, doi:https://doi.org/10.1016/S0167-7799(99)01389-X (2000).

9 Stigter, E. C. A., de Jong, G. J. & van Bennekom, W. P. Coupling surface-plasmon resonance and mass spectrometry to quantify and to identify ligands. *TrAC Trends in Analytical Chemistry* **45**, 107-120, doi:https://doi.org/10.1016/j.trac.2012.09.004 (2013).

10 Wang, A. X. & Kong, X. Review of Recent Progress of Plasmonic Materials and Nano-Structures for Surface-Enhanced Raman Scattering. *Materials* **8**, 3024-3052 (2015).

11 He, L. *et al.* Rapid Detection of Ricin in Milk Using Immunomagnetic Separation Combined with Surface-Enhanced Raman Spectroscopy. *Journal of Food Science* **76**, N49-N53, doi:10.1111/j.1750-3841.2011.02196.x (2011).

© 2020 Tous droits réservés.
lilliad.univ-lille.fr

12 Snyder, D. T., Pulliam, C. J., Ouyang, Z. & Cooks, R. G. Miniature and Fieldable Mass Spectrometers: Recent Advances. *Analytical Chemistry* **88**, 2-29, doi:10.1021/acs.analchem.5b03070 (2016).
13 Chakraborty, P. & Pradeep, T. The emerging interface of mass spectrometry with materials. *NPG Asia Materials* **11**, 48, doi:10.1038/s41427-019-0149-3 (2019).
14 Law, K. P. & Larkin, J. Recent advances in SALDI-MS techniques and their chemical and bioanalytical applications. *Analytical and Bioanalytical Chemistry* **399**, 2597-2622, doi:10.1007/s00216-010-4063-3 (2011).
15 Abdelhamid, H. N. Nanoparticle-based surface assisted laser desorption ionization mass spectrometry: a review. *Microchimica Acta* **186**, 682, doi:10.1007/s00604-019-3770-5 (2019).
16 Broza, Y. Y., Zuri, L. & Haick, H. Combined Volatolomics for Monitoring of Human Body Chemistry. *Sci Rep* **4**, 4611, doi:10.1038/srep04611 (2014).
17 Chiang, C.-K., Chen, W.-T. & Chang, H.-T. Nanoparticle-based mass spectrometry for the analysis of biomolecules. *Chemical Society Reviews* **40**, 1269-1281, doi:10.1039/c0cs00050g (2011).
18 Picca, R. A., Calvano, C. D., Cioffi, N. & Palmisano, F. Mechanisms of Nanophase-Induced Desorption in LDI-MS. A Short Review. *Nanomaterials (Basel, Switzerland)* **7**, 75, doi:10.3390/nano7040075 (2017).
19 Liu, L. *et al.* Analysis of intestinal injuries induced by ricin in vitro using SPR technology and MS identification. *International journal of molecular sciences* **10**, 2431-2439 (2009).
20 Wang, W. *et al.* Bimodal Imprint Chips for Peptide Screening: Integration of High-Throughput Sequencing by MS and Affinity Analyses by Surface Plasmon Resonance Imaging. *Analytical Chemistry* **86**, 3703-3707, doi:10.1021/ac500465e (2014).
21 Zhang, Y. *et al.* Interface for Online Coupling of Surface Plasmon Resonance to Direct Analysis in Real Time Mass Spectrometry. *Analytical Chemistry* **87**, 6505-6509, doi:10.1021/acs.analchem.5b01272 (2015).
22 Zhang, Y. *et al.* A dielectric barrier discharge ionization based interface for online coupling surface plasmon resonance with mass spectrometry. *Analyst* **141**, 3343-3348, doi:10.1039/c6an00561f (2016).
23 Marchesini, G. R. *et al.* Nanoscale Affinity Chip Interface for Coupling Inhibition SPR Immunosensor Screening with Nano-LC TOF MS. *Analytical Chemistry* **80**, 1159-1168, doi:10.1021/ac071564p (2008).
24 Buijs, J. & Franklin, G. C. SPR-MS in functional proteomics. *Briefings in Functional Genomics* **4**, 39-47, doi:10.1093/bfgp/4.1.39 (2005).

© 2020 Tous droits réservés.
lilliad.univ-lille.fr

25 Remy-Martin, F. *et al.* Surface plasmon resonance imaging in arrays coupled with mass spectrometry (SUPRA–MS): proof of concept of on-chip characterization of a potential breast cancer marker in human plasma. *Analytical and Bioanalytical Chemistry* **404**, 423-432, doi:10.1007/s00216-012-6130-4 (2012).

26 Pilolli, R., Palmisano, F. & Cioffi, N. Gold nanomaterials as a new tool for bioanalytical applications of laser desorption ionization mass spectrometry. *Analytical and Bioanalytical Chemistry* **402**, 601-623, doi:10.1007/s00216-011-5120-2 (2012).

27 Chen, C.-Y., Hinman, S. S., Duan, J. & Cheng, Q. Nanoglassified, Optically-Active Monolayer Films of Gold Nanoparticles for in Situ Orthogonal Detection by Localized Surface Plasmon Resonance and Surface-Assisted Laser Desorption/Ionization-MS. *Analytical Chemistry* **86**, 11942-11945, doi:10.1021/ac503808r (2014).

28 Wu, L., Chu, H. S., Koh, W. S. & Li, E. P. Highly sensitive graphene biosensors based on surface plasmon resonance. *Optics Express* **18**, 14395-14400, doi:10.1364/oe.18.014395 (2010).

29 Lamont, E. A., He, L., Warriner, K., Labuza, T. P. & Sreevatsan, S. A single DNA aptamer functions as a biosensor for ricin. *Analyst* **136**, 3884-3895 (2011).

30 Zagorodko, O. *et al.* Highly sensitive detection of DNA hybridization on commercialized graphene-coated surface plasmon resonance interfaces. *Analytical Chemistry* **86**, 11211-11216 (2014).

31 Penezic, A. *et al.* Carbohydrate–lectin interaction on graphene-coated surface plasmon resonance (SPR) interfaces. *Plasmonics* **9**, 677-683 (2014).

32 Maurer, T. *et al.* Enhancing LSPR Sensitivity of Au Gratings through Graphene Coupling to Au Film. *Plasmonics* **9**, 507-512, doi:10.1007/s11468-013-9649-0 (2013).

33 Sepúlveda, B., Angelomé, P. C., Lechuga, L. M. & Liz-Marzán, L. M. LSPR-based nanobiosensors. *Nano Today* **4**, 244-251, doi:https://doi.org/10.1016/j.nantod.2009.04.001 (2009).

34 Anker, J. N. *et al.* Detection and Identification of Bioanalytes with High Resolution LSPR Spectroscopy and MALDI Mass Spectrometry. *The Journal of Physical Chemistry C* **113**, 5891-5894, doi:10.1021/jp900266k (2009).

35 Sagle, L. B., Ruvuna, L. K., Ruemmele, J. A. & Van Duyne, R. P. Advances in localized surface plasmon resonance spectroscopy biosensing. *Nanomedicine* **6**, 1447-1462, doi:10.2217/nnm.11.117 (2011).

36 McLean, J. A., Stumpo, K. A. & Russell, D. H. Size-Selected (2−10 nm) Gold Nanoparticles for Matrix Assisted Laser Desorption Ionization of Peptides. *Journal of the American Chemical Society* **127**, 5304-5305, doi:10.1021/ja043907w (2005).

© 2020 Tous droits réservés.
lilliad.univ-lille.fr

Thèse de Ioana Silvia Hosu, Université de Lille, 2020

37 Singh, P. SPR Biosensors: Historical Perspectives and Current Challenges. *Sensors and Actuators B: Chemical* **229**, 110-130, doi:https://doi.org/10.1016/j.snb.2016.01.118 (2016).

38 Trasobares, J. *et al.* High speed e-beam lithography for gold nanoarray fabrication and use in nanotechnology. *Beilstein J Nanotechnol* **5**, 1918-1925, doi:10.3762/bjnano.5.202 (2014).

39 Kawasaki, H. *et al.* Layer-by-Layer Self-Assembled Mutilayer Films of Gold Nanoparticles for Surface-Assisted Laser Desorption/Ionization Mass Spectrometry. *Analytical Chemistry* **80**, 7524-7533, doi:10.1021/ac800789t (2008).

40 Hall, W. P., Ngatia, S. N. & Van Duyne, R. P. LSPR Biosensor Signal Enhancement Using Nanoparticle−Antibody Conjugates. *The Journal of Physical Chemistry C* **115**, 1410-1414, doi:10.1021/jp106912p (2011).

41 Szunerits, S., Maalouli, N., Wijaya, E., Vilcot, J.-P. & Boukherroub, R. Recent advances in the development of graphene-based surface plasmon resonance (SPR) interfaces. *Analytical and Bioanalytical Chemistry* **405**, 1435-1443, doi:10.1007/s00216-012-6624-0 (2013).

42 Singh, M. *et al.* Noncovalently Functionalized Monolayer Graphene for Sensitivity Enhancement of Surface Plasmon Resonance Immunosensors. *Journal of the American Chemical Society* **137**, 2800-2803, doi:10.1021/ja511512m (2015).

43 He, L. *et al.* Label-free femtomolar cancer biomarker detection in human serum using graphene-coated surface plasmon resonance chips. *Biosensors and Bioelectronics* **89**, 606-611, doi:https://doi.org/10.1016/j.bios.2016.01.076 (2017).

44 Zhou, D. *et al.* Mass spectrometry imaging of small molecules in biological tissues using graphene oxide as a matrix. *Analytica Chimica Acta* **962**, 52-59, doi:https://doi.org/10.1016/j.aca.2017.01.043 (2017).

45 Tang, L. A. L., Wang, J. & Loh, K. P. Graphene-based SELDI probe with ultrahigh extraction and sensitivity for DNA oligomer. *Journal of the American Chemical Society* **132**, 10976-10977 (2010).

46 Zhou, X. *et al.* Reduced graphene oxide films used as matrix of MALDI-TOF-MS for detection of octachlorodibenzo-p-dioxin. *Chemical Communications* **46**, 6974-6976, doi:10.1039/c0cc01681k (2010).

47 Wang, J. *et al.* An antibody-graphene oxide nanoribbon conjugate as a surface enhanced laser desorption/ionization probe with high sensitivity and selectivity. *Chemical Communications* **51**, 4619-4622, doi:10.1039/c4cc10401c (2015).

48 Lee, G., Bae, S.-E., Huh, S. & Cha, S. Graphene oxide embedded sol–gel (GOSG) film as a SALDI MS substrate for robust metabolite fingerprinting. *RSC Advances* **5**, 56455-56459, doi:10.1039/c5ra11497g (2015).

© 2020 Tous droits réservés.

lilliad.univ-lille.fr

49 Kong, X. & Huang, Y. Applications of graphene in mass spectrometry. *J Nanosci Nanotechnol* **14**, 4719-4732 (2014).
50 Sunner, J., Dratz, E. & Chen, Y.-C. Graphite surface-assisted laser desorption/ionization time-of-flight mass spectrometry of peptides and proteins from liquid solutions. *Analytical Chemistry* **67**, 4335-4342, doi:10.1021/ac00119a021 (1995).
51 Kajal, P., Ghosh, K. & Powar, S. in *Applications of Solar Energy* (eds Himanshu Tyagi, Avinash Kumar Agarwal, Prodyut R. Chakraborty, & Satvasheel Powar) 341-364 (Springer Singapore, 2018).
52 Panda, D., Nandi, A., Datta, S. K., Saha, H. & Majumdar, S. Selective detection of carbon monoxide (CO) gas by reduced graphene oxide (rGO) at room temperature. *RSC Advances* **6**, 47337-47348, doi:10.1039/c6ra06058g (2016).
53 Chavez-Valdez, A., Shaffer, M. S. P. & Boccaccini, A. R. Applications of Graphene Electrophoretic Deposition. A Review. *The Journal of Physical Chemistry B* **117**, 1502-1515, doi:10.1021/jp3064917 (2013).
54 Subramanian, P. *et al.* Lysozyme detection on aptamer functionalized graphene-coated SPR interfaces. *Biosensors and Bioelectronics* **50**, 239-243 (2013).
55 Liu, Q. & He, L. Quantitative study of solvent and surface effects on analyte ionization in desorption ionization on silicon (DIOS) mass spectrometry. *Journal of the American Society for Mass Spectrometry* **19**, 8-13, doi:10.1016/j.jasms.2007.10.002 (2008).
56 Ma, J. *et al.* Wavelength-versatile graphene-gold film saturable absorber mirror for ultra-broadband mode-locking of bulk lasers. *Sci Rep* **4**, 5016 (2014).
57 Deokar, G. *et al.* Towards high quality CVD graphene growth and transfer. *Carbon* **89**, 82-92, doi:https://doi.org/10.1016/j.carbon.2015.03.017 (2015).
58 Ferrari, A. C. *et al.* Raman Spectrum of Graphene and Graphene Layers. *Physical Review Letters* **97**, 187401, doi:10.1103/PhysRevLett.97.187401 (2006).
59 Szunerits, S. & Boukherroub, R. Preparation and Characterization of Thin Films of SiOx on Gold Substrates for Surface Plasmon Resonance Studies. *Langmuir* **22**, 1660-1663, doi:10.1021/la052773c (2006).
60 Lu, J.-Y. *et al.* Insights into graphene wettability transparency by locally probing its surface free energy. *Nanoscale* **11**, 7944-7951, doi:10.1039/c9nr00155g (2019).
61 Rafiee, J. *et al.* Wetting transparency of graphene. *Nature Materials* **11**, 217-222, doi:10.1038/nmat3228 (2012).
62 Ghosh, S. *et al.* Effect of 1- Pyrene Carboxylic-Acid Functionalization of Graphene on Its Capacitive Energy Storage. *The Journal of Physical Chemistry C* **116**, 20688-20693, doi:10.1021/jp303339f (2012).

© 2020 Tous droits réservés.
lilliad.univ-lille.fr

63 Hayyan, M., Abo-Hamad, A., AlSaadi, M. A. & Hashim, M. A. Functionalization of graphene using deep eutectic solvents. *Nanoscale Research Letters* **10**, 324, doi:10.1186/s11671-015-1004-2 (2015).

64 Vasilescu, A. *et al.* Surface Plasmon Resonance based sensing of lysozyme in serum on Micrococcus lysodeikticus-modified graphene oxide surfaces. *Biosensors and Bioelectronics* **89**, 525-531 (2017).

65 Chung, K. *et al.* Systematic Study on the Sensitivity Enhancement in Graphene Plasmonic Sensors Based on Layer-by-Layer Self-Assembled Graphene Oxide Multilayers and Their Reduced Analogues. *ACS Applied Materials & Interfaces* **7**, 144-151, doi:10.1021/am508103z (2015).

66 Kim, Y.-K. & Min, D.-H. Fabrication of Alternating Multilayer Films of Graphene Oxide and Carbon Nanotube and Its Application in Mechanistic Study of Laser Desorption/Ionization of Small Molecules. *ACS Applied Materials & Interfaces* **4**, 2088-2095, doi:10.1021/am300054z (2012).

67 Kuo, T.-R. *et al.* Layer-by-layer thin film of reduced graphene oxide and gold nanoparticles as an effective sample plate in laser-induced desorption/ionization mass spectrometry. *Analytica Chimica Acta* **809**, 97-103, doi:https://doi.org/10.1016/j.aca.2013.11.050 (2014).

68 Azevedo, J. *et al.* Versatile Wafer-Scale Technique for the Formation of Ultrasmooth and Thickness-Controlled Graphene Oxide Films Based on Very Large Flakes. *ACS Applied Materials & Interfaces* **7**, 21270-21277, doi:10.1021/acsami.5b05540 (2015).

69 Georgakilas, V. *et al.* Noncovalent Functionalization of Graphene and Graphene Oxide for Energy Materials, Biosensing, Catalytic, and Biomedical Applications. *Chemical Reviews* **116**, 5464-5519, doi:10.1021/acs.chemrev.5b00620 (2016).

70 Azevedo, J. l. *et al.* Versatile Wafer-Scale Technique for the Formation of Ultrasmooth and Thickness-Controlled Graphene Oxide Films Based on Very Large Flakes. *ACS applied materials & interfaces* **7**, 21270-21277 (2015).

71 Chen, Y. C. & Tsai, M. F. Using surfactants to enhance the analyte signals in activated carbon, surface-assisted laser desorption/ionization (SALDI) mass spectrometry. *Journal of mass spectrometry* **35**, 1278-1284 (2000).

72 Walch, N. J., Nabok, A., Davis, F. & Higson, S. P. J. Characterisation of thin films of graphene-surfactant composites produced through a novel semi-automated method. *Beilstein J Nanotechnol* **7**, 209-219, doi:10.3762/bjnano.7.19 (2016).

73 Rienzie, R., Ramanayaka, S. & Adassooriya, N. M. in *Pharmaceuticals and Personal Care Products: Waste Management and Treatment Technology* (eds Majeti Narasimha Vara Prasad, Meththika Vithanage, & Atya Kapley) 279-296 (Butterworth-Heinemann, 2019).

© 2020 Tous droits réservés.
lilliad.univ-lille.fr

74 Alessandri, I. *et al.* "RaMassays": Synergistic Enhancement of Plasmon-Free Raman Scattering and Mass Spectrometry for Multimodal Analysis of Small Molecules. *Sci Rep* **6**, 34521, doi:10.1038/srep34521 (2016).

75 Zhang, X., Zhao, J., Whitney, A. V., Elam, J. W. & Van Duyne, R. P. Ultrastable Substrates for Surface-Enhanced Raman Spectroscopy: Al2O3 Overlayers Fabricated by Atomic Layer Deposition Yield Improved Anthrax Biomarker Detection. *Journal of the American Chemical Society* **128**, 10304-10309, doi:10.1021/ja0638760 (2006).

76 Galopin, E. *et al.* Silicon Nanowires Coated with Silver Nanostructures as Ultrasensitive Interfaces for Surface-Enhanced Raman Spectroscopy. *ACS Applied Materials & Interfaces* **1**, 1396-1403, doi:10.1021/am900087s (2009).

77 Guinan, T. M., Gustafsson, O. J. R., McPhee, G., Kobus, H. & Voelcker, N. H. Silver Coating for High-Mass-Accuracy Imaging Mass Spectrometry of Fingerprints on Nanostructured Silicon. *Analytical Chemistry* **87**, 11195-11202, doi:10.1021/acs.analchem.5b02567 (2015).

78 Szlag, V. M. *et al.* SERS Detection of Ricin B-Chain via N-Acetyl-Galactosamine Glycopolymers. *ACS Sensors* **1**, 842-846, doi:10.1021/acssensors.6b00209 (2016).

79 Evlashin, S. *et al.* Optical and IR absorption of multilayer carbon nanowalls. *Carbon* **70**, 111-118, doi:https://doi.org/10.1016/j.carbon.2013.12.079 (2014).

80 He, L. *et al.* Aptamer-based surface-enhanced Raman scattering detection of ricin in liquid foods. *Chemical Science* **2**, 1579-1582, doi:10.1039/c1sc00201e (2011).

81 Wang, M. *et al.* Combination of inverted pyramidal nanovoid with silver nanoparticles to obtain further enhancement and its detection for ricin. *Nanoscale Research Letters* **10**, 92, doi:10.1186/s11671-015-0806-6 (2015).

82 Zengin, A., Tamer, U. & Caykara, T. Fabrication of a SERS based aptasensor for detection of ricin B toxin. *Journal of Materials Chemistry B* **3**, 306-315, doi:10.1039/c4tb00290c (2015).

83 Tang, J.-j. *et al.* New Surface-Enhanced Raman Sensing Chip Designed for On-Site Detection of Active Ricin in Complex Matrices Based on Specific Depurination. *ACS Applied Materials & Interfaces* **8**, 2449-2455, doi:10.1021/acsami.5b12860 (2016).

84 Dyakonov, P. *et al.* Carbon nanowalls as a platform for biological SERS studies. *Sci Rep* **7**, 13352, doi:10.1038/s41598-017-13087-8 (2017).

85 Mehigan, S., Smyth, C. A. & McCabe, E. M. Bridging the Gap between SERS Enhancement and Reproducibility by Salt Aggregated Silver Nanoparticles. *Nanomaterials and Nanotechnology* **5**, 5, doi:10.5772/60125 (2015).

© 2020 Tous droits réservés.
lilliad.univ-lille.fr

86 Fargašová, A. *et al.* Influence of various chloride ion concentrations on silver nanoparticle transformations and effectiveness in surface enhanced Raman scattering for different excitation wavelengths. *RSC Advances* **5**, 9737-9744, doi:10.1039/c4ra13881c (2015).

87 Guerra-López, J. R., Güida, J. A. & Della Védova, C. O. Infrared and Raman studies on renal stones: the use of second derivative infrared spectra. *Urological Research* **38**, 383-390, doi:10.1007/s00240-010-0305-2 (2010).

88 Szunerits, S., Coffinier, Y. & Boukherroub, R. Diamond Nanowires: A Novel Platform for Electrochemistry and Matrix-Free Mass Spectrometry. *Sensors* **15**, 12573 (2015).

89 Wang, H.-C. & Lee, A.-R. Recent developments in blood glucose sensors. *Journal of Food and Drug Analysis* **23**, 191-200, doi:https://doi.org/10.1016/j.jfda.2014.12.001 (2015).

90 Hosu, I. S. *et al.* Carbon nanowalls: a new versatile graphene based interface for the laser desorption/ionization-mass spectrometry detection of small compounds in real samples. *Nanoscale* **9**, 9701-9715, doi:10.1039/c7nr01069a (2017).

91 Wang, Q., Wang, Q., Li, M., Szunerits, S. & Boukherroub, R. Preparation of reduced graphene oxide/Cu nanoparticle composites through electrophoretic deposition: application for nonenzymatic glucose sensing. *RSC Advances* **5**, 15861-15869, doi:10.1039/c4ra14132f (2015).

92 Wang, Q. *et al.* Non-enzymatic glucose sensing on long and short diamond nanowire electrodes. *Electrochemistry Communications* **34**, 286-290, doi:https://doi.org/10.1016/j.elecom.2013.07.014 (2013).

93 Wang, S., Zhao, L., Xu, R., Ma, Y. & Ma, L. Facile fabrication of biosensors based on Cu nanoparticles modified as-grown CVD graphene for non-enzymatic glucose sensing. *Journal of Electroanalytical Chemistry* **853**, 113527, doi:https://doi.org/10.1016/j.jelechem.2019.113527 (2019).

94 Zhang, Z. *et al.* Lactonization and Protonation of Gluconic Acid: A Thermodynamic and Kinetic Study by Potentiometry, NMR and ESI-MS. *Journal of Solution Chemistry* **36**, 1187-1200, doi:10.1007/s10953-007-9182-x (2007).

95 Vuorinen, T. Cleavage of the intermediate hydroperoxides in the oxidation of d-glucose and d-fructose with oxygen. *Carbohydrate Research* **141**, 319-322, doi:https://doi.org/10.1016/S0008-6215(00)90463-4 (1985).

96 Cannella, D., Hsieh, C. W., Felby, C. & Jorgensen, H. Production and effect of aldonic acids during enzymatic hydrolysis of lignocellulose at high dry matter content. *Biotechnol Biofuels* **5**, 1754-6834 (2012).

© 2020 Tous droits réservés.
lilliad.univ-lille.fr

97 Daniel, J., Fetter, L., Jett, S., Rowland, T. J. & Bonham, A. J. Electrochemical Aptamer Scaffold Biosensors for Detection of Botulism and Ricin Proteins. *Methods Mol Biol*, 6958-6956_6952 (2017).
98 Chai, C., Lee, J. & Takhistov, P. Direct detection of the biological toxin in acidic environment by electrochemical impedimetric immunosensor. *Sensors* **10**, 11414-11427 (2010).
99 Ribeiro, W. F. *et al.* Electrochemical study of ricin at glassy carbon electrode. *Analyst* **138**, 4565-4573, doi:10.1039/c3an00227f (2013).

© 2020 Tous droits réservés.
lilliad.univ-lille.fr

Thèse de Ioana Silvia Hosu, Université de Lille, 2020

General Conclusions and Perspectives

© 2020 Tous droits réservés.
lilliad.univ-lille.fr

Thèse de Ioana Silvia Hosu, Université de Lille, 2020

General Conclusions and Perspectives

General Conclusions and Perspectives 235
Publications and scientific presentation of the results 240
References 242

© 2020 Tous droits réservés.
lilliad.univ-lille.fr

Thèse de Ioana Silvia Hosu, Université de Lille, 2020

General Conclusions and Perspectives

This thesis focused on the development of surface assisted laser desorption/ionization mass spectrometry (SALDI-MS) surface for direct detection of ricin B chain (32 kDa). As ricin B chain is the lectin moiety of the entire ricin protein (64 kDa), we also presented proofs-of concept of how the developed methods can be transferred to the entire molecule.
In the **General introduction** section we did asked ourselves different questions. In this General Conclusions and perspectives part, we will describe the results we obtained in order to answer the questions.

In **Chapter I**, we have described the following milestones: what is ricin and its importance, we have presented the classical methods of detection for ricin and the MALDI/SALDI-MS analytical methods and why those two techniques are important for the detection of ricin. Ricin, a lethal bioterrorist agent, was recently used as biological warfare. It is composed of two protein chains: ricin B chain (the lectin part, that binds to galactose moieties on the surface of the cells) and ricin A chain (the toxic part, a glycosidase, having a depurination action over the RNAr 28S from the 60S ribosomal subunits, followed by the inhibition of protein synthesis). The toxicity mechanism can be also used as affinity strategy for development of specific sensors.

Even though classical methods (such as ELISA and other immunoassays methods, colorimetric, SPR) are quite sensitive, they are time and reagent consuming and cannot distinguish between biologically active or inactive ricin. MS was used in several literature studies to detect ricin, as it can follow the depurination enzymatic capacity of ricin. The biggest disadvantage of the classical MS methods (ESI-MS, LC-MS, MALDI-MS) is that it needs complex and tedious sample preparation, as it requires digestion of the proteins.

In **Chapter I,** we have also described the variety of SALDI-MS materials used in literature until now. They can be divided in three main categories: semiconductor based (desorption ionization on silicon, main drawback is the upper limit range), metal based and carbon based materials.

In **Chapter II** we described that CNWs can be used for the detection of small molecules, by SALDI-MS. Indeed, thanks to SEM, reflectivity, photoluminescence, Raman, water contact angle, XPS characterizations CNWs have shown very good light absorption properties, high conductivity, high surface area, good mechanical resistance and hydrophobicity. These properties are important when developing SALDI-MS interfaces. To emphasize this, the detection and quantification of glucose in buffer and real samples, were

© 2020 Tous droits réservés.
lilliad.univ-lille.fr

Thèse de Ioana Silvia Hosu, Université de Lille, 2020

achieved by SALDI-MS. This part of this work was published in Nanoscale, in 20171 and the article is joined to this thesis in the Appendix.

We have demonstrated a dynamic range for glucose detection for concentration ranging from 5 to 400 pmol with a sensitivity of 36.58±0.58 pmol/0.5 μL. A calculated LOD of 0.32±0.02 pmol was achieved. Glucose was also quantified in real samples: 5.61 mM were detected in blood serum (in accordance with the normal glucose values) and 3.94 g/100mL in a soft drink. A conventional colorimetric carbohydrate detection method was used for comparison and low percentage errors (19%) were calculated between the colorimetric method and the proposed SALDI-MS method, for blood serum. The SALDI-MS method was also used to determine the total sugar content in Coca-Cola present on the label and compared with the one determined with the colorimetric method (difference was lower than 3%). The high salt tolerance of the CNWs surface allowed the detection of melamine in urine, with an actual limit detection of 63±8.19 ng/μL. A paracetamol's metabolite (3-nitro-paracetamol) was also detected in the collected urine, as a consequence of oral uptake of 2 g, three days in a row. Other small molecules were also detected.

As CNWs acted as great platform for SALDI-MS of glucose and other types of biomolecules and encouraged by these results, we moved to the main goal of my subject: the detection of proteins by SALDI-MS.

In **Chapter III**, we have presented the optimization of the physical properties of the surface and of the experimental conditions for the detection of a model protein (cytochrome C). The physico-chemical properties that we studied are: boron doping level, height of the nanowalls, surface morphology, optical properties (reflectivity, photoluminescence) and vibrational modes of graphene-like material. We compared these results with literature and with other physico-chemical properties of materials already used for detection of cytochrome C, in SALDI-MS. As vertically grown graphene sheets create a maze-like structure, as the boron doping levels increase, small pores are also created until a certain doping level (5.0 K). Roughness increases with the length of nanowalls, as doping levels is twining the graphene sheets. The sp2 graphene-like structure is present at the surfaces of nanowalls, thus they absorb UV light. Photoluminescence is low and absorbance is high, together with the low thermal conductivity, low melting point and low heat capacitance, the energy is confined in a small area, enhancing desorption and the ionization of the proteins. Hydrophobicity of the surfaces confines also the analyte deposition in small spots (cca. 1.5 mm2). Boron doping level also increase electrical conductivity and proton donors are extrinsically available from the ammonium citrate dibasic (150 mM) and as well from oxidized carbon species such as

© 2020 Tous droits réservés.
lilliad.univ-lille.fr

Thèse de Ioana Silvia Hosu, Université de Lille, 2020

hydroxyl, carbonyl, carboxyl at the surface of the nanowalls. Incubation of the analyte (around 5 minutes) with the surfaces seemed to be the crucial point between being able to detect cytochrome C or not.

SALDI-MS intensities of cytochrome C were measured for all the doping levels and all the growing periods and compared with internal energies. The conclusion was that a doping level of 5.0 K, having a height of 2.6 μm offers the best intensity in SALDI-MS, for the detection of cytochrome C, with a deposited internal energy of 2.1 eV, using as proton donor ammonium citrate dibasic (150 mM) and 5 minutes of incubation. Using the 5.0 K CNWs we have determined that the LOD for cytochrome C is 250 fmol/0.5 μL (RSD=10%. S/N=3). The linear range for the calibration curve is 0.25-7.00 pmol/0.5 μL, with R2=98.761 and according to our knowledge, this is the first procedure, ever described in the literature, to use a SALDI-MS method for the quantification of a protein.

Before applying the above optimized method to real samples, we did measure some semiquantitative parameters for ricin. The lowest concentration detected (LOD) on the surface of unmodified CNWs, was 5 μM/0.5 μL, corresponding to 2.5 pmol/0.5 μL (80 ng/0.5 μL). This limit of detection is sufficient to detect the lowest amounts of ricin that are able to bring death to the persons that interact with the toxin, even if the sample are to be diluted 10 or 20 times (samples like soft drinks or blood serum), because this would mean an initial ricin concentration of 1.6 μg. Injection of ricin has the highest lethal statistical percentage even if the LD50 = 10 μg/kg is comparable to LD50 = 5-10 μg/kg for inhalation and the least dangerous is the oral ingestion, with LD50 = 1-20 mg/kg. We can observe that our limit of detection is more than 3 timeslower than the lowest median lethal dose. The MS signal saturation can be observed after the concentration of 15 μM (7.5 pmol/ 0.5 μL) of ricin B chain.

After we have chemically modified the CWNs using an affinity strategy (introduction of galactose residues on CNWs), when we did spike ricin in Coca-Cola (diluted 10 times with ammonium citrate), 55% of the SALDI-MS signal was recovered. In the case of blood serum (diluted 10 times with ammonium citrate), 50% of the signal was recovered, in comparison with the control (only buffered ricin B chain solution). This method is perfect for a rapid screening of contaminated samples.

Finally, in **Chapter IV,** we have presented preliminary results and perspectives for the combination of complementary techniques as more powerful analytical tools. SPR (surface Plasmon resonance), SERS (surface enhanced Raman spectroscopy) and EC (electrochemistry) that can be combined with MS, using SALDI-MS graphene-based

© 2020 Tous droits réservés.
lilliad.univ-lille.fr

Thèse de Ioana Silvia Hosu, Université de Lille, 2020

surfaces. For each bimodal technique the most important parameters are described and characterizations and different studies are performed to obtain optimized surfaces to suit the combination purpose.

Our final goal, for this chapter was to show how these techniques could be used for the detection of ricin B chain, and in general for ricin-like toxins but not only. Our approaches are quite originals, detailed and the preliminary results are promising.

For LSPR-MS, we used three different deposition methods: self-assembled monolayer (SAM) of citrated gold nanoparticles (20 nm), deweting of thin films of gold (4, 6 and 8 nm) and e-beam writing for creating gold patterns. The best method (in terms of stability, LSPR signal and combination of LSPR-MS) was the SAM method, as we exchanged the ligand, played with incubation periods and obtained higher LSPR signals. The LSPR-MS combination proof of-concept was achieved using a cystein containing peptide.

Special and detailed attention was accorded to the combination of SPR-MS, as this is a more powerful technique as it can study real-time monitoring of molecular interaction and affinity purification, binding kinetics and capacities (SPR) and quantification, identification and, especially in the case of ricin, study of the enzymatic activity (MS). Graphene like materials are known to enhance SPR and MS signals, so different deposition techniques were also studied, to ensure a good surface coverage of the substrate: 1) bubble surfactant method of graphene oxide, 2) wet transfer of CVD pristine graphene, 3) electrophoretic deposition of graphene, 4) layer by layer using a polycation and graphene oxide, 5) drop casting of both graphene and reduced graphene. Each method was described and characterized, and both SPR (scanning angle mode) and MS signals (using mixtures of peptides and/or proteins) were evaluated. Cytochrome C (as model protein) was detected using the first three methods and only peptides were detected for the last two methods, as the mentioning order is in correlation with decreasing SALDI-MS efficiency towards proteins.

In the SERS/MS part we did actually used ricin B chain, and the results are interesting as we were able to select specific Raman bands at which ricin B chain vibrates. This being a plasmonic-free SERS platform, it can be used for molecular interaction, orientation and functionalization of ricin, as “hot plasmonic spots” can disturb molecular interactions. It could be also used to determine the depurination of RNA/or synthetic DNA that mimics RNAs. This means it could be used as an analytical method able to distinguish between biologically active ricin and inactive one.

For the EC-MS we have shown that CNWs can be used for the detection of glucose, using both EC and MS. We demonstrated the mutual assistance on this combination of techniques:

© 2020 Tous droits réservés.
lilliad.univ-lille.fr

Thèse de Ioana Silvia Hosu, Université de Lille, 2020

quantitative measurements with both techniques, studying the electrochemical reaction of glucose (EC) and elucidating the mechanism and he electrochemical oxidation by-products using (MS). Common MS peaks determined after and before performing electrochemistry on the same surface, determined that gluconic acid is a by-product of the electrochemical oxidation of glucose.

If we would need to compare these 3 methods for the detection of ricin, SPR-MS would be the best combination as it offers more complimentary advantages (kinetics, binding capacities, it can be used to develop the sensor itself, and quantification (SPR), whereas MS is high resolved and highly sensitive, can offer quantification, identification and distinction between active or inactive ricin). But it is more time consuming as SPR need equilibration and longer time for measurements preparation. SERS compensates with rapidity of measurements, determination of nature of functionalization, but requires more time for data manipulation. EC compensates with studying electrochemical reactions and quantification and SALDI-MS gives complementary information about the by-products of the redox reaction. We did not study the electrochemical detection of ricin, but as literature showed, this is possible. The proof-of concept was described for all three cases, so we concluded at the end of **Chapter IV**, that all three methods deserve further developments.

We can finally state that boron doped carbon nanowalls were characterized, optimized and applied for detection in complex samples of small molecules and proteins (cytochrome C and ricin B chain), using SALDI-MS. Quantification was also achieved for small proteins and cytochrome C and semi-quantitative was achieved for ricin B chain spiked complex samples. As we were also able to observe the dimeric form of ricin B chain (at 64 kDa) and as the affinity strategy successfully captured ricin B chain from these samples, we can conclude that detection of intact ricin molecules is highly likely to be detected in the same manner. Our method is rapid (less than 10 minutes), sensitive, selective, high throughput, low cost and low reagent consuming. The same CNWS based SALDI-MS method was also proven to be suitable for combination with SERS and EC. Deposition of different graphene-based materials on a gold surface, is the alternative of this CNWs method and this is suitable for combination with SPR, as we demonstrated in this these.

© 2020 Tous droits réservés.
lilliad.univ-lille.fr

Thèse de Ioana Silvia Hosu, Université de Lille, 2020

Publications and scientific presentation of the results

We have published the results for detection of small molecules using CNWs in Nanoscale (IF=6.9, 2017, Annex 1)[1] and I have contributed to the development of other SALDI-MS methods (molybdenum disulfide/titanium oxide/silicon nanowires for detection of glucose and glutathione and buried oxide layer nanostructured Silicon-On-Insulator for detection of peptides and antibiotics). These results were also published in Talanta (second author, IF= 3.54, 2017, Annex 2)[2] and Analyst (second author, IF=3.6, 2019, Annex 3).[3] I have also contributed to another work published in Talanta (third author, 2017)[4] for the detection of dopamine, in meat samples, using polyethylenimine/reduced graphene oxide deposited by EPD.

Other 3 manuscripts are in preparation:

1. The detection of ricin in complex samples using chemically modified boron doped nanowalls
2. Different methods of deposition of graphene-like materials for creating dual surfaces compatible with SPR-MS.
3. Using carbon nanowalls for dual detection of ricin in SERS/MS and EC/MS.

I have participated in 6 conferences, during my PhD:

1. I.S. Hosu*, M. Sobaszek, M. Ficek, R. Bogdanowicz, R. Boukherroub, Y. Coffinier, *Carbon nanowalls interfaces for the detection of glucose by mass spectrometry andelectrochemistry*, Poster at ElecNano7 "Nanomaterials for sensing and energy driven applications", Mai 23-25, **2016**, Polytech'Lille, Lille, France.

2. I.S. Hosu*, M. Sobaszek, M. Ficek, R. Bogdanowicz, H. Drobecq, O. Melnyk, Y.Coffinier, R. Boukherroub, *Glucose sensing using electrochemistry and mass spectrometry on carbon nanowall interfaces*, Poster at Premières Journées du GDR Bioingénierie des interfaces, 29-30 June, **2016**, Ecole Centrale de Lyon, France.

3. I. S. Hosu*, M. Sobaszek, M. Ficek, R. Bogdanowicz, H. Drobecq, Luc Boussekey, O.Melnyk, A. Barras, R. Boukherroub, Y. Coffinier*, Carbon nanowalls, new versatile graphene based interface for laser desorption/ionization of small compounds in mass spectrometry*, Poster accepted at Spring EMRS, Mai 22-26**, 2017**, Strasbourg, France, Abstract ID : 2T4.

4. A. Hamdi*, **I. S. Hosu**, H. Ezzaouia, R. Boukherroub and Y. Coffinier, *Hydrothermal preparation of MoS2/TiO2/Silicon nanowires as an effective substrate*

© 2020 Tous droits réservés.
lilliad.univ-lille.fr

Thèse de Ioana Silvia Hosu, Université de Lille, 2020

for LDI-MS detection of biomarkers in serum, Oral presentation accepted at Spring EMRS, Mai 22- 26**, 2017**, Strasbourg, France

5. I.S. Hosu, R. Bogdanowicz and Y. Coffinier*. *Graphene based nanostructures for matrix-free laser desorption/ionization mass spectrometry detection of ricin from complex media*. Poster at Colloque LN2, July 8-11, **2018**, Autrans, France.

6. I.S. Hosu, Y. Coffinier*, invited paper. *Nanomaterials for mass spectrometry*, Oral presentation at NanoSmat, Septembre 11-14, **2018**, Gdansk, Pologne.

© 2020 Tous droits réservés.

lilliad.univ-lille.fr

References

1. Hosu I.S., Sobaszek M, Ficek M, Bogdanowicz R, Drobecq H, Boussekey L, et al. Carbon nanowalls: a new versatile graphene based interface for the laserdesorption/ionization-mass spectrometry detection of small compounds in real samples. Nanoscale. 2017;9(27):9701-15. (Annex 1).

2. Hamdi A, **Hosu I.S.**, Addad A, Hartkoorn R, Drobecq H, Melnyk O, et al. MoS2/TiO2/SiNW surface as an effective substrate for LDI-MS detection of glucose and glutathione in real samples. Talanta. 2017;171:101-7. (Annex 2).

3. Hamdi, A., **Hosu, I. S.** & Coffinier, Y. Influence of buried oxide layers of nanostructured SOI surfaces on matrix-free LDI-MS performances. Analyst 145, 1328-1336, doi:10.1039/c9an02181g (2020). (Annex 3).

4. Kahlouche K, Jijie R, **Hosu I**, Barras A, Gharbi T, Yahiaoui R, et al. Controlled modification of electrochemical microsystems with polyethylenimine/reduced graphene oxide using electrophoretic deposition: Sensing of dopamine levels in meat samples. Talanta. 2018;178(Supplement C):432-40. (Annex 4).

© 2020 Tous droits réservés.
lilliad.univ-lille.fr

Thèse de Ioana Silvia Hosu, Université de Lille, 2020

Appendix – Experimental part – Procedures

© 2020 Tous droits réservés.
lilliad.univ-lille.fr

Thèse de Ioana Silvia Hosu, Université de Lille, 2020

Appendix-Experimental part-Procedures

V.1. Materials....246
V.2. Synthesis of organic compounds....247
V.3. Preparation of surface based materials....247
V.3.1 Synthesis and modification of carbon boron doped nanowalls....247
V.3.2 Growth of carbon boron-doped nanowalls (CNWs)....247
V.3.3 Ionic implantation of boron atoms on undoped CNWs....248
V.3.4 Functionalization of CNWs with OTS and surface patterning....248
V.3.5 Modification of the carbon nanowalls with 1-Pyrenecarboxylic acid (pyrene-COOH CNWs)....249
V.3.6 Functionalization of the carbon nanowalls with D-(+)-Galactosamine hydrochloride (NH_2GAL CNWs)....249
V.3.7 Functionalization of the carbon nanowalls with ovalbumin (OVA CNWs)....250
V.3.8 Ligand exchange (AuNPs with citrate ligand into thiol ligand)....250
V.4. Graphene and graphene-like deposition methods....250
V.4.9 Electrophoretic deposition....250
V.4.10 Preparation of drop casted graphene based sensors....250
V.4.11 Preparation of layer by layer graphene based sensors....251
V.4.12 Modification with CVD graphene through a wet-transfer procedure....251
V.4.13 Preparation of thin bubble graphene sensors....252
V.5. Deposition of SiOx films by Plasma-enhanced chemical vapor deposition (PECVD) 252
V.6. Glucose determination in serum....252
V.7. Preparing the solutions of analyte....253
V.7.14 Preparing the stock solution of ricin B chain....253
V.7.15 Preparing the blood serum samples....253
V.7.16 Preparation of peptides mixture from calibration kit for analysis of peptides. 253
V.8. Preparing real samples for SALDI-MS analysis....254
V.9. How to calculate/approximate the thickness of the film of glucose on the surface carbon nanowalls:....255

© 2020 Tous droits réservés.
lilliad.univ-lille.fr

V.10. UV-VIS parameters for LSPR measurements 255
V.11. Sample deposition and mass spectrometry measurements 255
V.12. Instrumentation 256
V.13. References 259

© 2020 Tous droits réservés.
lilliad.univ-lille.fr

Thèse de Ioana Silvia Hosu, Université de Lille, 2020

V.1. Materials

Sodium chloride (NaCl), Dopamine, α-D-glucose, D– (+) xylose, D– (-) fructose, D– (+) mannose, D– (+) galactose, D-(+)-Galactosamine hydrochloride (NH_2GAL), D-(+)-Glucosamine hydrochloride (NH_2GLC), 1-Pyrenecarboxylic acid (pyreneCOOH), dextran from Leuconostoc mesenteroides (MW=9000-11000), sucrose, trifluoroacetic acid (TFA), ammonium citrate dibasic, ammonium phosphate monobasic, insulin solution from bovine pancreas, deuterated chloroform (CDCl3), deuterated dimethyl sulfoxide (DMSO-d6), dimethyl sulfoxide (DMSO), dimethylformamide (DMF), melamine, paracetamol, octadecyltrichlorosilane (OTS), acetonitrile, sulfuric acid (H2SO4), phenol, dichloromethane (CH2Cl2), isopropyl alcohol, ethanol (EtOH), hydrogen peroxide 30% (w/w), pyridine anhydrous (99.8%), benzyl chloride (99%), 4-chlorobenzyl chloride (95%), 4-fluorobenzyl chloride (99%) , 4-nitrobenzyl chloride (99%), 4-cyanobenzyl chloride (97%), D-glucose-2-13C, sinapic acid, EDC (), using Sephadex G-25 in PD-10 Desalting Columns, were purchased from Sigma-Aldrich and used as received. Calibration mixtures were purchased from SCIEX (Sequazyme™ Peptide Mass Standards Kit) and the components peptides/proteins are displayed in **Table V.7-1**. Fetal bovine serum (FBS) was purchased from Thermo Fischer Scientific (South America). Photoresist AZ4562 and developer were purchased from Microchemicals GmbH. Ultrapure water (Milli-Q, 18 MΩ/cm) was used for the preparation of the solutions and for all rinsing steps.

Lecithin (from soya) was purchased from Soyatica® Vitall+ (France) and a stock solution was prepared in EtOH (50 mM). Human urine was collected freshly and used as collected or after 2 centrifugations (13500 rpm) and 2 filtrations (Thermo Fischer Scientific, 0.2 µm/25 mm nylon membrane). The un-spiked urine was supposed to contain paracetamol, due to the fact that the subject consumed previously high amounts (2 g/day during 3 days). Coca Cola was purchased from a local store and it was used decarbonized by π orbital stirring (150 rpm) during 1 h.

Ricin B chain is the lectin assuring transportation in the ricin structure. Ricin B chain solution (1 mg/ml in 10 mM sodium phosphate, 0.15 M NaCl, pH 7.5 0.08% sodium azide, 50 mM 2-mercaptoethanol) was purchased from Vector Laboratories. The producer recommends that acidic conditions and strong oxidizers (that may react with lead and copper plumbing to form highly explosive metal azides) should be avoided and that the solution shouldn't be lyophilized.

© 2020 Tous droits réservés.
lilliad.univ-lille.fr

Thèse de Ioana Silvia Hosu, Université de Lille, 2020

V.2. Synthesis of organic compounds

Benzylpyridinium compounds were synthesized from the condensation of the corresponding parasubstituted benzyl chloride (BzPy), with pyridine, using an excess of pyridine:benzylchloride (20:1 moles). The mixture was refluxed for 5 h at 60°C. After the reaction was completed, the mixture was cooled down at room temperature and benzylpyridinium was precipitated with diethyl ether. The excess of pyridine was removed under vacuum, at 80°C, and then dried at 60°C. No further purification was performed. All the benzylpyridinium compounds were named as follows, according to the element in the para position of the benzyl ring: BzPy (no substitute), CNBzPy (ciano group), ClBzPy (chloride group), FBzPy, (fluoride group) and NO_2BzPy (nitro group).[1] As FBzPy, ClBzPy were hygroscopic, the powder was kept in the glove box, under nitrogen flow.

Solutions of benzylpyridnium compounds were prepared in water (1 mM), as follows: FBzpy (1.88 mg/10 ml), ClBzPy (20.04 mg/ml), NO_2BzPy (21.5 mg/ 10ml) and CNBzPy (19.5 mg/ml). These solutions were used to determine deposited internal energies. NMR (example in **Figure V.2-1**) and MS were used as characterization methods after synthesis.

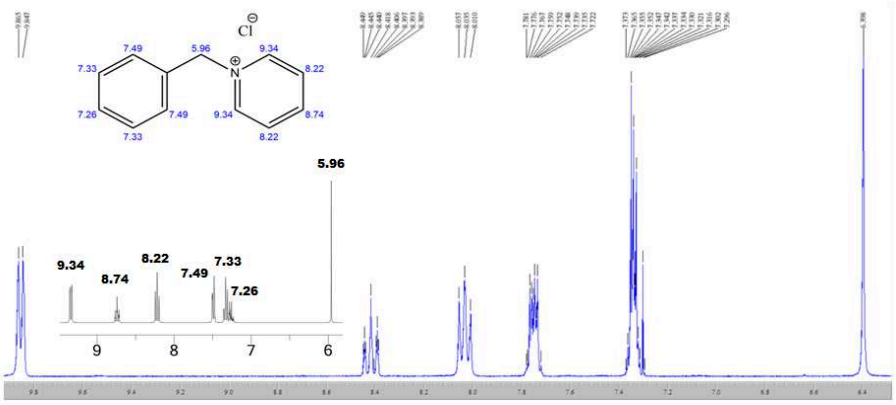

Figure V.2-1 ^{1}H NMR spectrum of the benzylpyridinium chloride, in chloroform-d (Inset is the ChemDraw prediction of the spectrum of the analyzed compound).

V.3. Preparation of surface based materials.

V.3.1 Synthesis and modification of carbon boron doped nanowalls

V.3.2 Growth of carbon boron-doped nanowalls (CNWs)

CNWs were synthesized in an MW PA CVD system (Seki Technotron AX5400S, Japan) on *p*-type Si wafers with (100) orientation. Substrates were cleaned by sonication in acetone and 2-propanol for 5 min in each solvent. Next, the substrates were seeded in nanodiamond suspension (crystallite size of 5–10 nm) for 60 min under sonication. Finally, the substrates were dried under a stream of nitrogen. Previously, we have shown that seeding procedure

© 2020 Tous droits réservés.

lilliad.univ-lille.fr

yields high seeding densities in the range up to 10^{10} cm^{-2}.[2,3] The substrate temperature was kept at 700°C during the deposition process. Excited plasma was ignited by microwave radiation (2.45 GHz). The microwave power was kept at 1300 W to achieve highly ionized plasma. The base pressure was about 10^{-6} Torr, while the process pressure was kept at 50 Torr. The source gas mixture of $H_2/CH_4/N_2$ at gas volume 300 sccm of total flow rate was applied. Moreover, the doping level of boron in the gas phase, expressed as [B]/[C] ratio, was kept at 1200 ppm using diborane (B_2H_6) as dopant precursor. The growth time was 6 h, producing surfaces with randomly vertically aligned nanowalls with the height of approx. 4 µm.

V.3.3 Ionic implantation of boron atoms on undoped CNWs

In this process, the boron ions were accelerated with energies up to 200 keV, for different doses: 10^{15}, 10^{18} and 10^{21} expected boron atoms/cm^2. After the targets (the undoped CNWs sufaces) were implanted at the interstitial surface, the annealing process (300°C, during several minutes) helped with the recovery of the crystalline structure, by the bonding of the dopant with carbon atoms. The process was performed with an Eaton-AxcelisGA 3204 ionic implanter, which is a medium current, very high dose and low/medium energies implanter.

V.3.4 Functionalization of CNWs with OTS and surface patterning

In order to study the influence of the surface chemistry and to compare the MS performance for the as-synthesized CNWs with the oxidized CNWs (oxCNWs), several procedures were followed: for cleaning the surface of any remaining analyte, the sample was immersed in a piranha solution (H_2O_2:H_2SO_4=1:3) during 15 min. This process was repeated 2 times. The surface was activated 20 min under UV/ozone to create hydroxyl groups on the surface and after this treatment, the WCA was 13°. After rinsing abundantly with water and drying with a nitrogen flow, the surface was coated with OTS, using the following procedure: the CNWs surfaces were immersed into a 10^{-3} M solution of OTS in hexane for 6 h at room temperature, in a dried nitrogen-purged glovebox and the resulting surfaces were rinsed with CH_2Cl_2, isopropyl alcohol, and dried under a gentle stream of nitrogen. The WCA after OTS-modification[4] was ~127°. To create patterns that will concentrate the analyte in a specific hydrophilic surface area, we used UV lithography to locally remove the OTS. The first steps consist of spin-coating of the photoresist A4562 (using a speed of 3000 RPM, acceleration 2000, during 40s) and soft baking during 2.5 min at 110°C. For the UV exposure, an optical mask bearing patterns consisting of circles of 800 µm in

© 2020 Tous droits réservés.
lilliad.univ-lille.fr

Thèse de Ioana Silvia Hosu, Université de Lille, 2020

diameter with an interspacing of 1800 µm was used. The exposure was done for 60s and the gap distance was 100 µm. After the exposure, the surface was annealed 60s at 110°C and then dipped in A351 developer during 15s, and rinsed with water and dried under nitrogen flow. The patterns can be observed after this step. Oxygen plasma treatment was performed during 30s using RIE (reactive ion etching), with the following parameters: RF power 200W, pressure 100 mT and 30 sccm flow. This step is mandatory to remove the remaining resist inside the apertures and destroy the OTS layer. Then, the non-irradiated resist was removed by dipping the surface in acetone at 30°C during 20 min, rinsing with isopropanol and drying under nitrogen flow.

Safety Considerations - The mixture H_2SO_4/H_2O_2 (piranha) solution is a strong oxidant. It reacts violently with organic materials. It can cause severe skin burns. It must be handled with extreme care in a well-ventilated fume hood while wearing appropriate chemical safety protection.

V.3.5 Modification of the carbon nanowalls with 1-Pyrenecarboxylic acid (pyrene-COOH CNWs)

1-Pyrenecarboxylic acid solution was prepared in DMF (2.4 mg in 2 ml, 5 mM). The CNWs surfaces were dipped in the solution, during 1 hour, at room temperature and covered, to prevent evaporation. 1 cm^2 was covered with 400 µL solution. Rinsing was done by pipetting DMF on the surfaces, 2 times. The surfaces were dry gently with a N_2 flow.

Protocol 2: In order to be able to create amide bond with the carboxylic groups, activation of these groups was necessary. N,N′-Dicyclohexylcarbodiimide (DCC, 20 mM, 20.6 mg) and N-Hydroxysuccinimide (NHS, 20 mM, 11.5 mg) solutions were prepared in 5 ml DMF. The surfaces were dipped in solution during 40 min at room temperature. Rinsing was done with DMF using the π-stirring platform, using 100 RPM, during 5 min. Rinsing was repeated 2 times.

Initially (Protocol 1), the water based procedure included EDC (N-(3-Dimethylaminopropyl)-N'-ethylcarbodiimide hydrochloride, 16 mM, 15 mg) and N-Hydroxysuccinimide (NHS, 26 mM, 15 mg), dissolved in 5 ml of water/PBS 100 mM, for 40 minu, at room temperature. XPS results did not show any increase in nitrogen, and we do suppose that the modification was not complete.

V.3.6 Functionalization of the carbon nanowalls with D-(+)-Galactosamine hydrochloride (NH_2GAL CNWs)

Protocol 2: D-(+)-Galactosamine hydrochloride solution (10 mM, 10.78 mg in 5 ml) was prepared in DMSO, under styring during 1 hour. The pyrene-COOH CNWs surfaces were

© 2020 Tous droits réservés.
lilliad.univ-lille.fr

Thèse de Ioana Silvia Hosu, Université de Lille, 2020

dipped in solution overnight (16 H), without being dried from the previous step. Rinsing was done with DMF (2 times) and after with ethanol (2 times), using the π-stirring platform, using 100 RPM, during 5 min. Drying was done gently in a flow of N_2. In Protocol 1, initially, we dissolved galactosamine in water or in ammonium citrate dibasic, even though usually PBS pH 7.4 is used. As salts tend to inhibit the LDI-process, we avoided using PBS.

V.3.7 Functionalization of the carbon nanowalls with ovalbumin (OVA CNWs)

Ovalbumin solutions (1000 and 6 μM) were prepared in water. Solutions of 1 μL were dropped on the surface of carbon nanowalls and dried at room temperature. Ricin B chain solutions in ammonium citrate (150 mM) were incubated with the drops and dried solutions during 5 minutes.

V.3.8 Ligand exchange (AuNPs with citrate ligand into thiol ligand)

1-Dodecanethiol (Mw=202.4 g/mol, 98%) was diluted to 1mM (using ethanol, 20 ml). The glass/AuNPs surfaces were dipped in solution during 30 minutes or 20 hours.

V.4. Graphene and graphene-like deposition methods.

V.4.9 Electrophoretic deposition

First, the glass slides were cleaned following several steps: 10 minutes of π stirring (at 100 RPM) in acetone, IPA (isopropyl alcohol) and water, strong oxidation in piranha solution (H_2O_2:H_2SO_4=1:3) during 15 min, followed by a sonication during 10 minutes in water. The glass surfaces were cleaned in N_2 flow. A graphene oxide solution (1 mg/ml) was prepared using by sonication during 24 hours.

Electrophoretic deposition (EPD) of rGO onto Au thin film electrodes were carried out using a two-electrode cell containing GO aqueous dispersion (0.1, 0.5 and 1 mg/mL) by applying a DC voltage (15 V, 60 V or 150 V) for 2 min, or other specified period of times. In the case of EPD of rGO, platinum (Pt) foil (1 × 2 cm^2) acts as the cathode and the gold electrode as the anode. The two electrodes are separated by 1 cm and are placed parallel to each other in the GO. The surfaces were dipped several times Milli-Q water to get rid of the physical absorbed graphene oxide/reduced graphene oxide and let to dry in air, in horizontal position.

V.4.10 Preparation of drop casted graphene based sensors

Solutions of GO (4 mg/ml in water) and rGO (1 mg/ml in DMF) were prepared by dispersing GO or rGO with the help of ultrasounds (power 100% and frecquency 37 Hz) and vortex shaking during 24 h. The solutions were diluted to the desired concentrations (0.1, 0.5

© 2020 Tous droits réservés.
lilliad.univ-lille.fr

Thèse de Ioana Silvia Hosu, Université de Lille, 2020

and 1mg/ml) and drop casted onto a cca. 1cm^2 surface (using 20 µL). The surfaces were dried in air.

V.4.11 Preparation of layer by layer graphene based sensors

Au coated glass substrates were prepared by thermal evaporation of 5 nm of titanium and 50 nm of gold onto cleaned glass slides. The titanium is used as an adhesion layer between the glass surface and the gold layer.

Cleaning glass slides with ultra-sonication (power 100, frequency 37 Hz) using acetone, isopropanol and water (5 minutes) and piranha solution (10 minutes in 1:3 for H_2O_2:H_2SO_4). For rinsing, 5 minutes, ultra-sonication in water and rinsing after with the water flow and dry with nitrogen flow. Glass slides are metallized using E-beam evaporation of Ti 5 nm and Au 50 nm as described often in the literature, for SPR purposes (glass cover slides with 1 mm and 0.24 mm thickness). Before modification with Poly(diallyldimethylammonium chloride) solution (PDDA) and GO or rGO , the surface were again cleaned in acetone, isopropanol and water, using the π stirring plate, during 5 minutes each and drying with air flow.

The surfaces were immersed alternatively (during 15 minutes) in a 5% PDDA aqueous solution and GO solutions (0.1 mg/ml). Between this steps the surfaces were dipped in water several times and dried under a nitrogen flow. For the rGO the same procedure was followed, but the solutions were prepared in DMF and the rinsing was done with DMF also. Particular treatment was performed for the dissolution of PDDA in DMF. DMF was added over the PDDA aq. Solution and the mixture was ultrasonicated 2 hours; followed by 12 hours of continuous stirring (at 800 RPM). The rGO dispersion in DMF was obtained after 24 hours sonication.

V.4.12 Modification with CVD graphene through a wet-transfer procedure

The CVD graphene grown on copper was transfered by a wet method onto the Au slide.[5] Briefly, PMMA 5% (950K) is spin coated on the Cu/CVD interface and for better adhesion the surface is annealead at 110°C, during 30, with a temperature step rumping up and down of 3.6 °C/min. The backside graphene is removed using oxygen plasma during 1 min. The copper is etched during 60 h, in a 0.8 % solution of HCl and H_2O_2 in water. The floating graphene/PMMA surface is transfered several times in water, in order to rinse the Cu particles and finally transfered onto the host interface (glass/Au). After drying most of the water trapped under the graphene/PMMA layer, the glass/Au/graphene/PMMA surface is annealed at annealead at 110°C, during 30, with a temperature step rumping up and down of 3.6°C/min. In order to remove PMMA, the surface is exposed to UV (337 nm) during 30 min.

© 2020 Tous droits réservés.
lilliad.univ-lille.fr

Thèse de Ioana Silvia Hosu, Université de Lille, 2020

The surface is diped in warm in acetone baths during 30 min and 10 min, and in isopropylic acid (IPA) during 10 min. The surface is gently rinsed with an IPA flow and dryed with a gentle nitrogen flow.

V.4.13 Preparation of thin bubble graphene sensors

Solutions of GO (4 mg/ml in water) and rGO (1 mg/ml in DMF) were prepared by dispersing GO or rGO with the help of ultrasounds (power 100% and frecquency 37 Hz) and vortex shaking during 24 h. The solutions were diluted to the desired concentrations (0.1, 0.5 and 1.0 mg/ml). Using as surfactant sodium sodium dodecylsulfonate, SDBS (0.5mg/ml) or sodium dodecyl sulfate, SDS (0.5mg/ml) and a solution of GO, the surface of clean gold was pushed through the thin layer of graphene oxide bubble, and the thin was transferred to the surface.[6] Annealing was performed during 5 min at 60°C during 3 times intercalated with rinsing 2 times, in water.

The same procedure was applied for rGO in DMF, due to the solubility of SDBS in DMF, but the bubble was not formed. Even though the concentration was increased at around 6 mg/ml, the situation was the same.

V.5. Deposition of SiOx films by Plasma-enhanced chemical vapor deposition (PECVD)

SiOx materials are used as high K dielectric materials, on top of gold/AuNPs. This is done using Plasma-enhanced chemical vapor deposition (PECVD) equipment, during 1 hour, at 300°C, at 1 Torr. Passivation process is first launched, using a procedure equivalent for 50 nm deposition of SiOx, at 300 °C. A refractive index of 1.48 is chosen. The speed deposition was 450 Å/min. The gas mixture is composed of 156 sccm of SiH_4 and 700 sccm of N_2O, the power is 10W. After the passivation step is finished, and actual deposition step is launched, using the same parameters, with glass/Au slides inside the chamber.

V.6. Glucose determination in serum

For the UV-Vis detection of glucose, 50 µL of serum was diluted in 250 µL of water, and 250 µL of 5% phenol solution was added over. After vortexing the solution, 1.25 mL of sulfuric acid was added rapidly over the mixture, in order to dehydrate glucose and form furan derivatives, that will condensate with the phenol, and form colored compounds.[7] After 10 min at room temperature and 10 min of shaking at 200 RPM, the UV-vis spectra were recorded. The same procedure was followed for the calibration, using glucose dissolved in water. For the MS analysis, 5 µL of serum was dissolved in 25 µL and the solution was drop-casted as described above, without or with spikes of glucose.

© 2020 Tous droits réservés.
lilliad.univ-lille.fr

Thèse de Ioana Silvia Hosu, Université de Lille, 2020

V.7. Preparing the solutions of analyte

V.7.14 Preparing the stock solution of ricin B chain

Ricin B chain stock solutions (30 µM) were first desalted using Sephadex G-25 in PD-10 Desalting Columns, using the next procedure: centrifugation (1000G, during 2 min), remove the solution, cut the tip of the column, take out the filter, add 3 ml of water 3 times and let it drop by gravitation, add another 3 ml volume of water and use centrifugation during 3 min at 1000G, add 0.5 ml o salted ricin B chain solution in the middle of the packed gel beads and use centrifugation during 2 min, at 1000G. During centrifugation and water filtration, 50 ml plastic tubes were used. The desalted stock solutions were kept at 4 °C fridge, during 6 months. Usually, ammonium citrate dibasic was dissolved in the desalted solution, for the desired concentration, depending on the volume needed.

V.7.15 Preparing the blood serum samples

Blood was collected freshly and no coagulant or other chemical was added. After the incubation at room temperature for 30 min, in upright position, the blood was centrifuged during 15 min at 2000 RCF (relative centrifugal force) and the supernatant was pipetted in a new Eppendorf tube. Acetonitrile (ACN) was added over to precipitate the high abundant proteins (ACN:serum = 3:1, v/v), incubated 10 min at 4°C, and centrifuged again 10 min at 13500 RPM. The supernatant was collected again and the serum was analyzed with UV-Vis and MS or stored at -20°C.

For ricin B chain determination, the blood serum was also VivaSpin 500 (100 K) centrifugal concentration, to eliminate proteins and particles above 100 kDa. For this centrifugation at 13.500 RPM was applied during 30 min. Ricin B chain was spiked before or after the cut-off. Usually, the blood serum was diluted 10-20 times and incubated 1 H with the spiked ricin B chain and 30 min on the CNWs surface.

V.7.16 Preparation of peptides mixture from calibration kit for analysis of peptides.

The peptides mixtures came in lyophilized form and must be reconstituted with 100 µL of Standard Dilutent, that contains 30% acetonitrile in 0.01% TFA. IN the case where the peptides mixtures were not as calibrants, but as a method of performance for different SALDI-MS surfaces, dilutant was replaced with MQ water (100 µL). Usually, 1 µL of the stock peptride solution was dissolved in the appropriate buffer, usually ammonium citrate dibasic, 1 mM. The composition and the concentrations of the peptides are presented in **Table V.7-1**.

© 2020 Tous droits réservés.
lilliad.univ-lille.fr

Thèse de Ioana Silvia Hosu, Université de Lille, 2020

Table V.7-1 Composition of calibration mixtures, protonated masses expected in MS and final concentrations of the prepared solutions (MIX 1 reflector mode, MIX 2 linear mode)

Compound	Abbreviated name	Charge (n)	$(M+nH)^{n+}$ Average	Final concentration for MS analysis (fmol/0.5 µL)	Signal/noise (S/N)		
					CNWs This work	BDDNWs [8a]	SiNWs [9b]
Calibration Mixture 1 (MIX 1)							
des-Arg1-Bradykinin	DAB	+1	905.05	25	465	1078	641
Angiotensin I	AI	+1	1,297.51	32.5	77	431	532
Glu1-Fibrinopeptide B	FPB	+1	1,571.61	32.5	71	55	100
Neurotensin	NT	+1	1,673.96	12.5	10	59	40
Calibration Mixture 2 (MIX 2)							
Angiotensin I	AI	+1	1,297.51	500	160	-	11
ACTH (clip 1–17)	ACTH1	+1	2,094.46	500	66	-	6
ACTH (clip 18–39)	ACTH18	+1	2,466.72	350	72	-	11
ACTH (clip 7–38)	ACTH7	+1	3,660.19	750	493	-	4
Insulin (bovine)	INS	+1	5,734.59	875	18	-	2
		+2	2,867.80	-	-	-	-

V.8. Preparing real samples for SALDI-MS analysis

Coca Cola was purchased from a local store and was used after being decarbonized by π orbital stirring (150 rpm) for 1 h. Dilutions of Coca Cola were obtained by using the appropriate amount and type of proton donor. In the case of sugar detection, in 10 mM NaCl and in the case of ricin B chain, 150 mM of ammonium citrate. The lowest dilution that allowed a good detection was 10 times.

© 2020 Tous droits réservés.

lilliad.univ-lille.fr

V.9. How to calculate/approximate the thickness of the film of glucose on the surface carbon nanowalls:

As for the dynamic range, a constant decrease it is observed after concentrations higher than 1000 pmol. The term "dynamic range' refers actually to the linear range, which was determined to be 10-800 pmol, after further measurements. As the roughness of the CNWs was determined to be 50 nm, with the help of AFM, this may be one of the explanation: 1000 pmol of glucose, correspond to $6.022*10^{14}$ molecules (according to Avogadro's number). As a ring of glucose, has a size of approximatively 2.27 nm^2, the total area occupied by the total number of molecules is around $13.66994*10^{14}$ nm^2, thus 1366.994 mm^2.[10]

In conclusion, 1000 pmol will occupy 1366 mm^2, and the available surface area/specific surfaces are is approximately 3 mm^2, even if we take in consideration the roughness of the surface. To fit 1000 pmol of glucose in 3 mm^2 of surface, we would need around 455 glucose layers (0.25 nm each layer), which would can be ideally arranged as a layer-by-layer film. This film has, by approximation, 110 nm, that may be difficult to desorb from the CNWs surfaces. By comparison, 500 pmol would occupy approximatively 57 nm in thickness, comparable with the surface roughness, being easier to desorb from the CNWs. Thus, a maximum limit of the linear range of 1000 pmol it is rather logic and normal, as the above calculations do prove.

V.10. UV-VIS parameters for LSPR measurements

For this purpose a surface module was used. The methods and the measurements were performed as usual, in a 200-900 nm range, as gold nanoparticles have an LSPR peak around 520. The baseline was done using the glass or glass/AZO surfaces.

V.11. Sample deposition and mass spectrometry measurements

The deposition method is the following, unless otherwise stated: droplets of 0.5 µL were drop-casted on at least 3 different locations on 3 different as-received CNWs surfaces and were let to dry in air, during 1 h. Then, CNWs were fixed with a carbon conductive double-side adhesive tape on MTP TLC adapter (Bruker). The plate was then introduced into the mass spectrometer ion source. External calibration was performed with commercial peptide mixtures. The calibration curve and relative standard deviation calculations were obtained from inter-spot ($I \geq 6$), intra-spot ($I \geq 3$) and surface to surface ($I \geq 3$) mean values. Quantitative measurements of ricin B chain in blood serum and soft drinks and detection of other compounds were also performed using 6 different drop-casted spots.

© 2020 Tous droits réservés.
lilliad.univ-lille.fr

Thèse de Ioana Silvia Hosu, Université de Lille, 2020

Internal energies measurements were performed in similar way, using 3 spots for each benzylpyridinium compound. For the survival yield (S.Y.) determination the following equation was used:

$$S.Y. = \frac{I_{[M]^+}}{I_{[M]^+} + I_{[M-79]^+}} \quad \text{Eq.1}$$

Where the I represent the MS intensities of $[M]^+$ (benzylpyridinium compound) and $[M-79]^+$ (benzylium cation), after neutral loss of pyridine.

MALDI mass spectra were recorded on a Bruker Autoflex Speed instrument (Bruker Daltonics, Wissembourg, France) equipped with TOF analyser and LIFT module. A pulsed Smartbeam II 2 kHz laser at a wavelength of 355 nm (~3.49 eV) was operated at a frequency of 1000 Hz (MS data) with a delayed extraction time of 130 ns for smaller molecules and 350 ns for proteins. the source was operated in the positive mode. An acceleration voltage of 25.0 kV (IS1) was applied for a final acceleration of 21.95 kV (IS2).

Reflectron positive mode was used for peptides surface characterization and linear mode was chosen for proteins. Random laser irradiation was performed according to the partial sample mode with 5000 shots/point, for peptides and 500 shots/point for reflectron mode. Ions were detected over different mass ranges, according to the analysed samples. Data was acquired with the FlexControl software and processed with the Flex Analysis software. The mass range used in the protein cases was 4000-100000 m/z and below 10000 for refletron mode. Similar ranges and parameters were used for other molecules. The signal to noise ratio (S/N) was set to be minimum 3 and all the laser percentages represent the absolute value of the laser, not the relative laser power presented in the GUI (Graphical User Interface), from Flexcontrol 3.4 software.

V.12. Instrumentation

Scanning Electron Microscopy. SEM images were obtained using an electron microscope ULTRA 55 (Zeiss) equipped with a thermal field emission emitter with three different detectors: EsB detector with filter grid, high efficiency In-lens SE detector and Everhart-Thornley Secondary Electron Detector.

Water contact angle measurements. Water contact angles values were measured using deionized water. We used a remote-computer controlled goniometer system (DIGIDROP by GBX, France) for measuring the contact angles. The accuracy is ± 2°. All measurements were made in ambient atmosphere at room temperature, three times for each surface.

© 2020 Tous droits réservés.
lilliad.univ-lille.fr

Reflectance and UV-Vis measurements. The reflectance measurements were performed using an UV−vis spectrophotometer (Perkin- Elmer Lambda UV/vis 950 spectrophotometer, with Universal Reflectance Accessory Snap-on module), equipped with an integrating sphere. Reflectance was measured in the 200 – 900 nm range at an incident light angle of 45°.

Photoluminescence spectroscopy. The 351 nm line of a 30 MW argon laser was used to record the PL spectra at room temperature. The laser beam was focused with a 100 mm focal length lens to produce a 300 micron diameter spot on the sample, during 20 s. The incident power on the sample was 5 MW. The luminescence emitted by the specimen was analysed by a triple monochromator Dilor RT 30, and then detected using a Hamamatsu R943 photomultiplier in the photon counting mode. The PL spectra have not been corrected for the detection response.

Raman spectroscopy. Micro-Raman spectroscopy measurements were performed on a Horiba Jobin Yvon LabRam HR Micro-Raman system combined with a 473-nm laser diode as excitation source. Visible light was focused by a 100× objective. The scattered light was collected by the same objective in backscattering configuration, dispersed by a 1800 mm focal length monochromator and detected by a CCD. (software for data analysis: LabSpec5).

Diffuse reflectance spectroscopy. The diffuse reflectance absorption spectra (DRS) of the CNW samples were recorded on a UV–Vis-NIR spectroradiometric system (OL 750, Gooch & Housego, US) attached with an integrated sphere, and the spectra were recorded in the range of 350–1800 nm.

X-ray photoelectron spectroscopy. For X-ray photoelectron spectroscopy (XPS) measurements (Type 5600, Physical Electronics Inc., Chanhassen, MN, USA), we used a monochromatic Al Kα X-ray source and an analyzer pass energy of 12 eV. The acceptance angle of the analyzer has been set to 14°, and the angle between the incident X-rays and the analyzer is 90°. The detection angle of the photoelectrons is 25°, as referenced to the sample surface. The intensities of the various XPS core levels (CLs) are measured as the peak area after standard background subtraction according to the Shirley procedure. (software for data analysis: CasaXPS).

Mass Spectrometry. MALDI mass spectra were recorded on a Bruker Autoflex Speed instrument (Bruker Daltonics, Wissembourg, France) equipped with TOF analyser and LIFT module. A pulsed Smartbeam II 2 kHz laser at a wavelength of 355 nm (~3.49 eV) was

© 2020 Tous droits réservés.
lilliad.univ-lille.fr

operated at a frequency of 1000 Hz (MS data) with a delayed extraction time of 130 ns. The source was operated in the positive mode. An acceleration voltage of 25.0 kV (IS1) was applied for a final acceleration of 21.95 kV (IS2).

Linear and reflectron positive mode was used for peptides and reflectron mode was chosen for the saccharides and other compounds. Random laser irradiation was performed according to the partial sample mode with 10 shots/point. Ions were detected over different mass ranges, according to the analysed samples. Data were acquired with the FlexControl software and processed with the Flex Analysis software. The mass range used in the analysis of saccharides was 100-1000 m/z (or 100-11000 m/z for dextran, respectively). Similar ranges and parameters were used for other molecules. The signal to noise ratio (S/N) was set to be minimum 3 and all the laser percentages represent the absolute value of the laser, not the relative laser power presented in the GUI (Graphical User Interface), from Flexcontrol 3.4 software.

Zeta-potential measurements. Zeta-potential measurements were performed using a Zeta-sizer Nano-ZS (Malvern Instruments Inc. Worcestershire, UK). Samples were diluted to 25 µg/mL and measured in Milli-Q water at pH 7.0.

Atomic force microscopy (AFM). (software for data analysis: WSxM4)

Safety Considerations. The mixture H_2SO_4/H_2O_2 (piranha) solution is a strong oxidant. It reacts violently with organic materials. It can cause severe skin burns. It must be handled with extreme care in a well-ventilated fume hood while wearing appropriate chemical safety protection.

© 2020 Tous droits réservés.
lilliad.univ-lille.fr

V.13. References

1 Tang, H.-W., Ng, K.-M., Lu, W. & Che, C.-M. Ion desorption efficiency and internal energy transfer in carbon-based surface-assisted laser desorption/ionization mass spectrometry: Desorption mechanism (s) and the design of SALDI substrates. *Analytical chemistry* **81**, 4720-4729 (2009).

2 Bogdanowicz, R. *et al.* Improved surface coverage of an optical fibre with nanocrystalline diamond by the application of dip-coating seeding. *Diamond and Related Materials* **55**, 52-63, doi:https://doi.org/10.1016/j.diamond.2015.03.007 (2015).

3 Bogdanowicz, R. Characterization of optical and electrical properties of transparent conductive boron-doped diamond thin films grown on fused silica. *Metrology and Measurement Systems* **21**, 685-698 (2014).

4 Piret, G., Drobecq, H., Coffinier, Y., Melnyk, O. & Boukherroub, R. Matrix-Free Laser Desorption/Ionization Mass Spectrometry on Silicon Nanowire Arrays Prepared by Chemical Etching of Crystalline Silicon. *Langmuir* **26**, 1354-1361, doi:10.1021/la902266x (2010).

5 Deokar, G. *et al.* Towards high quality CVD graphene growth and transfer. *Carbon* **89**, 82-92, doi:https://doi.org/10.1016/j.carbon.2015.03.017 (2015).

6 Azevedo, J. l. *et al.* Versatile Wafer-Scale Technique for the Formation of Ultrasmooth and Thickness-Controlled Graphene Oxide Films Based on Very Large Flakes. *ACS applied materials & interfaces* **7**, 21270-21277 (2015).

7 BeMiller, J. N. in *Food analysis* 147-177 (Springer, 2010).

8 Coffinier, Y., Szunerits, S., Drobecq, H., Melnyk, O. & Boukherroub, R. Diamond nanowires for highly sensitive matrix-free mass spectrometry analysis of small molecules. *Nanoscale* **4**, 231-238 (2012).

9 Piret, G., Drobecq, H., Coffinier, Y., Melnyk, O. & Boukherroub, R. Matrix-free laser desorption/ionization mass spectrometry on silicon nanowire arrays prepared by chemical etching of crystalline silicon. *Langmuir* **26**, 1354-1361 (2009).

10 Lourvanij, K. *Partial dehydration of glucose to oxygenated hydrocarbons in molecular-sieving catalysts*, (1995).

© 2020 Tous droits réservés.
lilliad.univ-lille.fr

Annexe 1

Thèse de Ioana Silvia Hosu, Université de Lille, 2020

Nanoscale

PAPER

View Article Online
View Journal | View Issue

Check for updates

Cite this: *Nanoscale*, 2017, **9**, 9701

Published on 09 June 2017. Downloaded by Univ Lille 1 on 24/08/2017 11:52:11.

Carbon nanowalls: a new versatile graphene based interface for the laser desorption/ionization-mass spectrometry detection of small compounds in real samples†

I. S. Hosu,[a] M. Sobaszek,[b] M. Ficek,[b] R. Bogdanowicz,[b] H. Drobecq,[c] L. Boussekey,[d] A. Barras,[a] O. Melnyk,[c] R. Boukherroub[a] and Y. Coffinier *[a]

Received 13th February 2017,
Accepted 7th June 2017

DOI: 10.1039/c7nr01069a

rsc.li/nanoscale

Carbon nanowalls, vertically aligned graphene nanosheets, attract attention owing to their tunable band gap, high conductivity, high mechanical robustness, high optical absorbance and other remarkable properties. In this paper, we report for the first time the use of hydrophobic boron-doped carbon nanowalls (CNWs) for laser desorption/ionization of small compounds and their subsequent detection by mass spectrometry (LDI-MS). The proposed method offers sensitive detection of various small molecules in the absence of an organic matrix. The CNWs were grown by microwave plasma enhanced chemical vapor deposition (MW-PECVD), using a boron–carbon gas flow ratio of 1200 in H_2/CH_4 plasma, on silicon <100> wafer. The hydrophobicity of the surface offers a straightforward MS sample deposition, consisting of drop casting solutions of analytes and drying in air. Limits of detection in the picomolar and femtomolar ranges (25 fmol μL^{-1} for neurotensin) were achieved for different types of compounds (fatty acids, lipids, metabolites, saccharides and peptides) having clinical or food industry applications. This rapid and sensitive procedure can also be used for quantitative measurements without internal standards with RSDs <19%, as in the case of glucose in aqueous solutions (LOD = 0.32 ± 0.02 pmol), blood serum or soft drinks. Moreover, melamine (63 ± 8.19 ng μL^{-1}), a toxic compound, together with creatinine and paracetamol, was detected in urine samples, while lecithin was detected in food supplements.

Introduction

Carbon nanowalls (CNWs) consist of vertically aligned and packed nanosheets of graphene that can be grown using low temperature plasma based processes (DC, RF and microwave discharges). Whereas one of the most used techniques is PECVD (plasma-enhanced chemical vapour deposition), its main advantage is a catalyst-free based process, making possible the growth of CNWs on different substrates, without metallic contamination. Microwave plasma PECVD is known to create high quality and free-standing CNWs.[1]

Recently, many researchers showed a great deal of interest in CNWs and many applications have already been described in the literature (Fig. 1) such as field electron emitters, catalyst supports/templates, and hydrophobic coating (due to the H or F terminations).[2] Thanks to their remarkable optical properties (very low reflectance, high specific absorbance in thin transparent films), there is the possibility of using CNWs as dark coating for a bolometer absorber.[3] The ability to tailor the band gap of CNWs opens new doors to their usage in modern nano-electronics, as they can have semiconducting features. After the modification of the CNWs with metal nanoparticles, detection of the Rhodamine 6G dye was performed using surface enhanced Raman spectrometry,[4] while the change in their resistivity was used to detect volatile organic compounds (VOCs).[5] Biocompatible scaffolds for osteoblast culture and tissue engineering were also created using CNWs.[6] Electrophoretic deposition can be used to fabricate composite CNWs/graphite electrodes for the electrochemical detection of DNA sequences with estimated zeptomolar LODs.[7]

MALDI-MS (matrix-assisted laser desorption/ionization mass spectrometry) discovered in the 1980s.[8] Mixing the analyte with specific light-absorbing organic compounds and

[a]*Univ. Lille, CNRS, Centrale Lille, ISEN, Univ. Valenciennes, IEMN, UMR CNRS 8520, Avenue Poincaré, BP 60069 59652 Villeneuve d'Ascq, France. E-mail: yannick.coffinier@univ-lille1.fr; Fax: +333 20 19 78 84; Tel: +333 20 19 79 87*

[b]*Faculty of Electronics, Telecommunication and Informatics, Gdansk University of Technology, 11/12 Narutowicza St. 80-233, Gdansk, Poland*

[c]*Institut de biologie de Lille, UMR CNRS 8160, 59000 Lille, France*

[d]*Unité Matériaux et transformations (UMET), UMR CNRS 8207, Université Lille1, Cité Scientifique, 59655 Villeneuve d'Ascq, France*

†Electronic supplementary information (ESI) available. See DOI: 10.1039/c7nr01069a

Annexe

Blank page

© 2020 Tous droits réservés.

lilliad.univ-lille.fr

Thèse de Ioana Silvia Hosu, Université de Lille, 2020

Talanta 171 (2017) 101–107

Contents lists available at ScienceDirect

Talanta

journal homepage: www.elsevier.com/locate/talanta

MoS_2/TiO_2/SiNW surface as an effective substrate for LDI-MS detection of glucose and glutathione in real samples

Abderrahmane Hamdi[a,b,c,e], Ioana Silvia Hosu[a], Ahmed Addad[d], Ruben Hartkoorn[f], Hervé Drobecq[e], Oleg Melnyk[e], Hatem Ezzaouia[b], Rabah Boukherroub[a], Yannick Coffinier[a,*]

[a] Univ. Lille, CNRS, Centrale Lille, ISEN, Univ. Valenciennes, IEMN, UMR CNRS 8520, Avenue Poincaré, BP 60069, 59652 Villeneuve d'Ascq, France
[b] Laboratory of Semi-conductors, Nano-structures and Advanced Technologies, Research and Technology Centre of Energy, Borj-Cedria Science and Technology Park, BP 95, 2050 Hammam-Lif, Tunisia
[c] Faculty of Science of Bizerte, University of Carthage, 7021 Zarzouna, Tunisia
[d] Unité Matériaux et transformations (UMET), UMR CNRS 8207, Université Lille1, Cité Scientifique, 59655 Villeneuve d'Ascq, France
[e] Institut de biologie de Lille, UMR CNRS 8160, 59000 Lille, France
[f] Chemical Biology of Antibiotics, Center for Infection and Immunity, Inserm U1019, CNRS UMR8204, Institut Pasteur de Lille, Université de Lille, Lille, France

ARTICLE INFO

Keywords:
Silicon nanowires
MoS_2 nanosheets
LDI-MS
Glucose
Glutathione detection
Serum

ABSTRACT

Here, we report for the first time, the use of molybdenum disulfide/titanium oxide/silicon nanowires (MoS_2/TiO_2/SiNW) surfaces for SALDI-MS detection as alternative to MALDI-MS method. Silicon nanowires were fabricated by the well-known metal-assisted chemical etching process followed by the deposition of TiO_2 by atomic layer deposition. MoS_2 deposition was achieved through hydrothermal treatment. The MoS_2/TiO_2/SiNW substrate has shown high performance for the detection of small compounds of different molecular weights, including glutathione, glucose, amino acids, antibiotics to name a few. All of the tested compounds, in pure or in mixed solutions were successfully detected in positive ion mode. Therefore, we have also attempted quantitative measurements of GSH and glucose in human blood serum.

1. Introduction

Glucose and glutathione (GSH) are two compounds involved in many biochemical processes. Their chronic disorders (*e.g.* changes in their plasma level) are used as biomarkers for disease diagnosis. Glutathione, a tripeptide (Glu–Cys–Gly), plays a crucial role as an antioxidant compound involved in many detoxification procedures (*e.g.* help for heavy metal removal), but also has a protective role against oxidative stress (free radicals) preventing damage to cellular components. Irregular level of GSH is an indication of several diseases such as aging, Parkinson, Alzheimer and Huntington neurodegenerative diseases, cancers, diabetes, heart problems, AIDS and liver damage. The usual range of GSH concentrations in healthy human is in a range of 0.684–2.525 mmol L^{-1} in blood and 2.22–11.36 μmol L^{-1} in plasma [1,2]. Various methods have been developed to assess the level of GSH. Among the most used, we can find electrochemical analysis, high performance liquid chromatography (HPLC), surface-enhanced Raman scattering (SERS), fluorescence and colorimetric methods [3].

On the other hand, diabetes is a chronic disease that has devastating human, social, and economic consequences. According to the World Health Organization (WHO) and the International Diabetes Federation, its worldwide prevalence is projected to double over the next couple of decades, from 347 million people in 2005 to 700 million people in 2030. There are 3 types of diabetes. Type I diabetes, an insulino-dependent diabetes also called mellitus or juvenile diabetes. It is caused by deficient insulin production within the body and typically manifests among the youth. Type II diabetes is noninsulino-dependent and is caused by insulin resistance, a condition in which the target organs develop a failure to properly respond to insulin. Type II diabetes is termed adult-onset diabetes and makes up > 95% of all cases. The last one is a gestational diabetes appearing during pregnancy. Despite the lack of any known cure for diabetes, researchers managed to improve treatment efficiency to alleviate its symptoms and diminish its complications through appropriate medication and blood sugar monitoring, to improve treatment decisions and glucose control. So, many efforts have been made to develop sensitive, reliable, and robust glucose sensors for glycemia monitoring. Among them, electrochemical sensors have been considered as excellent analytical tools for rapid and efficient glucose-determination. Most of them are based on the use of enzymes. But some drawbacks arised such as a lack of stability over

* Corresponding author.
E-mail address: yannick.coffinier@univ-lille1.fr (Y. Coffinier).

http://dx.doi.org/10.1016/j.talanta.2017.04.061
Received 7 January 2017; Received in revised form 25 April 2017; Accepted 26 April 2017
Available online 27 April 2017
0039-9140/ © 2017 Elsevier B.V. All rights reserved.

Annexe

Blank page

© 2020 Tous droits réservés.

lilliad.univ-lille.fr

Annexe 3

Analyst

Thèse de Ioana Silvia Hosu, Université de Lille, 2020

ROYAL SOCIETY OF CHEMISTRY

PAPER

View Article Online
View Journal | View Issue

Check for updates

Cite this: *Analyst*, 2020, **145**, 1328

Influence of buried oxide layers of nanostructured SOI surfaces on matrix-free LDI-MS performances†

Abderrahmane Hamdi, Ioana Silvia Hosu and Yannick Coffinier *

In this paper, we report on the nanostructuration of the silicon crystalline top layer of different "home-made" SOI substrates presenting various buried oxide (BOx) layer thicknesses. The nanostructuration was achieved *via* a one-step metal assisted chemical etching (MACE) procedure. The etched N-SOI substrate surfaces were then characterized by AFM, SEM and photoluminescence. To investigate their laser desorption/ionization mass spectrometry performances, the different surfaces have been assessed towards peptide mixtures. We have shown that the matrix-free LDI process occurred from surface heating after laser irradiation and was fostered by thermal confinement in the thin nanostructured Si surface layer. This thermal confinement was enhanced with the increase of the buried oxide layer thickness until an optimal thickness of 200 nm for which the best results in terms of signal intensities, peptide discrimination and spot to spot and surface to surface variations were found.

Received 30th October 2019,
Accepted 20th December 2019

DOI: 10.1039/c9an02181g

rsc.li/analyst

Published on 23 December 2019. Downloaded by Univ Lille 1 on 5/6/2020 3:50:47 AM.

1. Introduction

A matrix-free laser desorption/ionization (LDI) process known as SALDI (surface-assisted laser desorption/ionization) has been developed to limit the background coming from adducts and fragments of organic matrices present in the low molecular mass region during matrix assisted laser desorption ionization mass spectrometry (MALDI-MS). The detection of small compounds, below 700 Da, is thus hampered when MALDI-MS is performed. The SALDI process mainly uses nanomaterials made of semi-conductors, metals, metal oxides and carbon-based structures. They present several advantages for the analysis of small compounds:[1] (i) no need of co-crystallization of the analytes with the organic matrix, thus suppressing the intense background from matrix peaks.[2–4] (ii) Simplicity of sample deposition and (iii) better reproducibility of results. All these advantages make the SALDI surface suitable for high throughput analyses and make possible their integration in lab-on-chip devices.[5,6] Moreover, by controlling their shape, morphologies, porosities and dimensions (particles, nanowires...) their optical, electrical and thermal properties can be tuned for SALDI-MS applications.[1,7] For decades, SALDI surfaces presenting different shape and dimensions such as 0D (particles), 1D (nanowire/nanotubes) or 2D films (graphene, MoS_2) have been tested as LDI materials.[8–11] Recently, a new class of plasmonic metal materials has emerged as LDI-MS substrates. Indeed, gold particles, mesoporous organosilica@Ag Janus particles or magnetic@SiO_2@Ag particles have shown very promising applications for the detection of nutrients, cervical and lung cancers and bacterial metabolism analysis.[12–17] However, porous silicon is still one of the most used SALDI materials, notably due to its high specific surface area, straightforward preparation, UV absorption, and anti-reflective and low thermal properties (heat confinement) (see Table 1).[18]

The matrix-free LDI process is mainly based on a thermal driven mechanism. It comprises several occurring concomitant phenomena such as energy absorption (from laser), desorption and ionization steps.[19] So, to perform SALDI-MS ana-

Table 1 SALDI interface properties and their advantages *vs.* MALDI

Surface properties	Advantages/MALDI
Optical properties: UV absorbent, anti-reflectiveness	No organic matrices Simple deposition method, uniform distribution of analytes – no "hot spots"
Thermal properties: low thermal conductivity, heat confinement	Low laser fluence-limitation of fragmentation Low background
Chemical modifications: reproducibility, affinity capture, activation energy	High specific surface area Great adsorption capacity of analytes
Other parameters influencing LDI performances: porosity, dimensions, doping	Sensitive towards small compounds <10 000 Da Salt tolerant, adaptable to any MALDI-ToF instrument

Univ. Lille, CNRS, Centrale Lille, ISEN, Univ. Valenciennes, IEMN, UMR CNRS 8520, Avenue Poincaré, BP 60069, 59652 Villeneuve d'Ascq, France.
E-mail: yannick.coffinier@univ-lille.fr; Fax: +33 (0)3.62.53.17.01;
Tel: +33 320197987

†Electronic supplementary information (ESI) available. See DOI: 10.1039/c9an02181g

This journal is © The Royal Society of Chemistry 2020

Annexe

Blank page

© 2020 Tous droits réservés.

lilliad.univ-lille.fr

Talanta 178 (2018) 432–440

Contents lists available at ScienceDirect

Talanta

journal homepage: www.elsevier.com/locate/talanta

Controlled modification of electrochemical microsystems with polyethylenimine/reduced graphene oxide using electrophoretic deposition: Sensing of dopamine levels in meat samples

Karima Kahlouche[a,b,c,d,1], Roxana Jijie[a,1], Ioana Hosu[a], Alexandre Barras[a], Tijani Gharbi[b], Reda Yahiaoui[b], Guillaume Herlem[b], Marhoun Ferhat[d], Sabine Szunerits[a,*], Rabah Boukherroub[a,*]

[a] Univ. Lille, CNRS, Central Lille, ISEN, Univ. Valenciennes, UMR 8520, IEMN, F-59000 Lille, France
[b] Laboratoire de Nanomédecine, imagerie et thérapeutique, EA 4662, Université de Franche-Comté, 16 Route de Gray, 25030 Besançon, France
[c] Centre for Development of Advanced Technologies (CDTA), Baba Hassen, Algeria
[d] Semiconductors and Functional Materials Laboratory, University of Laghouat, Algeria

ARTICLE INFO

Keywords:
Electrochemical microsystem
Reduced graphene oxide
Polyethylenimine
Electrophoretic deposition
Dopamine
Sensing
Meat

ABSTRACT

Microsystems play an important role in many biological and environmental applications. The integration of electrical interfaces into such miniaturized systems provides new opportunities for electrochemical sensing where high sensitivity and selectivity towards the analyte are requested. This can be only achieved upon controlled functionalization of the working electrode, a challenge for compact microsystems. In this work, we demonstrate the benefit of electrophoretic deposition (EPD) of reduced graphene oxide/polyethylenimine (rGO/PEI) for the selective modification of a gold (Au) microelectrode in a microsystem comprising a Pt counter and a Ag/AgCl reference electrode. The functionalized microsystem was successfully applied for the sensing of dopamine with a detection limit of 50 nM. Additionally, the microsystem exhibited good performance for the detection of dopamine levels in meat samples.

1. Introduction

Advances in different multidisciplinary areas, as is the case of microelectronics and materials science, open the door for the development of innovative solutions in many different fields, including sensing based devices. Electrochemical sensors represent, next to optical transducers, a commercially-proven concept and an attractive means capable of analyzing the content of real samples in a highly sensitive, miniaturized and cost-effective manner even in vivo [1]. Over the past decades, several electrochemical based sensing concepts and related devices have been developed [1–3]. However, when using classical electrode materials, sensitivity and selectivity issues have shown to limit their use for real applications.

Carbon-based materials are considered ideal electrode materials due to their wide anodic potential range, low residual current, chemical inertness, ease of processing, availability and low cost [4,5]. These electrodes possess attractive electrochemical activity with high mechanical stability, in addition to the availability of various forms of carbon in nature. Moreover, carbon-based electrodes exhibit fast response time and can easily be fabricated in different configurations and sizes. There are several critical aspects to improve the sensing ability of carbon-based sensing systems. For sensors of comparable size, the surface to volume ratio controls the number of active sites that are in contact with the analytes and thus the sensitivity. The efficiency of the electronic interactions between the electrochemical surface and the analyte on the other hand directly affects the measurement. Large surface area coupled with high mobility and conductivity are potential advantages of graphene for electrochemical sensors, widely explored since some years [6–15]. Next to pristine graphene, reduced graphene oxide (rGO) and its derivatives have in particular found large interest for electrochemical sensing applications. While drop-casting is commonly used for the formation of rGO modified electrical interfaces, this approach is not well adapted for the modification of electrochemical microsystems.

We have demonstrated in several reports that electrophoretic deposition (EPD) offers several advantages over other surface coating

* Corresponding authors.
E-mail addresses: sabine.szunerits@univ-lille1.fr (S. Szunerits), rabah.boukherroub@univ-lille1.fr (R. Boukherroub).
[1] Contributed equally to this work.

http://dx.doi.org/10.1016/j.talanta.2017.09.065
Received 21 August 2017; Received in revised form 19 September 2017; Accepted 22 September 2017
Available online 25 September 2017
0039-9140/ © 2017 Elsevier B.V. All rights reserved.

Annexe

Blank page

© 2020 Tous droits réservés.

lilliad.univ-lille.fr